



Delft University of Technology

Integrated Sensors for Organ-on-Chip Platforms

Aydogmus, H.

DOI

[10.4233/uuid:0c1d19c5-4196-4c62-9800-779974b74043](https://doi.org/10.4233/uuid:0c1d19c5-4196-4c62-9800-779974b74043)

Publication date

2024

Document Version

Final published version

Citation (APA)

Aydogmus, H. (2024). *Integrated Sensors for Organ-on-Chip Platforms*. [Dissertation (TU Delft), Delft University of Technology]. <https://doi.org/10.4233/uuid:0c1d19c5-4196-4c62-9800-779974b74043>

Important note

To cite this publication, please use the final published version (if applicable). Please check the document version above.

Copyright

Other than for strictly personal use, it is not permitted to download, forward or distribute the text or part of it, without the consent of the author(s) and/or copyright holder(s), unless the work is under an open content license such as Creative Commons.

Takedown policy

Please contact us and provide details if you believe this document breaches copyrights. We will remove access to the work immediately and investigate your claim.

*This work is downloaded from Delft University of Technology.
For technical reasons the number of authors shown on this cover page is limited to a maximum of 10.*

INTEGRATED SENSORS FOR ORGAN-ON-CHIP PLATFORMS

INTEGRATED SENSORS FOR ORGAN-ON-CHIP PLATFORMS

Proefschrift

ter verkrijging van de graad van doctor
aan de Technische Universiteit Delft,
op gezag van de Rector Magnificus Prof. dr. ir. T.H.J.J. van der Hagen,
voorzitter van het College voor Promoties,
in het openbaar te verdedigen op maandag 23 september 2024 om 10:00 uur

door

Hande AYDOGMUS

Master of Science in Mechanical Engineering, Bilkent University, Ankara, Turkije
geboren te Ankara, Turkije.

Dit proefschrift is goedgekeurd door de promotoren.

Samenstelling promotiecommissie:

Rector Magnificus,	Voorzitter
Em. Prof. dr. ir. P.M. Sarro,	Technische Universiteit Delft, Promotor
dr. M. Mastrangeli,	Technische Universiteit Delft, Promotor

Onafhankelijke leden:

Prof. dr. ir. R. Dekker,	Technische Universiteit Delft
Prof. dr. G. Barillaro,	University of Pisa, Italië
Dr. J.P. Frimat,	Leids Universitair Medisch Centrum
Prof. dr. M.S. Hanay,	Bilkent University, Turkije
Dr. M. Zevenbergen,	Stichting IMEC the Nederland
Prof. dr. ir. W. van Driel,	Technische Universiteit Delft, reservelid



Keywords: Organ-on-Chip, Microfabrication, pH Sensing, Charge Sensor, Floating-Gate Field-Effect-Transistor

Printed by: Proefschrift Maken

Front & Back: Proefschrift Maken

Copyright © 2024 by H. Aydogmus

An electronic version of this dissertation is available at
<http://repository.tudelft.nl/>.

If one day, my words are against science, choose science.

M. Kemal Atatürk

CONTENTS

Summary	xi
Samenvatting	xiii
1 Sensing in Organs-on-Chip	1
1.1 The Drug Development Process	2
1.2 Introduction to Organ-on-Chip	2
1.3 Sensing Types for Organs-on-Chip	4
1.3.1 Electrical Sensing	4
1.3.2 Optical Sensing	7
1.3.3 Microwave Sensing	7
1.3.4 Electrochemical Sensing	8
1.3.5 Selectivity in Electrochemical Sensors	10
1.4 OoC Platforms	11
1.5 Discussion	12
1.5.1 Importance of pH	12
1.5.2 Remarks	13
1.6 Research Questions	14
1.7 Thesis Overview	14
2 Silicon-Based FG-FET with MO_x Layer for Charge Sensing	23
2.1 Introduction	24
2.1.1 Metal Oxide Layers for pH Sensing	26
2.1.2 Aim of the Work	26
2.2 Electrode-Electrolyte Interface	28
2.3 Characteristics of the Field-Effect Transistor	32
2.4 Analysing The Electrode-Electrolyte Interface of the FET	36
2.5 Layout of the Sensor	39
2.6 Discussion & Conclusion	41
3 Fabrication and Characterization of Silicon-Based FG-FET	47
3.1 Fabrication	48
3.1.1 BICMOS Processing	48
3.1.2 Deposition of Metal Oxide to Enhance Sensitivity of pH Sensing	52
3.2 Characterization	56
3.2.1 Analysis of the Ion Implantation	56
3.2.2 Test Structures	58
3.2.3 Surface Analysis	59
3.2.4 Electrochemical Characterization	60
3.2.5 Electrical Characterization	63

3.3	Discussion & Conclusion	70
4	Silicon-Polymer-based FG-FETs for pH Sensing	75
4.1	Introduction	76
4.2	Characteristics of the Sensor	78
4.3	Discussion & Conclusion	80
5	Fabrication and Characterization of Silicon-Polymer FG-FET	85
5.1	Introduction	86
5.2	Polyimide Processing	87
5.3	Second Metal Layer	88
5.4	pdms Processing	91
5.5	Releasing the pdms Membrane	92
5.6	Packaging & Assembly	93
5.7	Remarks On Fabrication	95
5.8	Dry Measurements with Semiconductor Parameter Analyzer	96
5.9	Liquid Measurements with Semiconductor Parameter Analyzer	97
5.10	Real-time Measurements with Mobile Measurement Setup	97
5.10.1	Mobile Measurement Setup	97
5.10.2	Monitoring the Change in pH Levels	98
5.11	Remarks on Characterization	108
5.12	Conclusion	110
6	Functionalization of FG-FETs	115
6.1	Introduction	116
6.1.1	Potassium Selective Sensors	116
6.1.2	Potassium-Selective FG-FET-Based Sensor	118
6.1.3	Characterization	120
6.2	Sensing Surface Alteration via Gold Nanofilms	123
6.2.1	Post-processing for Electrode Surface Structuring	123
6.2.2	Characterization of Au NP Film Decorated FG Electrodes	124
6.3	Discussion & Conclusion	127
7	Microelectrodes for Monitoring Electrically-Active Cells	131
7.1	hiPSC-derived Cortical Neurons in Silicon-Polymer FG-FET Device	132
7.1.1	Introduction to hiPSCs	132
7.1.2	Utilization of Silicon-Polymer FG-FETs as Recording Electrodes	132
7.2	Biocompatibility Tests with Silicon-Polymer FG-FETs	133
7.3	Multi-Electrode Array-Compatible Recordings	133
7.3.1	Towards Measurements with Mobile Measurement Device	135
7.4	Discussion	138
7.5	Conclusion	139
8	Conclusion & Perspectives	143
8.1	Conclusions	144
8.2	Recommendations and Future Work	145
8.2.1	Multimodal Sensing	145
8.2.2	Integration of FG-FET Chips in the TOP	146

8.2.3	Going to High Frequencies: Using Microwave Resonators for Monitoring the Cell Wellbeing	148
APPENDIX		155
A	Circuit Analysis of the Device	157
B	MATLAB Model of the FET Device	159
C	Surface Analysis of MO_x Layers with EDX	165
D	Flowchart of the Silicon-Polymer FG-FET Device	167
E	Electrical Characterization	181
F	Biological Protocol	185
	Acknowledgements	189
	List of Publications	191

SUMMARY

Organs-on-Chip (OoC) has been an advancing biotechnological field for the last two decades. By combining engineering and biology, OoC technology makes it possible to mimic the in-vivo behavior of human organs to investigate personalized medicine and disease modeling in-vitro.

Integrating sensors into cell cultures is crucial since the well-being of the culture needs to be monitored in real-time and without compromising cell viability. Monitoring the pH level of the micro-environment is particularly important since it is an indicator of homeostasis for the cell well-being and products of cell metabolism can cause changes in pH, reflecting certain disease phenotypes.

In this work, the integration of electrochemical sensors into OoC devices was shown. The sensors are based on a floating-gate field-effect transistor (FG-FET), a variation of a common active electronic component, and are sensitive to local electric charge. The active component provides inherent amplification, which translates to higher sensitivity and resolution for smaller changes from segregated analytes. The FG-FET was capacitively coupled to two control-gates to determine the working point of the transistor. The sensing area (FG extension) was separated from the active FET area to ease the handling of analytes. When there is a net charge in close proximity to the extension of the FG, it induces a change in the formation of the channel of the transistor. This change can be monitored by the drain current.

Two different types of devices were fabricated and tested for pH sensing: Silicon-based and silicon-polymer-based hybrid FG-FETs. To investigate the sensitivity of silicon-based devices, TiO_x , HfO_x , and AlO_x layers were deposited at the sensing area and tested with liquids with different pH values.

In order to facilitate visual inspection for cell culturing, we integrated in the hybrid devices a transparent polymer membrane at the sensing area, where the sensing electrodes were suspended.

For both device types, we showed the functionalization of the sensing area as a post-processing step for further investigation of sensitivity and selectivity. For silicon-based devices, we decorated the sensing area with K^+ ionophore cocktail, and for silicon-polymer-based devices, we locally printed gold nanofilms on electrodes, and tested the device performance with analytes such as poly-d-lysine and KCl.

Finally, FG-FET extensions were used as passive microelectrode array electrodes to record electrical activity of hiPSC-derived cortical neurons. The OoC device with integrated sensors was suitably packaged with a printed circuit board to be compatible with a read-out unit for microelectrode arrays commonly used in biological laboratories. We also conducted preliminary experiments with FG-FETs run by means of a custom mobile measurement setup when the cells were cultured in the OoC device. The electrical recordings reflected the effect of the introduction of Picrotoxin, an epilepsy-inducing drug, by evidencing an increase in both mean value and fluctuations of the drain current.

Integrating FETs into OoC devices leads the way to obtaining relevant information, such as quantitative changes in the pH of the solutions under test (such as culture media) or recording electrical activity of electrically active cells (such as neurons), by easing the introduction of sensitive and very compact sensors into such inherently small devices as OoCs. By showing how this can be realized using wafer-scale microfabrication technology, this work additionally contributes to opening vistas on the scalable fabrication of advanced microphysiological devices.

SAMENVATTING

Organ-on-Chip (OoC) is de afgelopen 20 jaar een vooruitstrevende biotechnische sector geweest. Door het combineren van techniek en biologie heeft OoC het mogelijk gemaakt studies te doen naar levende menselijke organen. En daarnaast onderzoek te doen naar gepersonaliseerde medicatie en ziektes in-vitro.

Het integreren van sensoren in celculturen is van vitaal belang om de gesteldheid van de cellen continu te monitoren zonder dat dit de cellen schade toe brengt. Met is met name belangrijk de zuurtegraad te meten in de micro-omgeving van de cel. Dit is een indicator van de homeostase van de cel gesteldheid waar de producten van cel metabolisme de zuurtegraad doen wijzing. Het geen aanduidingen van bepaalde ziektebeelden doet voorkomen.

In dit werk wordt de integratie van elektrochemische sensoren in OoC beschreven. De sensoren zijn gebaseerd op een veldeffect transistor met zwevende poort als actief component en zijn gevoelig voor lokale elektrische lading. De transistor heeft intrinsieke versterking en draagt hierdoor bij aan het verkrijgen van een hogere resolutie. De resolutie wordt bereikt door de hoge gevoeligheid voor kleine veranderingen in gescheiden analieten. De transistor is capacitief gekoppeld aan de controle poorten welke het werkpoort van de transistor bepalen. Het sensor gebied is via een extensie van de zwevende poort gescheiden van het actieve deel van de transistor. Dit maakt het werken met de analieten gemakkelijker. Wanneer een lading zich in de buurt van het sensor gebied bevindt, induceert dit een verandering in het veld van de transistor. Deze verandering is te zien in de stroom die door de transistor loopt.

Twee verschillende soorten transistoren zijn gefabriceerd en getest voor het meten van zuurtegraad. Een silicium veldeffect transistor en een silicium polymeer hybride veldeffect transistor. Om de gevoeligheid van een silicium gebaseerde transistor te onderzoeken, zijn er TiO_x , HfO_x , en AlO_x lagen aangebracht en getest met vloeistoffen welke verschillende zuurtegraden hebben.

Om visuele inspectie van de cellen mogelijk te maken zijn bij de silicium polymeer hybriden transparante membranen gebruikt. Met name in het sensor gebied waar de voelende elektroden ingebed zijn.

Voor beide type transistoren tonen wij de functionaliteit van het sensor gebied als na bewerking stappen. Dit kan gebruikt worden voor verder onderzoek ter verbetering van gevoeligheid en selectiviteit. Voor silicium gebaseerde transistoren is een K^+ ionofoor laag toegepast. Voor de silicium polymeer hebben we lokaal gouden nano-film op de elektroden geprint. Vervolgens zijn de sensoren getest met analieten als poly-d-lysine en KCl.

Ten slotte zijn voor het detecteren van de activiteit van hiPSC gebaseerde corticale neuronen de extensies van de poorten als passieve array gebruikt.

De OoC chip met integrale sensoren was voldoende verpakt met een geprint circuit, welke op een veel voorkomende uitlees kaart in bio-laboratoria aan te sluiten was. Ook

hebben we experimenten uitgevoerd met transistoren in een op maat gemaakte mobiele opstelling waarin cellen zijn gekweekt. De elektronische opnamen reflecteren het inbrengen van Picrotoxine, een epilepsie inducerende drug, in de cellen. Hiermee aantonnende een toename in beide de gemiddelde waarde en de fluctuaties in de stroom door de transistor.

Het integreren van veldeffect transistoren in OoC chips leidt de weg naar het verkrijgen van relevante informatie, zoals kwantitatieve informatie van veranderingen in de zuurtegraad van de geteste oplossingen of de elektrische activiteit van neuronen. Door aan te tonen dat zulke hoog gevoelige en compacte chips met wafer-microfabricage gemaakt kunnen worden, draagt dit bij aan de introductie van zulke chips op grote schaal van zulke hoogwaardige chips.

1

SENSING IN ORGANS-ON-CHIP

1.1. THE DRUG DEVELOPMENT PROCESS

Understanding cell biology, disease, and drug delivery mechanisms is crucial for various research fields such as human physiology, but also for pharmaceutical companies and medical professionals to address unanswered questions.

The development of a drug constitutes a complex and costly endeavor, with billions of dollars typically expended per drug [1] (Fig. 1.1). Despite extensive research phases, some novel drugs are withdrawn from the market due to unforeseen side effects, which poses a significant constraint on their universal applicability. To cite an example, between 2002 and 2011, 19 drugs were withdrawn from the market in the EU for safety reasons [2].

Efforts to replicate human physiology for preclinical drug development involve static two-dimensional cell and tissue cultures, along with animal testing. Two-dimensional cell cultures helped with understanding disease mechanisms for decades, but in the recent three-dimensional cultures, it was shown that the three-dimensional approach improves cell proliferation, differentiation, and cell survival [3]. Moreover, 2-D cell culturing models, mostly accepted in the industry for preclinical drug testing, cannot be compared to 3-D studies where oxygen and nutrient exposure will not be adequate [4]. While animal models have provided invaluable insights into various physiological mechanisms [5], it is recognized that they often fall short of accurately mimicking human physiology, and ethical considerations surrounding animal usage are contentious. Notably, differences in membrane transporters between species can lead to varying drug toxicities [6], [7]. Furthermore, ethical debates persist regarding the ethical implications of animal testing, with many advocating for alternative approaches [8]. As highlighted by Hajar et al., the ethical dilemma persists: "The benefit to humans does not justify the harm to animals" [9].

In response to these concerns, scientists are exploring innovative biotechnological solutions, fostering interdisciplinary collaborations to develop dynamic culturing devices as alternatives to traditional animal models.

1.2. INTRODUCTION TO ORGAN-ON-CHIP

Organ-on-chip (OoC) has been an advancing biotechnological field for the last two decades. By combining engineering and biology, OoC technology makes it possible to mimic the *in vivo* behavior of human organs in a dynamic and physiologically-relevant *in vitro* microenvironment to enhance disease modeling and drug development [10] (Fig. 1.2). There is a push towards creating dynamic devices capable of mimicking mechanical forces experienced by cells, as well as replicating material properties such as stiffness and biocompatibility within the cellular microenvironment while demonstrating long-term cell viability in order to study disease mechanisms effectively. Integrating biosensors, a field focused on identifying specific molecules indicative of cellular health or disease within a culture [11], into OoC platforms is important to demonstrate such events and monitor relevant secreted analytes from cell cultures.

Depending on the cell and model type, different sensors were developed to monitor the microenvironment of the cells. Some of these sensed parameters include, among other factors, O_2 concentration, pH level, glucose consumption, and enzymatic activ-

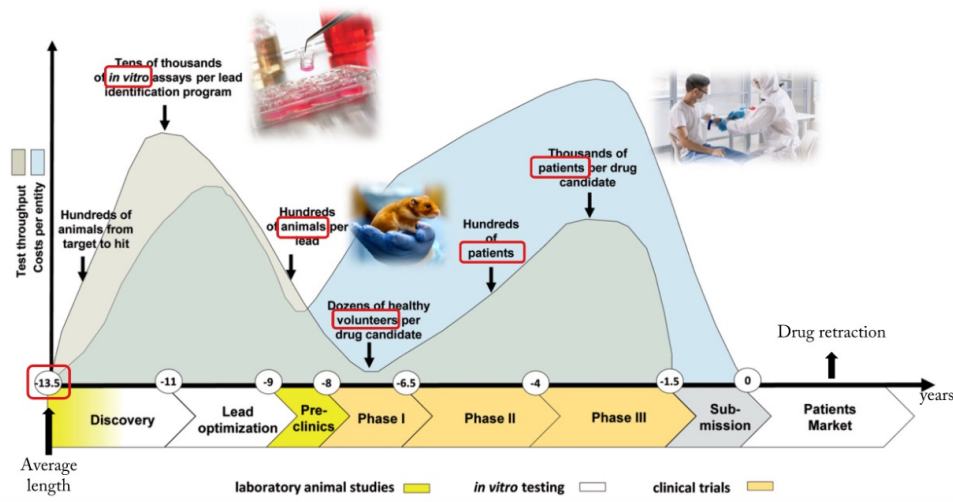


Figure 1.1: Development cycle for a new drug. X-axis shows the development time in years. Grey area shows the number of tests need to be performed for testing. Blue area shows the cost of the development of the drug. Adapted from [7].

ity [12]. Integration of such sensors with on-chip assays that usually rely on fluorescent microscopy, where the viability of the cells is at risk, increases the reliability of the concluded outcomes.

However, as stated before, to truly mimic *in vivo* cellular communication, there is a growing need for 3-D and more dynamic systems capable of simulating nutrient transport and waste removal in a miniaturized fashion and the integration of microfluidic channels for these purposes has propelled static biosensors to new heights.

While early microfluidic applications primarily served mass spectroscopy and inkjet nozzles [13], microfluidics quickly emerged as a solution for incorporating functionalities onto chips for biological purposes, notably in lab-on-a-chip technology. Beyond mere fluid transport, there is a growing emphasis on understanding cellular behavior.

In this regard, integrating microfluidics to deliver nutrients and ensure linkage between different organs and sensing modules became crucial for monitoring and controlling the environment to maintain the viability of the cells. This also led to having multiple OoCs in a single *platform*.

As a result, OoC is an interdisciplinary field that includes various research fields such as biosensors, microfluidics, mechanics, and materials to study the well-being of cell cultures and disease mechanisms. The main objective of this thesis is to demonstrate integrated sensors for OoCs in terms of robustness and biocompatibility. In the next section, the most common sensing types that were integrated into OoCs or which are good candidates for integration are reviewed. Depending on the analyte-under-test or cell/tissue culture, several sensors can be integrated into a chip.

Packaging of the chips is also crucial to have reliable electrical output. At the end of the fabrication, the chip is generally mounted to a printed circuit board (PCB), which pro-

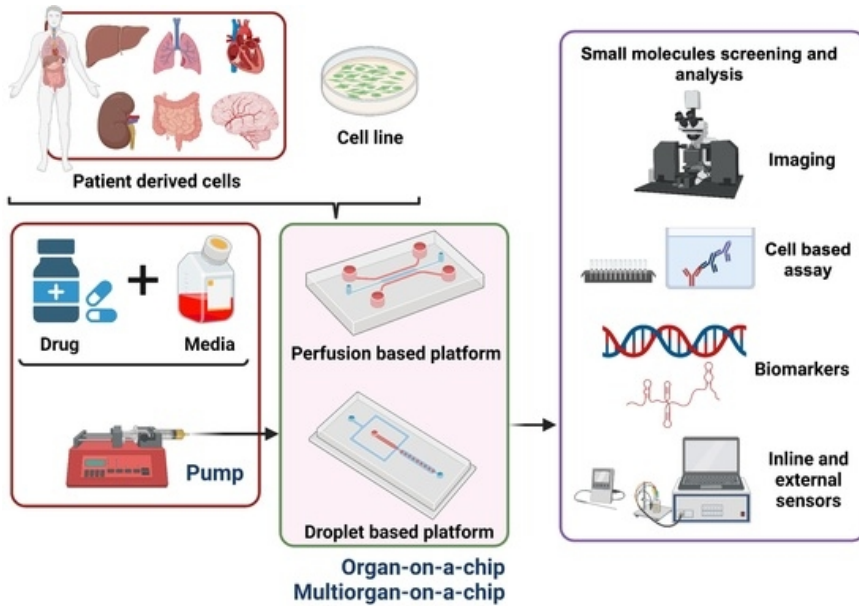


Figure 1.2: How does an OoC device work? Patient-derived or other types of cells are cultured with cell-specific medium and specific drug in a dynamic OoC device. Results can be based on optical imaging, electrical read-out, or cell-based assays. Adapted from [14].

vides an electrical connection to control electrical signals with electrical measurement equipment. Additionally, the PCB can also support the chip mechanically (Fig. 1.3).

1.3. SENSING TYPES FOR ORGANS-ON-CHIP

In this section, the most common sensing types will be reviewed. In particular, electrochemical sensing plays an important role in monitoring the viability of cell cultures. For this work, a specific electrochemical sensing method is chosen and will be highlighted and discussed in detail later in this section.

1.3.1. ELECTRICAL SENSING

In this section, barrier integrity analysis and monitoring of electrogenic cells will be described in detail in the context of OoC and biosensing experiments.

BARRIER INTEGRITY ANALYSIS

One of the most widely used electrical sensing systems for monitoring barrier integrity is transendothelial resistance analysis (TEER) [16]. This method is usually based on applying a voltage at DC or a single low frequency to evaluate the barrier integrity in terms of respective resistance or impedance. Examples of biological barriers focus on the vasculature, such as the blood-brain-barrier (BBB) [16] or intestinal vasculature [17], but can also include kidneys [18] or the skin [19].

Early TEER implementation was achieved by inserting mobile “chopstick” electrodes,

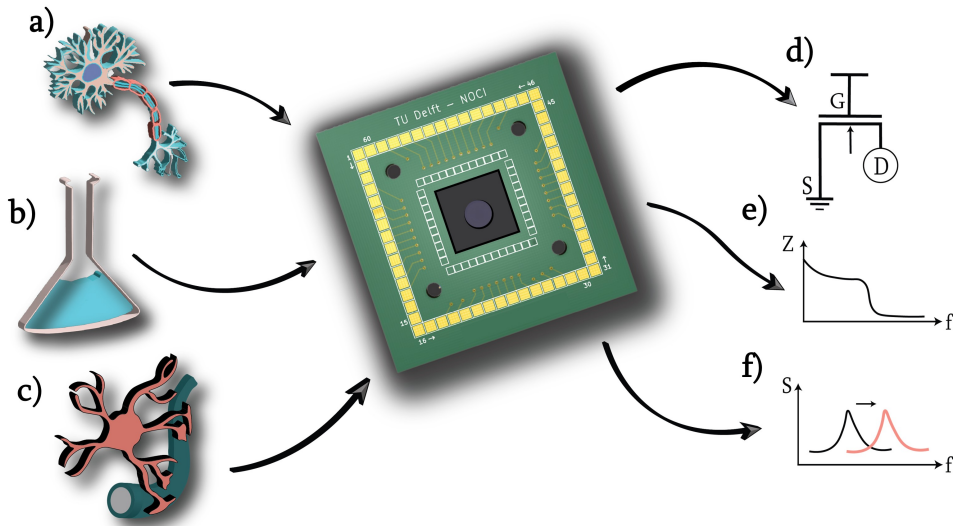


Figure 1.3: Schematic of a chip mounted on a PCB with various culture system compatibilities and sensing mechanisms. Examples of the former can be a) Cells such as neurons, b) Analytes such as medium after cell perfusion, or c) 3D tissue constructs such as the blood-brain-barrier or organoids. Examples of sensing mechanisms can be either d) Transistor-based circuits, e) Impedance spectroscopy, or f) Change in resonance frequency of a microwave resonator, depending on the cell conformation.

which were not integrated on chips [20] but rather in a transwell format. Later, integrated electrodes were employed in vasculature-on-chip (VoC) [21], gut-on-chip [22], and skin-on-chip [23] devices. Integrated electrodes allowed for the removal of any human-induced handling errors as the fixed placement of electrodes would eliminate the hardly reproducible placement of mobile electrodes for each measurement [24].

Although using single frequency or DC for resistance monitoring is straightforward, it is incomplete compared to impedance measurements, where capacitance can also reveal useful information about the well-being of the cells over time [25]. A more useful method for barrier integrity analysis can be impedance spectroscopy (IS). IS is based on frequency sweeps and is used to quantify the impedance spectrum (Fig. 1.4 a).

The main challenge in monitoring and measuring barrier integrity is the lack of standardized methods and setups, which makes it difficult to compare results in the literature. Some reasons for these inconsistencies stem from the difficulty in human-handling and fabrication of the chip or saturation of the electrodes after long-term use. In addition, the heterogeneity of biological materials is also an issue that can lead to a lack of data reproducibility. Furthermore, the methods can also vary, with differences occurring while monitoring the whole cell layer rather than locally around the electrodes, monitoring only the cell layer rather than cell media between electrodes and the cell layer, and addition of non-uniform current density over the cell coverage area.

One of the solutions to remove unwanted effects of media between the cell and electrode layers is the specific placing of electrodes, either on the membrane where the cells

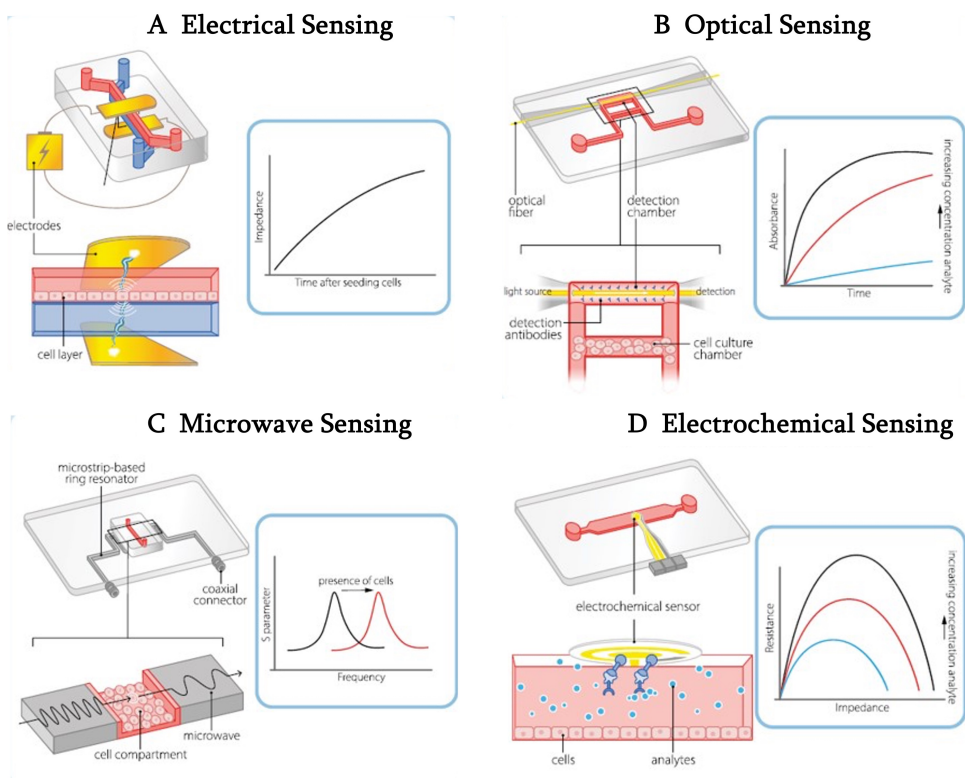


Figure 1.4: Schematic of common sensing modalities for OoCs: a) Electrical, b) Optical, c) Microwave, d) Electrochemical (Adapted from [15]).

are cultured or multiplexing the electrodes to have a more uniform current density [26, 27]. Going further, 3D measurements can provide more local and accurate information about the barrier integrity. For instance, tubular electroactive scaffolds can be useful for mimicking the vasculature structure while measuring the cell substrate coverage and vascular reactivity [28].

ELECTROPHYSIOLOGY MEASUREMENTS

Among organs, the brain consists of many different types of neurons and glial cells, which interact with each other in complex manners. Monitoring the activity of electrically-active cells, such as neurons, can lead to identifying various disease phenotypes [29, 30]. Researchers from interdisciplinary fields have been using electrodes for *in vivo* and *in vitro* recordings of action potentials [31] in various setups, in particular multi-electrode arrays (MEAs). Several brain-on-chip (BoC)-devices were developed which include MEAs. MEAs record the electrical activity of hundreds of neurons simultaneously in a relatively high-throughput manner, which is a robust functional readout to distinguish between healthy and diseased conditions [30]. Furthermore, MEAs have also been shown to be suitable for drug discovery and testing [32, 33, 34, 35]. Various neuronal and

glial cell types can be cultured on MEAs and form intricate neuronal networks. These neuronal networks can generate brain oscillations at various frequencies (from 0.05 Hz up to hundreds of Hz [36]). Different kinds of MEA devices exist including multiwell or single well MEAs, disposable MEAs [37], MEA with optical stimulation [38], and MEAs integrated with impedance spectroscopy in a microfluidic device for optimizing signal extraction [39].

Although there are commercially-available MEA systems to monitor the electrical activity of cells, moving towards 3D electrodes for accessing spatial information and transparent electrodes for optical visibility in standardized settings still needs to be addressed.

1.3.2. OPTICAL SENSING

Optical sensors usually consist of a light source and a detector, with an in-between analyte-under-test, which can be implemented into OoCs. Theoretically, optical waves from the source interfere with the test substrate, namely the cell layer, or segregated species from the cells, such as cytokines (small proteins that play an important role in cell-signaling [40]). Depending on the analyte properties, such as the refractive index, optical intensity variations can be monitored by the detector.

Several examples from the literature include an alternative for ELISA (enzyme-linked immunosorbent assay, used to examine the presence of antigens), a photonic lab-on-chip (Ph-LoC) device to measure optical absorbance to quantify cytokines [41], and an array of photonic microring resonators, which alters their resonance depending on the binding of the target molecules [42]. Since resonance is altered depending on the molecule, this method avoids additional specific labeling methods. These examples show that photonic sensors can monitor small biological cues such as cytokines, providing sensitive opportunities for OoC platforms to examine specific disease mechanisms (Fig. 1.4 b).

As an alternative to optical microscopy, optical coherence tomography (OCT) can be used externally to quantify physiological aspects such as tissue architecture and fluid flow in OoC devices. OCT uses coherent light sources to create an image in 3D. With OCT, real-time 3D imaging is possible without staining the cell layer. The backscattered light translates into reflection, which depends on the refractive index of the analyte [43]. Backscattered light is then used to reconstruct the substrate-under-test [44].

1.3.3. MICROWAVE SENSING

Microwave sensing holds great promise since it can allow label-free, non-intrusive, and real-time measurements. It is based on measuring the alteration of electromagnetic waves in a specific frequency spectrum. Wave penetration depends on the electrical characteristics of the materials, mainly the permittivity. For instance, even though different cells may have similar shapes, identification at microwave frequencies is possible from the specific permittivity of the cells since electromagnetic waves at microwave frequencies can penetrate the cells while leaving them intact and revealing information about the intracellular composition [45].

There has been already an ongoing research for microwave sensors in biology for the last 2 decades [46, 47, 48, 49, 50]. One example from lab-on-a-chip applications is a real-time and flow-through sensor that was developed within an integrated multi-mode microwave resonator, which was able to distinguish two different cancerous cell lines in

mixed populations [51] (Fig. 1.4 c).

Integration of such real-time sensors can reveal spatial information within a 3D tissue, without contact and functionalization.

1.3.4. ELECTROCHEMICAL SENSING

The working principle of all electrochemical sensors is based on converting measurements of chemical equilibrium to electrical signals. A conventional division of electrochemical sensors identifies potentiometric and amperometric devices. Potentiometric devices are based on the potential difference between a sensing electrode and a reference electrode, whereas amperometric devices usually employ a 3-electrode measurement setup (working electrode, counter electrode, and reference electrode), and flow of current is observed. Another division can be made between passive and active devices. Passive devices are based on a group of electrodes such as the working electrode (WE), reference electrode (RE), and counter electrode (CE) (Fig. 1.5), whereas active methods are based on active electronic devices such as Field-Effect Transistors (FETs). Arguably, transistor electrodes and terminals can also be classified as a 3-electrode system similar to the passive counterpart. The main difference between passive and active measurement systems is active devices can have built-in amplification since the control electrode of a FET, which is called the gate, can modulate the working point of the device. This gives the ability to FETs to be 3-terminal devices with controlled current.

Biomarkers can functionalize the sensing electrode (referred to as the WE) and thus can be tailored to monitor a specific chemical reaction, such as the ion release in a solution. When integrated within OoCs, electrochemical sensors can monitor real-time secreted biomarkers, a key step for revealing certain disease mechanisms.

The sensitivity of such sensors plays an important role in OoCs. Measurement of three different biomarkers (albumin, GST- α and CK-MB) with a detection limit of $0.1 \frac{\text{ng}}{\text{mL}}$ for albumin was reported recently [52, 53], which shows clinically relevant ranges and the possibility of using such sensors for extracting relevant information and quantitative comparison (Fig. 1.4 d).

Although common 3-electrode electrochemical sensors have been widely used, they usually have a macro-sized footprint, which can be problematic when integration into OoCs is desired. They cannot provide in-line amplification in cases where sensitivity and signal-to-noise ratio might not be sufficient.

Field-effect transistors (FETs) have been used for ion-sensitive electrochemical analysis for over four decades [54]. Depending on the sensing layer, different sensitivities and selectivities can be obtained [55, 56, 57].

Briefly, the working principle can be summarized as altering the charge density of the dielectric at the sensing area, depending on the monitored ions. The most commonly used and investigated types, ion-sensitive field effect transistors (ISFETs), were employed as biosensors where the external reference electrode (typically Ag/AgCl) serves as the gate of the transistor [58], rather than having a metal gate integrated to the silicon chip. Hence, the only difference with well-known metal-oxide-semiconductor FETs (MOSFETs) is the fact that ISFETs replace metal (as the gate) and oxide (as the dielectric) with reference electrode (as the gate)-electrolyte-oxide (as dielectric) layers (Fig. 1.6 (a)). It is worth noting that the first tissue-on-MOSFET was revealed 42 years ago [59] to record electrical

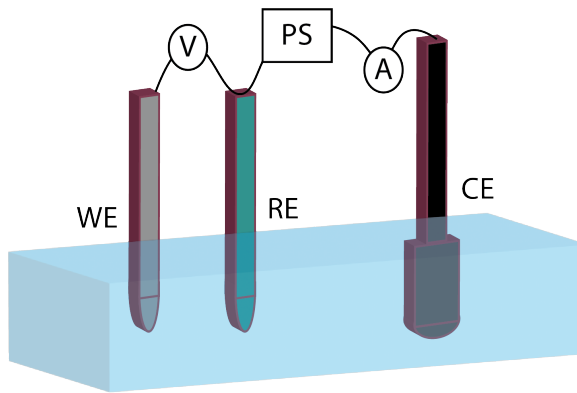


Figure 1.5: Schematic of a 3-electrode electrochemical setup. The blue block represents the analyte-under-test. WE is the working electrode, RE is the reference electrode, and CE is the counter electrode. Measurement units for voltage (V), current (A), and power supply (PS) are also shown.

activity from the mammalian nervous system. Hence, MOSFET also found applications in bio-FET field. The dielectric layer coated with a layer selectively affine to an ion registers the accumulation of the ions from the analyte and, in turn, changes the working point of the transistor. This can be monitored by measuring of the threshold voltage or drain current.

From the long history of bio-FETs, we generally see a direct application of reference voltage at the gate as explained for ISFETs above, and modulation of the charge carriers directly underneath the gate area, the channel, which is the semiconductor layer between the source and the drain terminals. This approach is very well known, and the measured drain current is directly related to the charges on top of the source-drain (S-D) [60], without having a separate sensing area. Hence, the analyte-under-test might be treated as the dielectric of the transistor (Fig. 1.6 (b)).

Being in a liquid environment as in the case of all bio-FET applications can cause degradation in time and affect the performance of the transistor [56]. Extended-gate FETs (EGFETs) solve this issue by having an extended gate, in the form of a metal line with a sensitive layer at the end, which eliminates the electrolyte's direct contact with the transistor's insulation layer. Hence, the active area of the transistor can be separated from the liquid environment [61, 62], as it is represented in Fig. 1.6 (c).

Organic FETs (OFETs) gained a reputation for being low-cost, transparent and biocompatible. Instead of using traditional semiconductors, they employ organic ones, namely conductive polymers which are doped and undoped depending on the analyte-under-test (Fig. 1.6 (d)). Even though there are various examples in the literature [63, 64, 65, 66], due to the lower carrier mobility of the polymer compared to silicon, they need higher voltage values to work, and there are studies to lower the operating voltage [67, 68]. Besides, doping and undoping cycles can also degrade the lifetime of the sensors.

Floating-Gate FETs (FGFETs) are also good candidates to prevent degradation in time. They involve a floating gate (FG), which does not have any terminals to apply voltage directly; instead, a second gate, usually called the control gate (CG), is capacitively cou-

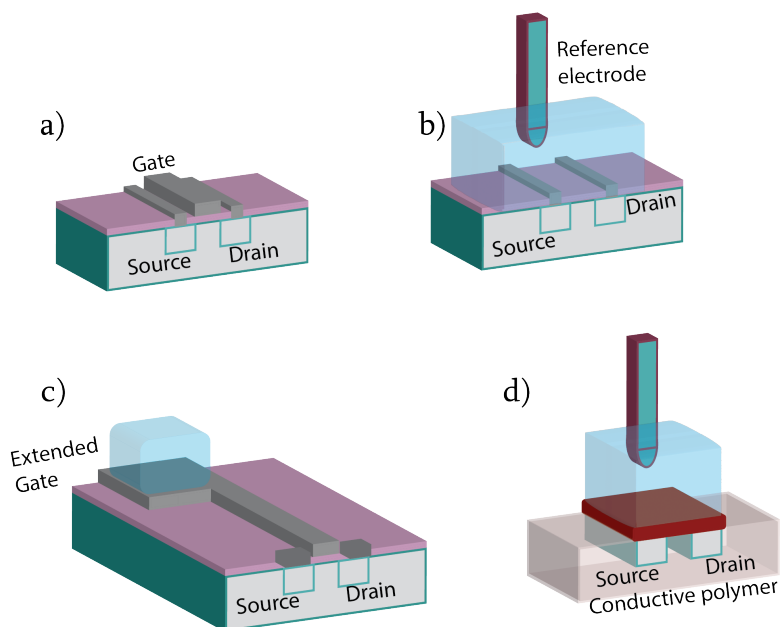


Figure 1.6: Schematic of different FETs. a) A typical MOSFET, b) ISFET, c) EGFETs, d) OFETs. The blue layer represents the analyte-under-test.

pled to the FG (Fig. 1.7).

FG-FETs have been used in flash memory cells as storage elements for decades [69]. They are isolated from their surroundings electrically by high resistivity materials. Since the FGs are floating nodes, they can store charge and this is the key characteristic that has been used for storage elements. In order to change the charge of the FG, Fowler-Nordheim tunneling can be employed [70], where applying high potential through CG moves electrons across a thin oxide layer and to the FG. Changing the charge of the FG can be seen as 'writing' or 'erasing' operations.

The FG behaves as a charge storage element, and any analyte in close proximity to the FG will cause charge separation, resulting in a change in the channel formation of the FET, and can be monitored as drain current change or change in the threshold voltage [71, 72, 73]. This will be explained in detail in Chapter 2. Due to extensive studies and long history, FET sensors are reliable for OoC integration, and the first commercialization of a FET-based pH sensor was revealed as early as 2003 [74].

1.3.5. SELECTIVITY IN ELECTROCHEMICAL SENSORS

For all electrochemical sensors, selectivity is an important issue. We can reference everyday life tests to understand selectivity before moving on to the literature. For example, we can consider a pregnancy test as an electrochemical test that is selective towards human chorionic gonadotropin (HCG), a hormone in urine, or a urinary tract infection (UTI) test, which basically checks the urine for white blood cells and pH.

Despite being a significant aid, these routine home tests also need a large volume of

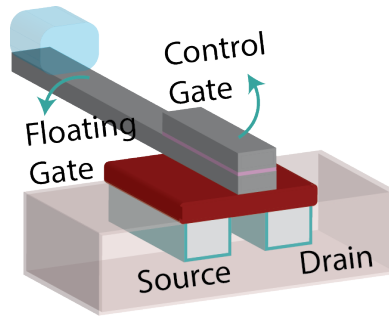


Figure 1.7: Schematic of the FG-FETs. A floating gate with a control-gate structure is shown with a semiconductor layer underneath. Blue represents the analyte-under-test.

samples. Such test devices are usually dipped into a few mL of the analyte. This might be problematic for more precious and specific analytes (for example, blood) where only a limited volume is obtainable. When we move to commercially available ion-selective electrodes (ISEs), we observe a similar problem. ISEs are electrodes with selective membranes and liquid contact electrodes [75] (Fig. 1.8). The selective ions in the membrane (which will be described in detail in Section 6.1.1) interact with the desired ions and create a potential difference between the two electrodes. Selective membranes with electrochemical measurements go back to the 1970s, when PVC membrane, which serves as a neutral matrix, was praised for its stability for Ca^{+} sensing in water [76]. ISEs should be dipped into the solution-under-test. However, when considering cell culture on a Petri dish or an OoC device with volumes of μL range, integration of such sensors needs additional advancements, including integrated fabrication methods such as cleanroom fabrication. Ion-selective electrodes have a specific membrane that can filter the desired ion, making the electrodes selectively responsive. One kind of selectivity agent is additional organic membranes, which have ion-exchange sites. For example, a selective carbon nanotube FET with K^{+} selective polymer membrane in μM range has been developed [77].

Selectivity of the electrochemical sensor plays a significant role to achieve ion-specific or analyte-specific sensing, crucial for analyzing disease mechanisms.

1.4. OoC PLATFORMS

Even when Fig. 1.2 is examined closely, it is apparent that the future of OoCs will be integrating several organ devices to monitor how different organs interact with each other while trying to investigate a disease. An OoC platform is a tool that can house and connect more than one organ model (for example, intestine, liver, and gut). Hence, it links organ models fluidically by culturing them close to each other and providing a specific microenvironment for each of them [78].

Single culturing devices cannot provide all realistic information for disease modeling or drug testing since they cannot mimic physiological interactions or homeostasis [4]. The communication between cells and organs, which is based on secreting soluble factors [79], should be taken into consideration for big-scale organ-on-chip platforms. In this

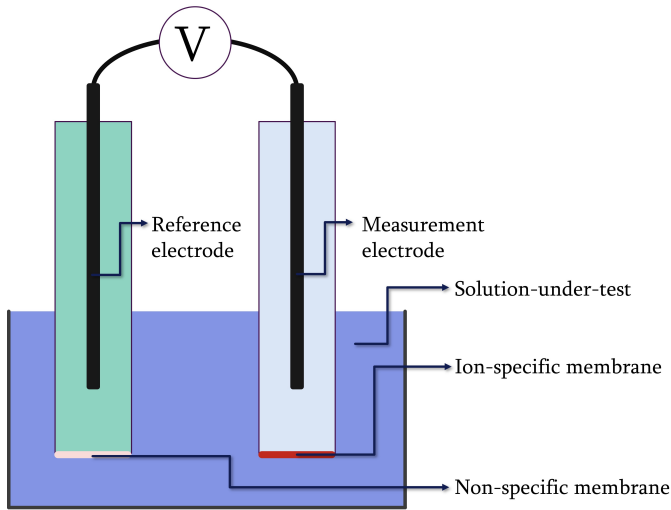


Figure 1.8: Schematic of ISE working principle, based on a differential measurement, where a reference electrode measures the potential without ion-rich liquid. The ion-specific membrane allows the ions to interact within the membrane, creating a potential difference.

sense, OoC platforms where a microfluidic circuitry is adapted for multiple organs are becoming useful and reliable choices [80] (Fig. 1.9).

1.5. DISCUSSION

1.5.1. IMPORTANCE OF pH

Monitoring the pH level of the micro-environment is crucial since it is an indicator of homeostasis for the cells' well-being. By definition, pH is the logarithmic concentration of H^+ ions of the analyte-under-test and depicts the acidity, and products of cell metabolism can cause changes in pH.

The effect of slight alteration from regulated pH on mammalian physiology is well-known. Generally, pH is an indicator of the viability of the cells, as well as of certain disease phenotypes [81, 82], as it is related to the medium acidification rate [83].

We cite a few organ-specific examples: In the brain, the cerebrospinal fluid (CSF) pH should be 7.3 [84]. It is important to monitor in a reliable manner any alterations from this value for the well-being of, for example, the blood-brain-barrier. Another example for the brain is the K^+ concentration for migraine monitoring. Cortical spreading depolarization (CSD) causes a shift in K^+ ions, a phenomenon that occurs during a migraine attack and for which monitoring the pH simultaneously would also be valuable [85] (More details will be given in Section 6.1.3). For the heart, beat-to-beat pH alterations can indicate the well-being of cardiomyocytes [86]. For the intestinal lumen, a change in pH can indicate inflammatory bowel diseases [87].

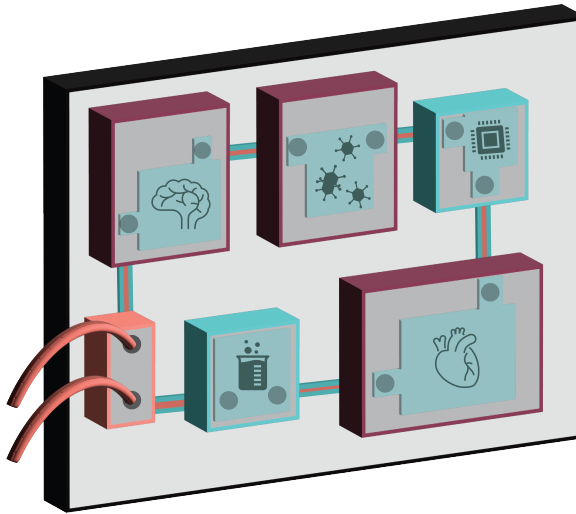


Figure 1.9: Concept of an OoC platform with different sensor modules and cell cultures. A microfluidic circuit makes the connection. The inlet and outlet ports of the microfluidic circuit are shown in orange. (See chapter 9 for an example.) Microchannels connect different modules, for example, a pH sensor module and a cell culturing module. Therefore, media from the cell culture can travel to the pH sensor and can be monitored.

1.5.2. REMARKS

This chapter briefly mentioned the most commonly used sensing methods for OoCs, possible improvements, and future works. A literature summary of their advantages and disadvantages was provided.

Even though the recent developments in on-chip technologies show great promise, quantitative comparisons of *in vivo* and *in vitro* cell- and tissue characteristics have not always been successful or possible. Various aspects need to be taken into account as described above.

Sensor applications for OoCs is a field that holds great promise for the future. Based on the literature, the work presented in this thesis has been based on the following considerations:

- An electrochemical sensor that does not depend on a bulky and external reference electrode and a bulky measurement setup, which can separate the measurement region from the wet environment for a sufficiently long lifetime, has optical transparency and biocompatibility, would be conveniently integrated into inherently small sized OoCs (i.e.: compatible with miniaturization).
- FET-based sensors that can amplify the signal on the chip without the need for additional circuitry. This gives the ability to have a higher signal-to-noise ratio and higher sensitivity compared to 3-electrode-based methods. Hence, Floating-Gate Field-Effect Transistors (FG-FETs) became an interesting research option since they do not need an external reference electrode and they can have transparent sensing areas [82, 88], and are developed in this work.

- Surface modification for specific analyte-sensing or sensitivity is crucial for all OoC sensors. This can be adapted by functionalizing the sensing surface. High-performance biosensors depend on efficient electron transfer between the analyte, sensing surface, and the sensing electrode. This is directly related to sensitivity. Some materials, like metal nanoparticles, can be integrated into the sensing surface to increase the binding area for acceptor molecules [89]. Another solution would be to integrate nano-films, as in the case of metal oxides, to have enough surface binding sites for pH sensing or selective polymers for specific ions.
- Besides having electrochemical sensors as active devices, the extensions of the gates can be employed as microelectrodes to record the electrical activity of electrogenic cells by changing the potential application terminal of the sensor, creating a multi-purpose sensor for various applications.

Thanks to the microfabrication capabilities of Else Kooi Laboratory (EKL) at ECTM, TU Delft, integrating electrodes and active devices compactly would be possible. Another important point to improve reproducibility would also be to adopt wafer-scale fabrication, obtaining multiple chips per wafer with nominally identical characteristics. Since cell biology is already heterogenous in nature, it is crucial to eliminate microfabrication methods with low yield and low reproducibility.

1.6. RESEARCH QUESTIONS

The following research questions will be addressed:

- How can we integrate an electrochemical sensor in an OoC device without bulky external electrodes and measurement setups for pH and ion sensing?
- How can we fabricate sensorized OoC Devices with transparent and elastic sensing areas without employing organic semiconductors?
- How can we alter the sensing surface to improve sensitivity and selectivity?
- How can post-processing functionalization be integrated into the fabrication process without damaging the devices?
- How can the fabricated OoC devices be integrated in OoC platforms?

1.7. THESIS OVERVIEW

The core of the thesis is composed of the following six chapters:

Chapter 2 explains the working principle of the FG-FETs. We analyzed the sensor in two parts: electrochemical sensing and FET characteristics. The analyte in close proximity to the FG causes charge separation, resulting in alteration of the channel formation. This behavior can be monitored as drain current. We analysed the electrode-electrolyte interface of the FET and solved the equations via MATLAB.

The wafer-scale fabrication and characterization of the silicon-based FG-FETs is explained in Chapter 3. The fabrication starts as a Bi-CMOS process. We deposited different MO_x layers to investigate their sensitivity for different pH liquids at the extension of the FG

electrodes. For the characterization of the devices, surface analysis of the MO_x layers, electrochemical analysis by electrochemical impedance spectroscopy, and electrical analysis by semiconductor parameter analyzer were performed.

Since silicon-based devices lack the transparency that is desired for imaging of the cells to prove physiological behaviors, Chapters 4 and 5 describe a novel silicon-polymer-based FG-FET device. Chapter 4 introduces the device concept, and Chapter 5 investigates the fabrication and characterization of the silicon-polymer-based device as a pH sensor. A mobile measurement setup developed for monitoring the pH in cell biology laboratories is also shown.

The wafer-scale process steps were CMOS-compatible. However, to introduce additional functionalization of the devices to increase sensitivity or to make the sensors selective, post-processing methods that can target single chips are beneficial for preliminary testing. Chapter 6 covers the additional functionalization of the sensing surface of the extension of the FG electrodes. We showed K^+ concentration sensing for silicon-based devices and spatial decoration of FG extension by employing Au nanofilms on silicon-polymer devices.

Until Chapter 7, electrochemical sensing is covered with silicon-based and silicon-polymer-based devices. Additionally, the FG electrodes can be used as recording electrodes for electrically active cells by changing the device's contact terminal and by using commercially-available MEA read-out setups. In Chapter 7, recording electrical activity from electrically active cells is demonstrated. Additionally, preliminary results with FG-FET measurements are shown.

Finally, Chapter 8 concludes with the findings of the thesis and mentions future work for FG-FET devices. Additionally, it shows how we can integrate the FG-FET chips into OoC platforms. As another type of sensor, early work for integrating microwave resonators for blood-brain-barrier monitoring will be discussed.

BIBLIOGRAPHY

- [1] Olivier J Wouters, Martin McKee, and Jeroen Luyten. “Estimated research and development investment needed to bring a new medicine to market, 2009-2018”. In: *Jama* 323.9 (2020), pp. 844–853.
- [2] Rhian McNaughton, Gwenaël Huet, and Saad Shakir. “An investigation into drug products withdrawn from the EU market between 2002 and 2011 for safety reasons and the evidence used to support the decision-making”. In: *BMJ open* 4.1 (2014), e004221.
- [3] Kayla Duval et al. “Modeling physiological events in 2D vs. 3D cell culture”. In: *Physiology* 32.4 (2017), pp. 266–277.
- [4] Uwe Marx et al. “‘Human-on-a-chip’developments: a translational cutting-edge alternative to systemic safety assessment and efficiency evaluation of substances in laboratory animals and man?” In: *Alternatives to laboratory animals* 40.5 (2012), pp. 235–257.
- [5] Thierry F Vandamme. “Use of rodents as models of human diseases”. In: *Journal of pharmacy & bioallied sciences* 6.1 (2014), p. 2.
- [6] Sangeeta N Bhatia and Donald E Ingber. “Microfluidic organs-on-chips”. In: *Nature biotechnology* 32.8 (2014), pp. 760–772.
- [7] Uwe Marx et al. “Biology-inspired microphysiological system approaches to solve the prediction dilemma of substance testing”. In: *Altex* 33.3 (2016), p. 272.
- [8] Donald E Ingber. “Human organs-on-chips for disease modelling, drug development and personalized medicine”. In: *Nature Reviews Genetics* 23.8 (2022), pp. 467–491.
- [9] Rachel Hajar. “Animal testing and medicine”. In: *Heart views: the official journal of the Gulf Heart Association* 12.1 (2011), p. 42.
- [10] Hande Avdogmus et al. “Dual-Gate Fet-Based Charge Sensor Enhanced by In-Situ Electrode Decoration in a MEMS Organs-On-Chip Platform”. In: *2021 21st International Conference on Solid-State Sensors, Actuators and Microsystems (Transducers)*. IEEE, 2021, pp. 180–183.
- [11] Hiroki Yasuga et al. “New Sensing Technologies: Microtas/NEMS/MEMS”. In: (2023).
- [12] Boyang Zhang et al. “Advances in organ-on-a-chip engineering”. In: *Nature Reviews Materials* 3.8 (2018), pp. 257–278.
- [13] Neil Convery and Nikolaj Gadegaard. “30 years of microfluidics”. In: *Micro and Nano Engineering* 2 (2019), pp. 76–91.
- [14] Berivan Cecen et al. “Multi-organs-on-chips for testing small-molecule drugs: Challenges and perspectives”. In: *Pharmaceutics* 13.10 (2021), p. 1657.

- [15] Dennis M. Nahon et al. "Taking Organ-on-Chip to the next level: Why quantification of physiological features is essential". In: *Nature Biomedical Engineering* (2022). (in press).
- [16] Balaji Srinivasan and Aditya Reddy Kolli. "Transepithelial/transendothelial electrical resistance (TEER) to measure the integrity of blood-brain barrier". In: *Blood-Brain Barrier* (2019), pp. 99–114.
- [17] Mengli Li et al. "Baicalin mitigates hypertension-linked alterations in the intestinal lymphatic vasculature in part through preserving the functional barrier integrity of lymphatic endothelial cells". In: *Biomedicine & Pharmacotherapy* 160 (2023), p. 114418.
- [18] Erin M Shaughnessey et al. "Evaluation of rapid transepithelial electrical resistance (TEER) measurement as a metric of kidney toxicity in a high-throughput microfluidic culture system". In: *Scientific Reports* 12.1 (2022), p. 13182.
- [19] Frank A Alexander Jr, Sebastian Eggert, and Joachim Wiest. "Skin-on-a-chip: Transepithelial electrical resistance and extracellular acidification measurements through an automated air-liquid interface". In: *Genes* 9.2 (2018), p. 114.
- [20] Philippe Pinton et al. "The food contaminant deoxynivalenol, decreases intestinal barrier permeability and reduces claudin expression". In: *Toxicology and applied pharmacology* 237.1 (2009), pp. 41–48.
- [21] Francois Chesnais et al. "Continuously perfusable, customisable, and matrix-free vasculature on a chip platform". In: *Lab on a Chip* 23.4 (2023), pp. 761–772.
- [22] Daniel Vera et al. "A 3D bioprinted hydrogel gut-on-chip with integrated electrodes for transepithelial electrical resistance (TEER) measurements". In: *Biofabrication* (2024).
- [23] Patricia Zoio and Abel Oliva. "Skin-on-a-chip technology: microengineering physiologically relevant in vitro skin models". In: *Pharmaceutics* 14.3 (2022), p. 682.
- [24] Balaji Srinivasan et al. "TEER measurement techniques for in vitro barrier model systems". In: *SLAS Technology* 20.2 (2015), pp. 107–126.
- [25] Marinke W van der Helm et al. "Non-invasive sensing of transepithelial barrier function and tissue differentiation in organs-on-chips using impedance spectroscopy". In: *Lab on a Chip* 19.3 (2019), pp. 452–463.
- [26] Isabelle Matthiesen et al. "Continuous Monitoring Reveals Protective Effects of N-Acetylcysteine Amide on an Isogenic Microphysiological Model of the Neurovascular Unit". In: *Small* 17.32 (2021), p. 2101785.
- [27] Elsbeth GBM Bossink et al. "Measuring barrier function in organ-on-chips with cleanroom-free integration of multiplexable electrodes". In: *Lab on a Chip* 21.10 (2021), pp. 2040–2049.
- [28] Chrysanthi-Maria Moysidou et al. "3D bioelectronic model of the human intestine". In: *Advanced Biology* 5.2 (2021), p. 2000306.
- [29] Andrea Trevisiol et al. "Monitoring ATP dynamics in electrically active white matter tracts". In: *Elife* 6 (2017), e24241.

- [30] Britt Mossink et al. “Human neuronal networks on micro-electrode arrays are a highly robust tool to study disease-specific genotype-phenotype correlations in vitro”. In: *Stem cell reports* 16.9 (2021), pp. 2182–2196.
- [31] Marie Engelen J Obien et al. “Revealing neuronal function through microelectrode array recordings”. In: *Frontiers in neuroscience* 8 (2015), p. 423.
- [32] Zhengyu Cao et al. “Clustered burst firing in FMR1 premutation hippocampal neurons: amelioration with allopregnanolone”. In: *Human molecular genetics* 21.13 (2012), pp. 2923–2935.
- [33] Helen S Bateup et al. “Excitatory/inhibitory synaptic imbalance leads to hippocampal hyperexcitability in mouse models of tuberous sclerosis”. In: *Neuron* 78.3 (2013), pp. 510–522.
- [34] Brian J Wainger et al. “Intrinsic membrane hyperexcitability of amyotrophic lateral sclerosis patient-derived motor neurons”. In: *Cell reports* 7.1 (2014), pp. 1–11.
- [35] Jenifer A Bradley et al. “In vitro screening for seizure liability using microelectrode array technology”. In: *Toxicological Sciences* 163.1 (2018), pp. 240–253.
- [36] Gyorgy Buzsaki and Andreas Draguhn. “Neuronal oscillations in cortical networks”. In: *science* 304.5679 (2004), pp. 1926–1929.
- [37] Hamid Charkhkar et al. “Novel disposable microelectrode array for cultured neuronal network recording exhibiting equivalent performance to commercially available arrays”. In: *Sensors and Actuators B: Chemical* 226 (2016), pp. 232–238.
- [38] Hyogeun Shin et al. “3D high-density microelectrode array with optical stimulation and drug delivery for investigating neural circuit dynamics”. In: *Nature communications* 12.1 (2021), pp. 1–18.
- [39] Franziska D Zitzmann et al. “A novel microfluidic microelectrode chip for a significantly enhanced monitoring of NPY-receptor activation in live mode”. In: *Lab on a Chip* 17.24 (2017), pp. 4294–4302.
- [40] Jun-Ming Zhang and Jianxiong An. “Cytokines, inflammation and pain”. In: *International anesthesiology clinics* 45.2 (2007), p. 27.
- [41] Ryo Usuba et al. “Photonic lab-on-a-chip for rapid cytokine detection”. In: *Acs Sensors* 1.8 (2016), pp. 979–986.
- [42] Matthew S Luchansky and Ryan C Bailey. “Rapid, multiparameter profiling of cellular secretion using silicon photonic microring resonator arrays”. In: *Journal of the American Chemical Society* 133.50 (2011), pp. 20500–20506.
- [43] Vijayakumar Subban and Owen Christopher Raffel. “Optical coherence tomography: Fundamentals and clinical utility”. In: *Cardiovascular Diagnosis and Therapy* 10.5 (2020), p. 1389.
- [44] Joris Pauty et al. “A vascular endothelial growth factor-dependent sprouting angiogenesis assay based on an in vitro human blood vessel model for the study of anti-angiogenic drugs”. In: *EBioMedicine* 27 (2018), pp. 225–236.

- [45] Claire Dalmay et al. "Ultra sensitive biosensor based on impedance spectroscopy at microwave frequencies for cell scale analysis". In: *Sensors and Actuators A: Physical* 162.2 (2010), pp. 189–197.
- [46] T Chen et al. "Microwave biosensor dedicated to the dielectric spectroscopy of a single alive biological cell in its culture medium". In: *2013 IEEE MTT-S International Microwave Symposium Digest (MTT)*. IEEE, 2013, pp. 1–4.
- [47] Hee-Jo Lee and Jong-Gwan Yook. "Biosensing using split-ring resonators at microwave regime". In: *Applied Physics Letters* 92.25 (2008), p. 254103.
- [48] Mohammad Hossein Zarifi et al. "Noncontact and noninvasive microwave-microfluidic flow sensor for energy and biomedical engineering". In: *Scientific reports* 8.1 (2018), pp. 1–10.
- [49] Jonathan Leroy et al. "Microfluidic biosensors for microwave dielectric spectroscopy". In: *Sensors and Actuators A: Physical* 229 (2015), pp. 172–181.
- [50] Claire Dalmay et al. "Ultra sensitive biosensor based on impedance spectroscopy at microwave frequencies for cell scale analysis". In: *Sensors and Actuators A: Physical* 162.2 (2010), pp. 189–197.
- [51] Mehmet Kelleci et al. "Towards microwave imaging of cells". In: *Lab on a Chip* 18.3 (2018), pp. 463–472.
- [52] Julio Aleman et al. "Microfluidic integration of regeneratable electrochemical affinity-based biosensors for continual monitoring of organ-on-a-chip devices". In: *Nature Protocols* 16.5 (2021), pp. 2564–2593.
- [53] Yu Shrike Zhang et al. "Multisensor-integrated organs-on-chips platform for automated and continual in situ monitoring of organoid behaviors". In: *Proceedings of the National Academy of Sciences* 114.12 (2017), E2293–E2302.
- [54] Luc Bousse, Nico F De Rooij, and Piet Bergveld. "Operation of chemically sensitive field-effect sensors as a function of the insulator-electrolyte interface". In: *IEEE Transactions on Electron Devices* 30.10 (1983), pp. 1263–1270.
- [55] Jeho Park et al. "Applications of field-effect transistor (FET)-type biosensors". In: *Applied science and convergence technology* 23.2 (2014), pp. 61–71.
- [56] Piet Bergveld. "Thirty years of ISFETOLOGY: What happened in the past 30 years and what may happen in the next 30 years". In: *Sensors and Actuators B: Chemical* 88.1 (2003), pp. 1–20.
- [57] Tanu Wadhera et al. "Recent advances and progress in development of the field effect transistor biosensor: A review". In: *Journal of Electronic Materials* 48.12 (2019), pp. 7635–7646.
- [58] Piet Bergveld. "Development of an ion-sensitive solid-state device for neurophysiological measurements". In: *IEEE Transactions on biomedical engineering* 1 (1970), pp. 70–71.
- [59] DT Jobling, JG Smith, and HV Wheal. "Active microelectrode array to record from the mammalian central nervous system in vitro". In: *Medical and biological engineering and computing* 19.5 (1981), pp. 553–560.

- [60] Michael J Schöning and Arshak Poghosian. “Recent advances in biologically sensitive field-effect transistors (BioFETs)”. In: *Analyst* 127.9 (2002), pp. 1137–1151.
- [61] Kanishk Singh et al. “Super Nernstian pH response and enzyme-free detection of glucose using sol-gel derived RuO_x on PET flexible-based extended-gate field-effect transistor”. In: *Sensors and Actuators B: Chemical* 298 (2019), p. 126837.
- [62] Jia-Chyi Chen et al. “Portable urea biosensor based on the extended-gate field effect transistor”. In: *Sensors and Actuators B: Chemical* 91.1-3 (2003), pp. 180–186.
- [63] A Caboni et al. “Organic-based sensor for chemical detection in aqueous solution”. In: *Applied Physics Letters* 95.12 (2009), p. 253.
- [64] David Nilsson et al. “Bi-stable and dynamic current modulation in electrochemical organic transistors”. In: *Advanced Materials* 14.1 (2002), pp. 51–54.
- [65] Caizhi Liao and Feng Yan. “Organic semiconductors in organic thin-film transistor-based chemical and biological sensors”. In: *Polymer reviews* 53.3 (2013), pp. 352–406.
- [66] Stefano Casalini et al. “Organic field-effect transistor for label-free dopamine sensing”. In: *Organic Electronics* 14.1 (2013), pp. 156–163.
- [67] Stefano Lai et al. “Ultralow voltage, OTFT-based sensor for label-free DNA detection”. In: *Advanced Materials* 25.1 (2013), pp. 103–107.
- [68] Piero Cosseddu et al. “Ultra-low voltage, organic thin film transistors fabricated on plastic substrates by a highly reproducible process”. In: *Applied Physics Letters* 100.9 (2012), p. 61.
- [69] Dawon Kahng and Simon M Sze. “A floating gate and its application to memory devices”. In: *The Bell System Technical Journal* 46.6 (1967), pp. 1288–1295.
- [70] Youngbin Jin and Ben Lee. “A comprehensive survey of issues in solid state drives”. In: *Advances in computers* 114 (2019), pp. 1–69.
- [71] Massimo Barbaro, Annalisa Bonfiglio, and Luigi Raffo. “A charge-modulated FET for detection of biomolecular processes: conception, modeling, and simulation”. In: *IEEE Transactions on Electron Devices* 53.1 (2005), pp. 158–166.
- [72] Ben Zhao et al. “Floating-Gate Ion Sensitive Field-Effect Transistor for Chemical and Biological Sensing”. In: *MRS Online Proceedings Library (OPL)* 828 (2004).
- [73] Baozhen Chen, Archana Parashar, and Santosh Pandey. “Folded floating-gate CMOS biosensor for the detection of charged biochemical molecules”. In: *IEEE Sensors Journal* 11.11 (2011), pp. 2906–2910.
- [74] Danai Galiti. “Integration of electro-chemical FET-based sensors in silicon-and polymer-based organs-on-chip”. In: (2021).
- [75] Jinbo Hu, Andreas Stein, and Philippe Bühlmann. “Rational design of all-solid-state ion-selective electrodes and reference electrodes”. In: *TrAC Trends in Analytical Chemistry* 76 (2016), pp. 102–114.
- [76] A_ Hulanicki and M Trojanowicz. “Calcium-selective electrodes with PVC membranes and solid internal contacts”. In: *Analytica Chimica Acta* 87.2 (1976), pp. 411–417.

- [77] K Melzer et al. "Selective ion-sensing with membrane-functionalized electrolyte-gated carbon nanotube field-effect transistors". In: *Analytst* 139.19 (2014), pp. 4947–4954.
- [78] Yuki Imura, Kiichi Sato, and Etsuro Yoshimura. "Micro total bioassay system for ingested substances: assessment of intestinal absorption, hepatic metabolism, and bioactivity". In: *Analytical chemistry* 82.24 (2010), pp. 9983–9988.
- [79] Kacey Ronaldson-Bouchard and Gordana Vunjak-Novakovic. "Organs-on-a-chip: a fast track for engineered human tissues in drug development". In: *Cell stem cell* 22.3 (2018), pp. 310–324.
- [80] Anke R Vollertsen et al. "Facilitating implementation of organs-on-chips by open platform technology". In: *Biomicrofluidics* 15.5 (2021), p. 051301.
- [81] Mathieu Odijk et al. "Microfabricated solid-state ion-selective electrode probe for measuring potassium in the living rodent brain: Compatibility with DC-EEG recordings to study spreading depression". In: *Sensors and Actuators B: Chemical* 207 (2015), pp. 945–953.
- [82] Monia Demelas et al. "Charge sensing by organic charge-modulated field effect transistors: Application to the detection of bio-related effects". In: *Journal of Materials Chemistry B* 1.31 (2013), pp. 3811–3819.
- [83] Bernhard Müller et al. "Measurement of respiration and acidification rates of mammalian cells in thermoplastic microfluidic devices". In: *Sensors and Actuators B: Chemical* 334 (2021), p. 129664.
- [84] N Joan Abbott et al. "Structure and function of the blood–brain barrier". In: *Neurobiology of disease* 37.1 (2010), pp. 13–25.
- [85] Mathieu Odijk et al. "Microfabricated solid-state ion-selective electrode probe for measuring potassium in the living rodent brain: Compatibility with DC-EEG recordings to study spreading depression". In: *Sensors and Actuators B: Chemical* 207 (2015), pp. 945–953.
- [86] Yankun Lyu et al. "Beat-to-beat dynamic regulation of intracellular pH in cardiomyocytes". In: *Isience* 25.1 (2022), p. 103624.
- [87] SG Nugent et al. "Intestinal luminal pH in inflammatory bowel disease: possible determinants and implications for therapy with aminosalicylates and other drugs". In: *Gut* 48.4 (2001), pp. 571–577.
- [88] Andrea Spanu et al. "An organic transistor-based system for reference-less electrophysiological monitoring of excitable cells". In: *Scientific reports* 5.1 (2015), pp. 1–7.
- [89] Fei Xiao, Lu Wang, and Hongwei Duan. "Nanomaterial based electrochemical sensors for in vitro detection of small molecule metabolites". In: *Biotechnology advances* 34.3 (2016), pp. 234–249.

2

SILICON-BASED FG-FET WITH *MO_x* LAYER FOR CHARGE SENSING

2.1. INTRODUCTION

Wafer-scale fabrication methods allow batch production, processing of multiple materials, high spatial resolution, and alignment precision. As it will be shown in this chapter, these enable the integration of multiple sensing units in as small as a 1cm x 1cm chip. Additionally, precise fabrication control of active devices can be realized. This is especially important when a sensor is developed for high sensitivity or high signal-to-noise ratio (SNR).

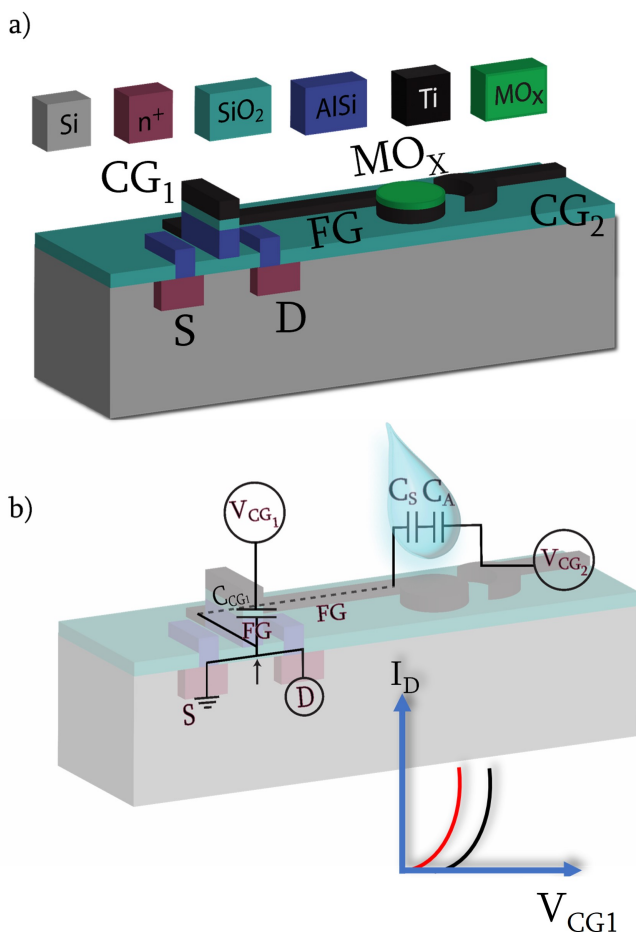


Figure 2.1: Schematic of the FG-FET-based sensor: a) Structural and functional layers. MO_x represents the metal oxide layer for charge sensing, b) Equivalent electric circuit. When there is an analyte in close proximity of the sensing extension, the working point of the transistor will change accordingly, which can be monitored by the changes in I_D , V_D , V_{CG1} , and V_{CG2} are shown, all of which are with respect to the ground.

To increase the amplification of the output signal without the need for external circuitry, field-effect transistors (FETs) have been implemented as electrochemical sensors to ex-

tract biochemically-relevant information [1]. In Chapter 1, ISFETs were described. However, ISFETs usually need an external and bulky reference electrode, which can hardly be integrated into inherently small-sized OoCs devices. Additionally, the reference electrode is usually based on Ag/AgCl, and the charge variations in close proximity might 'turn-off' the channel of the transistors [2]. Moreover, an external reference electrode is hard to combine with CMOS-compatible fabrication methods. This external reference electrode can be seen as the more stable version compared to the pseudo-counterparts. Even though both reference and pseudo-reference electrodes can be made of Ag/AgCl, for instance, a true reference electrode has a surrounding KCl solution, with a membrane separating it from the analyte-under-test. However, a pseudo-reference electrode may have a more simplistic construction and hence might not have a stable potential due to the interactions with the analyte-under-test.

As an alternative to ISFETs, charge-modulated FETs (CMFETs) were introduced [3]. In this case, instead of using the external reference electrode, floating gates (FGs) are capacitively coupled to a control gate (CG) and used without applying voltage to the FG terminal to set the working point of the transistor. Detection of the analyte in close proximity to the extension of the FG electrode is realized by modulation of the net charge, which in turn alters the working point of the transistor (Fig. 2.1). The latter can be monitored by the change in the drain current. Hence, CM-FETs-based charge and specifically pH sensors can be a robust alternative where reference electrodes cannot be used due to material or space concerns.

In the last decades, FGs have been integrated in biosensors for various applications. In order to have separation between the sensing area and the transistor terminals, Extended-Gate FETs (EGFETs) were combined to FG-FETs (Fig. 2.2 a). EG-FETs treat the sensing area and the FET area as two separate bodies, connected with a signal line [4]. There are also examples of folded FG sensors. In this case, the layout of the sensor is more compact. The FG layer is folded onto the CG, rather than extended across the surface with a signal line. The work in [5] shows the working principle of a folded FG-FET for a pH sensor. They explained the working mechanism by three Gauss surfaces: Between the solution and the sensing dielectric surface, between the sensing dielectric, FG, and the oxide of the semiconductor, and between the oxide and the semiconductor (Fig. 2.2 b). However, they assumed the trapped charges inside the FG to be zero. One example of a folded FG-FET is [6], where they use the sensor for charged bio-species (Fig. 2.2 c). The work in [7] showed a floating, extended-gate organic FET where the trapped charges inside the FG alter the working point of the transistor. Interestingly, the working principle depends on charge separation inside the metal gate, and not on the gate dielectric.

The physics of phase potentials can be considered to better understand the working principle. Considering conductive phases such as metals, electrolytes, and semiconductors (with mobile charge carriers), if there is no current flow, the charge carriers will not move, and the electrical field inside the bulk is zero [8]. If a chemical reaction causes a potential difference, this will cause a charge separation in the phase. Considering Gauss' law, the net charge within a conductive boundary is zero when there is no current application. This is the main reason for the charge separation. Hence, if there is an excess charge, the charge carriers will maintain the equilibrium by distributing the excess charge.

From the chemical bonding model of metals, the metallic bonding is described as fixed ions surrounded by a cloud of mobile electrons. Hence, when an electric field is applied, the free electrons can move and form an electric current [9].

In literature, electrochemical sensors are usually categorized according to their ability to sense the presence or effect of a specific analyte. The analyte can be H^+ ions, i.e., the pH of the solution, a specific biomarker in the solution (e.g., glucose), or a specific ion (for example, K^+). However, the selectivity of a sensor is difficult to assess. Technically, selectivity is defined as the process of extracting electrical signals from only one analyte [10]. This is a difficult aim to achieve in the real world. For example, when the solution's pH changes, the electrochemical sensor behavior towards a single ion also changes, and as a consequence of cross-sensitivity, a signal drift might be observed.

The potential of the electrode can change depending on the environment. It was shown almost 50 years ago that the potential increases 50 mV in an Argon environment [11]. Hence, the environment of the experimental setup can also change the base level of the potential of the electrodes. This can be observed if a cell culture is monitored in an incubator with a certain humidity and CO_2 level.

2.1.1. METAL OXIDE LAYERS FOR pH SENSING

Sensitive layers are essential respectively for specific and low-concentration ion detection in analyte-under-test. From industrial sites to cell culturing, sensing pH is crucial since it directly translates to a chemical state equilibrium. pH describes the concentration of hydrogen ions in a solution, making the solution acidic ($pH < 7$) or basic ($pH > 7$). Depending on the analyte-under-test, going from acidic to basic or basic to acidic can be detrimental for a chemical process to happen. Human physiology and homeostasis are directly related to the stability of the pH [12, 1, 13, 14].

In this regard, metal oxide layers (MO_x s) have been employed as the sensing layers of electrochemical sensors for decades due to the binding sites of the oxide [13]. Thanks to the oxygen stoichiometry, MO_x s behave as ionic and electronic conductors, with ion exchange surface sites [15]. To form covalent bonds and surface groups, metal electrodes are usually treated with oxygen [8]. There are various examples of electrochemical sensors with metal oxide as the sensing layer, such as metal oxide nanowires as chemoresistive sensors [16] for gas sensing [17]. There are several favourable aspects for MO_x to be a standard sensing layer for pH, such as high sensitivity, reversibility at the sensing area and biocompatibility [13].

The quality of the MO_x s layers is also significant since impurities on these layers can cause electron transfer by tunneling through the impurities and hence Faradaic reactions. The integration of MO_x layers into the FG-FET-based sensors was achieved in this work by means of cleanroom fabrication. To study the enhancement of the sensitivity of the extension of the FG, hafnium oxide (HfO_x), aluminum oxide (AlO_x), and titanium oxide (TiO_x) layers were chosen as the sensitive layer towards pH.

2.1.2. AIM OF THE WORK

In order to achieve a compact charge sensor for OoCs, we developed a wafer-scale fabrication process and FG-FET-based devices. The FG-FET is capacitively coupled to a control-gate, CG, and electrolytically gated to another control-gate, CG_2 . These cou-

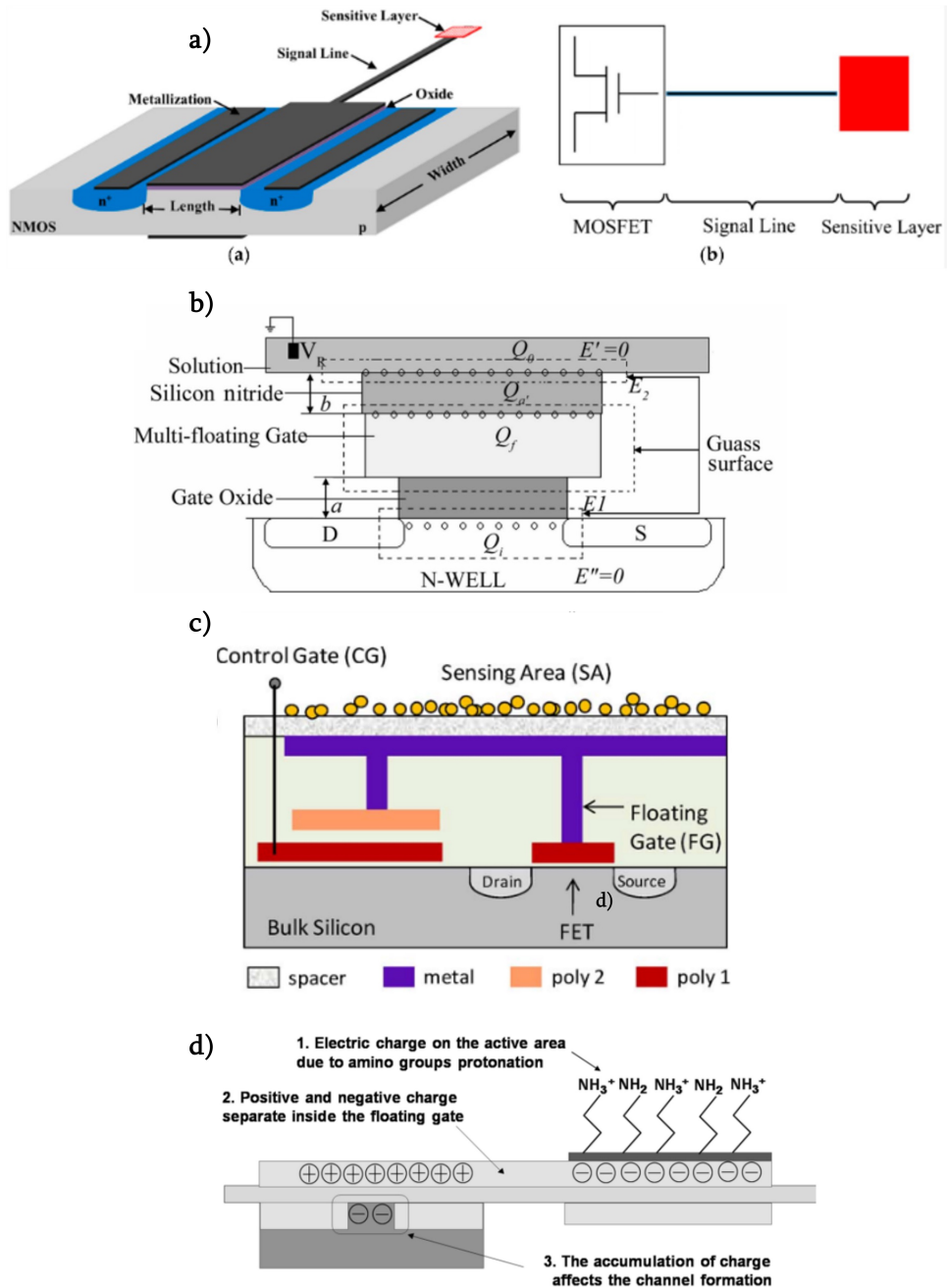


Figure 2.2: Key examples from the literature for this study: a) Schematic of EG-FET [4]. b) Analysis of FG-FET pH sensor [5]. c) Folded FG biosensor[6]. d) Working mechanism of FG charge-modulated pH sensor [7].

plings make the system free of external reference electrode, and provide a differential measurement, rather than a direct sensing mechanism, as in the case of ISFETs. When there are charges in close proximity of the FG extension, the V_{FG} is altered, resulting in difference in output drain current. Since it is difficult to monitor the changes in V_{FG} physically because the FG is floating and hence has no external terminal, the measurements were performed by tracking the changes in I_D . We wanted to implement the working principle for a pH sensor, since pH is an important indicator of cell and tissue metabolism, as explained in Chapter 1. To do so, we investigated different MO_x layers to serve as the sensing layer.

The advantages of silicon-based electrochemical sensors and the reasoning behind the work presented in this and the following chapters can be summarized as follows:

1. Preventing the need for external and bulky electrodes and measurement setups by integrating FG-FET-based charge sensors in an OoC device.
2. Investigating and comparing the metal oxide layers for sensitive FG-FET-based pH sensing.
3. Increasing reproducibility and yield of the sensors by decreasing human handling errors by the wafer-level cleanroom fabrication process.
4. Possibility of integration of the sensorized OoC device into OoC platforms with microfluidics.

In the following section, the interaction between the FG-FET-based electrochemical sensor and the electrolyte will be analyzed in two parts: 1) Electrode-electrolyte interface where the electrochemical reaction is happening, and 2) Characteristics of the FET.

2.2. ELECTRODE-ELECTROLYTE INTERFACE

When we consider the interaction of two conductive bodies, such as an electrode and an electrolyte, we have to consider their Coulombic interaction. For instance, if the potential of the electrolyte changes, this will alter the potential of the electrode as well.

For analyte sensing, the sensing mechanism depends on two processes. The first is Faradaic, where charge transfer takes place at the electrode-electrolyte interface [18]. It is based on Faraday's Law, where the chemical reaction is related to the electrical current, called Faradaic current [8]. The latter one is non-Faradaic, where the charge is stored by means of electrical double-layer (EDL) capacitance [19] (Fig. 2.3).

Depending on the energetically favorable states of the electrode interface, the charge transfer becomes unwanted at some potential levels. At these states, desorption and adsorption mechanisms occur when the solution's potential is different than the electrode potential and the electrode is assumed to be fully polarizable [8].

From GouyChapman-Stern model, which relates the electrostatic potential to the net charge density on the electrode-electrolyte surface [20], the electrode is assumed to be ideal polarizable (IDE), hence no Faradic current exists between the electrode surface

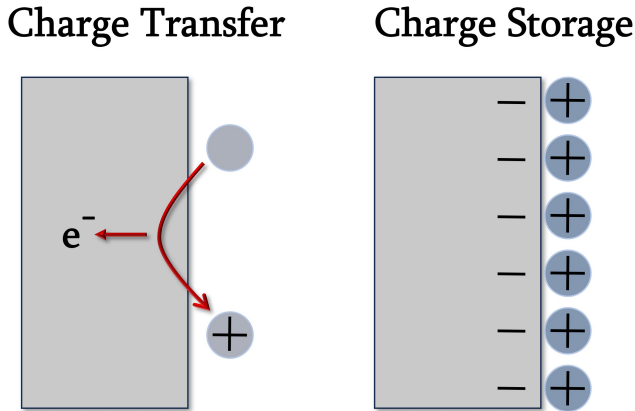


Figure 2.3: Schematic of a) Faradaic and b) non-Faradaic processes. a) A charge transfer happens to the electrode from the ions in the electrolyte. b) Ions in close proximity to the electrode create an Electrical Double Layer (EDL) and act as charge storage.

and the electrolyte [21].

As explained above, the electrode-electrolyte interface can be modeled as a capacitor [8]. At any potential, the amount of charges in the metal electrode will be the same but of the opposite sign of the charges in the solution (Eq. 2.1). The charges in the electrolyte make up a thin layer in close proximity to the electrode.

$$\sigma_1 + \sigma_2 = -\sigma_{metal} \quad (2.1)$$

Where the charge density (σ) is defined as the charge over the sensing area. Such charge organization is described as the EDL with cumulative dipole molecules in the solution. The charge layers which are in close proximity to the metal electrode are called the Inner and Outer Helmholtz layers (σ_1 and σ_2). Together they make up the charge density on the metal electrode surface but with the opposite sign (σ_{metal}) (Fig. 2.4 a). The charges will have chemical bonding at Inner Helmholtz Plane and Coulomb force at Outer Helmholtz Plane [22].

The charge density equation (Eq. 2.1) can be seen as a result of Gauss' Law since there is no current flow, and the net charge is zero in conductive bodies (Fig. 2.4 b). The work in [23] models the effect of polarization on the interface by treating the polarization by fictitious charges inside the electrode, which mirrors the surface charges.

In general, three main processes can occur at the electrode-electrolyte interface: Mass transfer, electron transfer for Faradaic operations, and adsorption-desorption for non-Faradaic processes. Non-Faradaic processes have the possibility to be reversible, which is also a desirable characteristic for sensors with long lifetimes. The sensor lifetime is important, for example, for long-term testing of cell cultures, as in the case of OoCs.

Additionally, we distinguish two types of adsorption. The first one is non-specific adsorption, in which electrostatic forces can alter the surface function of the metal layer with close proximity ions. The second one is specific adsorption, with a strong bond be-

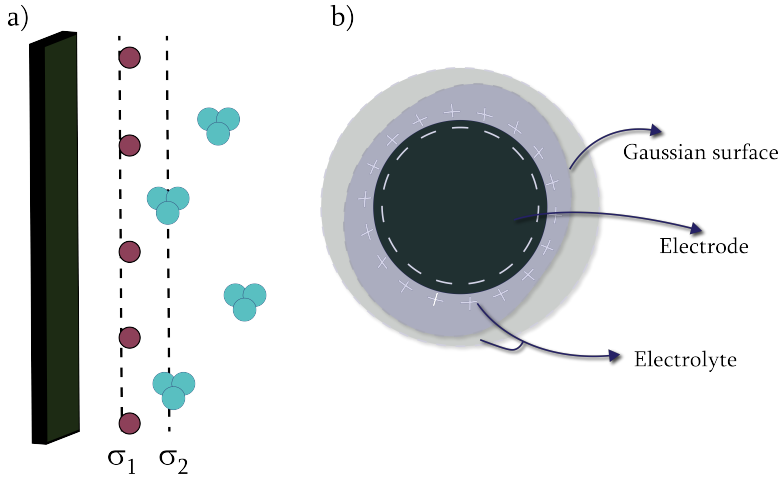


Figure 2.4: Electrode-electrolyte interface. a) Layers of EDL with the metal electrode (left). σ_1 contains specifically adsorbed layers, and is called Inner Helmholtz Plane. σ_2 converges to the bulk potential of the solution and is known as Outer Helmholtz Plane. The summation of these charge densities is equal and opposite to the one at the surface of the metal electrode (σ_{metal} not shown). b) Gaussian layer with the representation of net zero charges between electrode and electrolyte layers.

tween the electrode and the electrolyte layer. These adsorptions can alter the working point and hence the electrode's potential. For example, polar water molecules can form a layer on the electrode and thus change the potential.

Hydroxyl groups cover the MO_x layer, which is an intrinsic property of the material and can form a negatively- or positively- charged surface groups. This, in turn, form the EDL layer [13], (Fig. 2.5). The binding sites and hydroxyl group-density on the surface determine the sensitivity of the coating.

HfO_x , TiO_x and AlO_x are alternatives for MO_x layers. HfO_x is widely used in ISFETs with high sensitivity and beyond Debye limit monitoring (explained later in this chapter) due to high-k dielectric constant of HfO_2 [24, 25]. HfO_2 is a good candidate for pH detection [26]. Capacitance and impedance-based pH sensors were also reported based on HfO_x [27, 28]. TiO_2 is also a very well-known and studied MO_x for pH sensing [29, 30]. Another such MO_x layer for pH monitoring is Ta_2O_5 with a reported pH sensitivity across the entire range [31]. Ta_2O_5 can be a candidate for the MO_x layer for a future study.

Hydroxyl group densities on metal oxides are a measure of sensitivity and ion-exchange capacity [32]. For instance, Al_2O_3 has a high hydroxyl group density ($18OH/nm^2$), making it another great candidate for pH sensor sensing area. Additionally, the work in [33] shows Al_2O_3 has better sensitivity compared to SiO_2 for pH sensing. In literature, TiO_2 nanoparticles were reported to have a hydroxyl density of up to $12OH/nm^2$ [34]. For HfO_x , we could not find the reported hydroxyl group density.

When the electrode-electrolyte interface is discussed, describing the point of zero charge (PZC) and ionic screening layer, also known as Debye length λ_D , is important. PZC describes the point, especially for pH sensing, where the net charges on the sensing layer

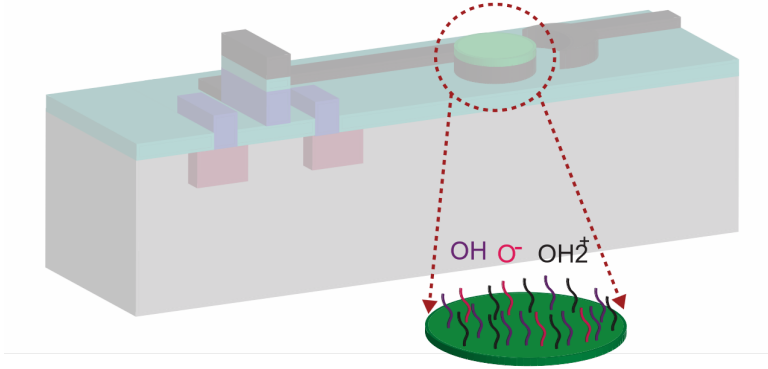


Figure 2.5: Metal oxide layer and its binding sites for charged analyte sensing.

(in this case, MO_x) are zero. Debye length is the distance from the electrode-electrolyte interface where the ionic effect of the surface is reduced by a factor of $1/e$. Eq. 2.2 shows the relation with the ionic strength of the solution, where ϵ is the dielectric constant of the solution-under-test, k_B is the Boltzmann constant, T is the temperature, e is the elementary charge, z and n are the valence number (characteristic of the element and the probability of the chemical bonds) and bulk ion density, respectively [35].

$$\lambda_D = \sqrt{\frac{\epsilon k_B T}{e^2 z^2 n}} \quad (2.2)$$

In summary, the Debye length is the defining factor for the sensing limit. If an analyte is at a distance beyond Debye length, it is not possible to monitor it. There are ways to alter the Debye length, such as increasing the frequency to alter the behavior of the ions or lowering the ionic strength of the solution, but this means diluting the solution under test, resulting in low detection [35]. For more details and derivation of the equations, refer to [21].

Depending on the pH of the PZC and the pH of the solution, the hydroxyl groups on the MO_x will be charged due to protonation or deprotonation, and a potential will be generated at the surface [22]. Depending on the sensing mechanism (3-electrode system or FET-based sensors), this potential will alter the working point of the sensor.

In other words, if the pH of the solution is higher than the pH of the PZC, the MO_x will become negatively charged. Conversely, if the pH of the solution is lower than the pH of the PZC, the surface will be positively charged [22] (Fig. 2.6).

As mentioned, HfO_x , Al_2O_3 , and TiO_2 are the most commonly chosen metal oxide layers for charge sensing, especially for pH sensing (Fig. 2.1 a). In this work, we wanted to compare these MO_x layers by fabricating compact extended FG-FET sensors and using them to monitor the pH of the solution-under-test without the need for an external reference electrode. This comparison includes sensitivity and reversibility.

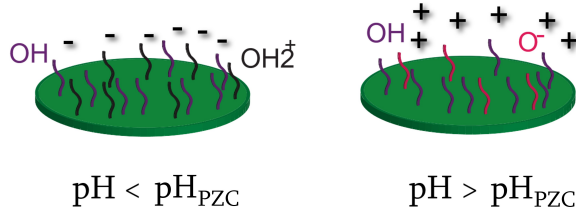


Figure 2.6: Schematic of how PZC affects the surface charge density in relation to pH.

2.3. CHARACTERISTICS OF THE FIELD-EFFECT TRANSISTOR

p-n junctions form the core of semiconductor devices. 'p' refers to the p-type semiconductor, which contains more holes than electrons, and 'n' refers to the n-type semiconductor with the opposite condition. The p-n junction allows the electrical current to only pass in one direction. Depending on the applied bias to the p-n junctions, devices such as diodes (Fig. 2.7) with two terminals can be realized.

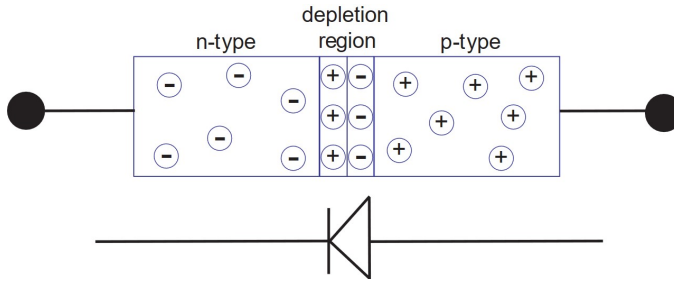


Figure 2.7: Schematic of an ideal p-n junction. For p-type semiconductors, holes are the majority carriers, whereas for n-type, electrons are the majority carriers. The depletion layer forms across the interface of the p and n regions. When a positive potential is applied from the p-terminal, the junction allows the current to flow, and when it is at a negative potential, the current cannot flow.

Even though there are numerous applications with 2-terminal devices such as photodiodes, light-emitting diodes, or Schottky diodes to give a few examples, 3-terminal devices can in addition amplify the signal and control the current, which results from their working principle. 3-terminal devices include another terminal, the gate, in addition to the source and drain, to control the output current by controlling the potential of the channel between the latter. Metal-oxide-semiconductor field-effect transistors (MOSFETs), which were explained in Chapter 1 briefly, are three-terminal devices with a metal-oxide-semiconductor capacitor to manipulate the channel formation (hence the working point) of the two-terminal device. They are active devices in which an electrode with an insulation layer (gate) determines the on/off state. Hence, the channel is formed between the two other electrodes (source and drain), implemented as high-doped regions inside the semiconductor substrate.

MOSFETs can be divided into 2 types by doping of the active regions: nMOS or pMOS. The working principle can be summarized into three regimes. If we consider the nMOS,

with the source and substrate of the device at ground potential, the first regime is when the channel is 'off,' meaning that the threshold voltage V_{TH} needed to establish the channel has not been reached by the voltage of the gate (V_G). In this case, V_G is smaller than V_{TH} , and V_D , the voltage applied to the drain terminal, is greater or equal to zero (Eq. 2.3, Fig. 2.8).

$$\begin{aligned} V_G &< V_{TH}, \\ I_D &= 0 \end{aligned} \quad (2.3)$$

When $V_G < V_{TH}$, the inversion layer underneath the gate and gate oxide cannot form. The inversion layer forms when V_G attracts the charge carriers between source and drain terminals to form a channel. The other two regimes of the FET are directly related to the formation of the inversion layer.

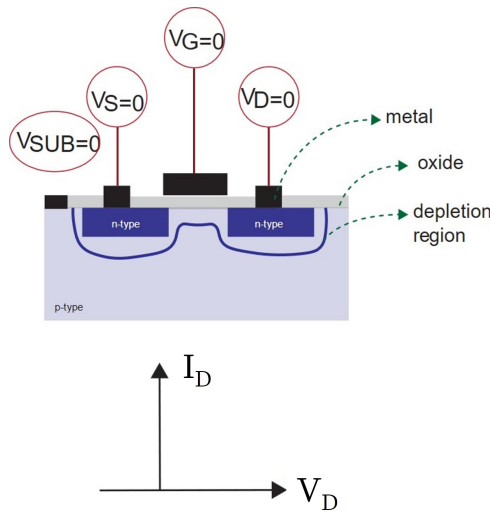


Figure 2.8: Schematic of nMOS, when the device is not 'turned on.'

The second regime is the linear region. In this region, the transistor is 'on,' the applied voltage on the gate is greater than the threshold voltage, and the inversion layer is created uniformly between source and drain terminals (Eq. 2.4).

$$\begin{aligned} V_G &> V_{TH}, 0 < V_D < V_G - V_{TH}, \\ I_D &= \mu_x C_{OX} \frac{W}{L} [(V_G - V_{Th})V_D - \frac{(V_D)^2}{2}](1 + \lambda V_D) \end{aligned} \quad (2.4)$$

In the I_D , μ_x is the carrier mobility, C_{OX} is the capacitance of the oxide, and W and L are respectively width and length of the gate. The voltage applied to the drain terminal is also larger than zero, contributing to the drift of the charge carriers from the source to the drain terminals, which we observe as the drain current. In this regime, the FET behaves as a voltage-controlled resistor (Fig. 2.9).

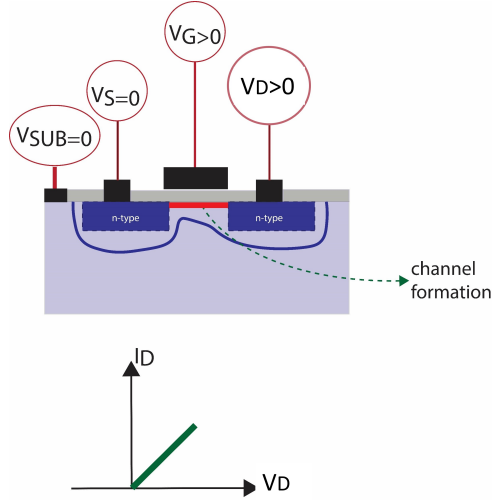


Figure 2.9: Schematic of nMOS in linear regime, when the gate voltage exceeds the threshold voltage, and the drain voltage is applied.

The third regime is the saturation mode, where the source-drain channel's current is active and highly dependent on the gate voltage (Eq. 2.5). The drain current reaches saturation, meaning that drain voltage cannot modulate the channel anymore, and there is a 'pinch-off' of the channel towards the drain terminal (Fig. 2.10). At the saturation regime, V_G modulates the I_D and the nMOS turns into a constant-current device [36].

$$V_G > V_{TH}, V_D > V_G - V_{TH},$$

$$I_D = \frac{1}{2} \mu_x C_{OX} \frac{W}{L} (V_G - V_{TH})^2 (1 + \lambda V_D) \quad (2.5)$$

In saturation regime, V_D should not change the pinched-off point of the channel. However, with higher V_D , this pinch point can vary and still change the I_D . The λV_D factor is added to the I_D , to represent this modulation of the length of the formed channel [37]. Another aspect we need to address is the 'mode' of the transistor. As explained above, when V_G is smaller than zero, the channel is not formed, so the device is 'off.' This behavior explains the Enhancement mode. However, for some transistors, even at null V_G , the transistor is 'on,' hence there is I_D . This type of mode is called Depletion.

The depletion mode has a thin N-type impurity layer between source and drain terminals. So when a negative voltage is applied through the gate terminal, it will repel the charge carriers (electrons). Hence, the conductivity of the channel decreases, resulting in lower and eventually null I_D .

When more positive V_G values are applied, we see the enhancement mode behaviour also in depletion mode devices (Fig. 2.11).

For the case of the FG-FET, the main gate electrode is replaced by a control-gate and a floating gate, which are capacitively coupled. The extension of the floating gate reaches into the sensing area, which is also coupled to another gate (CG_2) (Fig. 2.1 a). The sec-

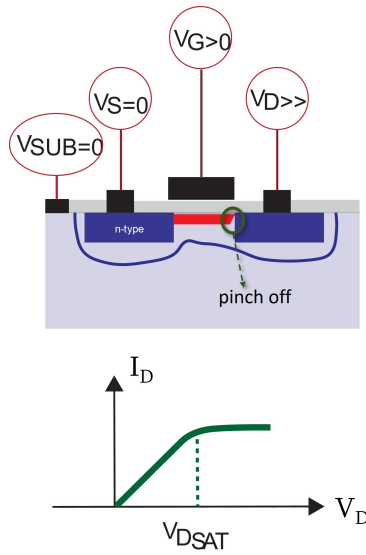


Figure 2.10: In saturation regime, the drain current reaches saturation, and the channel is 'pinched off' towards the drain terminal.

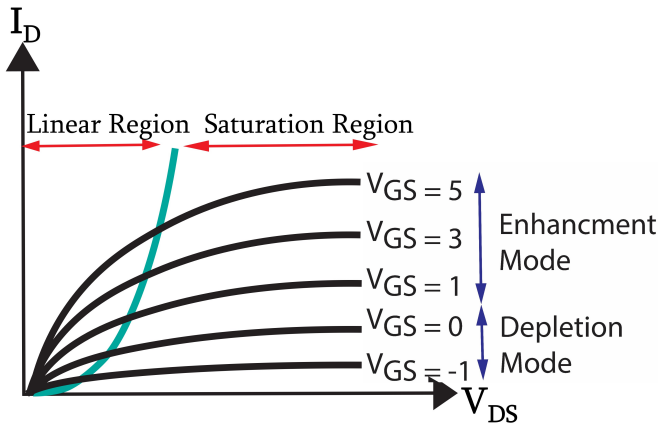


Figure 2.11: Plot of depletion and enhancement mode MOSFET. Depletion mode works when the $V_G < 0$, and more negative potential is needed to turn the transistor off. With higher potential, it will behave as enhancement mode MOSFET. Additionally, linear and saturation regions are shown.

ond gate can be considered as the in-plane reference of the bulk of the electrolyte and is needed to complete the circuitry and create a double layer on the sensing extension, with the placement of the analyte (electrolyte or cell culture). When there is an analyte between CG_2 and the sensing area of the FG extension, the charges in close proximity to the sensing area create the charge separation, as explained above. This separation

causes the change in the MOSFET properties (e.g., regulation of the channel), which in turn causes a shift in the threshold voltage and the drain current (Fig. 2.1 b).

Since the FG has an extension, the sensor is an EGFET, where the MOSFET part of the sensor is separated from the sensing area [4].

In the next section, combining FET and electrochemical behavior will be investigated.

2.4. ANALYSING THE ELECTRODE-ELECTROLYTE INTERFACE OF THE FET

As introduced in Section 2.1, the floating gate is capacitively coupled to 2 control-gates (CG_1 and CG_2). There is a SiO_2 dielectric between CG_1 and FG, and the applied voltage through CG_1 determines the initial working point of the transistor without introducing any electrolyte at the sensing area. CG_2 and FG are connected through the electrolyte since FG has an extension at the sensing area, as well as CG_2 . The drain current can be calculated from changes in V_{FG} and the threshold voltage, which is related to the characteristics of the transistor at the saturation regime:

$$I_D = \alpha(V_{FG} - V_{th})^2 \quad (2.6)$$

Where α is the constant associated with transistor characteristics such as the mobility, gate dimensions, and the drain-source voltage:

$$\alpha = \frac{\mu_{eff} W c_{ox}}{2L} \quad (2.7)$$

To calculate α , effective carrier mobility of the silicon $\mu_{eff} = 0.135 m^2/Vs$ and oxide capacitance ($c_{ox}WL$) are taken into consideration, where c_{ox} is the capacitance per unit area and W and L are gate width and length, respectively.

The initial threshold voltage of the FET can be determined by two approaches: 1) Experimental measurements and 2) Modeling the FET with software such as COMSOL. To find the threshold voltage from the experimental data, the intersection of the tangent of the transconductance curve (I_D vs. V_{FG}) with the gate voltage can be used (Fig. 2.12).

The drain current equation (Eq.2.6) is solved with respect to the change in the voltage at the FG, where in theory there is no direct application of an additional potential (hence 'floating'). The FG is capacitively coupled to the CG_1 and the potential (Ψ_S), which is created by the charges at the sensing area (Fig. 2.1 b).

$$V_{FG} = \frac{C_{CG1}V_{CG1}}{C_{tot}} + \frac{Q_0}{C_{tot}} + \frac{C_S\Psi_S}{C_{tot}} \quad (2.8)$$

The total capacitance, C_{tot} , contains the capacitance between the floating area and the silicon, C_{CG1} , and the sensing area capacitance, C_S . Here, we assume the voltage applied from CG_2 is zero.

Since there is no change in the CG_1 voltage and the initial trapped charges (Q_0), the change in the FG voltage is in direct relation to the change in the charges in close proximity to the sensing area (Eq. 2.9).

$$\Delta V_{FG} = \frac{\Delta C_S \Psi_S}{C_{tot}} = \frac{\Delta Q}{C_{tot}} \quad (2.9)$$

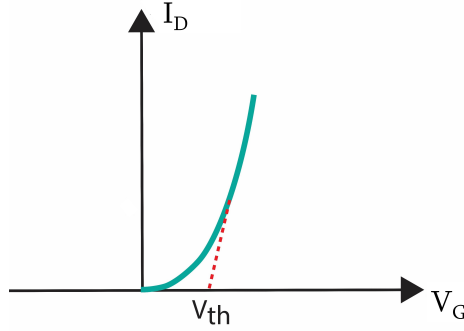


Figure 2.12: I_D vs. V_G graph for threshold voltage estimation. Where the slope intersects, the x-axis reveals the threshold voltage of the transistor [38].

However, to take a closer look at the relation between the solution-under-test and the FET, a set of equations is needed.

In order to evaluate the effect of the sensing area and the contribution to the I_D change, the potential at the sensing area (Ψ_S) and the capacitance (C_S) can be calculated from the dielectric constant of the sensing layer (ϵ_{MO_x}), its thickness (t_{MO_x}) and the sensing area (A_S):

$$C_S = \frac{A_S \epsilon_{MO_x}}{t_{MO_x}} \quad (2.10)$$

Without considering electrolyte and electrochemical equations, the charges at the sensing area can be modeled with a circuit by integrating a capacitor and a resistor. Details of this Falstad model can be found in APPENDIX A.

At a surface chemistry level, sensing area capacitance can be simplified as C_S but can also be thought of as a function of the EDL, as shown in Fig. 2.4. Various models to examine the charging of surfaces have been developed in the last decades. Here, we use the site-dissociation model with EDL [39, 40]. This model is based on both the site-binding theory and electric double-layer capacitance [41].

The total charge on the sensing surface (σ_{total}) is the difference of the surface charge σ_1 and the charges from the EDL σ_2 .

The surface charge (σ_1) is in direct relation to the FG voltage, the capacitance at the sensing area, and the potential at the surface. σ_2 is directly related to the Stern Capacitance, C_{stern} , which is due to the adherence of the ions to the electrode surface in close proximity [39], and the potential difference between surface charge layers (Fig. 2.13). The surface charge at the sensing area of the MO_x contains hydroxyl groups that the ions can bond to. These groups are shown in Fig. 2.5.

The total surface charge is then related to the number of available bonds, also known as binding sites. The number of binding sites, N_s , is fixed, depending on the material constants. Alteration of the surface chemistry by means of fabrication is possible.

$$N_s = \gamma_{O^-} + \gamma_{OH_2^+} + \gamma_{OH} \quad (2.11)$$

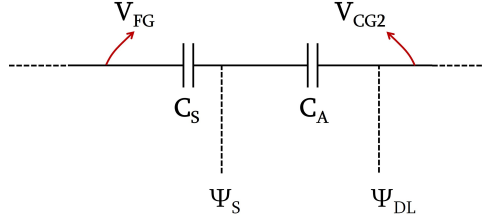


Figure 2.13: Close up view of Fig. 2.1 for surface-level analysis. Adapted from [39].

N_s contains all the amphoteric binding sites. To evaluate the equilibrium solution parameters and the ratio of charges (or ions) in the bulk solution, dissociation constants (K_B and K_A) are needed. These constants determine how many ions will be available for the binding sites.

If we assume the bulk potential of the electrolyte to be approximately equal to the potential applied from CG_2 or any 'pseudo'/real reference electrode, and is zero, the bulk potential and its charges (q_{bulk}) can be translated to the metal-oxide layer by means of the Boltzmann equation [41], which shows that the available charges decrease exponentially towards the sensing area:

$$q_s = q_{bulk} \exp\left(-\frac{e\Delta V}{kT}\right) \quad (2.12)$$

If we apply the Boltzmann equation to the surface charge with dissociation constants, the final equation describes how many ions in the bulk solution are contributing with the equilibrium limit (from dissociation constants) to the available binding sites. Eq. 2.13 also contains the constant from the neutral ions at the binding surface (A), which is the reason why we see the alteration of the drain current from the application of DI water (due to the dipole molecules), as will be shown in the experimental section.

$$\sigma_1 = A + \frac{-qN_s}{1 + \frac{H^+}{K_A}} \exp\left(-q\frac{\Delta V}{kT}\right) + \frac{qN_s}{1 + \frac{K_B}{H^+}} \exp\left(q\frac{\Delta V}{kT}\right) \quad (2.13)$$

To solve the relation between σ_1 and σ_2 , the Grahame equation can be adapted. This equation simply equates the surface potential to the surface charge [41].

$$\sigma_2 = B \sinh\left(\frac{q\Delta V}{2kT}\right) \quad (2.14)$$

In Eq. 2.14, B is the constant term that explains how much 'energy' is needed for a 'distance' (Debye length) of charges:

$$B = \frac{\epsilon 2kT}{\lambda_D} \quad (2.15)$$

From the equations above, the relations between the solution, the ions in the solution, and how they affect the potential at the surface are defined. Fig. 2.13 shows the relation between σ_1 , σ_2 , C_A and C_S . This set of equations can be solved together to obtain the

relation between FG, I_D , and the characteristics of the electrolyte (or solution-under-test). These equations will be used in the next sections to obtain parameters such as dimensions for the sensor realization. Since the working principle of the sensor is established, optimization can be introduced. The most important optimization is related to the sensor behavior, and how to increase the sensitivity of the sensor towards specific ions and/or analytes.

In the following Chapter, the fabrication and characterization of FG-FETs with different sensing layers will be described and compared.

2.5. LAYOUT OF THE SENSOR

Since the modulation of the FG voltage directly depends on the capacitance at the sensing surface and the total capacitance (Eq. 2.9), the sensing area surface dimensions were chosen concerning the capacitance that will be created at the sensing area and the capacitance between CG_1 and FG. The ratio between these capacitances plays a role in the sensitivity of the sensor, apparent from the equations derived above. A Matlab model was implemented to evaluate the relation between the sensing area charges and the resulting I_D change. Symbolic variables were defined to solve potential and charge density at the sensing area and their effect on the change in V_{FG} . The parameters for this calculation are shown in Table 2.1. (The details of the model and the code are available in Appendix B.)

Table 2.1: Chosen initial parameters for the Matlab model. HfO_2 was chosen as the sensing area dielectric. ϵ is the dielectric constant of the material, t is the thickness, r_s is the radius of the sensing area, and d_{CF} is the dimension of the CG_1 plate.

$\epsilon_{SiO_2 PECVD} = 5$	$\epsilon_{HfO_2} = 25$	$t_{HfO_2} = 21\text{nm}$	$\epsilon_{SiO_2} = 3.8$
$r_s = 350\mu m$	$d_{CF} = 490\mu m$	$L = 2\mu m$	$W = 20\mu m$

The model compares the change in I_D to the change in pH with an arbitrarily chosen dissociation constant of $pK_A = 8$. $V_{CG2} = 0V$, $V_{DS} = 0.1V$ were chosen. Firstly, the dielectric thickness between CG_1 and FG was changed from 83 nm to 52 nm, which is the minimum value to have coverage of the electrode that PECVD can reproduce (see next chapter). The results show that the thinner dielectric increases the change of I_D for the same pH values (Table 2.2).

Table 2.2: The effect of the thickness of the dielectric between FG and CG to pH sensitivity.

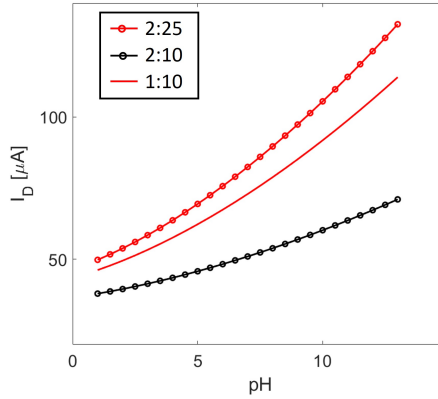
$t_{dielectric} = 83\text{nm}$	$t_{dielectric} = 52\text{nm}$
$\frac{I_{DpH_9}}{I_{DpH_7}} = 1.13$	$\frac{I_{DpH_9}}{I_{DpH_7}} = 1.15$
$\frac{I_{DpH_7}}{I_{DpH_4}} = 1.09$	$\frac{I_{DpH_7}}{I_{DpH_4}} = 1.12$

The sensing area is directly related to the binding site count, hence the number of possible bindings. However, when the radius of the sensing electrode ($r_{sensing}$) was chosen to be $500\mu m$ instead of $200\mu m$, the capacitance value increased, and the total sensitivity decreased (Table 2.3).

Table 2.3: The effect of the radius of the sensing surface (extension of the FG) on the pH sensitivity.

$r_{sensing} = 500\mu m$	$r_{sensing} = 200\mu m$
$\frac{I_{DpH9}}{I_{DpH7}} = 1.15$	$\frac{I_{DpH9}}{I_{DpH7}} = 1.17$
$\frac{I_{DpH7}}{I_{DpH4}} = 1.12$	$\frac{I_{DpH7}}{I_{DpH4}} = 1.3$

Another parameter is the geometry (W:L) of the gate dimensions, which is directly related to MOSFET oxide capacitance and hence the formation of the channel. The ratio is also related to the transconductance, g_m , which influences the performance of the FET. Higher g_m and larger surface area devices have lower flicker (1/f) noise [4]. For different values of W:L, changes in the I_D are observed (Fig. 2.14).

Figure 2.14: Graph of I_D vs. pH with different gate dimensions. When the ratio between $L:W$ is greater, the change is also linearly greater.

As an alternative utilization of the same structures, the extension of the FG can also be used as the working electrode (WE) for a passive electrochemical sensor. For the passive electrochemical sensor, CG_2 can be used as RE, and a CE electrode was included in the design (Fig. 2.15). From the literature, it was found that uniform current and potential distributions are important to have reliable measurements (and for cell viability for the experiments with cell cultures) [42]. To show the uniform electric field distribution, a COMSOL model was created (Fig. 2.16). The potential difference between the center electrode and the circular counter electrode was 3V.

COMSOL simulation showed a uniform current distribution, which is one of the main concerns of 3-electrode systems. For integrated planar electrodes on the chip level with geometry as we suggested, it is possible to eliminate a bulky CE (for example, Pt wire), which should not move during measurements. With the considerations from the sensor parameters, a mask was designed with 4 nMOS and 4 pMOS devices with different L:W ratios (Fig. 2.17). Even though the dielectric layer did not change the sensitivity significantly (Table 2.2), the dielectric layer between CG_1 and FG was chosen to be 53

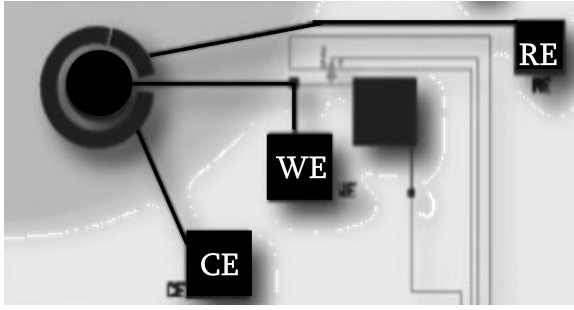


Figure 2.15: Conceptual design for the FG extension utilization as working electrode. The sensing area radius is $200\mu\text{m}$. Reference and counter electrodes are also shown in black.

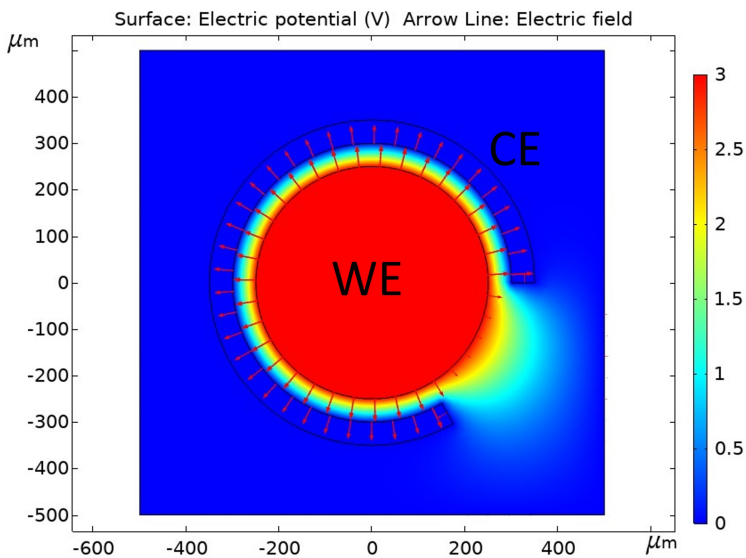


Figure 2.16: Comsol simulation of the passive electrode ($r = 250\mu\text{m}$ with a distance to the counter electrode of $75\mu\text{m}$) shows uniform current distribution.

nm, depending on the repeatability of the PECVD machine. Accordingly, the sensing area and capacitance should be less than the capacitance of the CG_1 . The radius of the sensing area electrode was chosen to be $200\mu\text{m}$.

2.6. DISCUSSION & CONCLUSION

In this chapter, we showed how to design FET-based electrochemical sensors without the need for external reference electrodes.

CG was coupled to FG to modulate the threshold voltage of the transistor. Firstly, the Falstad open-source circuit modeling platform was used to model the electrolyte interaction with the FG. Secondly, a Matlab code was developed to investigate the effect of the

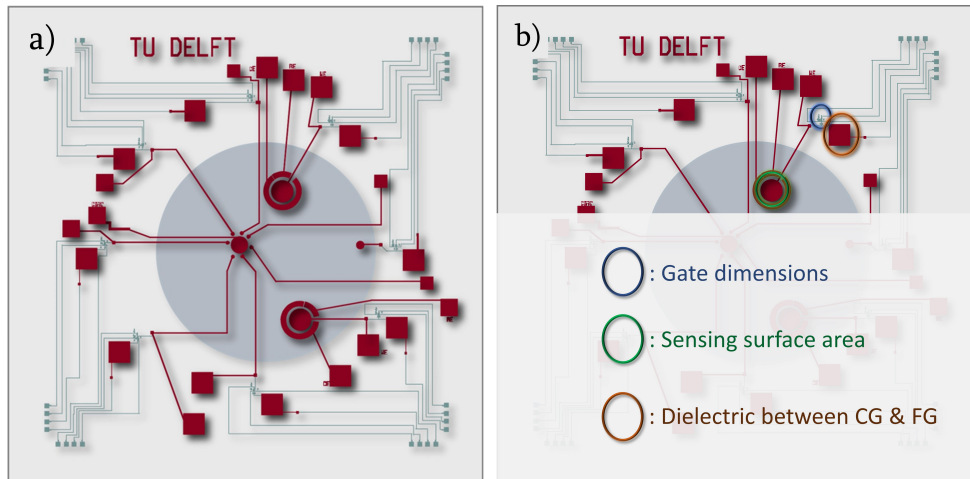


Figure 2.17: Design of the chip. a) The chip layout (1cm x 1cm). b) Main parameters investigated in this chapter for pH sensitivity.

FET parameters such as gate dimensions, capacitive coupling of the CG_1 and FG, capacitive coupling of a solution with different pH values to the sensing area, and integration of a pseudo electrode called CG_2 . The Matlab code specified electrochemical interaction at the surface of the electrode with different MO_x layers. The sensitivity of the designed FET regarding different pH solutions was investigated.

Due to the scalability of the cleanroom processing, a 3-electrode system was also included in the chip's design to serve as a set of passive electrodes for complementary electrochemical measurements. A 3-electrode sensor system consisting of a working electrode, reference, and counter electrodes was integrated into the design. The WE was connected to the FG extension. Hence, if the active region is distorted or the device is not functioning accordingly, these passive electrodes can also be used, for example, with a potentiostat measurement setup instead of FET terminals. The final design of the chip is shown in Fig. 2.17. This 1cm x 1cm chip provides the solutions for different electrochemical analyses to serve as an OoC device.

In the next chapter, the fabrication and characterization of the chips will be described.

BIBLIOGRAPHY

- [1] A Spanu et al. “A reference-less pH sensor based on an organic field effect transistor with tunable sensitivity”. In: *Organic Electronics* 48 (2017), pp. 188–193.
- [2] Monia Demelas et al. “Charge sensing by organic charge-modulated field effect transistors: Application to the detection of bio-related effects”. In: *Journal of Materials Chemistry B* 1.31 (2013), pp. 3811–3819.
- [3] Massimo Barbaro, Annalisa Bonfiglio, and Luigi Raffo. “A charge-modulated FET for detection of biomolecular processes: conception, modeling, and simulation”. In: *IEEE Transactions on Electron Devices* 53.1 (2005), pp. 158–166.
- [4] Salvatore Andrea Pullano et al. “EGFET-based sensors for bioanalytical applications: A review”. In: *Sensors* 18.11 (2018), p. 4042.
- [5] Shi Zhaoxia and Zhu Dazhong. “Modeling and discussion of threshold voltage for a multi-floating gate FET pH sensor”. In: *Journal of Semiconductors* 30.11 (2009), p. 114011.
- [6] Baozhen Chen, Archana Parashar, and Santosh Pandey. “Folded floating-gate CMOS biosensor for the detection of charged biochemical molecules”. In: *IEEE Sensors Journal* 11.11 (2011), pp. 2906–2910.
- [7] Alessandra Caboni et al. “Flexible organic thin-film transistors for pH monitoring”. In: *IEEE Sensors Journal* 9.12 (2009), pp. 1963–1970.
- [8] Allen J Bard, Larry R Faulkner, and Henry S White. *Electrochemical methods: fundamentals and applications*. John Wiley & Sons, 2022.
- [9] Stanley Wolf. *Microchip manufacturing*. Lattice press Sunset Beach, California, 2004.
- [10] M Valcárcel, A Gómez-Hens, and S Rubio. “Selectivity in analytical chemistry revisited”. In: *TrAC Trends in Analytical Chemistry* 20.8 (2001), pp. 386–393.
- [11] A_ Hulanicki and M Trojanowicz. “Calcium-selective electrodes with PVC membranes and solid internal contacts”. In: *Analytica Chimica Acta* 87.2 (1976), pp. 411–417.
- [12] Ying Lian et al. “Nanomaterials for intracellular pH sensing and imaging”. In: *Novel Nanomaterials for Biomedical, Environmental and Energy Applications*. Elsevier, 2019, pp. 241–273.
- [13] Libu Manjakkal, Dorota Szwagierczak, and Ravinder Dahiya. “Metal oxides based electrochemical pH sensors: Current progress and future perspectives”. In: *Progress in Materials Science* 109 (2020), p. 100635.

- [14] Jinghong Han et al. "A gastroesophageal tract pH sensor based on the H⁺-ISFET and the monitoring system for 24 h". In: *Sensors and Actuators B: Chemical* 66.1-3 (2000), pp. 203–204.
- [15] Peter Kurzweil. "Metal oxides and ion-exchanging surfaces as pH sensors in liquids: State-of-the-art and outlook". In: *Sensors* 9.6 (2009), pp. 4955–4985.
- [16] Navpreet Kaur, Mandeep Singh, and Elisabetta Comini. "Materials engineering strategies to control metal oxides nanowires sensing properties". In: *Advanced Materials Interfaces* 9.12 (2022), p. 2101629.
- [17] Chengxiang Wang et al. "Metal oxide gas sensors: sensitivity and influencing factors". In: *sensors* 10.3 (2010), pp. 2088–2106.
- [18] Christian F Chamberlayne and Richard N Zare. "What role does the electric double layer play in redox reactions at planar electrostatically charged insulating surfaces?" In: *Topics in Catalysis* 65.1-4 (2022), pp. 228–233.
- [19] PM Biesheuvel, S Porada, and JE Dykstra. "The difference between Faradaic and non-Faradaic electrode processes". In: *arXiv preprint arXiv:1809.02930* (2018).
- [20] Anis Allagui, Hachemi Benaoum, and Oleg Olendski. "On the Gouy–Chapman–Stern model of the electrical double-layer structure with a generalized Boltzmann factor". In: *Physica A: Statistical Mechanics and its Applications* 582 (2021), p. 126252.
- [21] Jianzhong Wu. "Understanding the electric double-layer structure, capacitance, and charging dynamics". In: *Chemical Reviews* 122.12 (2022), pp. 10821–10859.
- [22] Prashant Sharma et al. "Zinc-Oxide based EGFET pH sensors". In: *Nanostructured Zinc Oxide*. Elsevier, 2021, pp. 459–481.
- [23] Christopher W Outhwaite, Stanislaw Lamperski, and Lutful Bari Bhuiyan. "Influence of electrode polarization on the capacitance of an electric double layer at and around zero surface charge". In: *Molecular Physics* 109.1 (2011), pp. 21–26.
- [24] Hyun-June Jang and Won-Ju Cho. "Fabrication of high-performance fully depleted silicon-on-insulator based dual-gate ion-sensitive field-effect transistor beyond the Nernstian limit". In: *Applied Physics Letters* 100.7 (2012), p. 073701.
- [25] Shideh Kabiri Ameri, Pramod K Singh, and Sameer R Sonkusale. "Three dimensional graphene transistor for ultra-sensitive pH sensing directly in biological media". In: *Analytica chimica acta* 934 (2016), pp. 212–217.
- [26] Michael Lee et al. "Impedance characterization of the capacitive field-effect pH-sensor based on a thin-layer hafnium oxide formed by atomic layer deposition". In: *Sensors & Transducers* 27.5 (2014), p. 233.
- [27] Zina Fredj et al. "Capacitance electrochemical pH sensor based on different hafnium dioxide (HfO₂) thicknesses". In: *Chemosensors* 9.1 (2021), p. 13.
- [28] Michael Lee et al. "Impedance characterization of the capacitive field-effect pH-sensor based on a thin-layer hafnium oxide formed by atomic layer deposition". In: *Sensors & Transducers* 27.5 (2014), p. 233.
- [29] Rongrong Zhao et al. "A pH sensor based on the TiO₂ nanotube array modified Ti electrode". In: *Electrochimica Acta* 55.20 (2010), pp. 5647–5651.

- [30] Yi-Hung Liao and Jung-Chuan Chou. "Preparation and characterization of the titanium dioxide thin films used for pH electrode and procaine drug sensor by sol-gel method". In: *Materials Chemistry and Physics* 114.2-3 (2009), pp. 542–548.
- [31] Nancy Sharma et al. "Tantalum oxide thin films for electrochemical pH sensor". In: *Materials Research Express* 7.3 (2020), p. 036405.
- [32] Hiroki Tamura et al. "Surface hydroxyl site densities on metal oxides as a measure for the ion-exchange capacity". In: *Journal of colloid and interface science* 209.1 (1999), pp. 225–231.
- [33] N Choksi et al. "Modeling and Simulation of ISFET Using TCAD Tool for Various Sensing Films". In: (2017).
- [34] Chung-Yi Wu et al. "Markedly enhanced surface hydroxyl groups of TiO₂ nanoparticles with superior water-dispersibility for photocatalysis". In: *Materials* 10.5 (2017), p. 566.
- [35] Vladimir Kesler, Boris Murmann, and H Tom Soh. "Going beyond the debye length: Overcoming charge screening limitations in next-generation bioelectronic sensors". In: *Acs Nano* 14.12 (2020), pp. 16194–16201.
- [36] *Depletion mode MOSFETs*. <https://eepower.com/technical-articles/what-are-depletion-mode-mosfets/#>. Accessed: 2023-06-11.
- [37] *Harvard Lecture*. URL: https://in.ncu.edu.tw/ncume_ee/harvard-es154/lect_12_MOSFETs.pdf.
- [38] Mehmet C Oztürk. "Veena Misra and". In: *THE ELECTRICAL ENGINEERING HANDBOOK* (2004), p. 109.
- [39] Matti Kaisti et al. "An ion-sensitive floating gate FET model: operating principles and electrofluidic gating". In: *IEEE Transactions on Electron Devices* 62.8 (2015), pp. 2628–2635.
- [40] REG Van Hal, JCT Eijkel, and P Bergveld. "A general model to describe the electrostatic potential at electrolyte oxide interfaces". In: *Advances in colloid and interface science* 69.1-3 (1996), pp. 31–62.
- [41] Matti Kaisti, Qi Zhang, and Kalle Levon. "Compact model and design considerations of an ion-sensitive floating gate FET". In: *Sensors and Actuators B: Chemical* 241 (2017), pp. 321–326.
- [42] Morgan Binggeli, Tzu-Hsien Shen, and Vasiliki Tileli. "Simulating current distribution of oxygen evolution reaction in microcells using finite element method". In: *Journal of The Electrochemical Society* 168.10 (2021), p. 106508.

3

FABRICATION AND CHARACTERIZATION OF SILICON-BASED FG-FET

3.1. FABRICATION

Reproducibility and standardization in OoC device fabrication are crucial for robust organ models. Rather than having a single proof-of-concept chip, fabricating multiple identical chips at once in the same batch is important to show technical reproducibility and investigate biological relevancy by making available multiple identical chips to test biological cues. Therefore, BiCMOS-based wafer-level fabrication methods were used in this work to fabricate batches of nominally-identical chips, specifically OoC devices with integrated FET-based sensors [1]. The following sections will detail the choice of materials and fabrication methods. The transistors in Chapters 5 and 6 are fabricated similarly as described here. Hence, Chapters 5 and 6 present a variation and continuation of the fabrication described in this Chapter.

The schematic overview of the fabrication process is shown in Fig. 3.1.

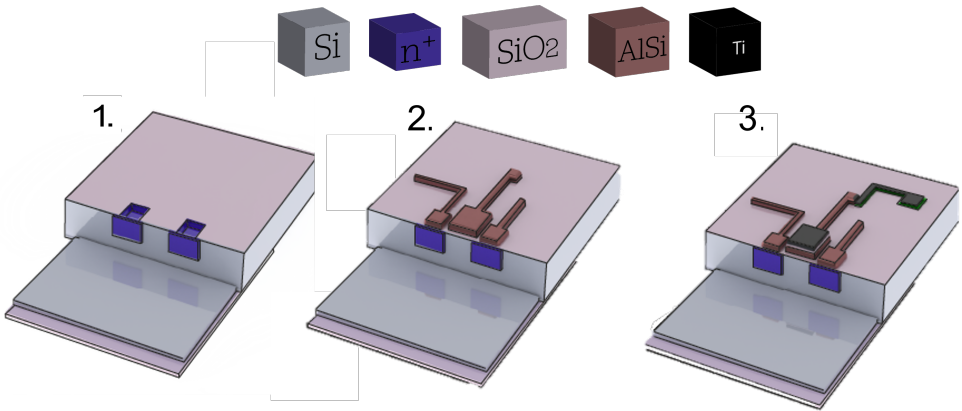


Figure 3.1: Schematic overview of the fabrication of the chips: 1) Implantation steps for source, drain, and substrate terminals, 2) Oxidation, deposition, and patterning of the first metal layer (for the FG and interconnects), 3) Deposition and patterning of the second metal layer with an underlying dielectric (for the CGs and extension of the FG. CG_2 is not shown in the schematic).

3.1.1. BICMOS PROCESSING

The BiCMOS process developed at TU Delft's Else Kooi Laboratory provides an a convenient solution for FET fabrication (Fig. 3.1 a) with few implantation steps. This enables the relatively low-cost realization of FETs [2].

4-inch, 525 μm -thick, double-side polished p-type Si wafers were used to fabricate nMOS- and pMOS-based sensors. For the first batch of wafers, high-resistivity ($1k - 10k\Omega\text{cm}$) wafers were chosen for fabrication to reduce leakage current through the wafer.

High-resistivity wafers mean intrinsically fewer mobile charge carriers, making it easier to deplete FET channel regions. Depleted regions might also act as resistive layers since there are no more mobile charge carriers to recombine. Hence, this situation can create a high series resistance at the whole device level. One advantage can be that the FET area will be isolated from the rest of the chip. Hence, the high resistivity substrate has both benefits and disadvantages. This issue will be discussed in the Characterization section

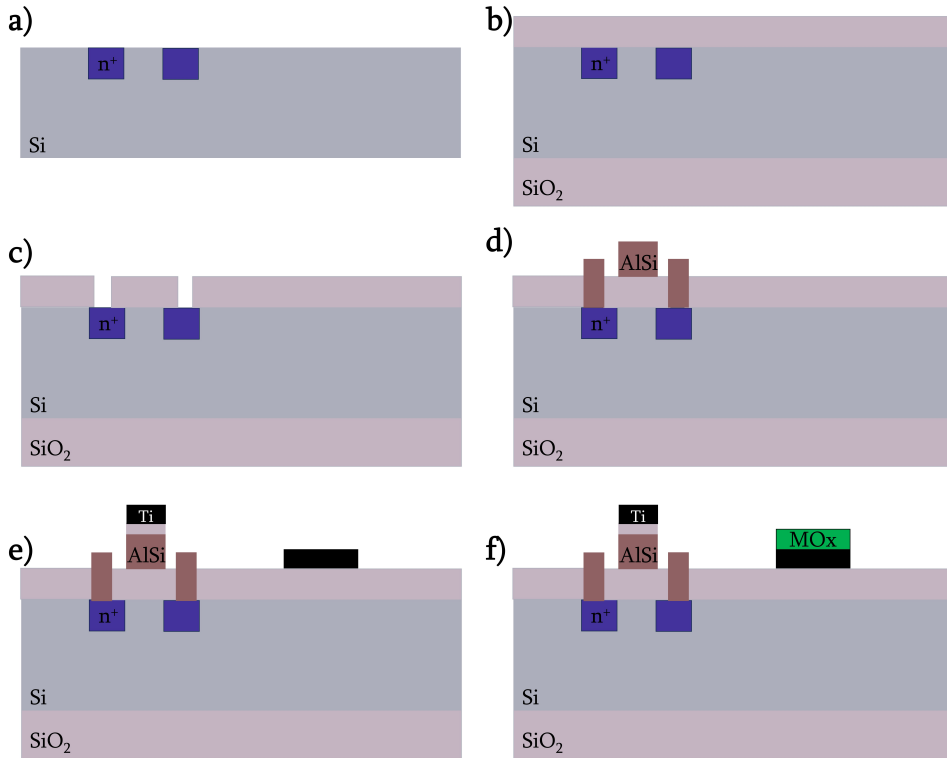


Figure 3.2: Overview of the flowchart of nMOS devices. a) Ion implantation, b) Oxidation, c) Dry etching of contact pads, d) First metalization for FG and interconnects with AlSi, e) PECVD oxide deposition for dielectric in between FG and CG, and second metalization for CG and FG extension, f) Deposition of MO_x layers.

in detail.

Ion implantation is a standard method to alter the electrical properties of silicon. Briefly, accelerated ions penetrate the semiconductor surface [3] and create damage [4]. Ions are extracted from an ion source by applying a voltage difference. Mass spectrometry makes the separation of the ions possible, where a magnetic field is applied towards the ions, and selected ions can pass through the tube of the implanter. Then, these ions are accelerated and penetrate into the wafer [4].

Three implantation steps were included in the flowchart (Fig. 3.2 a). Firstly, 20nm of SiO_2 dirt barrier were grown at 950°C . This step is essential to avoid possible channeling of the upcoming doping and to randomize the ion pathways. Lithography steps for N-Well definition (not shown in Fig. 3.2) were carried out by using a wafer stepper machine (ASML PAS 5500/80). The stepper is the key tool for photolithography, which uses 365 nm wavelength to expose photoresist through a chrome-glass plate with the mask design.

After the lithography, the wafers were implanted with phosphorus (150 keV, dose of $6 \cdot 10^{12} \text{cm}^{-2}$). The annealing (hence the drive-in) process was conducted at 1150°C for 4

hours. The annealing step helps the activation of the dopants and the silicon damaged by the implantation to recover its defect-free crystalline state.

The oxide was stripped by HF (hydrofluoric acid, 55%), and the wafers were cleaned with HNO_3 and DI water to remove any organic and metal contamination before continuing with other implantation steps. Cleaning the wafers and avoiding contamination was essential to obtain reproducible active devices at the end of the fabrication process.

For the source and drain terminals, shallow-N (SN) and shallow-P (SP) implantations were conducted consecutively, with similar fabrication steps. For SN, wafers were cleaned, and 4 minutes of HF dip was performed to remove native SiO_2 . Again, a 20 nm SiO_2 dirt barrier was grown under the same conditions as for the N-Well, and necessary lithography steps were carried out. For SN, the following parameters were chosen: As^+ , with energy and dose of 40keV and $5 \cdot 10^{15} cm^{-2}$, respectively. For SP, two different parameters were chosen to compare the operating performance of FETs. Boron was the dopant in both cases. The process parameters were: 1) 20keV, $4 \cdot 10^{14} cm^{-2}$ and 2) 15keV, $5 \cdot 10^{15} cm^{-2}$. As a light ion, Boron penetrates deeper into the silicon than heavy Arsenic atoms [4]. The high energy for ion implantation assists the ions to penetrate deeper. This is why the N-Well implantation has the highest energy compared to other implantations.

The mobility of electrons (μ_e) is higher than for the holes (μ_h) in Silicon ($\mu_e = 1400 \frac{cm^2}{Vs}$ and $\mu_h = 450 \frac{cm^2}{Vs}$ [5]). Hence, the electron flow will dominate the electric current if the same amount of holes and electrons are present. Therefore, nMOS devices are preferable for logic circuits [6] and were the preferred devices for electrochemical sensors in this thesis.

The gate oxide was grown using dry oxidation rather than wet to obtain higher quality oxide (Fig. 3.2 b). Dry oxidation is a process that involves oxygen gas, and wet oxidation is based on water vapor. Wet oxidation has a faster growth rate since water molecules can diffuse faster through silicon dioxide. Dry oxide is denser [7]. This quality can be appreciated when the oxide etching rates in HF solution are compared. Approximately 100nm of SiO_2 was measured by ellipsometry, and the Cauchy model was fitted on top of undoped regions to obtain the accurate thickness of the oxide.

Contact regions were opened by wet etching the oxide (Fig. 3.2 c) to land on silicon with implanted areas, and a 675 nm-thick layer of %99Al and %1Si (AlSi in the following) was sputtered for the interconnects and the floating-gate area. The sputtering occurred at 350°C, with a power of 10kW. DC sputtering was the deposition method, where the target material is bombarded with a carrier gas (Argon) in plasma conditions. A negative bias is applied to the target material, and a positive bias is applied to the plate and the wafer. Neutral argon atoms become ionized when they collide with the charged material target. Then, the target material atoms form a layer on the wafer [4].

The interconnect and floating-gate structures were defined by lithography. Etching of the layer took place in an inductively-coupled plasma reactive ion etcher (ICP-RIE). The main etching gas was Chlorine, whereas HBr was added to smooth the aggressive etching properties of Chlorine. The etching process consists of first a breakthrough etching of native Al oxide in Chlorine chemistry at 50W. The bulk etching of the layer consists of the same gas ratio (30:40 Chlorine:HBr) but at 40W. The recipe involves an end-point detection (Fig. 3.2 d). The wafers were annealed at 400 °C for 20 minutes in a nitrogen

environment to increase the Ohmic contact. Confocal microscope pictures confirmed selective dry etching of AlSi on oxide (Fig. 3.3).

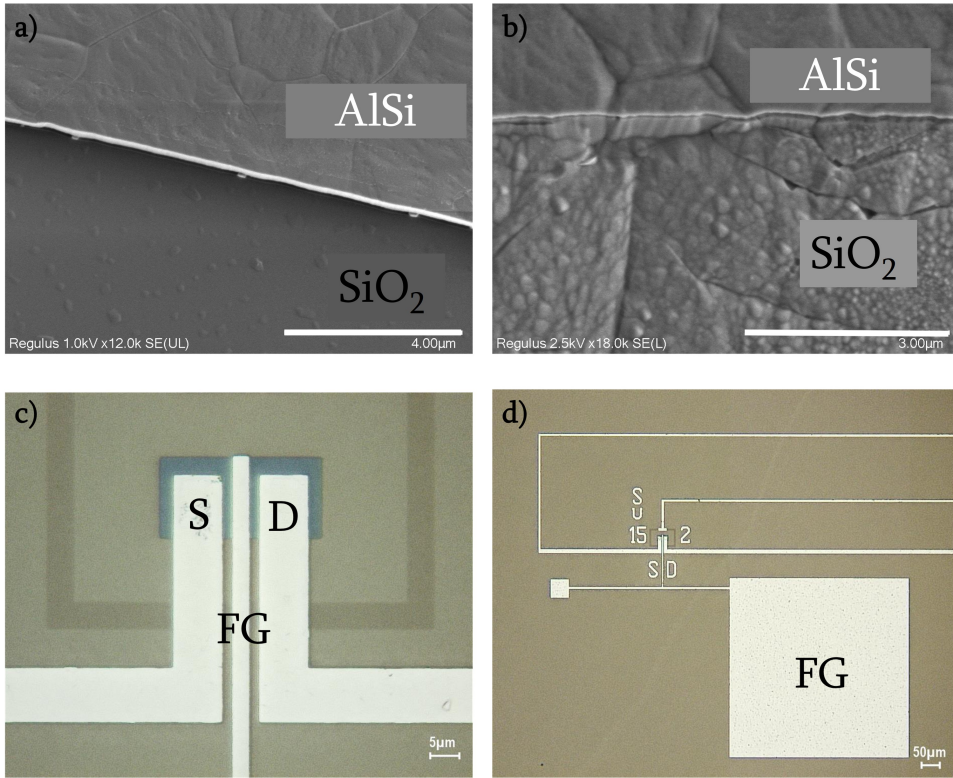


Figure 3.3: SEM images of the transistor after first metal (AlSi) etching: a) Before and b) After annealing of the first metal layer. Annealing did not visibly change the layers, but the effect was evidenced in the electrical measurements. Confocal microscopy pictures: c) Source, Drain, and FG terminals are visible with implantation altering the color underneath due to height difference, d) Overview with FG pad before the dielectric and second metal layer fabrications.

CHOICE OF DIELECTRIC MATERIAL

For the dielectric layer between FG and CG, plasma-enhanced chemical vapor deposition (PECVD) was used to obtain TEOS (Tetraethyl orthosilicate) and SiO_2 layers, respectively, on two identical wafers. TEOS is a precursor that results in SiO_2 when combined with water. The dielectric material choice depends mainly on the thermal budget due to the first metal layer (AlSi). AlSi has a melting point of 700° [8]. Because of this, low-pressure chemical vapor deposition (LPCVD) was not considered, even though the dielectric layers deposited with LPCVD have higher quality and conformality and, therefore, lower etch rates.

The TEOS layer was deposited at 350 °C, and PECVD SiO_2 layer was deposited at 400 °C. Even though TEOS was deposited at a lower temperature, the layer had a lower etch rate

than the PECVD oxide.

The most significant difference between the layers is the final stress they impose on the wafer, as caused by multiple depositions and fabrication steps. When TEOS was chosen as the dielectric, the bow of the wafer was 10-times higher than for the wafer coated with PECVD oxide. The thickness of the TEOS layer was measured on an ellipsometer with a Cauchy fitting model, and the thickness was 82 nm. PECVD oxide was deposited on the second wafer with a thickness of 53 nm (stress = -394MPa, bow of the wafer = 2.38 μm). For the process wafers, PECVD oxide was chosen to be the dielectric material between FG and CG layers (Fig. 3.2 e).

SECOND METALIZATION LAYER

After the deposition of the dielectric material, the second metal layer was sputtered (Fig. 3.2 e). The full wafer can be seen in Fig. 3.4 a. The second metalization layer constituted the CG, the extension of FG, a set of passive electrodes for electrical activity recordings, and a set of passive electrochemical sensors (Fig. 3.4 b). As mentioned in Chapter 2, a 3-electrode sensor system consisting of a working electrode (WE), reference and counter electrodes (RE and CE) was integrated into the design.

The second metal layer, 200 nm of Ti, was deposited at 350 °C, with 100 sccm Ar at 6 kW DC power in a sputtering machine (Fig. 3.4 c). After the lithography steps, the Ti layer was etched in ICP-RIE with Chlorine and HBr gases (30:40 ratio) with a power of 18 W. The grain formation can be observed in Fig. 3.4 d. It increases the surface area and the binding sites for the detection of analytes.

The electrical terminals were defined so that if the active devices were found to be not working optimally, the same electrodes could be used as a passive 3-electrode system from the contact pads.

One problem that can arise during Chlorine-based etching is that Chlorine can form HCl, when the machine is vented from the humidity of air. This HCl can continue etching the metals. To avoid this, the wafers were submerged into DI water to neutralize the residual HCl.

3.1.2. DEPOSITION OF METAL OXIDE TO ENHANCE SENSITIVITY OF pH SENSING

As explained in Chapter 2, metal oxide surfaces, specifically the binding sites with hydroxyl groups, are widely employed to functionalize sensing electrode areas in pH sensors. Here, we tested three options: TiO_x , HfO_x , and AlO_x . High-k dielectric materials, as in the case of these oxides, are beneficial for high charge storage capacity and high capacitance [9].

The first choice was to use native TiO_x . The wafer was placed in an oxygen-rich environment to enhance the oxidation process of Ti. For this, 1000 W oxygen plasma was used with 400 sccm of O_2 flow. Another option was using an oxidation furnace. However, the thermal budget due to the first metal layer prevented the latter option.

The increase in sheet resistance of the Ti layer proves the oxidation: 20 minutes of oxygen plasma increased the resistance by 0.128 Ω/sq .

The second choice was to deposit a thin HfO_x layer. In spite of being a high-k dielectric material and a favorable choice for gate oxide, to our knowledge, HfO_x has not been

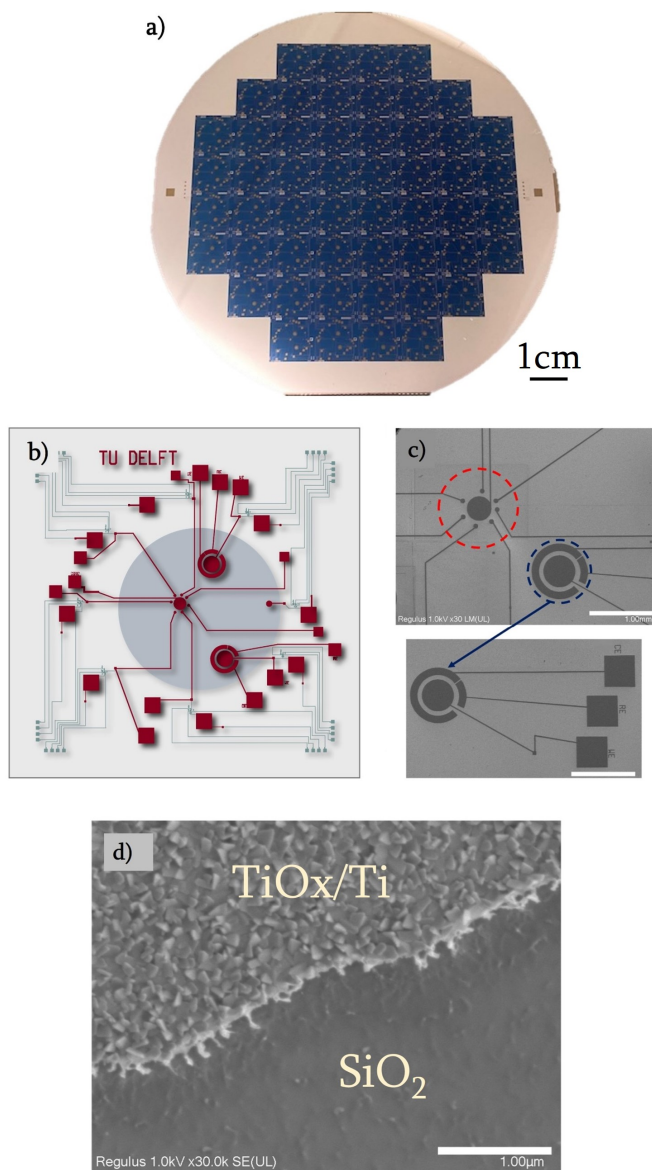


Figure 3.4: a) Full-wafer after Ti patterning. b) Schematic of the chip design explained in Chapter 2. The design shown in red is the second metal layer. c) SEM image of additional electrodes (red) and 3-electrode electrochemical sensing device (blue) with an inset showing the micrograph (Scale bars are 1 mm). d) SEM of Ti layer where grain formation can be appreciated.

integrated into FG-FETs before, and we wanted to study the enhancement of the sensitivity it could introduce. The third choice, as explained in Chapter 2, was to use AlO_x , owing to its high hydroxyl group density.

To deposit an MO_x layer, atomic layer deposition (ALD) or e-beam evaporation can be considered. With ALD, high-quality and highly conformal, single-atom-thick layers can be obtained. However, since each layer is formed atomically and sequentially, this fabrication method is time-consuming. Additionally, the lift-off patterning method is difficult to perform since ALD delivers a conformal deposition. The alternative to lift-off patterning could be to use BHF (1:7) to selectively etch HfO_x , as in the case of most oxides, due to the fluorine chemistry. However, the fluorine will also attack the Ti layer underneath HfO_x . Hence, a lift-off process is easier for this process architecture, where the deposition step follows the lithography for the openings at the sensing areas. To do so, before the e-beam deposition, lithography by direct laser writing was used. The laser writer prevents the need for a glass mask while working at i-line wavelength. Very similar exposure values as for the stepper can be expected. The lithography step was designed to have cured photoresist everywhere on the wafer, except where the MO_x layer was desired to stay, namely the sensing areas (Fig. 3.5). An e-beam evaporator with pallets of HfO_x or AlO_x was then used to deposit these layers on different wafers. 1-methyl-2-pyrrolidinone (NMP) at 70 °C with sonication was used for the lift-off process to remove MO_x where it was deposited on the photoresist (Fig. 3.6 a,b).

Diffusion of any ion can risk shortening the electrical connections and prevent the transistors from functioning correctly. To minimize this diffusion, no high-temperature process was performed after the previous step, and all active device areas (also the backside of the wafers) were covered with photoresist and oxide. For the evaporation of both

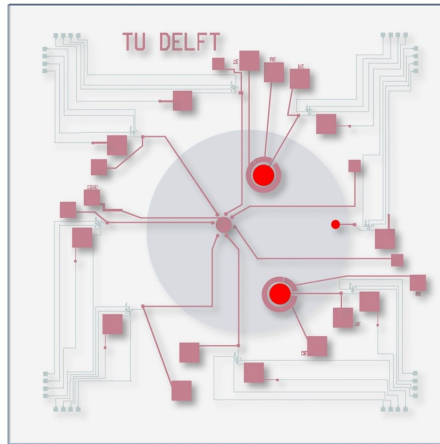


Figure 3.5: Mask design for the MO_x etching. The sensing area on the Ti electrodes (shown with bright red) was exposed to deposition whereas the other areas were covered by photoresist for the lift-off process.

AlO_x and HfO_x , to eliminate diffusion of ions in the equipment chamber, the backside of the wafer was coated with photoresist and the chamber was conditioned with evaporation of the same materials with dummy wafers. Since this was the last step of the process and no high-temperature steps were needed afterward, contamination risks were minimized. The chamber temperature during evaporation was monitored, and the maximum temperature was recorded as 72 °C.

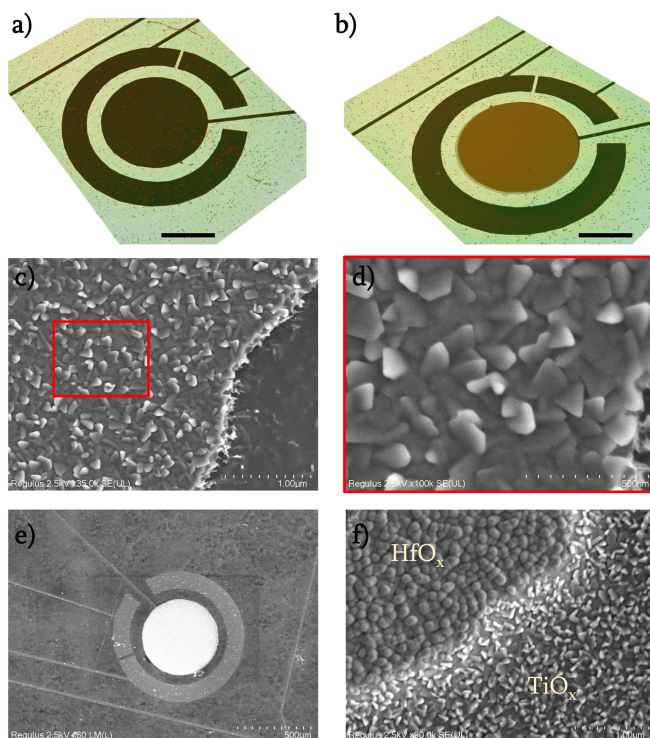


Figure 3.6: Laser confocal microscopy images of the electrodes with a) TiO_x and b) HfO_x layers (scale bar: $100\mu m$), after lift-off process. c,d) TiO_x surface and micrograph. e) HfO_x -decorated working electrode (FG extension) with circumferential electrode. f) Micrograph of HfO_x layer on Ti/TiO_x layers.

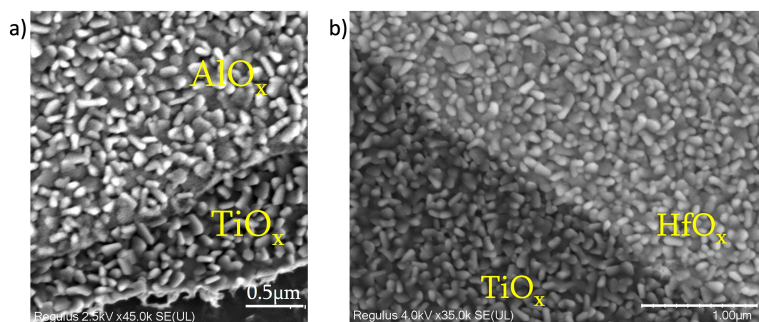


Figure 3.7: a) AlO_x and b) HfO_x layers on TiO_x and Ti. The difference in grain boundaries of the layers is apparent from the SEM images.

The specific features of the TiO_x surface (Fig. 3.6 c,d) are apparent when compared to HfO_x deposition on TiO_x (Fig. 3.6 e,f). Deposition of HfO_x layer without adhesion problems on Ti and its oxide was successful.

After the lift-off process with NMP, cleaning and inspection with confocal microscopy

and SEM, the wafers were ready for characterization steps.

3.2. CHARACTERIZATION

3.2.1. ANALYSIS OF THE ION IMPLANTATION

To examine the behavior of ion implantations, T-SUPREM4 was used. T-SUPREM4 is a process simulator commonly used for semiconductor fabrication steps [10]. Without fabricating and testing experimentally, T-SUPREM allows simulation of the process behavior. For a simplified simulation, a 1-D grid was used to observe the doping profile and obtain the implantation depth. This information is useful for understanding device behavior, which will later be examined with a COMSOL simulation. The starting material was initially assigned as Boron-doped silicon with <100> crystal orientation. The initial doping is correlated to the resistivity of the wafer. Then, the implantation dose and energies of different atoms (mentioned below) were set. Diffusion and annealing were also introduced after the implantations.

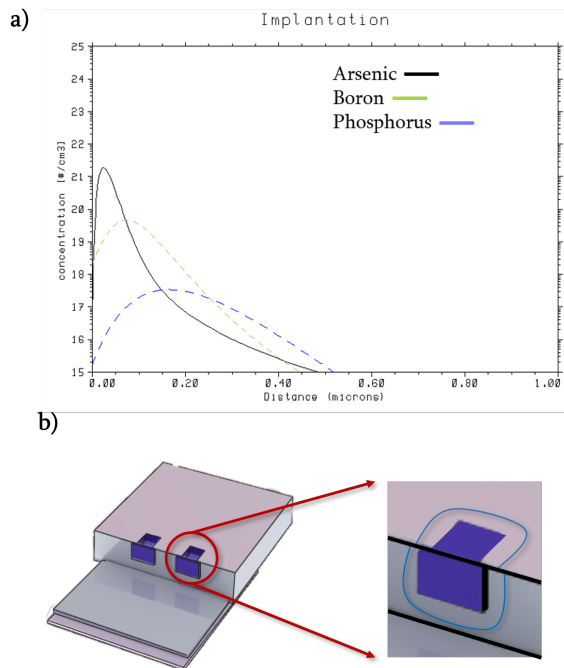


Figure 3.8: a) Simulations for ion implantation energy and doses. b) Schematic of the junction depth, shown with blue line. The junction depth is shown in a) as distance in the x-axis.

From Fig.3.8 a, the junction depth is apparent. The parameters for the ion implantation should be adjusted to have similar junction depths. The junction depth needs to be controlled not only in the direction orthogonal to the substrate but also in the lateral direction. Although the lateral direction might not have the same value as the junction depth, the implanted area for shallow-N, which will become the source or drain terminal,

goes underneath the gate electrode and effectively lowers the actual gate dimension by a value close to the junction depth (Fig. 3.8b). From the simulations, Arsenic implantation reaches a depth of $0.5\mu\text{m}$.

Simulations for different Boron parameters for shallow-P implantation showed similar penetration depths (Fig.3.9a and b). For Boron implantation, process parameters were: 1) 20 keV, $4 \cdot 10^{14}\text{cm}^{-2}$ (Fig. 3.9 a) and 2) 15 keV, $5 \cdot 10^{15}\text{cm}^{-2}$ (Fig. 3.9 b). However, the second case showed to reach the solid solubility limit. When this limit is exceeded, the ions cannot penetrate the silicon. They will be 'non-soluble' and they will form clusters. Additionally, the spiking in Fig. 3.9b was caused by the fact that the SiO_2 layer behaves as a sink for Boron atoms: not all the implanted dose will be used electrically. Some atoms will be damped in the oxide layer.

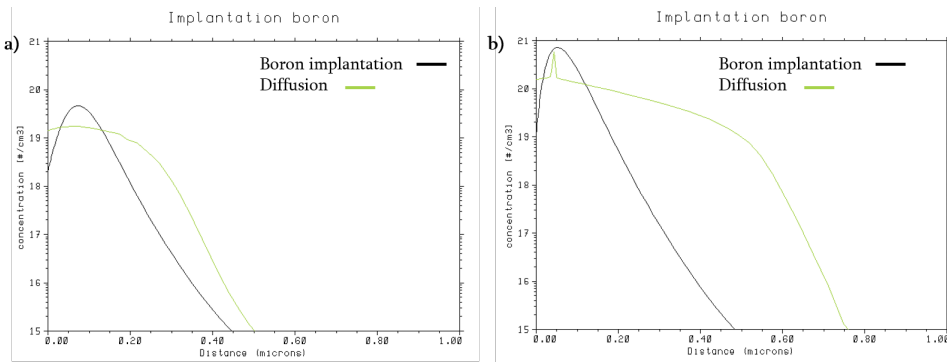


Figure 3.9: Simulations for Boron implantation and diffusion for a) 20 keV, $4 \cdot 10^{14}\text{cm}^{-2}$ and b) 15 keV, $5 \cdot 10^{15}\text{cm}^{-2}$. For both implantations, diffusion time was 10 minutes at 1000°C . The spiking (green line, diffusion) is apparent between $0 - 0.1\mu\text{m}$ distance.

To evaluate the effect of the junction depth, a 2-D COMSOL simulation of the nMOS was developed (Fig. 3.10). This simulation assigned source and drain terminals with the implantation dose and junction depth calculated with T-SUPREM4.

A 2-D model with Semiconductor Physics Module was used to simulate the transistor behavior. The source, drain, and gate terminals were adjusted by rectangles, corresponding to the dimensions obtained by cleanroom fabrication methods. For example, the length of the gate was $1.5\mu\text{m}$. The material was silicon, and the analytical doping model was chosen to adjust doping profiles with Gaussian distribution for source and drain terminals. A thin insulator gate module and metal contacts were assigned to indicate the gate oxide and the gate metal. A free triangular mesh was used to solve the boundary conditions [11] and the gate voltage was swept with a constant drain voltage.

Since the simulation is in 2-D, an out-of-plane thickness of $25\mu\text{m}$ was assigned to the silicon to mimic the interconnects. From Fig. 3.10, the formation of the inversion layer and the linear region was visible. From the simulation, it was apparent the nMOS device would work in depletion mode.

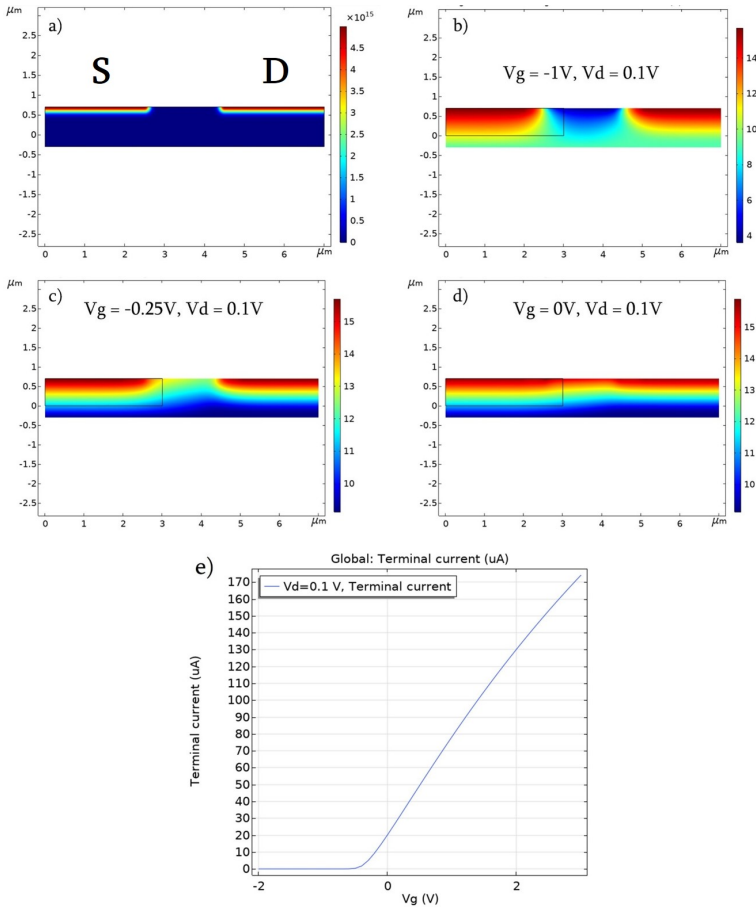


Figure 3.10: Consol simulations for the evaluation of nMOS behavior. Schematics show drain and source terminals. a) Implantation areas for source and drain terminals are shown [$1/\text{cm}^3$]. b) The FET is off, the depletion layer is visible (blue), and no inversion layer is apparent. c) Slight appearance of the inversion layer underneath the gate area, d) Almost uniform inversion layer, acting as a resistor underneath the gate area, and e) Linear characteristics of the FET, in depletion mode. The drain current is indicated as the Terminal current.

3.2.2. TEST STRUCTURES

After the first metal layer, test structures were measured using a semiconductor parameter analyzer to check whether the FETs worked as expected. The semiconductor parameter analyzer has a 4-needle probe station to apply and retrieve voltage and current values with source-measurement units (SMUs, Fig. 3.11). Over the whole wafer, 5 test structures were randomly chosen and measured, both for nMOS and pMOS structures (Fig. 3.12). The gate current was minimal (Fig. 3.12 a). As expected, the nMOS device behaved in depletion mode. In the I_D vs. V_D graph, with higher V_D values, the current tends to increase linearly, as in the case of a resistor. This behavior is due to the channel-length modulation [12].

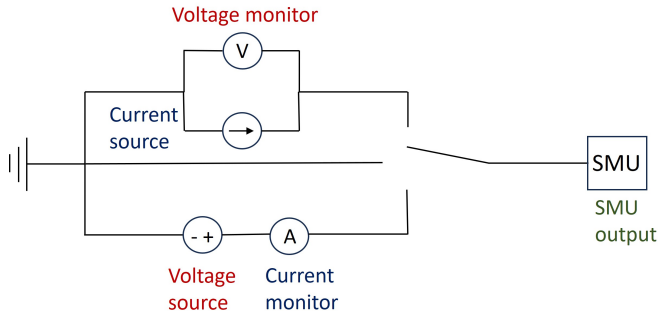


Figure 3.11: Working principle of the SMU unit. SMU unit works as the voltage source and current source, depending on the switch in the system (adapted from [13]).

The drain current (with a low dark current value) exponentially increases with positive gate voltage values. It starts in the depletion mode and with increasing V_G goes towards enhancement mode (Fig. 3.12). This behavior is also observed with low power and voltage sensors since they conduct at $V_{GS} = 0V$ and usually have negative threshold voltages [14].

Five nMOS test structures from 3 different wafers (15 measurements in total) were measured, and the dispersion of the I_D vs. V_G curves was attributed to a lack of threshold adjustment implantation (Fig. 3.12 b). Additionally, drain current versus drain and gate voltage values was monitored (Fig. 3.12 c). The measurements showed a minor variation for 20 keV Boron wafer. As explained above, two different doping parameters were examined for shallow-P, and the 20 keV implantation showed pMOS characteristics (Fig. 3.12 d).

The test structures had 20:2 W:L gate dimensions. Even though we observed channel-length modulation effects [15] on the behavior of the test structures, for the experiments, the change in the threshold voltage (V_t) is more significant than its initial value.

The fabrication continued after the initial characterization with the first metal layer, and the final devices with three different MO_x layers were characterized. The characterization involved surface analysis with X-ray spectroscopy and electrical measurements with potentiostat and Semiconductor Parameter Analyzer, with and without liquid-under-test, as described next.

3.2.3. SURFACE ANALYSIS

To evaluate the MO_x layers, energy dispersive X-ray spectroscopy (EDX) with SEM was used. This technique offers elemental analysis of materials. Depending on its atomic properties, the target material dissipates the kinetic energy of electrons, directed at it by an electron source in the form of X-rays. This phenomenon creates the 'fingerprint' of the material under concern. By monitoring the spectrum peaks, the material concentration can be characterized [16]. The analysis figures can be found in Appendix C.

EDX analysis showed higher count of Hf than O atoms (144:48) for 120 nm-thick HfO_x layer, whereas for 20 nm-thick HfO_x the ratio was 225:150. For AlO_x , the composition

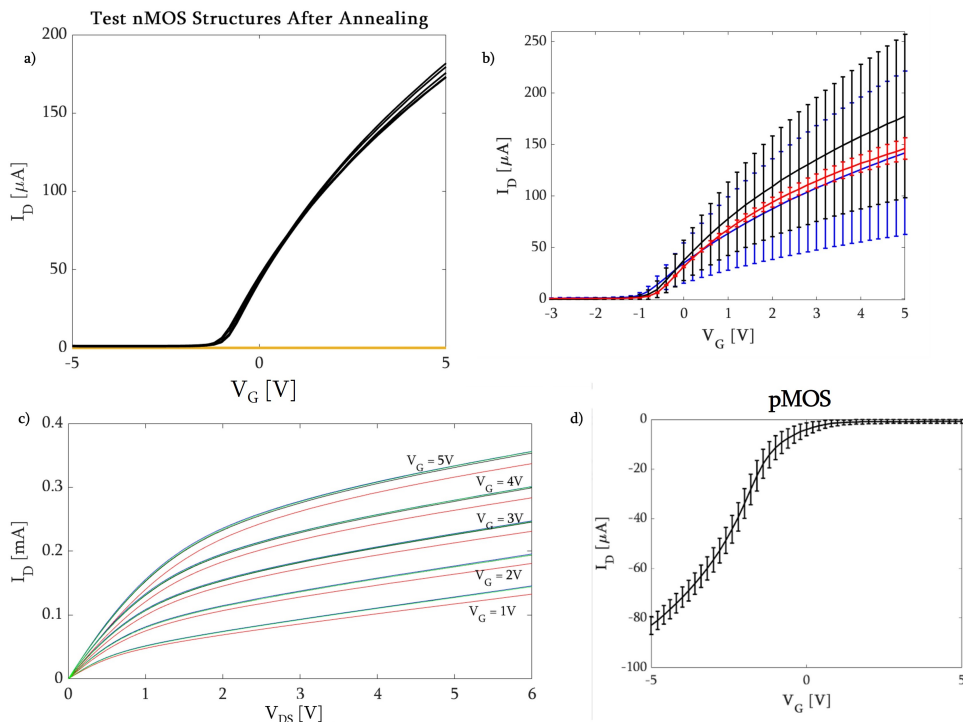


Figure 3.12: Drain current vs. gate and drain voltage measurements after annealing on a high-resistivity wafer. a) Five measurements from one wafer, with gate current (orange), b) Five randomly chosen test structures over three wafers with mean and standard deviation values ($V_D = 0.1V$ for all cases) Each color (blue, black, and red) shows a different wafer, c) I_D vs. V_{DS} curves of five nMOS devices and d) I_D vs. V_G measurements on a pMOS device.

was Al-rich, with a ratio of 324:72.

3.2.4. ELECTROCHEMICAL CHARACTERIZATION

Electrochemical Impedance Spectroscopy (EIS) is a well-known method for characterizing electrodes in a frequency range. In this way, the capacitive behavior and resistance of the sensor in electrolyte can be understood. Here, we wanted to compare the electrodes with different MO_x layers at the sensing area.

EIS measurements were performed with a 3-electrode setup (Fig. 3.13 a). The working electrode (WE) was the fabricated sensor. The chip was mounted on a custom-designed PCB (printed circuit board) and wirebonded to have electrical connections.

The wirebonder working principle is based on ultrasonic bonding. It bonds two metals (in this case, Al wire to Al contact pad) with ultrasonic force. First, a force is applied through the bonder head to create deformation on the surface, ultrasonic power is then applied to ensure surface cleanliness, and time is another parameter calibrated to make sure the diffusion of the metal is sufficient for stable connection between the two metals. Fig. 3.14 shows the steps of the wire-bonding. First, the bonder head with the chosen

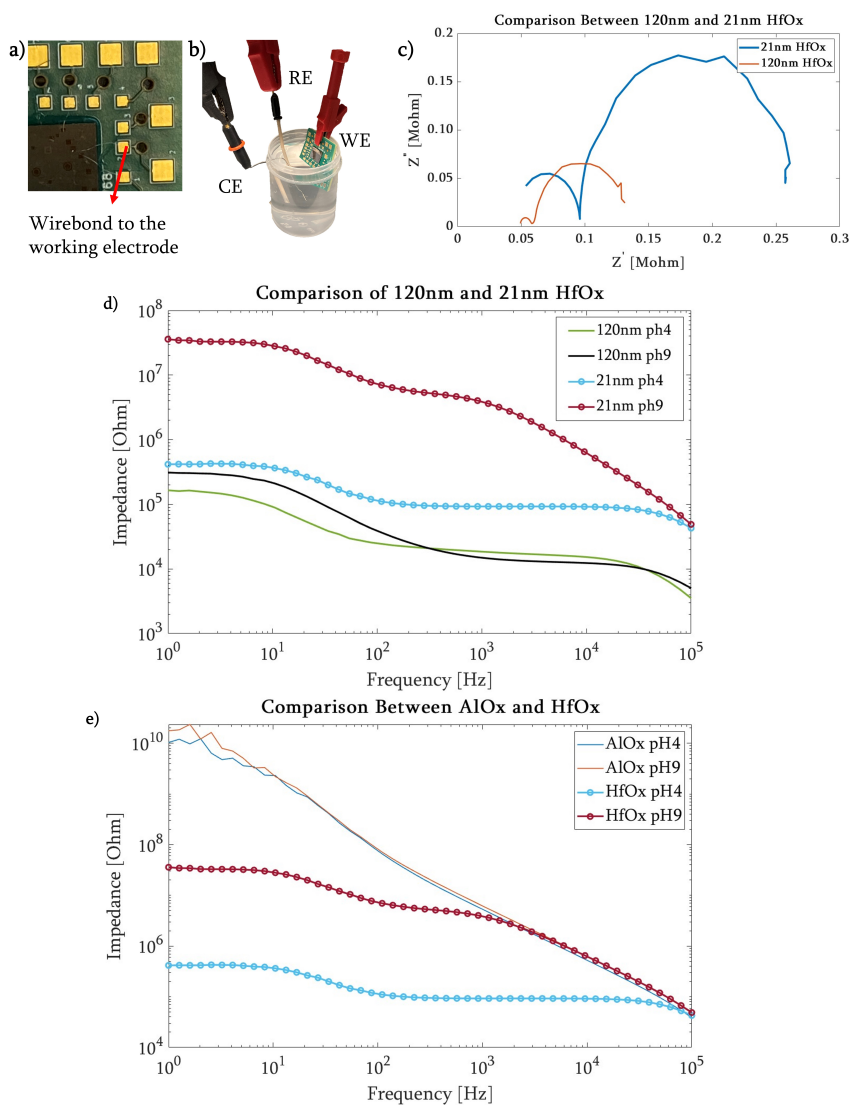


Figure 3.13: EIS measurement setup. a) The wirebonded chip serves as the WE. b) 3-electrode measurement setup in a Faraday Cage. c) Comparison of thick and thin HfO_x layers with the same pH 4 buffer solution. The thicker layer showed a lower impedance. d) Comparison of thick and thin HfO_x layers on impedance vs. frequency plot. pH4 and pH9 buffer solutions were used for both measurements on different chips. Thin HfO_x showed a higher shift in impedance with different pH solutions. e) Comparison of AlO_x and HfO_x (21 nm) with different pH solutions (pH4 and pH9). HfO_x showed a greater impedance difference to pH4 and pH9 than AlO_x . This result was attributed to the stoichiometry and possible higher hydrogen binding site density of HfO_x (the nominal value was not found in the literature).

metal wire goes down to the first metal pad under user's control (Fig. 3.14 a), the bond parameters are set and a bond is made (Fig. 3.14 b). Then the clamp of the bonder

opens, releasing wire from the head (Fig. 3.14 c), and the head can be directed to the second bond place (Fig. 3.14 d). The bonder head goes down again and creates the second bond (Fig. 3.14 e). The wire is finally cut, leaving a bonded structure (Fig. 3.14 f). The wirebonded chip to PCB can be seen at Fig. 3.13 a. The reference electrode (RE) was a commercially available Ag/AgCl electrode, and the counter electrode (CE) was a Pt wire (Fig. 3.13 b).

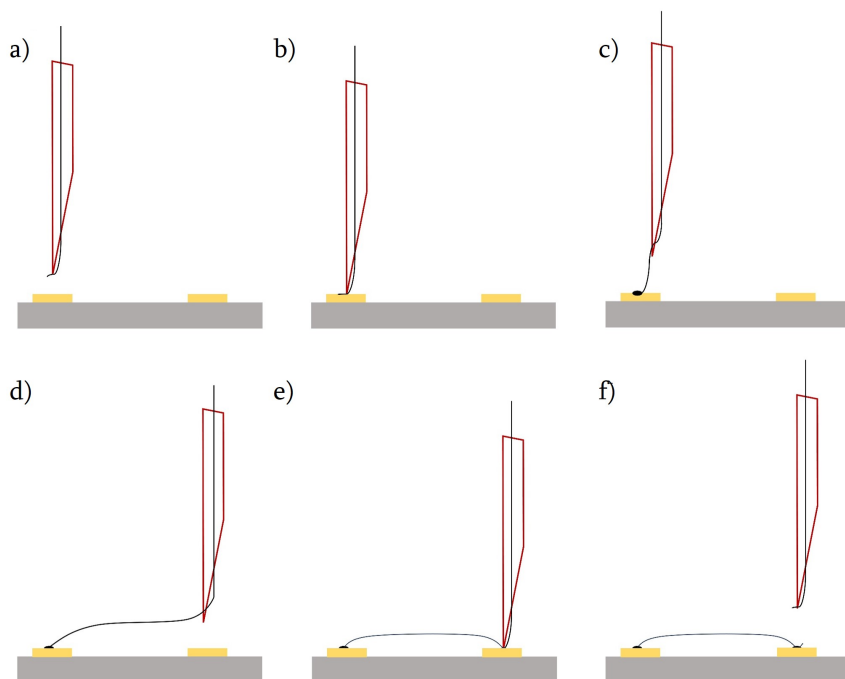


Figure 3.14: Schematic of the wirebonder working principle. a) The bonder head approaches to the first metal pad. b) The head bonds the first contact. c) After the first bond, the head feeds the wire, and d) goes to the second metal pad under the operator's control. e) The head bonds the second pad, f) and cuts the wire and leaves the bonded structure.

Nyquist plots show imaginary and real impedance values in a wide frequency range. We measured a labeled pH4 solution with two different HfO_x thicknesses on two chips with the same electrode diameter. Since the oxide thickness affects the capacitance, and assuming the dielectric constants are similar, impedance values were expected to differ. The frequency range was $1 - 10^5$ Hz (Fig. 3.13 c). The thick HfO_x layer (120 nm) gave lower imaginary and real impedance values than the thinner (21 nm). This difference was attributed to the ability of the thinner layer to store more charge and contribute to the EDL.

pH 4 and pH 9 solutions were also used to test the response of both HfO_x layers (Fig. 3.13 d). The thin layer showed a higher shift in impedance from pH4 to pH9 than the thicker layer.

To compare AlO_x and HfO_x layers in the EIS setup, pH 4 and pH 9 solutions were used (Fig. 3.13 e). HfO_x gave a more significant difference between pH 4 and pH 9 solutions than AlO_x in both the low and high-frequency regimes. Both layers had a higher impedance for pH9 than pH 4 solution since pH 4 solution contains more H^+ ions for the same solution volume. Additionally, the higher dielectric constant of HfO_x than AlO_x explains the higher charge storage capacity and lower impedance.

For FET-based measurements, even though the 21 nm-thick HfO_x layer was chosen as superior in sensitivity, the AlO_x layer was also tested. Thicker (120 nm) HfO_x was disregarded.

3.2.5. ELECTRICAL CHARACTERIZATION

In this section, FET-based measurements with a semiconductor parameter analyzer are explained. While 3-electrode measurement systems are the standard for electrochemical measurements, human errors can affect these measurements since the reference and counter electrodes need to be placed every time for a new measurement ideally in the same relative position. Since the measurements are done with respect to the reference electrode, its placement should be repeatable. Also, the membrane inside the reference electrode for saturation should be kept stable. Moreover, the system is incompatible with cell measurements because a large volume is needed for the test analyte rather than the μ L range, which is appropriate for cell culturing applications.

With the semiconductor parameter analyzer, active measurements can be conducted more easily since we do not need to submerge the chip inside the solution-under-test. Instead, a well-like PDMS slab can be used to house the electrolyte.

MEASUREMENTS IN AIR

After the fabrication and characterization of the MO_x layers, FET characteristics were monitored by a semiconductor parameter analyzer (Fig. 3.15 a,b). These measurements were crucial to show the functionality of the FG-FETs, even in the absence of direct voltage application to the gate, and the measurements proved the capacitive coupling between FG and CG. The gate voltage was applied through CG. The dielectric layer between CG and FG was 53 nm-thick PECVD SiO_2 .

Four different gate dimensions (W:L) were designed on the same die to compare sensitivities (nmos8 = 15:2, nmos7 = 25:2, nmos6 = 10:2, nmos5 = 20:2, Fig. 3.15 c). Depending on the length and width of the channel, I_D values showed slight variations at the saturation region but preserved the FET characteristics (Fig. 3.15 d). Compared to the test structure (20:2, explained previously), FG-FETs, where the voltage was applied through CG, show a slight variation in the threshold voltage. CG and FG are two plates of a capacitor, with a SiO_2 dielectric layer in between. When a potential was applied through CG, FG was at a lower potential. Fig. 3.15 e shows the difference between voltage application from CG or FG. When the voltage was biased from CG, the threshold voltage was greater. After the evaporation of HfO_x , the wafer was characterized again with the semiconductor parameter analyzer. Fig. 3.16 shows measurements for three devices from the same die, before and after evaporation of HfO_x . The negligible change in the I-V curve was attributed to the possible alteration of the trapped charges inside the FG, due to the electron-beam evaporation process. Even a small defect during fabrication can alter the

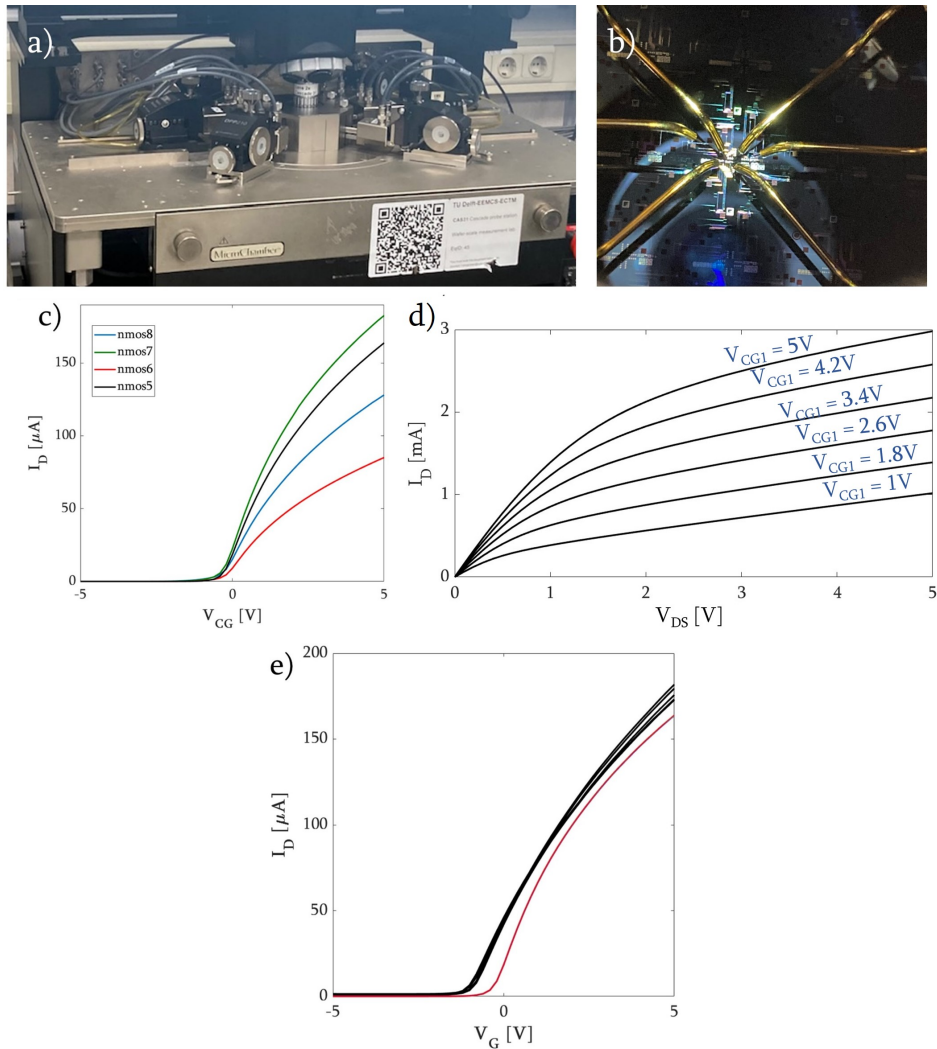


Figure 3.15: Electrical measurements: a) 4-probe station with b) needles on the wafer. The wafer was placed on the chuck, inside the probe station. c) Measurements of FG-FETs with the application of gate voltage through CG. Different gate dimensions show slight differences in threshold voltage values and in the saturation region. d) I_D vs. V_{DS} of nMOS 5. e) Difference between the biasing from FG (black) and CG (red) of the same device of d).

properties of the layers [17] by creating defective boundaries.

MEASUREMENTS WITH DI WATER

Even though DI water should not have ions, the polar water molecules will create a layer on the MO_x surface (as mentioned in Chapter 2). Introducing DI water to the sensing area is thus a step forward to investigate the performance of the devices.

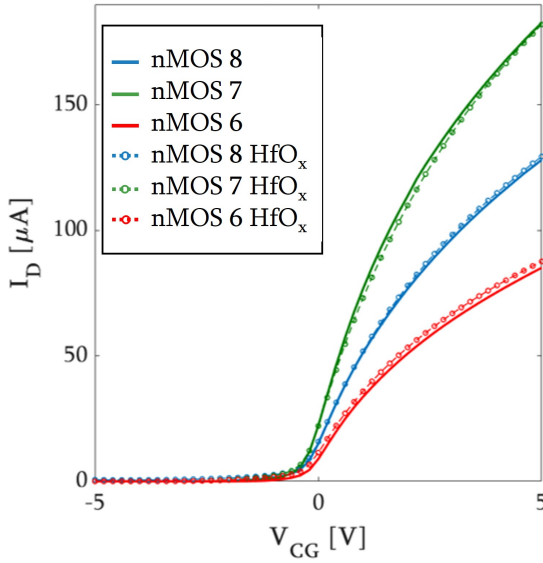


Figure 3.16: Comparison of I-V curves: Measurements from the same die before (continuous lines) and after HfO_x evaporation (dotted lines).

Before measuring, the wafer was diced with a blade dicer (see Chapter 5) to singulate the chips and ease the measurement process. To serve as a well for the liquids-under-test, a PDMS (polydimethylsiloxane, 10:1 ratio for elastomer to the curing agent) slab was made and cured at room temperature for a day. Then, it was cut according to the die size and the center was opened with a puncher (0.5 mm diameter). This piece was bonded with low-power (100W, 60s) O_2 plasma to the chip (Fig. 3.17).

A micropipette introduced the water droplet ($5\mu L$) to the sensing area. Fig. 3.18 shows the change in I_D with respect to DI water addition to the chip. When DI water molecules are on the sensing area, the dielectric constant changes from air to water (1 to 78), changing the sensing surface capacitance. This alters the change in threshold voltage and I_D .

MEASUREMENTS WITH pH BUFFER LIQUID

The pH is the negative logarithm of the concentration of H^+ ions in a solution. When two solutions with the same volume and different pH values are mixed, the resulting pH can be calculated from:

$$[H^+] = \frac{H^+_{total}}{V}, \quad (3.1)$$

$$pH = -\log[H^+]$$

Where V is the total volume of the solution and H^+_{total} is the total number of H^+ ions, after neutralization takes place (For instance, OH^- groups of pH11 should be taken into consideration).

pH tests were conducted with a semiconductor parameter analyzer on different chips

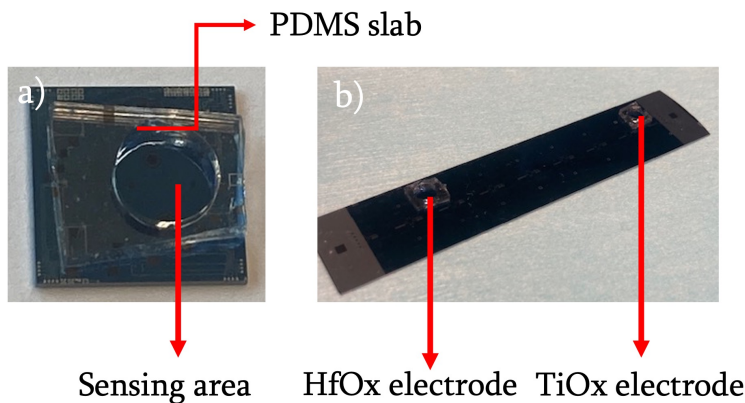


Figure 3.17: Bonding of PDMS slab to the silicon chips. a) Singulated chip with PDMS slab. The sensing area is shown. The size of the chip is 1cm x 1cm. b) Wafer piece with 16 chips after HfO_x evaporation on eight of them. The other eight chips were protected from evaporation by photoresist, and thus had TiO_x electrodes.

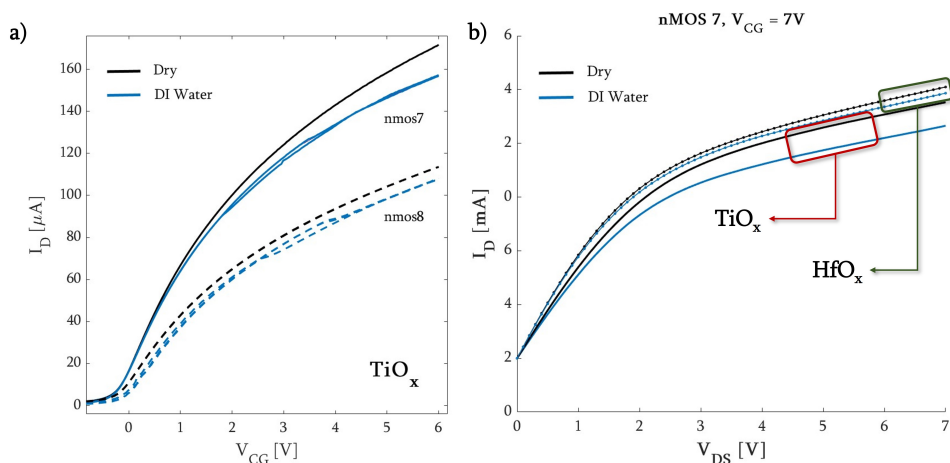


Figure 3.18: Dry vs. DI water measurements for sensors with a) TiO_x and b) HfO_x electrodes. Decrease in the I_D values attributed to the dipolar molecules of the DI water. DI water creates a layer on the electrodes, altering the sensing surface charge. The difference in the I_D was due to the different materials at the sensing surface.

from the same wafer, each coated with a different MO_x layer. During the experiments, pH solutions with the same values were introduced to the sensing area in different order to randomize the measurement process and minimize measurement error. The V_{CG2} was 0 V, and the V_G was swept while drain voltage (V_D) was kept constant at 3 V. We observed an increase in I_D with increasing pH values, in all cases. This might arise because lower pH liquids (higher H^+ concentration) create a greater change in the V_{FG} (mentioned in Chapter 2), and since I_D is calculated with $\alpha(V_{FG} - V_{th})^2$, more acidic

liquids cause lower I_D . The charges in close proximity of the sensing area change the V_{FG} value in the opposite sign, underneath the transistor gate, where the channel is forming. This was also explained in Chapter 2.

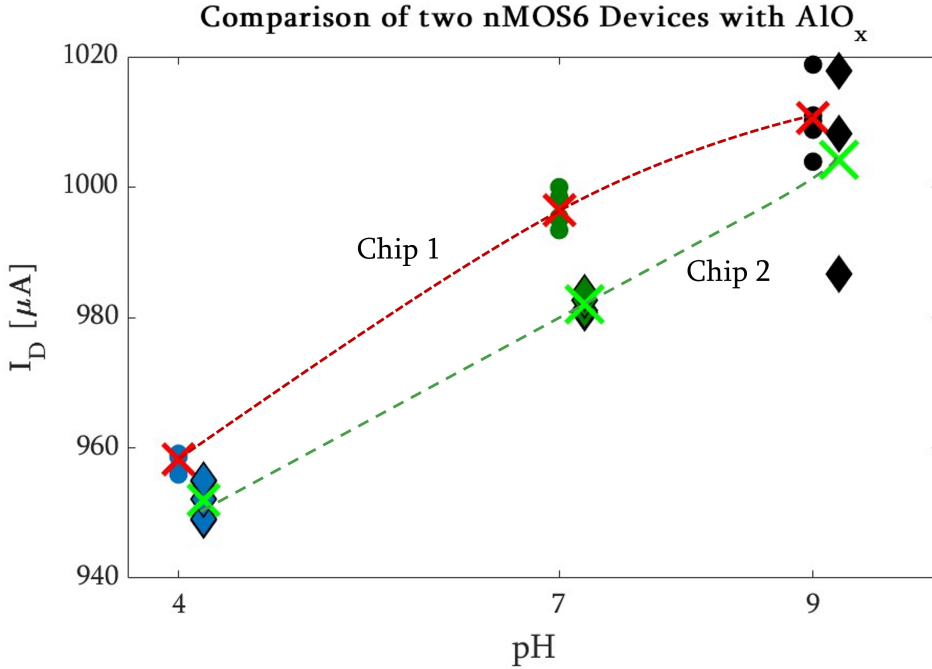


Figure 3.19: pH measurements with AlO_x layer. We recorded an increase in I_D with increasing pH values. Between pH measurements, the chip was cleaned with DI water. Two chips (Chip 1 and Chip 2) from the same wafer were measured and compared for pH4, pH7 and pH9 buffer liquids at $V_{CG1} = 3.8V$, $V_{CG2} = 0V$. The mean values are shown with 'x', reported in Table 3.1.

For each MO_x surface, we observed sensitivity towards the pH of the solution. For all the tests, consecutive measurements with the same pH buffer were recorded. Then, the solution was removed by micropipette, and the surface was cleaned with DI water before introducing another pH solution. Fig. 3.19 reported a similar trend of I_D changes for two chips with the AlO_x NMOS6 device. Even though the chips were on the same wafer, the mean values of I_D for different pH solutions differed (Table 3.1). For different MO_x layers, the sensitivity between different pH values showed differences (Fig. 3.20).

We also recorded current data where the current was less than $1\mu A$ when the pH solution leaked and covered the gate area. This measurement can be found in Appendix E.

For native TiO_x , the I_D for pH 4, pH 7 and pH 9 is distributed between $1.14mA$ to $1.16mA$. We observed more overlapping values between pH 7 and pH 9, whereas, for pH 4, a more distinctive dataset was obtained (Fig.3.20 a). For the case of HfO_x (Fig. 3.20 b), pH 9 created a greater shift in I_D , compared to pH4. We also observed sensitivity towards smaller changes around pH7 (Fig. 3.20 c). $\Delta I_D = 10\mu A$ was recorded for the change of pH 7.2 to pH 7. For AlO_x, we observed a similar behavior as for the TiO_x layer.

Table 3.1: Mean I_D values with different pH solutions at $V_{CG} = 3.8V$ and $V_D = 3V$ for two nMO6 AlO_x sensors.

-	pH4	pH7	pH9
Chip 1	$958.3\mu A$	$996.46\mu A$	$1010.5\mu A$
Chip 2	$952\mu A$	$982\mu A$	$1004\mu A$

The change in I_D is greater for pH 4 than pH 9 (Fig. 3.20 d). To avoid experimental errors and variations, all the measurements were conducted on the same type of transistor (nMOS6) with the same pH buffer liquids. The V_{CG} was 5V, and V_D was 3V for every measurement. Table 3.2 shows the mean value of I_D s as function of the pH of the solution and MO_x layers.

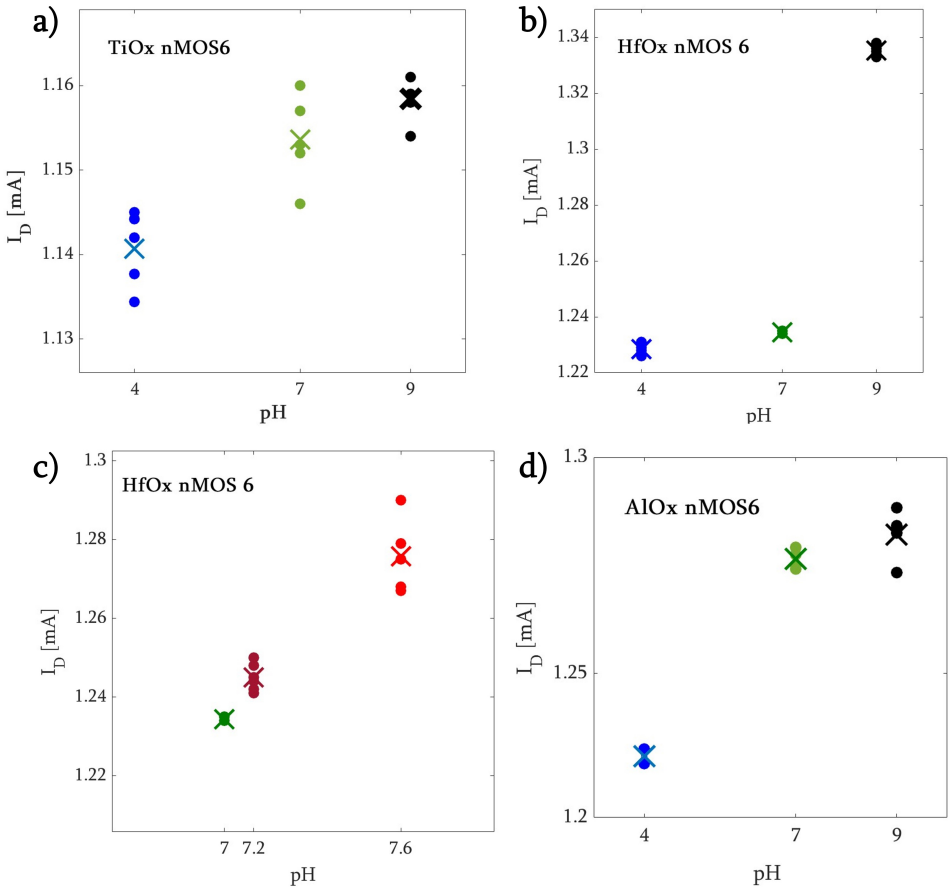


Figure 3.20: I_D vs. pH for different MO_x layers (blue = pH 4, green = pH 7, black = pH 9), X marks the mean values: a) TiO_x , b) HfO_x , c) Sensitivity study with HfO_x layer and pH 7, pH 7.2, and pH 7.6, d) AlO_x .

From the experiments and the difference on the MO_x layers, there are possible reasons

Table 3.2: Mean of I_D values for different pH solutions and layers at $V_{CG} = 5V$ and $V_D = 3V$ for nMOS6 device

-	pH4	pH7	pH9
HfO_x	1.23mA	1.24mA	1.34mA
AlO_x	1.22mA	1.27mA	1.28mA
TiO_x	1.14mA	1.15mA	1.16mA

Table 3.3: Comparison of threshold voltages seen from CG_1

nMOS6	V_{th}
HfO_x	24 mV/pH
AlO_x	41 mV/pH
TiO_x	5.6 mV/pH

for the difference in sensitivity. The first reason depends on the dielectric constant of these layers. Since we observed different stoichiometry with EDX measurements (Appendix C), it is unreliable to use the previously reported dielectric constant values of TiO_2 , HfO_2 , or Al_2O_3 . The dielectric constant will affect the capacitance of the sensing layer and the charge storage capacity, and hence the V_{FG} and I_D . Additionally, the O_2 concentration of the MO_x changes the charge binding sites (Appendix C Fig. C.1 and Fig. C.2).

Finally, depending on the point of zero charge (PZC) of the sensing surface, the sensitivity of MO_x s towards certain pH values can be different.

From the preliminary measurements, we observed that for applications with small pH changes around pH7 (for example, change in homeostasis for cardiomyocytes), HfO_x can be a good candidate for an OoC device with an integrated pH sensor. If a greater range is desired (pH 4, pH 7, pH 9), a native TiO_x layer can be chosen. This layer does not need additional processing steps. For sensitive measurements towards larger acidity ($pH < 7$), AlO_x FETs can be used.

For a more conventional comparison between pH sensors, the Nernst limit (59mV/pH) can be employed. This limit defines the equilibrium of the hydroxyl groups on the sensing layer and the proton concentration of the solution-under-test. However, our sensor provides a more differential measurement when compared to counterparts such as IS-FETs, since we are measuring the change in the threshold voltage from CG_1 . For a more direct comparison to Nernst limit, the change in threshold voltage should be monitored directly from FG. As a secondary validation, we calculated the change in the threshold voltage for different MO_x s (Fig. 3.21). From these values, AlO_x showed a more sensitive response than HfO_x and TiO_x for nMOS6 devices (Table: 3.3). We also compared nMOS7 and nMOS6 devices with TiO_x layers, and nMOS7 showed a higher sensitivity (Table: 3.4). For a more realistic comparison, all different gate sizes should be measured.

An insulation layer that covers the metal tracks and only leaves the sensing pads open should be integrated into the processing of the device. Even though the analyte-under-test was only introduced at the sensing area, metal tracks without the insulation layer can still interact with the liquid, changing the pH response of the sensor.

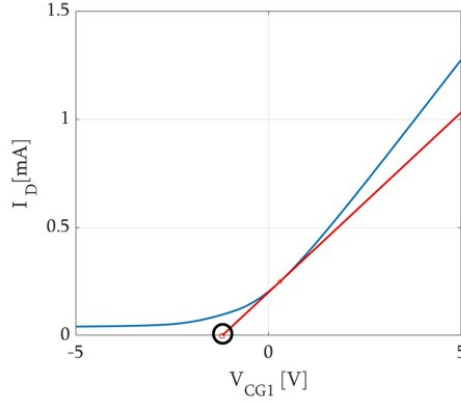


Figure 3.21: Calculation of threshold voltage from I_D vs. V_{CG1} measurement. The derivative of the measurement line where it intersects the V_{CG1} provides the threshold voltage.

Table 3.4: Comparison of threshold voltages seen from CG_1 for nMOS6 and nMOS7 devices with TiO_x Layers.

TiO_x	V_{th}
nMOS6	5.6 mV/pH
nMOS7	26 mV/pH

3.3. DISCUSSION & CONCLUSION

FG-FET-based sensing devices provide useful solutions where it is desired to avoid the use of bulky external reference electrodes. The sensing mechanism is based on monitoring the drain current, hence the change in the threshold voltage, which is directly related to the charges in close proximity of the floating gate extension. In this chapter, we showed that altering the sensing layer material can be beneficial. We showed this by implementing three different MO_x layers at the sensing area. We tested these layers by introducing pH 4, pH 7, and pH 9 solutions and recorded the change in I_D . For all three layers, the FET-based sensors showed a shift in I_D when exposed to different pH liquids. Depending on the characteristics of the layer (dielectric constant, oxygen concentration, PZC, hydroxyl density), we observed differences in sensitivity towards different pH liquids. In order to characterize the MO_x surfaces, we used SEM and EDX. EDX results revealed O_2 concentration of the layers, with AlO_x having the highest O_2 to metal ratio. In order to compare the effect of the O_2 concentration on pH sensitivity, thicker layers can be evaporated on the devices and used in experimental settings.

From the electrical characterization, the sensor with HfO_x layer showed a higher increase in I_D from pH 7 to pH 9, whereas for AlO_x layer, ΔI_D was greater between pH 7 and pH 4. For the TiO_x layer, a more linear change of I_D was observed.

Preliminary experiments showed promising results towards pH sensitivity with different MO_x layers. However, for biological experiments, it is crucial to test a lot of variations in a short amount of time. The chips could be implemented in a multiwell format (Fig. 3.22). By doing so, the chips can be used directly below the cell culturing area, revealing

real-time pH analysis of cell media in a high-throughput system.

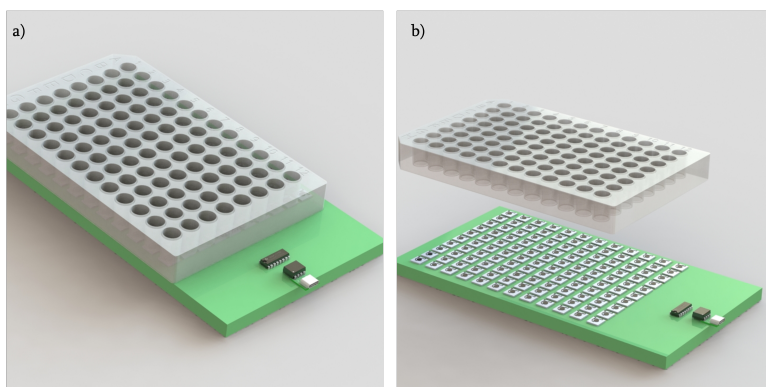


Figure 3.22: Concept design of PCB with sensors, multiplexer unit and USB port for electrical connection. 96-well plate can be inserted on top for pH characterization of cell media.

It is also desired by cell biologists to have monitoring capabilities of pH while recording the activity from electrically active cells. We integrated passive electrodes into the design to establish multi-modal sensing and have simultaneous sensing capabilities (both pH of culture medium and action potential from the cells). These electrodes (Fig. 3.4 b) can be wire-bonded to a custom-designed PCB, to be used as a microelectrode array (MEA). Silicon is biocompatible, but optical microscopy techniques are crucial to working efficiently in-vitro for cell culturing applications. Hence, the transparency of the chips becomes relevant. For OoCs where simultaneous measurements are needed, transparency of the chip and substrate stiffness closer to the micro-physiological environments of cells are essential. Optical transparency also provides a reliability factor: electrochemical measurements and, at the same time, imaging to prove physiological behaviors.

Hence, we wanted to combine the technology of active devices with polymers to obtain silicon-polymer hybrid FG-FETs. The next chapter will detail the integration of PDMS in the sensing area of the ion sensor chip and how sensing electrodes can be integrated into polymers.

BIBLIOGRAPHY

- [1] Hande Aydogmus et al. "FET-based integrated charge sensor for organ-on-chip applications". In: *2020 IEEE SENSORS*. IEEE. 2020, pp. 1–4.
- [2] HW Van Zeijl and LK Nanver. "A low-cost BiCMOS process with metal gates". In: *MRS Online Proceedings Library (OPL)* 611 (2000), pp. C7–2.
- [3] M Saleem J Hashmi. *Comprehensive materials finishing*. Elsevier, 2016.
- [4] Sami Franssila. *Introduction to microfabrication*. John Wiley & Sons, 2010.
- [5] New Semiconductor Materials. Biology systems. *Electrical Properties of silicon*. http://www.matprop.ru/Si_electric, [Accessed: 17/8/23]. 2023.
- [6] Stanley Wolf. *Microchip manufacturing*. Lattice press Sunset Beach, California, 2004.
- [7] Pure Wafer. *Thermal Oxidation*. <https://www.purewafer.com/films///thermaloxidation> [Accessed: 5/2/24]. 2024.
- [8] AZO Materials. *Aluminium/Aluminum Silicon (AlSi) Master Alloy*. <https://www.azom.com/article.aspx?ArticleID=7872> [Accessed: 17/8/23]. 2023.
- [9] Yuxin Wang, Yan Wang, and C Daniel Frisbie. "Electrochemistry at Back-Gated, Ultrathin ZnO Electrodes: Field-Effect Modulation of Heterogeneous Electron Transfer Rate Constants by 30× with Enhanced Gate Capacitance". In: *ACS Applied Materials & Interfaces* 15.7 (2023), pp. 9554–9562.
- [10] Taurus. *TAURUS T-SUPREM Website*. <https://www.synopsys.com/silicon/tcad/process-simulation/taurus-tsuprem-4.html> [Accessed: 17/8/23]. 2023.
- [11] COMSOL. *DC Characteristics of a MOS Transistor (MOSFET)*. <https://www.comsol.com/model/dc-characteristics-of-a-mos-transistor-mosfet-14609> [Accessed: 17/8/23]. 2023.
- [12] Mehmet C Oztürk. "Veena Misra and". In: *THE ELECTRICAL ENGINEERING HANDBOOK* (2004), p. 109.
- [13] Keysight. *Semiconductor Parameter Analyzer Manual*. <https://www.keysight.com/us/en/assets/9018-07935/service-manuals/9018-07935.pdf> [Accessed: 25/8/23]. 2023.
- [14] Gaël Pillonnet and Thomas Martinez. "Sub-threshold startup charge pump using depletion MOSFET for a low-voltage harvesting application". In: *2015 IEEE Energy Conversion Congress and Exposition (ECCE)*. IEEE. 2015, pp. 3143–3147.
- [15] T Dutta et al. "Origins of the short channel effects increase in III-V nMOSFET technologies". In: *2012 13th International Conference on Ultimate Integration on Silicon (ULIS)*. IEEE. 2012, pp. 25–28.

- [16] Thermo Fisher. *EDX*. https://www.thermofisher.com/nl/en/home/materials-science/eds-technology.html?cid=cmp-05675-y6b2&utm_source=google-ads&utm_medium=cpc&utm_campaign=ms_xmarket_gl_eds_search_google-adwords_2022_05&utm_term=7Bkeyword7D&gclid=CjwKCA/jwoIqhBhAGEiwArXT7Ky1Q-Dl1Bq00YPSakh01KAiAdwPPz57w0e2YC_4p--3_FIuJ3LqiKxoC5kAQAvD_BwE [Accessed on 03/28, 2023].
- [17] MA Martinez-Puente et al. "ALD and PEALD deposition of HfO₂ and its effects on the nature of oxygen vacancies". In: *Materials Science and Engineering: B* 285 (2022), p. 115964.

4

SILICON-POLYMER-BASED FG-FETs FOR PH SENSING

FG-FETs and CM-FETs have various applications. To cite some examples from the literature, charges on the probe area generate an electric field that induces a charge separation in FG. The charge causes, in turn, a polarization into the dielectric layer [7] (Fig. 4.1 a), allowing monitoring cell activity by OCM-FET with an extended FG (Fig.4.1b), and monitoring the change in pH by OCM-FET and parylene-C layer. As in the case of the findings of this thesis (Chapters 2 and 3), smaller change of I_D with solutions of pH 4 than with pH 7 and pH 10 was reported (Fig. 4.1 c).

We propose a variation of the full-silicon approach with a silicon-polymer hybrid device to achieve optical transparency and mechanical softness in the cell culturing area. With the silicon-polymer device, it is possible to harness the superior characteristics of both materials (Fig. 4.2).

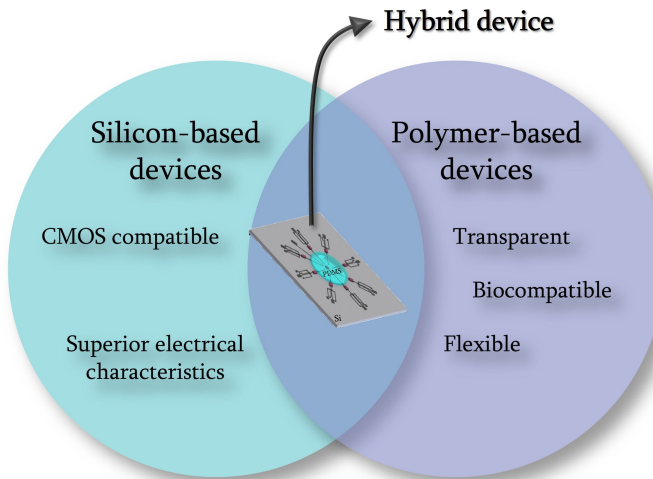


Figure 4.2: Advantages of silicon- and polymer-based OoC devices. The proposed device with silicon-polymer parts combines them.

Silicon, a well-known semiconductor, can house complex electrical circuits based on CMOS-compatible fabrication methods and has superior electrical characteristics, as shown in Chapters 2 and 3. Polydimethylsiloxane (PDMS) was chosen to implement a membrane with embedded extended FG electrodes to meet the demands of biology for transparency and biocompatibility (Fig. 4.3). Hence, we combined silicon frames with transparent PDMS membranes, and used the silicon as the semiconductor substrate for S-D terminals and for channel formation in the FETs.

The working principle of the silicon-polymer FET was explained in Chapters 2 and 3. Here, the novelty is using a polymer-suspended membrane with extended electrodes of FG as the sensing area (Fig. 4.4).

Depending on the material at the sensing area (in this case, metal oxide), sensors can be selective towards specific ions, e.g., K^+ when ionophore cocktails are integrated, which will be explained in Chapter 6. An additional advantage of using a gate extension is that the selective layer can be included in the device as a post-processing step rather

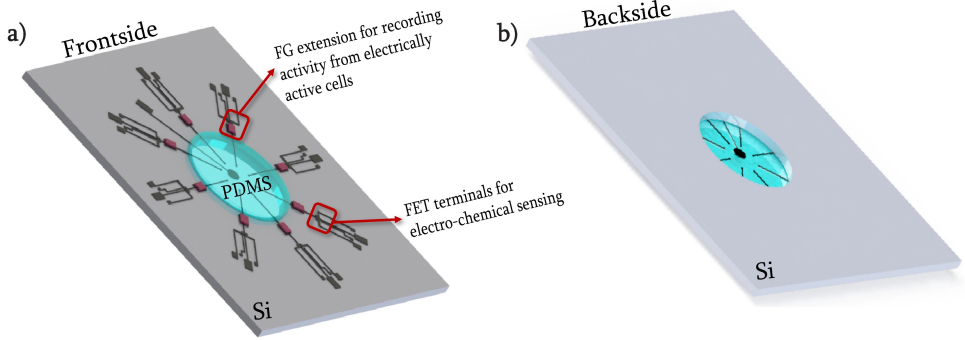


Figure 4.3: Schematic of the device from a) frontside and b) backside. Silicon and PMDS parts are shown with electrodes.

than upfront by changing the gate dielectric material, which would make it necessary to modify the fabrication flow. This post-processing functionalization approach will also be demonstrated in Chapter 6.

4.2. CHARACTERISTICS OF THE SENSOR

As explained in Chapter 2, charges in close proximity to the extension of the FG alter the potential at FG. This can also be analyzed as the change in the drain current.

As already mentioned in Chapter 2, the drain current of an FG-FET in the saturation region can be calculated from the changes in gate potential and threshold voltage, according to the following equation, where α was defined in Chapter 2:

$$I_D = \alpha(V_{FG} - V_{th})^2 \quad (4.1)$$

In theory, since there is no direct application of voltage to the FG, the trapped charge in the FG should remain constant. As explained in Chapter 2, from the principle of conservation of charges, a charge relation can be established [1, 9, 2, 8]. The floating-gate voltage and, therefore, the change in drain current depends on three variables. The first is the surface charge (σ_S) due to the electrolyte-electrode interface coupled to CG_2 , which impacts the surface potential at the sensing area (Ψ_1). This potential induces a potential $\Psi_S = -\Psi_1$. The second variable is related to the trapped charge inside the FG (Q_0), and the last variable depends on CG_1 (Eq. 4.2). Coupling of CG_2 through the PDMS membrane to the FG was also included in the equation, although C_{PDMS} was calculated to be on the order of $\approx 10^{-16} F$. Hence, the potential applied from CG_2 can also be included only as a bulk reference value (as V_{ref}), which would reflect the assumption of negligible electrical double layer (EDL) effect on C_{CG_2} . But when a non-zero voltage is applied from CG_2 , it is also necessary to integrate the EDL of CG_2 when calculating the actual addition of the potential from this terminal. These sources are summed up for the final result for the floating-gate voltage (Fig. 4.4 b).

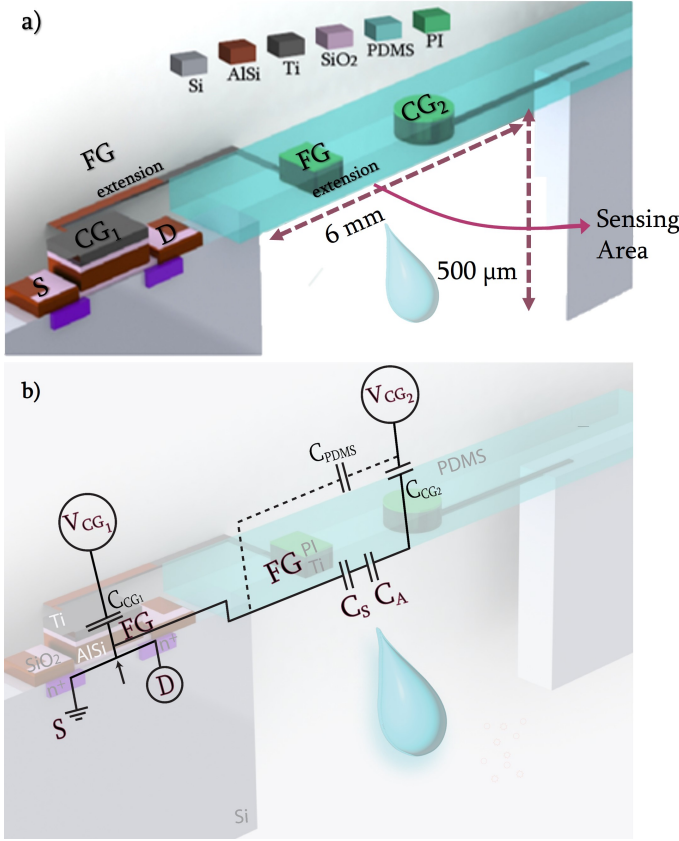


Figure 4.4: a) Schematic of the building blocks of the sensor. The chip with electrodes and the sensing area (well-like structure) is shown. b) Proposed equivalent circuit where the electrolyte-electrode interface is creating an EDL (shown with capacitance S and A). The PDMS layer is also inducing a capacitance, which is shown as C_{PDMS} . CG_2 is on the PDMS layer, introducing the additional potential to the solution. The other electrode is the sensing electrode, which is the extension of the FG. CG_1 is the electrode where the gate voltage is applied and capacitively coupled to FG.

As a result, all the elements in the circuit contribute to the floating-gate voltage as the sum of capacitive couplings [10]:

$$V_{FG} = \frac{C_{CG1}V_{CG1}}{C_{tot}} + \frac{Q_0}{C_{tot}} + \frac{C_S\Psi_S}{C_{tot}} + \frac{C_{PDMS}V_{CG2}}{C_{tot}} \quad (4.2)$$

The CG_2 modulates the potential at the sensing surface. The total capacitance C_{tot} includes the parasitic capacitance between the FG and the silicon body, C_{CB} , the capacitance from the PDMS membrane, C_{PDMS} , and the capacitance respectively of the sensing surface and the CG_1 , C_S . The potential at the sensing surface Ψ_S depends on V_{FG} , the potential at the EDL Ψ_A , and the corresponding surface charges σ_S and σ_A .

If the only variable in the system is the charge concentration and the other parameters are constant, the only shift on the I_D arises from the potential created at the sensing area

due to the charges at the surface.

The binding of different ions and polar water molecules on the sensing surface can be realized differently depending on different materials. Within the Matlab code and the equations explained in Chapter 2, we characterized the surface potential at the sensing area for different surface dissociation constants and implemented it to the voltage of the floating gate and hence the drain current (Fig. 4.5). The change in pH modulates the surface charge formation and, thus, the change in potential at the EDL and the sensing surface. These changes modulate the shift in threshold voltage and the drain current of the FET.

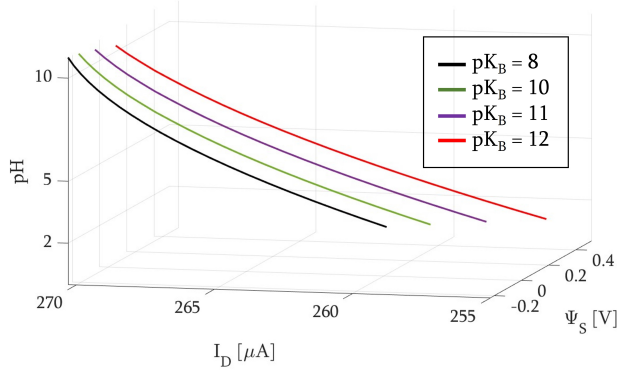


Figure 4.5: Matlab model of FG-FET-based pH sensor with different dissociation constants, showing how the change in pH affects the change in the surface potential and the output drain current. The device was nMOS8, with $V_{CG2} = 0$, $V_D = 3V$.

SIZE OF THE SENSING AREA ELECTRODE

The size of the sensing area is directly proportional to the number of binding sites for the ions, capacitive coupling of the sensing area to the FG potential, and hence the drain current modulations.

For optical transparency, the size of the (non-transparent) electrode and the CG_2 should be in a range such that the sensor is still sensitive to pH changes but also not blocking the visualization of the cells. From Fig. 4.6, it can be extracted that the modulation of I_D for pH change from pH4 to pH7 is $9.1\mu A$ and from pH7 to pH9 is $5.04\mu A$ for a square electrode with a side dimension of $80\mu m$ ($pK_B = 13$). For the other dissociation constants, we observed a similar change.

4.3. DISCUSSION & CONCLUSION

Since optical transparency is the key to the biological relevancy of OoCs, we transformed our silicon-based devices into silicon-polymer chips, where the FG extensions lie on a PMDS membrane. This membrane serves as the sensing and culturing area. This is especially crucial if spatial information is needed from cell cultures (for example, local pH change of a neuronal network).

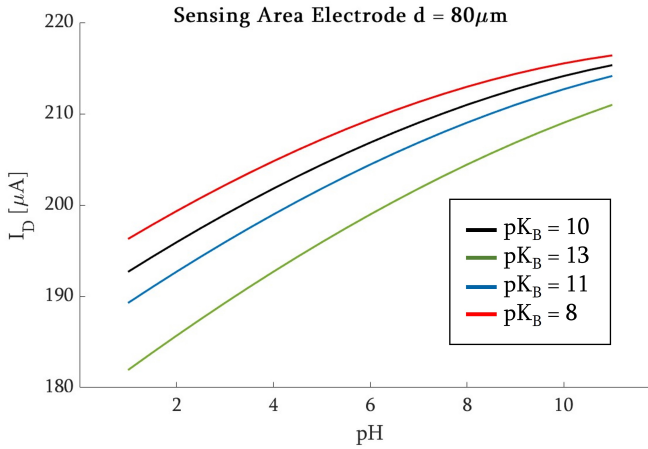


Figure 4.6: The change in I_D vs. pH from the Matlab model. Sensing electrode with a side dimension of $80\mu m$. $V_{CG2} = 0$, $V_D = 3V$, nMOS8 device, with different dissociation constants.

In this Chapter, we implemented the equations that were explained in Chapter 2 and designed the chip according to the findings. We did not change the electrical connections, S-D terminal dimensions, and main FG and CG electrode sizes, which were all housed by the silicon frame. We only changed the size of the FG extensions (sensing electrodes), and we implemented one circular CG_2 (Fig. 4.7).

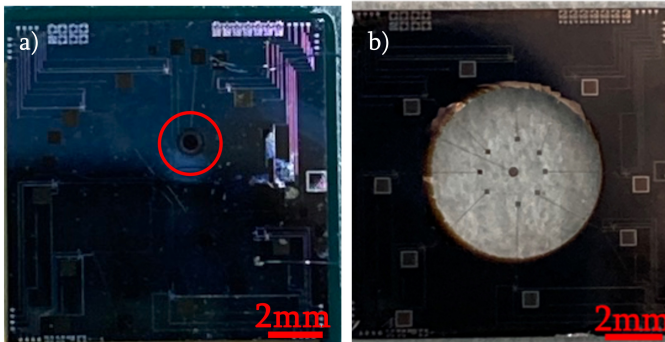


Figure 4.7: Images of a) Silicon and b) Silicon-polymer OoC device with integrated FET-based sensors. Red inset shows one FG extension. Silicon-polymer device will be explained in detail in the following section.

The main reason not to adopt the exact sensor structure as Chapter 3 was to have the transparent PDMS membrane area as open as possible (i.e., without electrodes that are limiting visual inspection due to non-transparency). Real-time visual inspection of cells during culturing can be beneficial next to cell imaging protocols such as staining. In spite of optically-blocked access, the sensorized chip developed in Chapter 3 can be

employed in OoC platforms with microfluidics, where the culture medium from the cells to be investigated is delivered to the sensor. With the silicon-polymer device introduced in this chapter, these measurements can be done directly under the cell culture. In Chapter 5, the fabrication and characterization of the sensor will be explained in detail.

BIBLIOGRAPHY

- [1] Monia Demelas et al. “Charge sensing by organic charge-modulated field effect transistors: Application to the detection of bio-related effects”. In: *Journal of Materials Chemistry B* 1.31 (2013), pp. 3811–3819.
- [2] Andrea Spanu et al. “An organic transistor-based system for reference-less electrophysiological monitoring of excitable cells”. In: *Scientific reports* 5.1 (2015), pp. 1–7.
- [3] Tsuyoshi Minami et al. “An extended-gate type organic field effect transistor functionalised by phenylboronic acid for saccharide detection in water”. In: *Chemical Communications* 50.98 (2014), pp. 15613–15615.
- [4] Qi Zhou et al. “Extended gate-type organic transistor functionalized by molecularly imprinted polymer for taurine detection”. In: *Nanoscale* 13.1 (2021), pp. 100–107.
- [5] Chang-Geun Ahn et al. “Modified ion sensitive field effect transistor sensors having an extended gate on a thick dielectric”. In: *Applied Physics Letters* 96.20 (2010), p. 203702.
- [6] Stefano Lai et al. “Ultralow voltage, OTFT-based sensor for label-free DNA detection”. In: *Advanced Materials* 25.1 (2013), pp. 103–107.
- [7] Monia Demelas et al. “An organic, charge-modulated field effect transistor for DNA detection”. In: *Sensors and Actuators B: Chemical* 171 (2012), pp. 198–203.
- [8] A Spanu et al. “A reference-less pH sensor based on an organic field effect transistor with tunable sensitivity”. In: *Organic Electronics* 48 (2017), pp. 188–193.
- [9] Andrea Spanu. *Organic transistor devices for in vitro electrophysiological applications*. Springer, 2016.
- [10] Tadashi Shibata and Tadahiro Ohmi. “A functional MOS transistor featuring gate-level weighted sum and threshold operations”. In: *IEEE Transactions on Electron devices* 39.6 (1992), pp. 1444–1455.

5

FABRICATION AND CHARACTERIZATION OF SILICON-POLYMER FG-FET

5.1. INTRODUCTION

The fabrication and characterization of the silicon-based devices were explained in Chapter 3. In this chapter, a variation and expansion of the same fabrication flow for silicon-polymer devices is described. An overview of the layout and fabrication steps that are included in this section is shown in Fig. 5.1. Steps 1 and 2, respectively definition of transistor terminals and of first metal layer for electrodes, were explained in Chapter 3. Briefly, ion implantation for source and drain terminals was followed by a thermal oxidation step for the gate oxide. The first metallization layer with AlSi was deposited by DC sputtering. This layer served as the FG and interconnects. Then, a thin layer of PECVD oxide was deposited to serve as the dielectric between CG and FG. Until this

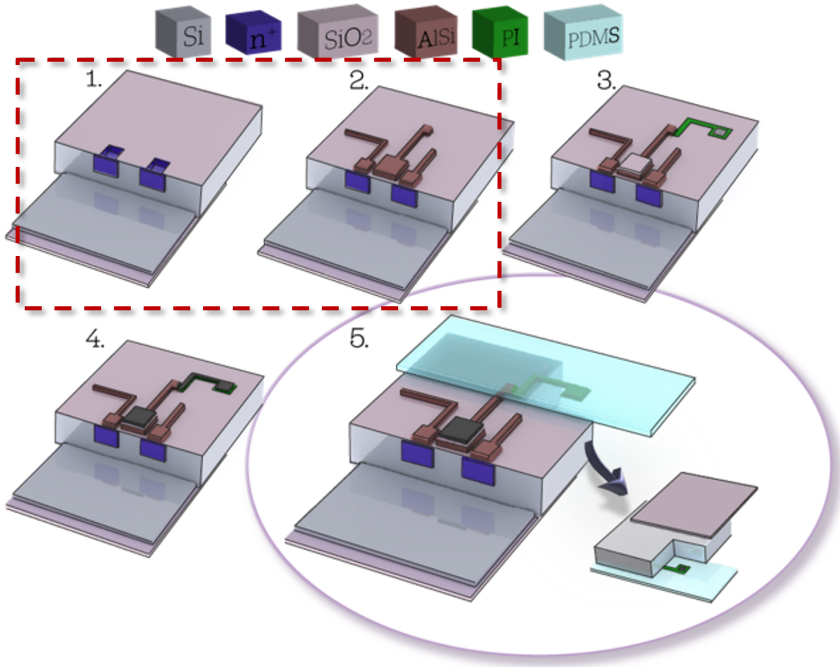


Figure 5.1: Overview of the fabrication steps for silicon-polymer FG-FET-based sensor. Steps 1 and 2 (shown in red) are explained in Chapter 3. Step 3 defines the deposition of the dielectric layer and patterning of the first Polyimide layer. Step 4 shows the second metal layer, which serves as the CG and the extension of the FG. Step 5 is PDMS processing and etching the silicon from the backside, to form the well-like structure.

point, both silicon-based and silicon-polymer-based devices share the same fabrication flow. Silicon-based devices continued with a second metal layer for FG extension. However, for silicon-polymer-based devices, since the second metal layer will be partially suspended on the polymer membrane, the electrode was encapsulated between 2 polyimide layers.

Additionally, since the polymer membrane needed to be suspended, we needed to implement fabrication methods to remove excess silicon and end up with a 'sensing well'

(as shown in Section 5.3). To do so, a 6 μm -thick PECVD oxide was deposited on the backside of the silicon substrate as the hard mask for deep reactive ion etching at later steps.

This chapter will describe the fabrication steps and characterization of the silicon-polymer FG-FETs in detail. Fig. 5.2 details the flowchart.

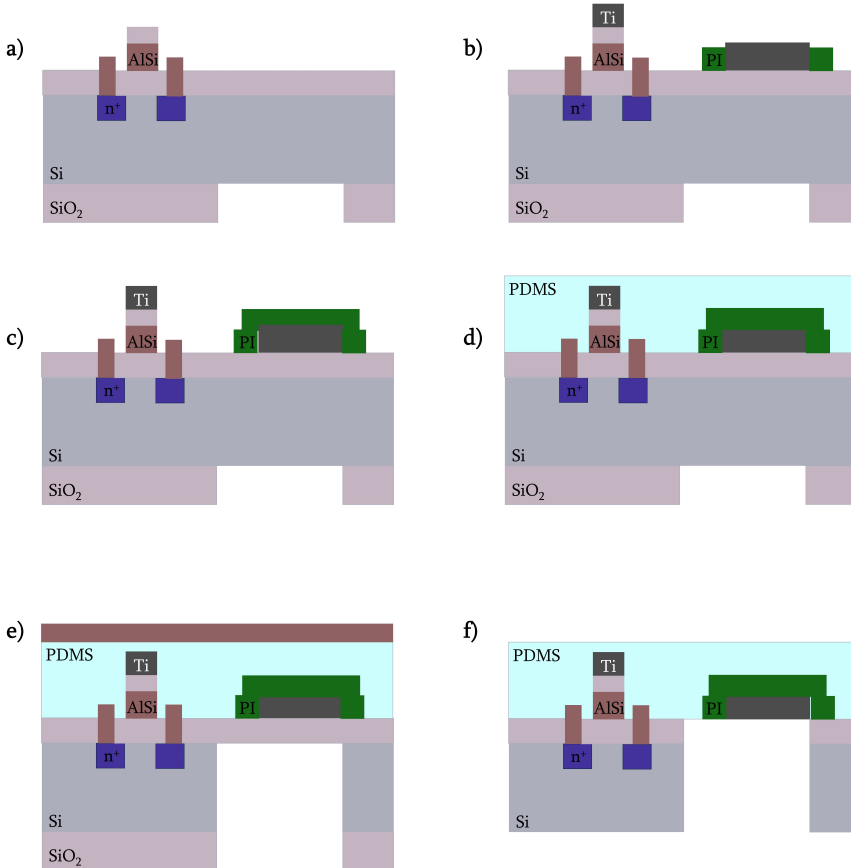


Figure 5.2: Fabrication flowchart of silicon-polymer-based devices after fabrication steps 1 and 2 from Chapter 3. a) PECVD SiO_2 deposition and patterning as hard mask on the backside, b) first layer of polyimide and second metal layer sputtering, c) second polyimide layer, d) PDMS coating to serve as the membrane, e) Al hard mask sputtering on the frontside and etching of the silicon from the backside, f) Removal of the Al hard mask and SiO_2 .

5.2. POLYIMIDE PROCESSING

Polyimide (PI) is a polymer that can withstand high-temperature environments and is biocompatible. PI's Young's Modulus value shows it is a good candidate between metals and PDMS layers since PDMS has Young's Modulus values around 2MPa [1], whereas for Ti, it is on the order of few hundred GPa [2], and for polyimide (Durimide 200), E

= 3.1GPa [3]. It can be seen as a 'transition material' between metal and PDMS. There are different types of PI, and for this study, we used a UV-patternable PI (FUJIFILM LTC9305), which acts as a negative photoresist.

PI was employed for two purposes: 1) to serve as a mechanical buffer and adhesion layer between the metal and PDMS membrane because of its intermediate Young's Modulus, and 2) as an insulation layer, since it is not electrically conductive [4]. These characteristics of the PI eased the fabrication steps, since it is possible to pattern PI without an additional physical etching step but with only development, as in the case of lithography and patterning steps.

FIRST POLYIMIDE LAYER

The first polyimide layer serves as the insulation layer. This is because after deep reactive ion etching of the silicon to release the polymer membrane (see Section 5.5), the membrane will contain electrodes, and we want only the sensing area of the electrodes to be in direct contact with the solution (Fig. 5.2 b). Later in the chapter, this will be explained in more detail.

The fabrication involves a 2-step spin coating process, a soft bake to evaporate the solvent in the polyimide, and exposure. The first spinning was conducted at 1000 rpm for 10 s to spread the relatively viscous polyimide, and the second step at 6000 rpm for 75 s. After exposure with SUS Mask Aligner, post-exposure bake (PEB) was performed for 90 s at 100°C. After post-exposure bake, development and hard bake of the PI at the same temperature as PEB (Fig. 5.3) were performed. For development, HTR-D2 and RER chemicals were used. Then, curing in an oven (KOYO) at 350°C for 2.5 hours was used. This oven has N₂ environment, providing necessary evaporation and hardening of the PI (Fig. 5.4).

After developing the PI, it is crucial not to rinse the surface with acetone since it alters the surface chemistry. Profilometer measurements revealed a thickness between 492 and 512 nm.

5.3. SECOND METAL LAYER

For the extension of the FG and CG, Ti was sputtered at room temperature and low power (1kW, Fig. 5.5 a). The sputtering parameters are different than for the first Ti layer (explained in Chapter 3), even though polyimide can withstand a higher thermal budget. This is because exposing the polymer with high power and temperature is not desired. This might create difficulties while etching the excessive Ti. Additionally, before the sputtering step, a leak-up rate test in another chamber than the Ti sputtering chamber was performed to monitor the degassing from PI. The degassing step is important to analyze how the PI can withstand high vacuum environments and to understand whether further fabrication is possible in cleanroom equipments. The wafer was placed in a chamber with a controlled environment and a known volume, and the pressure values were recorded before and after 10 minutes of the vacuum regime.

After the sputtering, lithography steps were carried out to define CG and FG extensions. The etching of the Ti layer was performed as described in Chapter 3 in a RIE machine (Fig. 5.5 b).

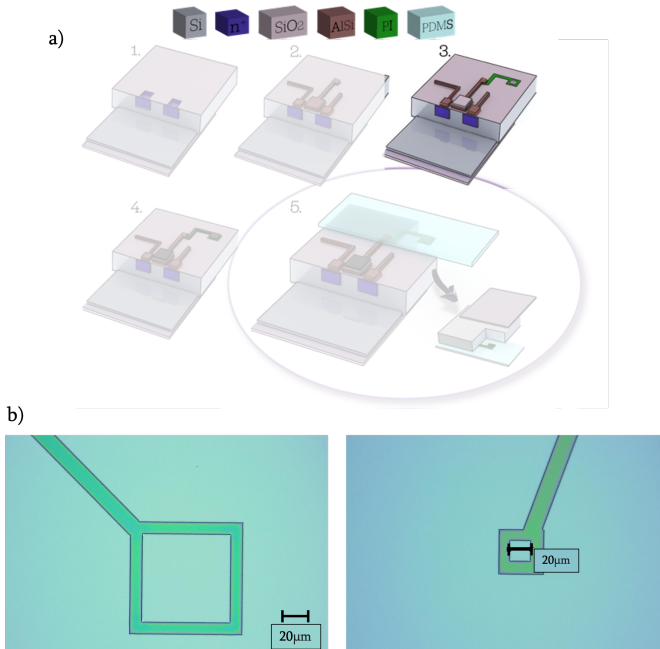


Figure 5.3: a) Schematic of the fabrication step of the first polyimide layer. b) First polyimide layer patterned for different extended gate dimensions before second metal deposition. With the developed process flow, it is possible to obtain a relatively uniform thickness of polyimide layer.

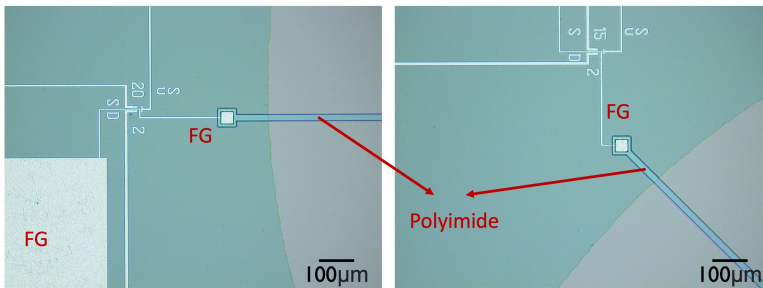


Figure 5.4: First PI layer after hard baking and curing steps (blue). The two images were taken from the same wafer, on different FETs and different dies, showing the wafer-scale uniformity of the polyimide processing.

SECOND POLYIMIDE LAYER

The second PI layer, which serves as the mechanical buffer between Ti and PDMS, was fabricated using the same steps on top of the second Ti layer (Fig. 5.2 c).

For another batch of wafers, as the second PI layer, Durimide was chosen to replace LTC9305, because of its availability in the laboratory. Spin coating parameters were 1000 rpm for 10 s and 6000 rpm for 120 s, followed by a soft bake of 120 s at 110°C. After exposure, PEB was held at room temperature for 30 minutes. With the same recipe, the PI

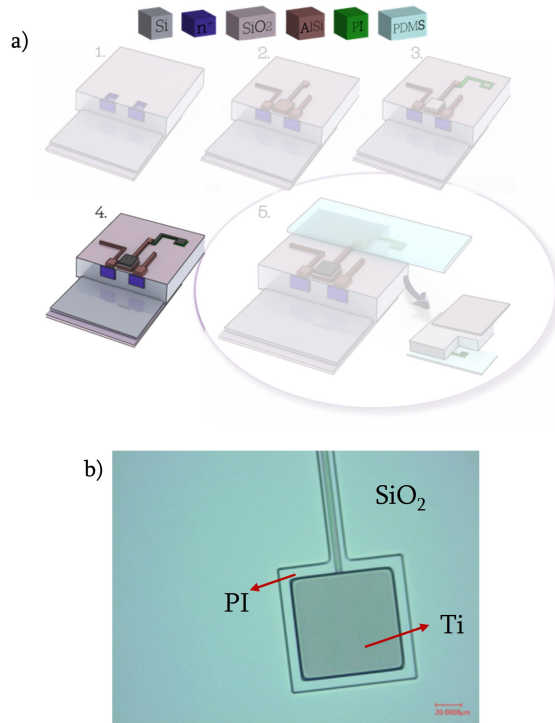


Figure 5.5: a) Schematic of the fabrication step 4: The second metal layer (Ti) sputtering. b) Confocal Laser microscope image of Ti on the first PI layer, after dry etching and landing on oxide and partially on PI.

was cured in the oven (KOYO) (Fig. 5.6), revealing a thickness of $2.03 \mu\text{m}$ in total.

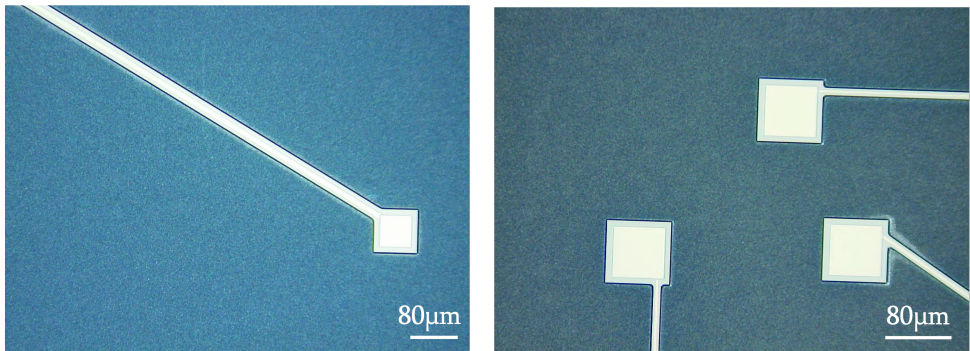


Figure 5.6: Second PI layer after curing. Encapsulation of second metal layer (Ti) is visible, with uniform thickness since the colour of the layer is uniform.

After encapsulation of the extended Ti layer with PI, SEM images revealed good step coverage of the PI by Ti and survival of the PI layer from the dry etching of Ti (the recipe was

explained in Chapter 2) (Fig. 5.7).

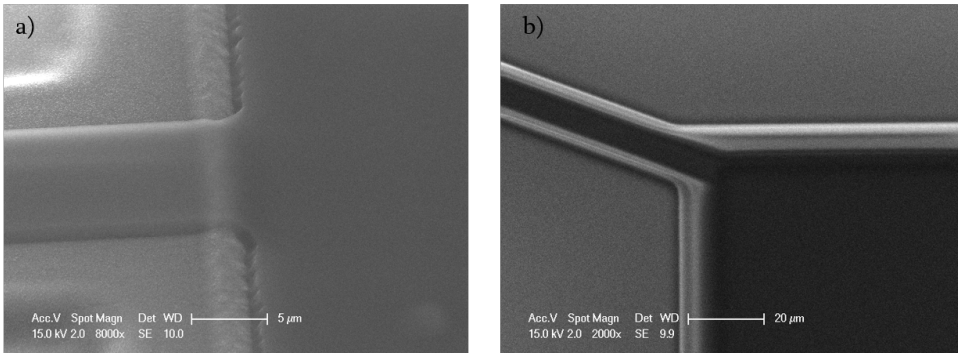


Figure 5.7: SEM images of a) second metal layer (Ti) on first PI layer and b) second PI layer to encapsulate the FG extension. Coverage of the Ti layer on PI is visible. The PI layer creates a smoother transition region, rather than a sharp edge, hence even with thin Ti layers (such as 100 nm, 200 nm-thick), it is possible to have continuous coverage.

Since there was polyimide underneath, the photoresist used to pattern the Ti layer was not removed by high-power O_2 plasma (1000 W with 400 sccm of O_2) to avoid delamination and the probability of etching the polyimide (Fig. 5.8). Instead, low-power (400 W) and lower-flow rate (200 sccm) O_2 plasma were used to remove the photoresist with a cyclic acetone cleaning step. Since polyimide was cured before this step, acetone did not damage the layer.

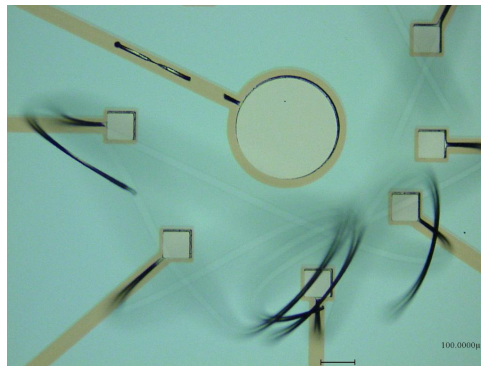


Figure 5.8: Microscopy image of the sensing area and FG extensions after high-power O_2 plasma ashing of the resist. The plasma removed the second layer of the polyimide, delaminating the Ti interconnect layer underneath. We did not observe the delamination of the Ti at the sensing areas since there was no polyimide in these areas.

5.4. PDMS PROCESSING

One of the most common materials for lab-on-a-chip and organ-on-chip applications is Polydimethylsiloxane (PDMS, Sylgrad 184, Dow Corning, Midland, MI, USA), due to its

ease of use and moldability, gas-permeability, transparency, elasticity and biocompatibility [5]. It consists of two parts: the elastomer, and the curing agent. For this study, we used a ratio of 10:1; however, to tune the mechanical properties of the structures, this ratio can be adjusted.

PDMS was employed as the membrane layer that houses the suspended electrodes (Fig. 5.2 d). The mixture was processed in a mixer and degasser equipment (Thinky Mixer ARE-250) and then spin-coated with a manual spin coater to obtain a $20\mu\text{m}$ -thick layer (Fig. 5.9 a). At this stage, to remove the air bubbles trapped inside the PDMS layer, a second degassing can be done, or the coated membrane can be left at room temperature for a couple of hours for the natural evacuation of trapped air.

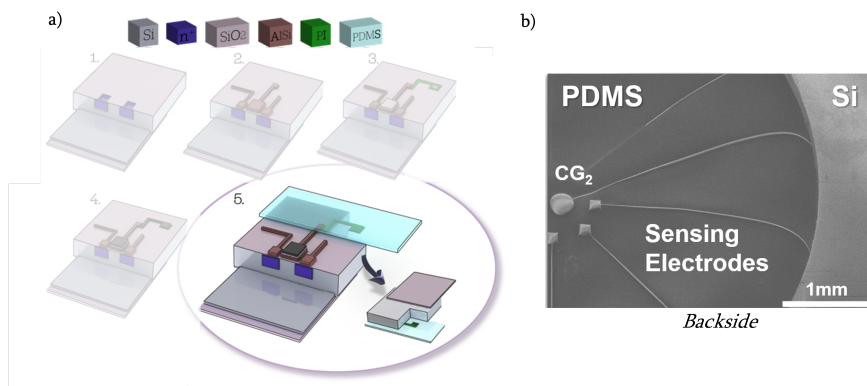


Figure 5.9: a) Schematic of the fabrication step with PDMS spinning, curing, and later stage deep reactive ion etching. b) Etching of silicon and landing on PDMS membrane. PDMS and Si layers are shown with extended FG electrodes.

For the curing of the PDMS, an oven at 80°C for 2 hours or up to 24 hours at room temperature can be used. Both ways were used for different wafers, and no difference was observed.

5.5. RELEASING THE PDMS MEMBRANE

As a landing and thermal uniformity layer when performing deep reactive ion etching and to have better thermal conduction between the chuck and the wafer, a 200 nm-thick Al layer was sputtered on PDMS at room temperature and low power (1 kW, Fig. 5.2 e). Before sputtering on the PDMS, a leak-up rate test was performed, similarly as explained for sputtering on polyimide.

To etch the silicon, membrane sites were patterned to the backside of the wafer. $6\mu\text{m}$ -thick PECVD oxide was used as a hard mask. Etching of the silicon well and landing on the oxide layer underneath (which also forms the gate oxide for transistor sites) was conducted by deep reactive ion etching (DRIE). DRIE is a cyclic process that consists of 1) etching with SF_6 and 2) coating the etched surface with Teflon (PTFE, Polytetrafluoroethylene, C_4F_8). In this way, high-aspect-ratio structures can be obtained (Fig 5.10). Here, we used a carrier wafer to avoid damaging the equipment. However, a $12\mu\text{m}$ -thick AZ12XT chemically-amplified photoresist can also be used to have a reliable landing

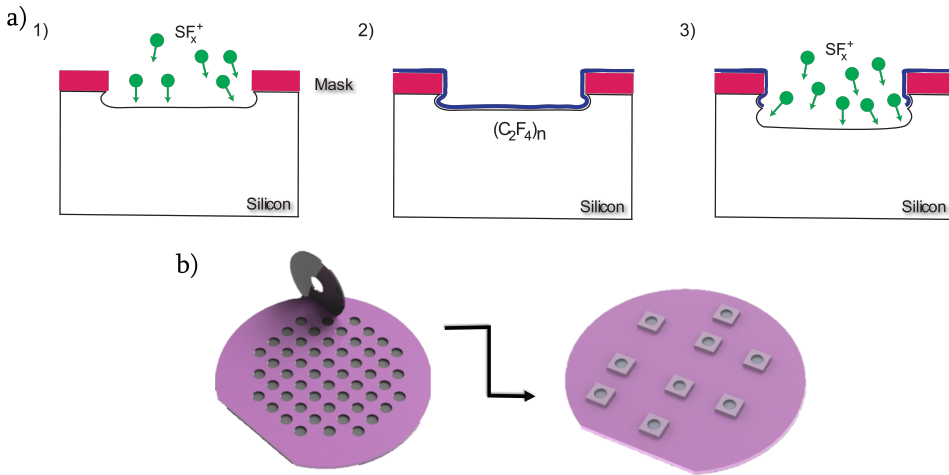


Figure 5.10: a) Schematic of deep reactive ion etching process. b) DRIE was performed until $50\mu m$ Si layer was left to be etched to mechanically support the wafer during dicing. The wafer was diced, and dies were placed on a SiO_2 -deposited carrier wafer. DRIE was completed on the die-level.

layer. Chemically-amplified photoresists have an additional photoacid generator component, which helps the sensitivity towards UV. With this, it is possible to have high sensitivity during exposure, even with thick resist layers.

To have a smooth landing and not damage the chips with dicing, the wafer was etched until approximately $50\mu m$ of Si was left as a mechanical support layer for the blade dicing (Fig. 5.10 b). Blade dicing was performed under vacuum with UV-foil. Singulated chips were later placed on a carrier wafer with fomblin oil and further etched with DRIE to complete the removal of the silicon on the backside.

After etching the silicon, the oxide layer was removed by wet etching with BHF (Fig. 5.2 f). Special attention needs to be given to this step since PDMS can absorb BHF, which can cause cell viability issues when cell culturing occurs.

Another problem with BHF can arise because BHF can etch Ti. If the timing of the BHF etch is not optimized, the extended electrodes can be etched even though they have been encapsulated with PI.

The final chip from the backside can be seen in Fig. 5.12.

5.6. PACKAGING & ASSEMBLY

After the cleanroom process, 52 dies ($1 \times 1 cm^2$) were obtained from each wafer (Fig. 5.11). The chips were cleaned with acetone and IPA, and placed on custom-made printed circuit boards (PCBs) to be wire-bonded. PCBs can have very complex circuits with electronic components. Here, we used them to establish the connection from the chip to the external source and measurement devices. The characteristics of this PCB were to have an opening at the center to ease the visual inspection process for the cells and to have the layout of contact pads compatible with commercial microelectrode array (MEA)

measurement setups. Fig. 5.12 a,b shows the final assembly and ready-to-use chip from the frontside and the backside, as well as the singulated chip (Fig. 5.12 c). The wire-bonding needs special attention since it has to be done through PDMS.

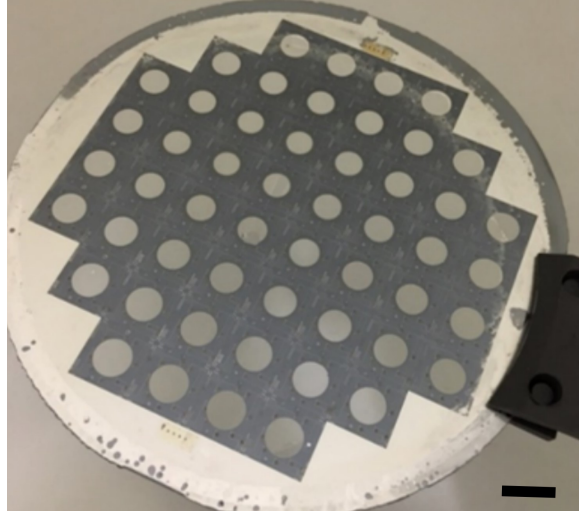


Figure 5.11: The wafer after cleanroom processing with 52 OoC devices. With some of the wafers, rather than dicing and continuing the Si etching process at single-die level, the full wafer was processed until the release of the membranes by careful timing of the etching. The scale bar is 1cm.

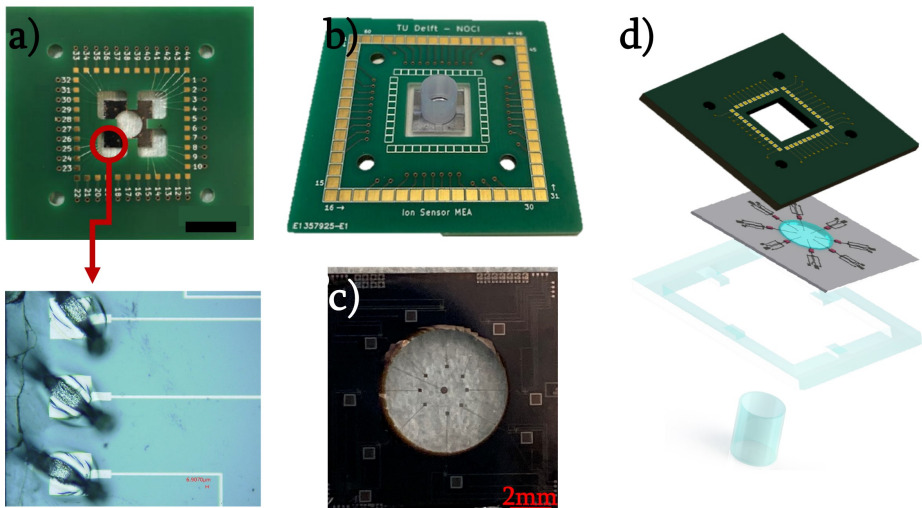


Figure 5.12: Packaging of the chip: a) Frontside, b) Backside of the final assembly. A novel approach, wirebonding through PDMS was achieved and is shown with a red arrow. c) The chip after dicing. d) Assembly of the PCB, the chip, 3D printed holder, and the well,

To reach to Al contact pads, the first trials were made in Fluorine environment to remove PDMS from the contact pads. However, long etching times and byproducts and re-deposition from the etching made the surface contaminated with particles. For this reason, PDMS was kept on top of the contact pads, and wire-bonding through PDMS was attempted.

In order to go through the PDMS membrane and reach to the contact pad, wirebonder parameters were adjusted. The force of the bonder was set to 850 mN, the power to 1100 mW and time to 850 ms. The wire-bonding was successful, as seen in Fig. 5.12 a.

To house the solution-under-test, a 3-D printed well and a holder were assembled to the PCB (Fig. 5.12 d). These parts were designed in SolidWorks, and the well was cured by UV light pulsing before assembly. Depending on the pulsing time, the hardening of the well can be adjusted. However, fully-cured wells are needed for biocompatibility reasons. In several cases, photo-active non-cured resin showed toxicity toward biological cells, as explained in Chapter 7.

5.7. REMARKS ON FABRICATION

This Chapter explained the fabrication of the silicon-polymer OoC device, especially the polymer processing, wafer-scale to single chip-scale transition and packaging.

The most important points during the polymer processing on active devices revealed to be:

- Monitoring the degassing of the polymers before using high-vacuum tools.
- Cleanroom processing with physical and chemical effects influences the surface chemistry, which in turn affects the electrochemical performance of the sensors.
- BHF solution etches the Ti electrodes rapidly. Monitoring the oxide etching and landing on Ti electrodes is crucial for successful devices.
- Saw dicing requires the wafers to be under vacuum during dicing. This vacuum can harm the membranes and the extended electrodes. Stealth dicing can be an alternative to saw dicing used here with fragile membranes, since it employs a laser beam which is focused in the silicon wafer and creates a defect in the form of a dicing line. Then, the foil which the wafer was placed onto is stretched and the pre-damaged dicing lines break controllably [6]. This way, harsh blade dicing can be prevented.
- Through-PDMS wire-bonding is possible, and the parameters need to be calibrated to prevent damage to the PDMS membrane.
- Even though not investigated in the thesis, through-silicon deep reactive ion etching might cause depletion of the active devices [7]. This might be investigated in the future to analyze the change in device behavior and effect on the transistor performance.

In the rest of the chapter, the characterization of the silicon-polymer devices is described.

We use the sensor to evaluate pH due to the usage of metal oxide at the sensing area. However, after the device is fabricated, it can be turned into a specific ion sensor with a post-processing step. The post-processing step needs to be performed at the sensing area; hence, the fabrication of the chips can remain the same as in this chapter. This functionality is beneficial since different ion sensors can be obtained from a batch of chips by having different post-processing steps on different chips. Two examples are described in Chapter 6.

5.8. DRY MEASUREMENTS WITH SEMICONDUCTOR PARAMETER ANALYZER

After the processing of the wafers, and before dicing and packaging of the chips, dry measurements were conducted with a Semiconductor Parameter Analyzer at wafer-scale, which was described in Section 3.2.2.

From the measurements, we found the nMOS FET threshold voltage to yield an average value of 0.44V over 52 dies with a variance of $7 \cdot 10^{-4}$ V [8]. These measurements were performed at wafer-scale, over all the nMOS FET types.

Similar to wafer-scale measurements in Chapter 3, we observed that the FETs fabricated on low-resistivity wafers are not working in depletion mode but rather in enhancement mode. nMOS transistors on a low-resistivity wafer showed typical nMOS characteristics (Fig. 5.13) over the full wafer. However, the availability of low-resistivity double-side polished wafers was limited. Hence, for later batches, high-resistivity wafers were used with double-side polishing. This polishing is especially important since we used back-side etching (DRIE), and a non-polished rough silicon surface introduces imperfections and difficulty in DRIE process.

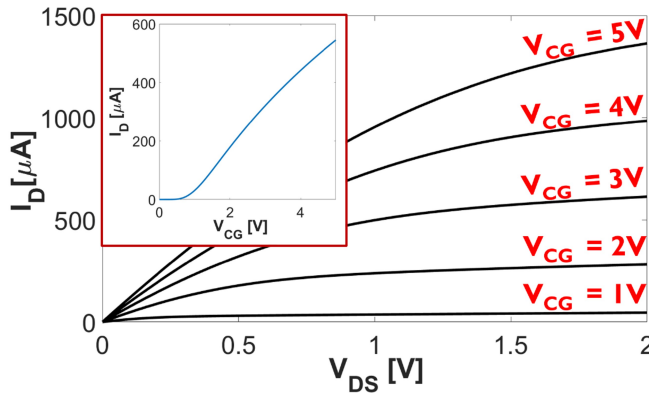


Figure 5.13: Electrical characterization of an nMOS transistor on low-resistivity wafer. Drain current measurements vs. drain voltage with different gate voltage values are shown. In the inset, the nMOS is showing enhancement mode characteristics ($V_{DS} = 0.1V$).

5.9. LIQUID MEASUREMENTS WITH SEMICONDUCTOR PARAMETER ANALYZER

PBS (Phosphate-buffered saline) is a solution that has been used widely for cell culturing applications in biology laboratories. It contains KCl (2.67 mM), KH_2PO_4 (1.47 mM), NaCl (137 mM) and Na_2HPO_4 (8.06 mM). As a preliminary test, we wanted to test our chips with PBS, which is relevant to OoC applications and cell culturing.

Before testing the chips with PBS, surface functionalization utilizing oxygen plasma treatment was performed (100 W, 40 s). O_2 plasma changes the surface wettability of the PDMS membrane to be more hydrophilic, meaning that the number of OH^- groups on the surface is increased [9]. Additionally, it can cause more oxidation on the MO_x layer even though low power (100 W) might be seen as negligible.

Table 5.1: Change in I_D from DI water to PBS solution at the sensing area of an nMOS8 device. Both measurements were performed after oxygen plasma. The measurements were done consecutively.

I_{DI}	I_{PBS}
384.35 μA	386.45 μA
383.7 μA	386.91 μA

Table 5.1 shows the shift in I_D in presence of PBS, compared to DI water. The first measurement was done by introducing DI water to the sensing area, the measurement was recorded and the DI water was removed. Then, PBS was introduced and I_D was monitored. After cleaning and drying the sensing area, the experiment was repeated in the same order (DI water and PBS). We observed the PBS causes an increase of the I_D as opposite to DI water.

After the initial test with the semiconductor parameter analyzer, we wanted to develop a mobile measurement setup to measure pH in biology laboratories, without the need for the (non-mobile) analyzer.

5.10. REAL-TIME MEASUREMENTS WITH MOBILE MEASUREMENT SETUP

A mobile measurement setup was constructed to reproduce actual lab-on-chip characteristics on demand rather than needing fixed laboratory characterization equipment such as a semiconductor parameter analyzer. The reason is that not all biology laboratories have (the same) electrical characterization setups, and the chip should be as mobile as possible (to be able to be moved while measuring in real-time the relevant cue in an incubator or under an optical microscope).

Hence, the mobile measurement setup was meant to replace a commercially available source measurement unit, provide real-time I_D measurements, and be portable.

5.10.1. MOBILE MEASUREMENT SETUP

The mobile measurement setup was developed by Lovro Ivancevic in collaboration with the ELCA Group (Prof. Marco Spirito) of the Microelectronics Department of TU Delft,

on the basis of a partial prototype available at ELCA. The overview of the setup can be seen in Fig. 5.14 a. The main components of the system include a sensing board to bias the sensor and convert the current to voltage by switchable resistors. The resistors tolerate a range of mA to nA currents. An SPI I/O expander controlled the switching through signal relays that can switch between different resistance values.

An 18-bit analog-to-digital converter (ADC) was included in the setup to transmit the data. The ADC converts the voltage value to a digital code to be transmitted.

For user-friendly communication, Bluetooth was chosen, and a custom graphical user interface (GUI) was designed to ease the usage by the operator. The GUI includes real-time monitoring of the measurements in terms of I_D and time by a MATLAB script.

An ultra-low-noise digital-to-analog converter (DAC) was employed to achieve a broad range of voltage values (-10 V to 10 V to bias the sensors). A lithium-ion battery pack (Samsung INR18650-35E) was also used with voltage regulators to power the mobile device with specific voltage values.

The feedback resistor was used to sense the output current from the FG FET (I_D), and the voltage change over it was amplified by an instrumentation amplifier and converted to a digital signal.

The system additionally included a microcontroller (STM32-L475VG) to control the sensing unit with a discovery board. The microcontroller included the Bluetooth low energy (BLE) communication, which was paired with a laptop, to monitor and store the measurements. For compactness and protection, the setup was placed in an enclosed rigid plastic case. On the sides of the casing, panel mount connectors were placed to charge the batteries and connect the chip with a micro USB port. The inside of the casing and the system under use can be seen in Fig. 5.14 b.

For more information regarding the mobile measurement setup, the report on Portable Parameter Analyzer by Lovro Ivancevic can be examined [10].

5.10.2. MONITORING THE CHANGE IN pH LEVELS

To monitor the pH changes in single chips, the sensors were connected one by one to the measurement setup. Even though each chip houses 4 nMOS devices, multiple FETs could not be monitored simultaneously due to the limitations of the mobile measurement setup.

First, an nMOS7 sensor was connected to the system where V_{CG1} was 5 V, and V_{CG2} was 3.3 V due to the capability of the system. The V_D was 3 V and $V_S = V_{sub} = 0V$. All the measurements were conducted with the same values to avoid uncertainties, unless otherwise explained. Fig. 5.15 shows the methodology of the pH experiments used in this chapter. For the first experiment, after the connection was secured via Bluetooth, real-time I_D measurements were monitored. The nMOS7 device was tested with consecutive introductions of pH4 solution (pH4 solution introduction, cleaning the sensing area, and again the introduction of pH4 solution). Fig. 5.16 shows consecutive measurements of cleaning the sensing surface and introducing pH4 liquid. The noise was due to the removal of the liquid from the surface. It is worth mentioning the electrodes were not disturbed while removing the liquid after measurements. The liquid was removed by a micropipette, and the device was flushed 3 times with DI water. The new liquid was introduced when the sensor returned to the initial state as determined by I_D monitoring.

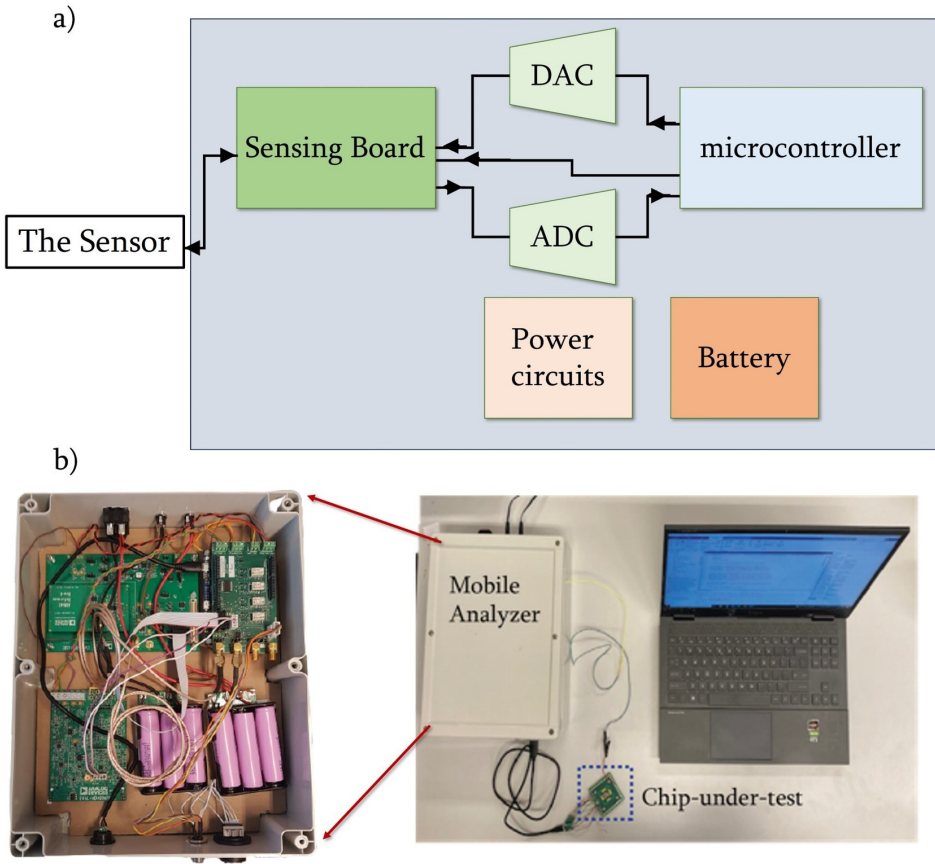


Figure 5.14: a) Schematic overview of the mobile measurement setup. b) The device inside the casing and connected to a laptop via Bluetooth, with the chip-under test.

Even though the initial I_D shifted by $\approx 1\mu A$, the shift in I_D from pH4 solution was roughly $5.5 - 6\mu A$.

It is worth mentioning that when flushing the device before measurements with DI water, the response of the sensor might change, since this step can change the point of zero charge by changing the hydrogen ion concentration at the surface when the surface is electrically neutral [11]. Additionally, the ionic screening layer is altered by the pH on the surface [12]. If there is already a large number of buried OH^- sites in the sensing area, which can be due to oxidation or flushing the device with DI water, the sensitivity can deteriorate in time [13].

Another chip was used with the same FET (nMOS7) for another test, with pH9, pH4, and pH7 liquids. Fig. 5.17 shows corresponding I_D shifts measured in real time.

When we compare Fig. 5.16 to Fig. 5.17, response to pH 4 liquid changed from $5.5 - 6\mu A$ to $5.1\mu A$, which is on the same order of I_D change. $0.4\mu A$ difference between chips was

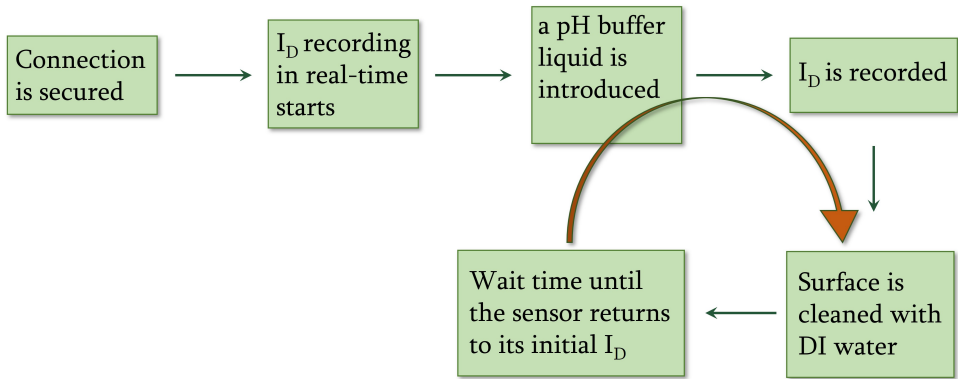


Figure 5.15: Schematic of the experimental protocol with the portable measurement setup. This method was used for all the pH experiments mentioned in this chapter. After the connection via Bluetooth was secured, I_D values were recorded, a solution with a different pH was introduced, the shift in I_D due to the liquid was monitored in real-time, the liquid was removed, and the sensing area was flushed with DI water. The sensor returned to its original I_D value. This experiment was repeated for several runs.

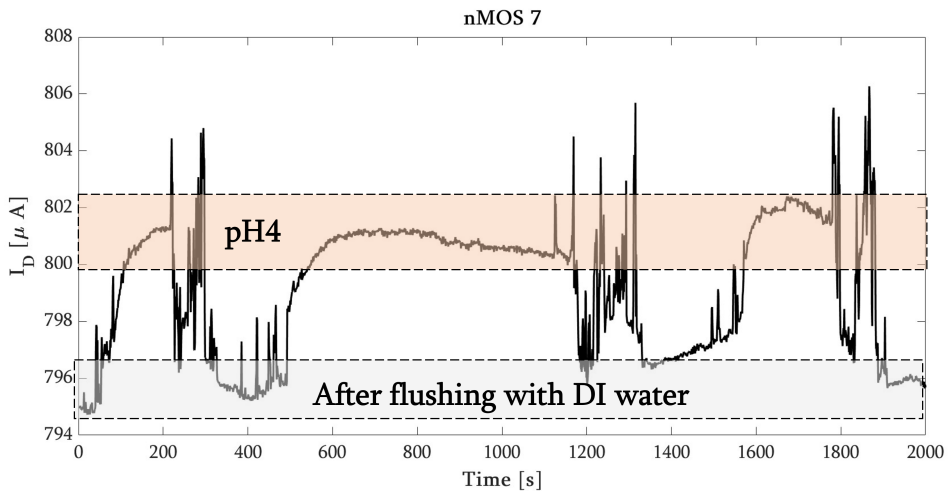


Figure 5.16: Real-time measurement of an nMOS7 with pH4 liquid and cleaning of the sensing area. Consecutive measurements created a $5.5 - 6 \mu A$ shift in I_D .

a good indication of wafer-scale fabrication's reproducibility and uniformity.

I_D shifts caused by pH 9 was $8.54 \mu A$ and $6.2 \mu A$ for pH7. The characteristics of the different liquids were detected by measurements.

As explained in Chapter 2, we have 4 different nMOS devices on a single chip with different gate dimensions. An nMOS5 was tested with pH4, pH9, and pH7 liquids (Fig 5.18). In this case we observed a constant output current drift. This can be caused by a leakage current through the gate. The FET cannot reach saturation, and is having a constant linear increase of I_D values with a fixed V_{CG} . For this device, the introduction of pH4 liquid

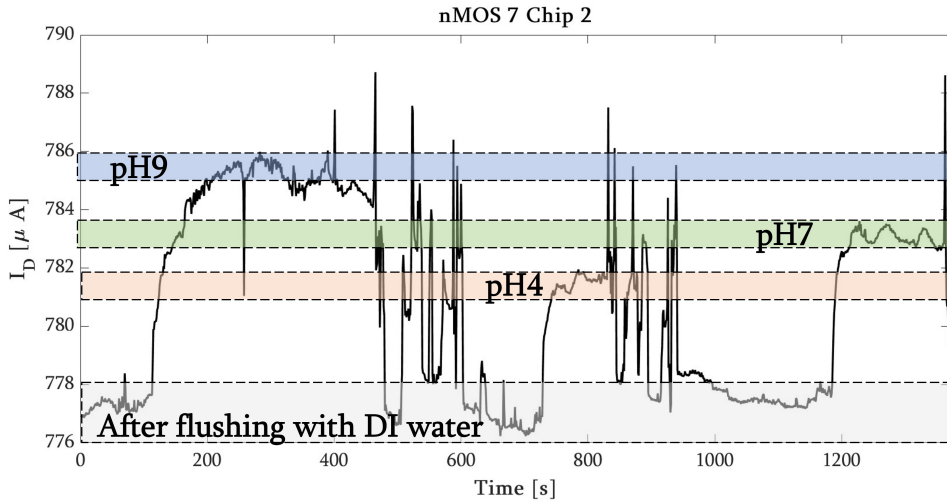


Figure 5.17: Real-time measurement of another nMOS7 (different chip compared to Fig.5.16) with different pH liquids.

caused a shift of $4.5\mu A$, pH9 liquid was $6.3\mu A$ and pH7 liquid was $5\mu A$.

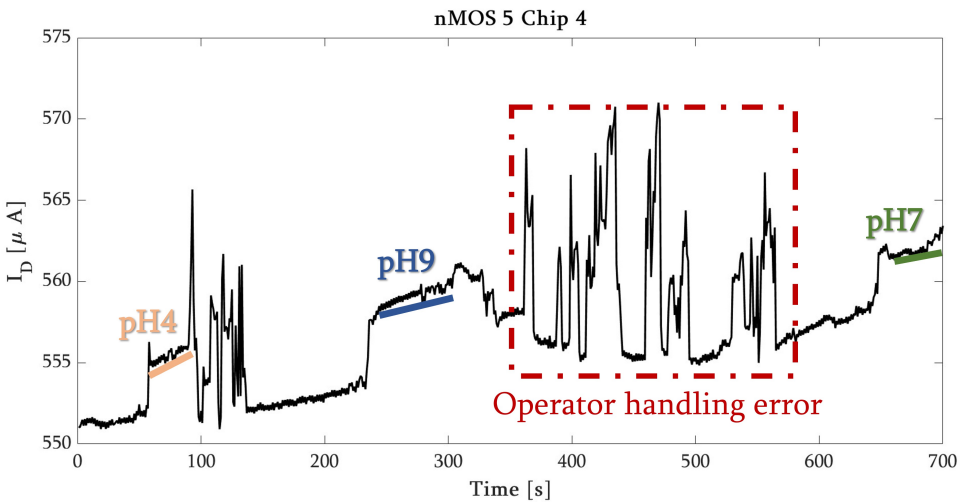


Figure 5.18: Change in I_D in time with pH4, pH9 and pH7 liquids for an nMOS5 device. Human intervention is visible through the monitoring, caused by touching the sensing area while cleaning between the liquid introduction. The baseline current shift is because of the drift of the sensor.

On another chip from the same wafer, an nMOS 8 device was tested with pH9 and pH4 liquids. Fig. 5.19 shows a long relaxation time, as going back to the initial I_D after removing the pH9 liquid took approximately 400s, whereas for other measurements, this recovery time after cleaning the sensing area was approximately 16s. This behavior re-

sembles an RC time constant. One reason for this behavior can be a possible gate current leakage from CG, or a local defect on the FET area. This might be due to a fabrication error (for example, if the gate oxide is not uniform and there are pinholes in the layer). A second possibility can be related to the use of a high-resistivity wafer as a substrate and having a high series resistance at the channel formation area. However, we did not encounter this issue for other nMOS8 measurements on the same wafer.

Even though there was a long recovery time during the measurement, a higher sensitivity was recorded. For pH4 liquid, the shift was $25.7\mu A$ and for pH9 liquid, it was $39.7\mu A$. Hence, this chip could still be used for monitoring the pH after further calibration, and the dataset is created with different pH liquids.

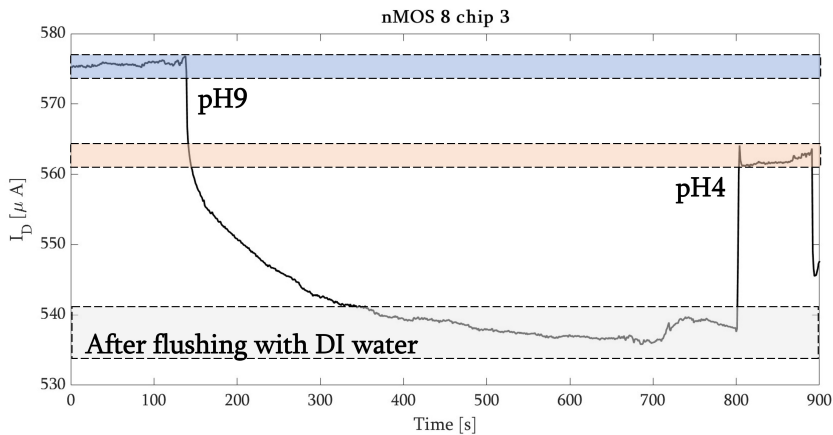


Figure 5.19: Real-time measurement of an nMOS8. The relaxation time after removing pH9 liquid, flushing the sensing area with DI water and reaching to steady-state I_D was 400s.

After initial measurements with different chips and nMOS devices, we saw that the FETs could distinguish different pH liquids. The sensitivity of the nMOS sensors was different (due to different gate dimensions), as explained in Chapter 2. From the experimental confirmations, we found that nMOS8 was the most sensitive towards different pH values. Hence, another chip was used to further test nMOS8 (Fig. 5.20). The data showed the reversibility of the sensor, and we hypothesized that Faradaic reactions were not occurring dominantly.

For these measurements, the introduction of the liquid was randomized to prevent any misconduct in the experiment. We observed distinct fingerprints of I_D with different pH liquids.

As mentioned for the previous measurements, spikes in the measured data were caused by DI water handling between events. The average response time of the sensor shown in Fig. 5.20 was 6 s with a standard deviation of 1.3 s from 15 measurements (Fig. 5.21). This time was calculated from the measured data when the signal reached a steady value before and after introducing the pH liquid.

From this experiment, a sensitivity value $\frac{\Delta I_D}{\Delta pH}$ was obtained as $1.5305 \frac{\mu A}{pH}$ for the change between pH 7 and pH 9 and $1.3574 \frac{\mu A}{pH}$ between pH 7 and pH 4.

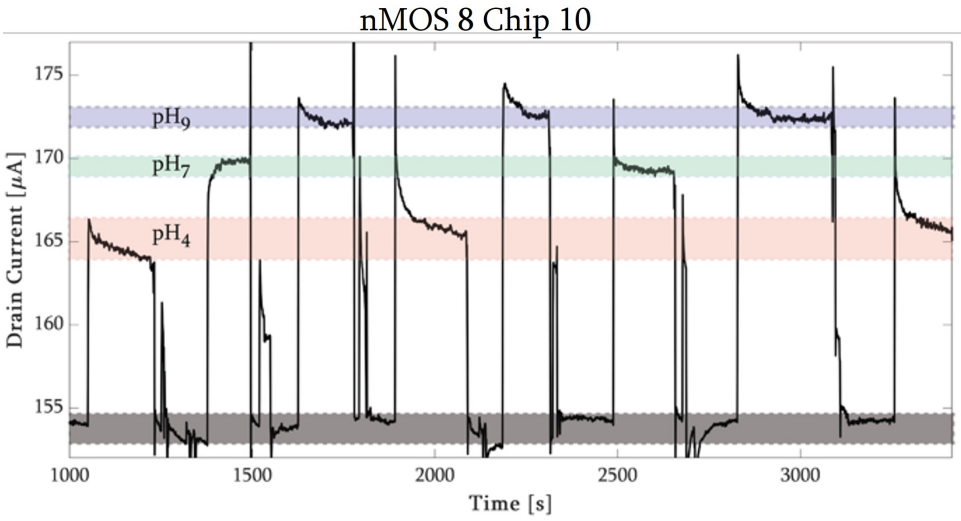


Figure 5.20: Real-time measurement of nMOS8 on chip 10. The long measurement time did not cause a drift (for example, due to heating), and the device could go back to its initial current value when the sensing area was cleaned with DI water.

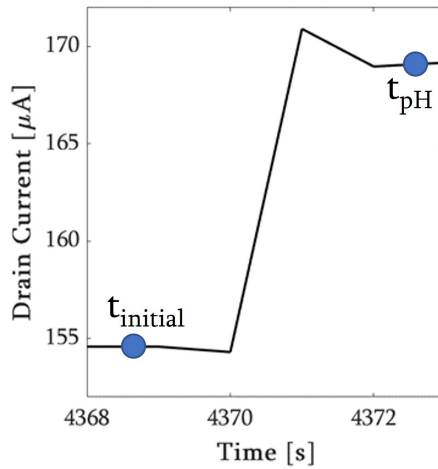


Figure 5.21: Response time of the sensor from Fig. 5.20. The time was calculated from the events when the initial I_D value was steady, and after introducing the pH liquid and waiting until reaching to steady-state ($t = t_{\text{pH}} - t_{\text{initial}}$).

All the experiments that were described in this chapter are compared in Fig. 5.22. From the measurements, the most sensitive device was confirmed to be the nMOS8, even though it was possible to distinguish different pH solutions with nMOS5 and nMOS7 devices as well.

We also observed that if the initial I_D value was relatively high, the shift in I_D due to the pH solution tends to be high. However, the ratio between I_D shifts due to pH solutions were in the same order. Hence, comparing different nMOS devices with the same gate dimensions is possible by comparing the ratio of the I_D shifts.

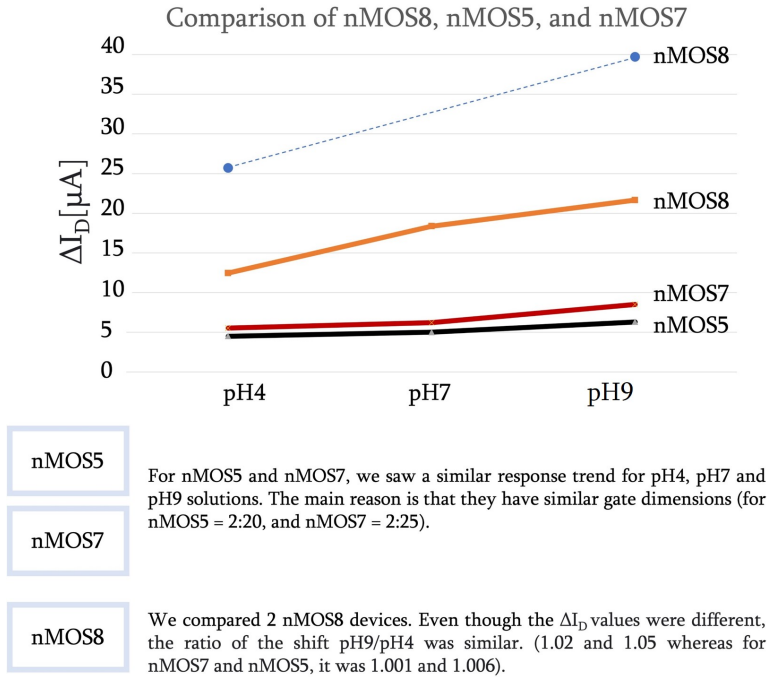


Figure 5.22: Comparison and remarks about measurements with nMOS7, nMOS5 and nMOS8 devices shown in this chapter.

To test the chip reliability with nMOS8, the same measurements (Fig. 5.23 a) were repeated after two weeks. Fig. 5.23 b shows a minor decrease in the initial current value (from $154\mu A$ to $149\mu A$) but the same order of ΔI_D with the same pH liquids.

With the same chip from Fig. 5.20, we wanted to test mixing of different pH solutions on the chip, without intermediate flushing step. Without cleaning the sensing area, the pH 9 buffer was added after the pH 4 buffer in equal volume. From Fig. 5.24, the first event showed the increase of the current due to pH9 buffer liquid addition on pH4 liquid. The second and third events showed an initial increase of I_D with pH9 liquid, following a decrease due to pH4 liquid addition. The resulting I_D values were on the same band since the resulting liquid had the same pH in all 3 cases. With this test, we aimed to prove that the binding of ions at the sensing area was reversible since we were able to record the addition of pH9 solution on top of the pH4 solution.

To compare the measurement to the MATLAB model from Chapter 2, average values of I_D shifts with respect to pH liquids were calculated. In the model, we found the same

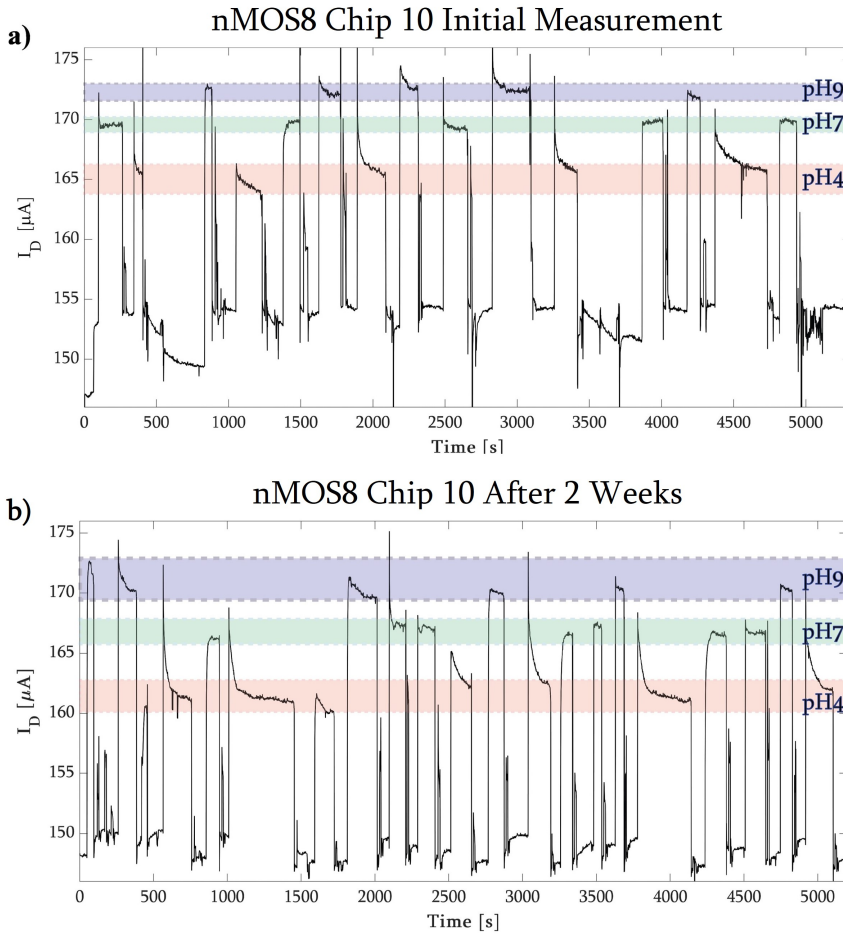


Figure 5.23: a) Real-time measurement of the nMOS8 from Fig. 5.20, and 2) repetition of the same experiment after 2 weeks.

order of magnitude for I_D values. The ratio of the I_D change due to different pH solutions was compared. Similar ratios were recorded both for the analytical result explained in Chapter 2 and measurement of the nmos8 device (Fig. 5.25)

The surface dissociation constants were chosen for comparison with the model as $pK_A = 8$ and $pK_B = 4.5$ [14, 15]. The same trend was observed both for the model and the experimental data. The mismatch of the experimental values and the analytical model was attributed to the unknowns in the model, such as the trapped charge inside the FG, Stern layer capacitance, dielectric constant, and the thickness of the MO_x (TiO_x in this case). For example, Stern layer capacitance was calculated as $1.078 \cdot 10^{-11} F$ with the assumptions based on [16].

To test the sensitivity of the device, small volumes of pH4 liquid (2 and 3 μL) were added

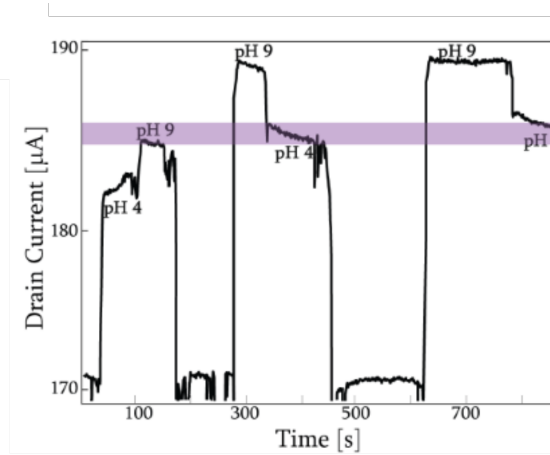


Figure 5.24: Liquid mixing on chip. pH4 and pH9 solutions of equal volumes were added sequentially without intermediate flushing. Results from all 3 events are similar, since they were all reaching to the same pH plateau.

Analytical Solution	nMOS8
$I_{DpH9}/I_{DpH7} = 141 \mu\text{A} / 137 \mu\text{A} = 1.029$ $I_{DpH9}/I_{DpH4} = 141 \mu\text{A} / 133 \mu\text{A} = 1.06$	$I_{DpH9}/I_{DpH7} = 173 \mu\text{A} / 169 \mu\text{A} = 1.024$ $I_{DpH9}/I_{DpH4} = 173 \mu\text{A} / 165 \mu\text{A} = 1.05$

Figure 5.25: Comparison between the analytical model and experimental data for chip 10 nMOS8 device.

to the sensing area without removing the previous solution, making the pH of the solution at the sensing area pH4.4 and pH4.3, respectively (Fig. 5.26). Potentially, smaller changes might have been investigated. However, the mobile measurement setup must be revised to perform at lower current level shifts (on the order of nA).

EFFECT OF CG_2 POTENTIAL

Due to the limitation of the mobile measurement setup, V_{CG2} was applied as 3.3 V for silicon-PDMS devices. We also wanted to test 0 V (as in the case of Chapter 3 experiments) and 5 V to evaluate whether the change in V_{CG2} creates a major shift in I_D . For instance, if the FG extension potential is lower than CG_2 potential, the electric field between these two electrodes and the ions in the electrolyte might migrate to the opposite potential.

Fig. 5.27 shows ΔI_D for pH4, pH7 and pH9 liquids, with different applied CG_2 potentials on nMOS8 device from Fig. 5.20. When $V_{CG2} = 0\text{V}$ was applied, the sensitivity between pH7 and pH9 decreased, whereas when a positive (3.3 V or 5 V) voltage was applied, it increased. For $V_{CG2} = 5\text{V}$, we used an external power supply. For pH4, we always observed the largest shift in I_D . The possible reason might be the overall ion concentration in pH4 liquid (H^+ ions) is greater than in the others; in every situation, the pH4 to pH7 value was greater than the pH7 to pH9 value. This test was inconclusive to say whether

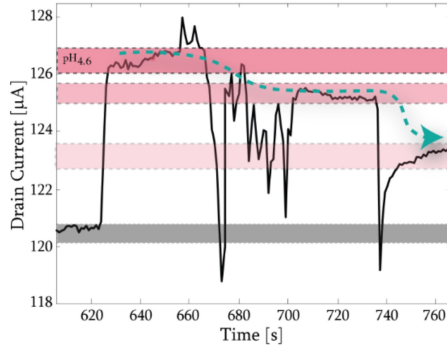


Figure 5.26: Sensitivity analysis on a chip with nMOS6. Without removing the initial liquid, pH4 solution was added two times, decreasing the overall pH of the solution (making it more acidic). Therefore, a decrease in I_D is apparent.

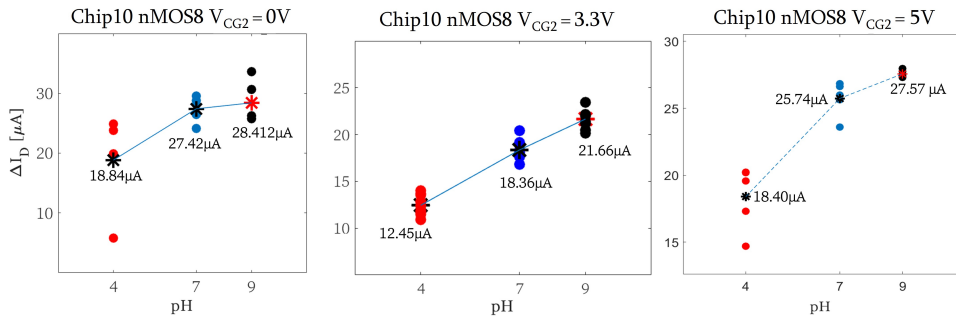


Figure 5.27: Change in I_D with different V_{CG2} values on nMOS8 device from Fig. 5.20. 0V, 3.3V and 5V were applied. The largest ΔI_D was observed for $V_{CG2} = 3.3V$ between pH9 and pH7.

the electric field drove ions toward the FG sensing area.

The CG_2 served as a 'pseudo' reference electrode, altering the potential of the bulk solution. We call this electrode 'pseudo', since it is not a non-polarizable electrode (as in the case of Ag/AgCl), and will form an EDL in close proximity, when a potential is applied.

We also wanted to test the effect of applying negative potential from CG_2 by an external power supply, from the same ground. We recorded events from pH4, pH7, and pH9 solutions. This time, we observed smaller sensitivity and the ΔI_D in the opposite direction. This behavior is due to negative bulk potential, changing the formation of EDL (Chapter 2).

Through this experiment, we showed the effect of CG_2 on the bulk liquid to test the coupling of CG_2 through the electrolyte. Even with the negative bias from CG_2 , it is still possible to use the FET as a pH sensor, for example, if complex circuitry requires a negative potential (Fig. 5.28).

Even though we did not register a significant change in ΔI_D with $V_{CG2} > 0V$, we also compared the time for the events to reach a steady-state value. For instance, the time

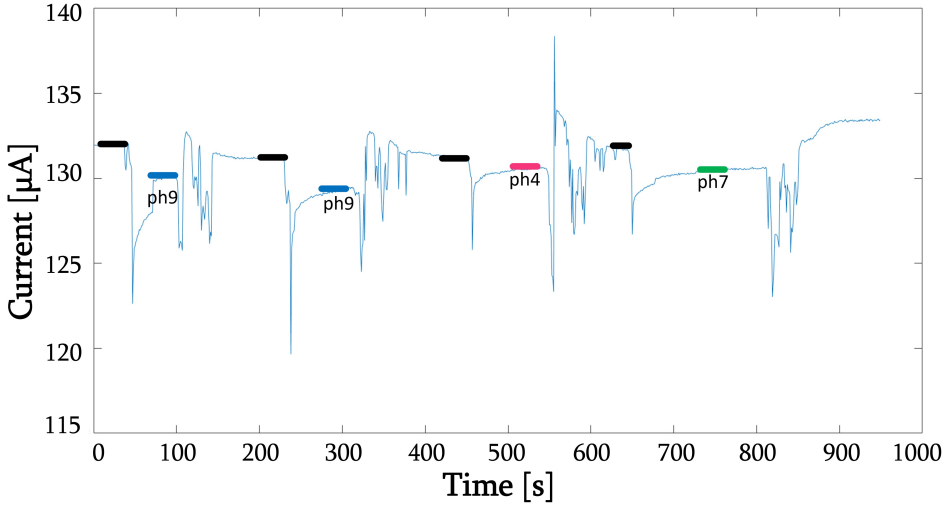


Figure 5.28: Same nMOS8 device as in Fig. 5.20 with negative CG_2 potential ($V_{CG2} = -3.3V$). We recorded shifts in opposite directions compared to positive V_{CG2} due to changes in the bulk potential. Additionally, the sensitivity of the sensor degraded.

it needs for the sensor to change the I_D signal from a pristine initial condition to when the pH4 liquid was introduced at the sensing area. Fig. 5.29 a shows a conventional charging graph of a capacitor (charging current vs. time). Here, the charging current follows from $(V/R) * \exp(-t/(RC))$. Here, V is the applied potential, R is the resistance, C is the capacitance, and t is time. Fig. 5.29 b shows the measurement results of Fig. 5.20 when different CG_2 potentials were applied. Interestingly, for different CG_2 potentials, we observed different response times. To analyze this effect, the equation above can be solved for $V = V_{CG2} - V_{FG}$. When V_{CG2} potential is higher than V_{FG} , the charging current has also a higher value. Additionally, depending on the ion concentration of the liquid, steady-state time will differ since the ion concentration affects the capacitance and resistance values. For instance, pH4 would induce lower resistance compared to pH9 due to higher concentration of H^+ ions (Fig. A.1).

The effect of the charging current is visible when the time response of the pH events is considered. The charging current will flow to equalize the EDL capacitance when the potential of the electrode changes [17]. Hence, we might say high CG_2 potential interacts with the FET, and the FET goes to steady-state after overshooting.

5.11. REMARKS ON CHARACTERIZATION

We showed the characterization of different chips with pH buffer liquids and different nMOS devices by means of the mobile measurement setup. The sensors gave repeatable results while consecutively changing the liquid during hours-long measurements. The analytical solution from MATLAB code from Chapter 2 compared satisfactorily with the results as shown in Fig. 5.25. We also characterized the effect of different CG_2 potentials

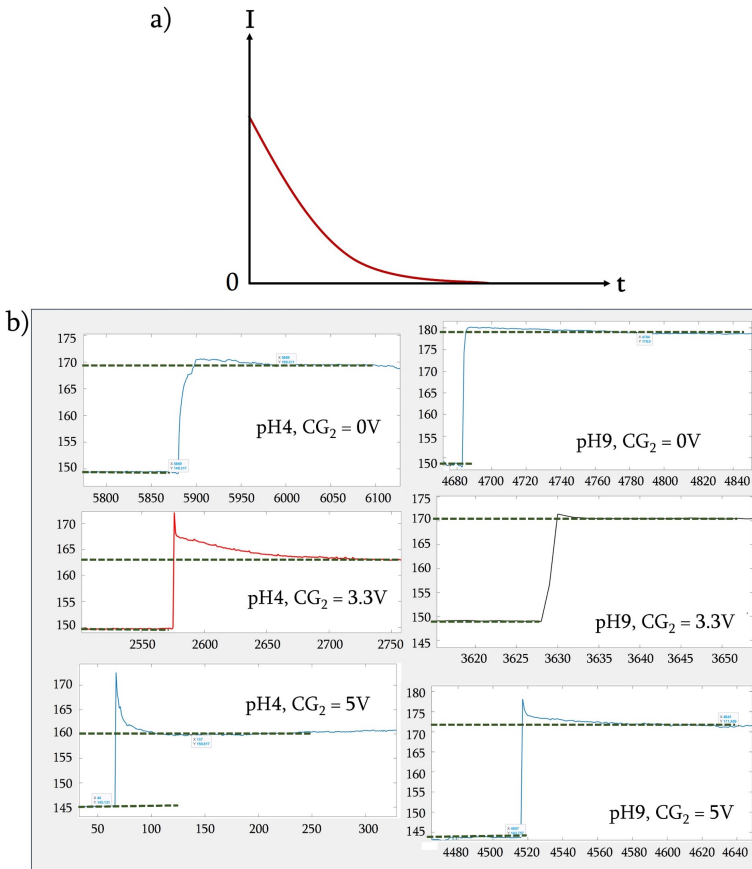


Figure 5.29: a) Typical charging current vs time graph. b) Reaching sensor current steady-state with different CG_2 potentials for nMOS8 device. We observed charging behavior when we introduced the pH4 or pH9 liquids. When we increased the CG_2 potential, the charging current peak also increased without significantly increasing the time to steady-state.

on the sensing of different pH liquids and explained it with the charging current. Different initial values of threshold voltage were obtained depending on the width and length of the channels of the FETs. The difference in the initial drain current values was caused by different gate dimensions and possible defects that might arise during fabrication and wirebonding to the PCB. When using the portable measurement setup, additional wiring can cause noise and change in the characteristics of the sensor when compared to measurements with a probe station where the measurement unit is in direct contact with the contact pads of the sensor. Importantly and generally, calibration of each FET with pH buffer liquids would be necessary to obtain the fingerprint of the sensor before testing liquids in physiologically-relevant environments. Additionally, the salt content of the buffer solutions should be taken into account for a more realistic comparison in the future.

As mentioned in Section 3.2, the comparison of threshold voltage change due to different pH buffer liquid introductions can be a secondary validation for the sensor. Since the mobile measurement setup was just monitoring the I_D , we calculated the change in voltage from the saturation drain current formula (Eq. 5.1), which resulted in 27.27 mV/pH.

$$\Delta V = \sqrt{\Delta I_D / \alpha} \quad (5.1)$$

When we consider the time response of the sensors, it is also necessary to consider the saturation of the electrode surface, in other words, the isotherm point of the layer. This layer defines the condition when there is no change in output signal with different pH liquids. There are a finite number of binding sites on the surface and the rate of adsorption of the analyte can be calculated from the mass transfer to the electrode.

5.12. CONCLUSION

In this chapter, we showed the fabrication and characterization of silicon-polymer FG-FETs. Important findings are reported below:

- The greatest difference in the fabrication of hybrid vs. silicon devices was etching the silicon as a well-like structure and leaving the PDMS membrane with extended electrodes as the transparent sensing area. With hybrid devices, we eliminated the leakage of the liquid to the FET terminals, since the terminals were on the opposite side of where the liquid was introduced. This way, handling of the liquid is easier, compared to the silicon-based device.
- Since the sensors were used in DC, a high-resistivity wafer or PDMS as a substrate did not change the behavior of the FG-FETs.
- We used TiO_x as the sensing layer for pH and successfully monitored the devices response while introducing liquids with different pH values. TiO_x was chosen since it did not require additional post-processing steps. Additionally, in Chapter 2, TiO_x was shown to be sensitive towards the pH buffer liquids with pH4, pH7 and pH9.
- In addition to using a semiconductor parameter analyzer, we developed a mobile measurement system to facilitate monitoring in cell biology labs and to avoid bulky laboratory equipment. The mobile measurement set up made it possible to monitor the pH changes in real-time, with low noise.
- We compared the effect of different CG_2 potentials and different gate dimensions of the FETs. The most sensitive device had gate dimensions of 15:2 (W:L). CG_2 potentials played a role in the relaxation time of the sensors.
- We showed the sensitivity of the sensor by altering the pH of the solution on chip. It is possible to investigate further the sensitivity of the sensors by changing the range of the mobile measurement setup. We successfully showed the difference between liquids with pH4, pH7, and pH9 by means of I_D of the sensors. We also

showed how I_D changes while making the liquid more acidic at the sensing area in real-time.

As future work, medium from cells should be used and recirculated. Here, we wanted to avoid contamination and prepared the initial calibration dataset with liquids with known pH values. The next step would be to use media from cell cultures.

After establishing the sensor, we studied the functionalization of the surface of the sensing area by introducing post-processing steps. The next chapter discusses alternative approaches to decorating the sensing area to alter sensitivity and selectivity.

BIBLIOGRAPHY

- [1] Miao Liu et al. “Thickness-dependent mechanical properties of polydimethylsiloxane membranes”. In: *Journal of micromechanics and microengineering* 19.3 (2009), p. 035028.
- [2] Yong Luo, Li Yang, and Maocai Tian. “Application of biomedical-grade titanium alloys in trabecular bone and artificial joints”. In: *Biomaterials and medical tribology*. Elsevier, 2013, pp. 181–216.
- [3] Fujifilm. *Durimide Properties*. https://asset.fujifilm.com/www/us/files/2020-03/1fcf5e6b68d06204cfa8d2f59d272bdf/Durimide-200_US12.pdf [Accessed: 30/1/24]. 2024.
- [4] Xuhua He and Yuechuan Wang. “Highly thermally conductive polyimide composite films with excellent thermal and electrical insulating properties”. In: *Industrial & Engineering Chemistry Research* 59.5 (2020), pp. 1925–1933.
- [5] J Cooper McDonald et al. “Fabrication of microfluidic systems in poly (dimethylsiloxane)”. In: *ELECTROPHORESIS: An International Journal* 21.1 (2000), pp. 27–40.
- [6] Disco. *Disco Stealth Dicing*. <https://www.disco.co.jp/eg/solution/library/laser/stealth.html> [Accessed: 10/4/24]. 2024.
- [7] LJ Klein et al. “Quantum dots and etch-induced depletion of a silicon two-dimensional electron gas”. In: *Journal of Applied Physics* 99.2 (2006), p. 023509.
- [8] Hande Aydogmus et al. “FET-based integrated charge sensor for organ-on-chip applications”. In: *2020 IEEE SENSORS*. IEEE. 2020, pp. 1–4.
- [9] Say Hwa Tan et al. “Oxygen plasma treatment for reducing hydrophobicity of a sealed polydimethylsiloxane microchannel”. In: *Biomicrofluidics* 4.3 (2010), p. 032204.
- [10] Lovro Ivancevic. “Portable Parameter Analyzer”. In: *PPA Report, Extra Project for ET4399* (2020).
- [11] Luc Bousse, Nico F De Rooij, and Piet Bergveld. “Operation of chemically sensitive field-effect sensors as a function of the insulator-electrolyte interface”. In: *IEEE Transactions on Electron Devices* 30.10 (1983), pp. 1263–1270.
- [12] Matti Kaisti et al. “Field-effect based chemical and biological sensing: theory and implementation”. In: (2017).
- [13] Luc Bousse and Piet Bergveld. “The role of buried OH sites in the response mechanism of inorganic-gate pH-sensitive ISFETs”. In: *Sensors and Actuators* 6.1 (1984), pp. 65–78.

- [14] REG Van Hal, JCT Eijkel, and P Bergveld. "A general model to describe the electrostatic potential at electrolyte oxide interfaces". In: *Advances in colloid and interface science* 69.1-3 (1996), pp. 31–62.
- [15] Su-Hsia Lin et al. "Photocatalytic degradation of phenol on different phases of TiO₂ particles in aqueous suspensions under UV irradiation". In: *Journal of Environmental Management* 92.12 (2011), pp. 3098–3104.
- [16] Matti Kaisti et al. "An ion-sensitive floating gate FET model: operating principles and electrofluidic gating". In: *IEEE Transactions on Electron Devices* 62.8 (2015), pp. 2628–2635.
- [17] Allen J Bard, Larry R Faulkner, and Henry S White. *Electrochemical methods: fundamentals and applications*. John Wiley & Sons, 2022.

6

FUNCTIONALIZATION OF FG-FETs

6.1. INTRODUCTION

As explained in Section 1.3.5, selectivity and sensitivity are important factors in establishing electrochemical sensors that can sense a specific analyte. However, especially commercially-available selective sensors are usually bulky and in need of large analyte volumes, compared to the size of an OoC or even a Petri dish for cell culturing.

Towards miniaturized selective electrochemical sensors, solid-state selective electrode devices became popular where the electrode is in direct contact with the analyte-under-test, serving as an ion-electron transducer [1]. The charge carriers inside the selective electrode membrane are the ions. At the interface of the membrane and the electrode, the charge transfer of ion to electron happens. Depending on the charge conversion, the working principle of the ion-selective sensor can be based on two transduction mechanisms: 1) Faradaic and 2) Non-Faradaic. These mechanisms were explained in Section 2.2.

Hence, integrating selective miniaturized solid-state electrodes to OoCs can be a solution to overcome the inconvenience of bulky setups.

In this chapter, we wanted to explore functionalization methods for both silicon- and silicon-polymer-based FETs, without changing the device architecture. Firstly, we developed Potassium-selective sensing for silicon-based FETs. For silicon-polymer FETs, we decorated the sensing area with Au nanoparticles.

6.1.1. POTASSIUM SELECTIVE SENSORS

In this section, the increased sensitivity of the FET-based sensor specifically towards K^+ ions with the help of a functionalized sensing electrode will be introduced. In human physiology, ions play an important role in homeostasis, cell-to-cell communication, and electrical activity. Hence, it is important to integrate ion-selectivity towards OoC sensors. Potassium is one of the most significant ions in the body. It especially plays a critical role in the action-potential levels of electrically active cells, where the movement of the ions polarizes the cell membrane (Fig. 6.1). More specifically, K^+ can be found in intracellular fluid and in the extracellular fluid [2]. It can provide fingerprints towards certain diseases such as hypokalemia, where the K^+ levels in the blood are too low ($< 3mMol/L$) [3]. The permeability of ions such as K^+ was investigated in the 1980s to understand disease mechanisms [4]. The earlier research was mostly based on understanding the K^+ pathways, but more recently, the correlation with disease mechanisms became significant. For example, cortical spreading depression (CSD), which is the mechanism behind migraine aura, can be related to K^+ concentrations [5]. Researchers found that Alzheimer's disease might alter the levels of Rubidium and Potassium [6]. Additionally, absorption of K^+ from nutrients depends on the nephron and its ability to process. Hence, irregularities in K^+ balance might be a sign of irregularities of filtration and abnormal reabsorption [2] (Fig. 6.2). This analysis can pave the way for understanding kidney diseases [7].

In the literature, even though there are on-chip examples where a microfluidic channel was integrated to commercially available pH and K^+ sensors [9], there is still a lack of bridging between biology and technology. Most disease mechanism studies were conducted with brain slices [5]. Integrating OoCs with relevant selective electrochemical sensors can minimize the number of cells needed for analysis, compared to a brain slice.

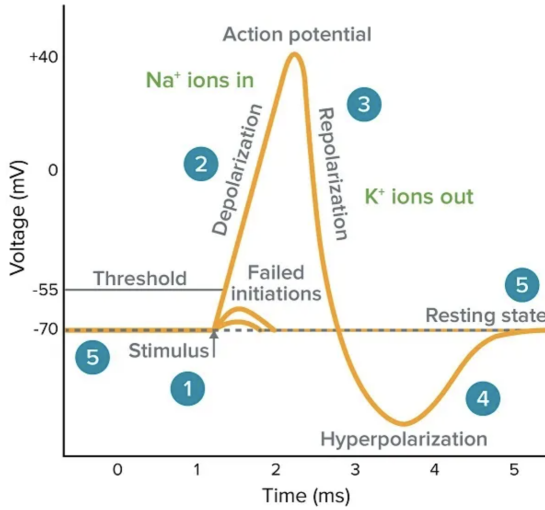


Figure 6.1: Schematic of the working mechanism of action potential. When there is an electrical stimulus, the stimulus polarizes the cell membrane, leading to the migration of Na^+ ions inside the cell, following the depolarization and followed by migration of K^+ ions. The membrane will reach the resting state at the end of the stimulus [8].

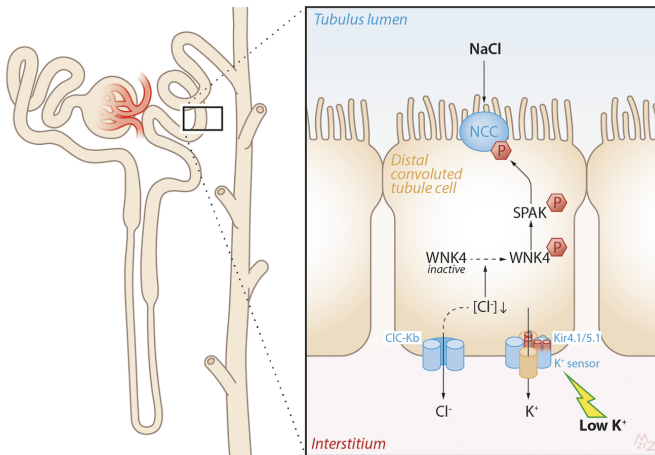


Figure 6.2: Schematic of kidney elements and how low intake of K^+ is affecting the cellular pathways. Low intake results in polarization of the cellular membrane, changing the concentration of K^+ and Cl^- in the channels (Kir4.1/5.1 and ClC-Kb). These channels work as 'sensors' for the specific ions [7].

POTASSIUM IONOPHORE COCKTAIL

Potassium ionophore cocktail, a solution widely employed for selectivity measurements against K^+ ions, mimics a biological cell transport phenomena. There are two ion transportation mechanisms: The formation of a channel to release the ion from one side of a cell membrane to the other, depending on the concentration, and mobile ion carriers.

Passive ion transport across the cell membrane is supported by the lipophilicity of the membrane [10].

For K^+ selective coatings, valinomycin, an antibiotic and an ionophore that induces permeability towards K^+ , is commonly used. The ionophore cocktail contains solvents which evaporate after deposition, and the remaining composition forms the ion selective membrane. (Fig. 6.3). Valinomycin is a ring-shaped polymer that assists the transportation of K^+ , since K^+ ions can bind to valinomycin. Its chemical formula is $C_{54}H_{90}N_6O_{18}$. It has 12 amino acids and esters crucial for metal ion binding [11].

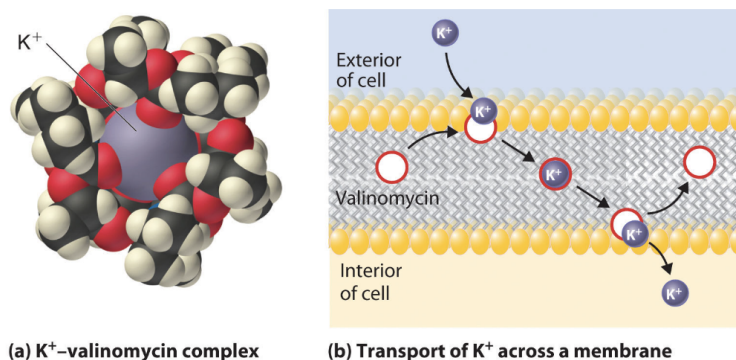


Figure 6.3: Schematic of ion transport with valinomycin [11]. Valinomycin has a circular structure with a gap in the center that can capture K^+ ions from the environment.

Next to valinomycin, the components of ionophore cocktails include polyvinyl chloride (PVC), and plasticizer for the stability of the membranes on an electrode surface [12, 13]. Another important component is the lipophilic salt, which is crucial for the stability of the ion-selective membrane. It prevents the targeted ion (K^+) from forming unwanted pairs with other ions in the solution by providing counter ions [14].

6.1.2. POTASSIUM-SELECTIVE FG-FET-BASED SENSOR

We previously showed the working principle of FG-FET and how MO_x s can be beneficial for pH sensing. If we integrate a selective layer, FG-FETs can become specific sensors towards the analyte of interest. Since they have an extended gate structure, the selective layer can be introduced as a local post-processing step without changing prior fabrication steps. This also increases the possible types of tests that can be performed from a batch of chips (Fig. 6.4).

To investigate K^+ selectivity, a commercially-available ionophore cocktail (CleanGrow Sensors) was integrated into the silicon chips. In literature, process integration of ionophores is usually based on drop casting, and patterning is uncommon. Here, we wanted to introduce the cocktail after patterning the wafer, as a lift-off process [15]. Fig. 6.5 shows the steps of the fabrication. First, a $3.1\mu m$ -thick positive resist was spin-coated on the wafer containing the sensors. A direct laser-writer was used to expose the wafer with a pattern of openings on top of the FG sensing pad, and the wafer was developed (Fig. 6.5 b). After the lithography, the wafer was diced. After a resist hard bake step in an oven

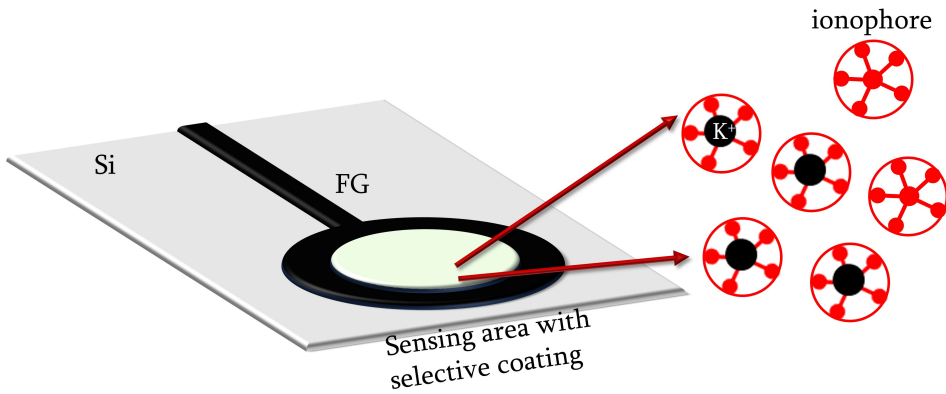


Figure 6.4: Schematic of K^+ ionophore cocktail-decorated FG-FET extension. The extension works as the sensing area. The primary target ion for the ionophore is K^+ . The specific ionophore is valinomycin which has a circular structure.

for 30 minutes at 100°C , the ionophore cocktail was introduced to the chip (Fig. 6.5 c). The chips were left for 24 hours at room temperature to evaporate the solvents such as tetrahydrofuran (THF) and form the selective membrane. After 24 hours, the chips were then put in acetone for ultrasound cleaning and resist lift-off (Fig. 6.5 d).

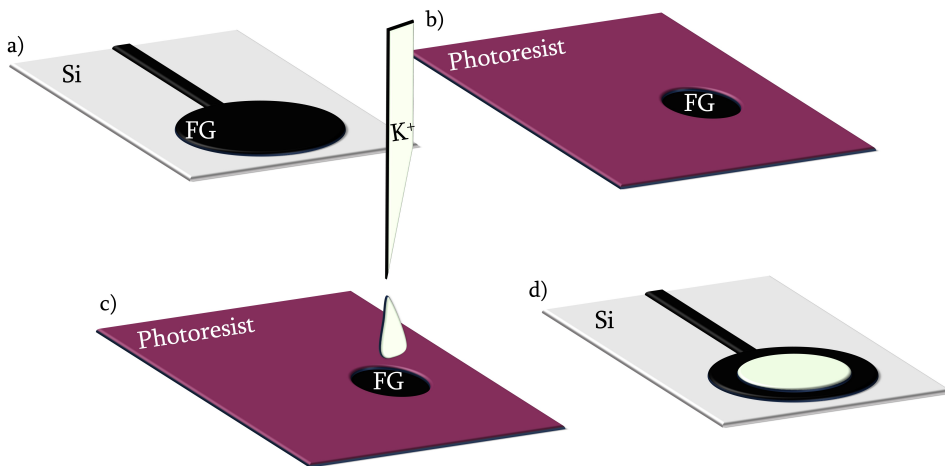


Figure 6.5: Steps of post-processing to obtain K^+ selective FG sensing area. a) Schematic of the electrode after fabrication (Chapter 3). b) Introducing a resist-based pattern for openings on the FG pad. c) Introducing K^+ ionophore cocktail. d) Lift-off with acetone to form the selective layer on the FG pad.

After the fabrication steps, we realized that the solution attacked some of the photoresist. One of the reasons can be that THF is an ether-based organic solvent, which can dissolve the photoresist. A more chemically stable photoresist (for example, SU-8) can therefore

be preferred. However, we managed to have functionalized areas (Fig. 6.6).

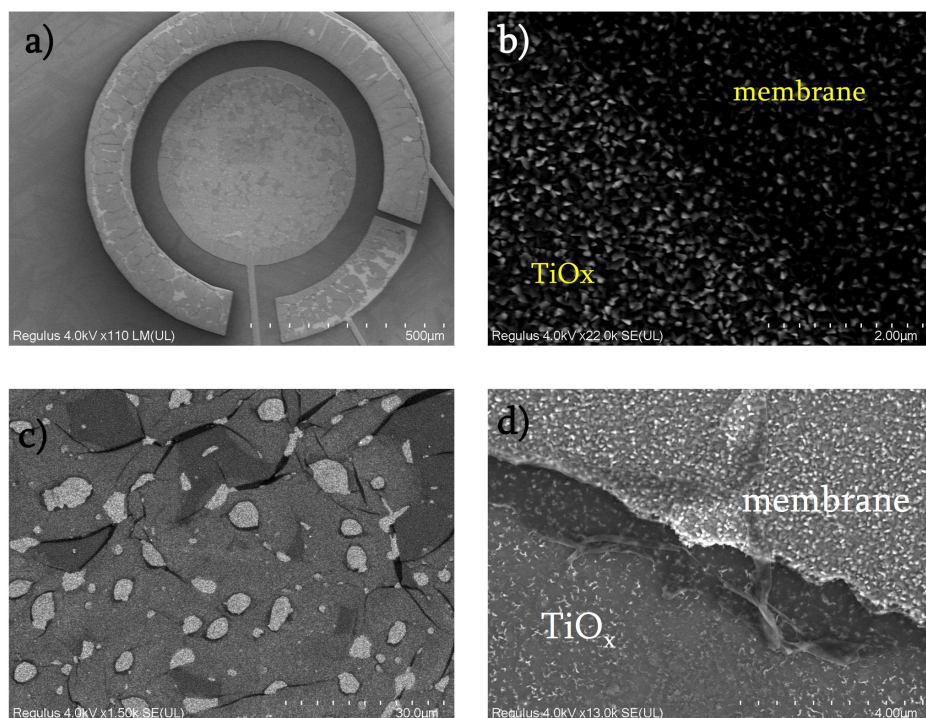


Figure 6.6: SEM images after fabricating the selective membranes on FG-FETs: a) Functionalized sensing area with K^+ ionophore cocktail. b) Micrograph of membrane on Ti/TiO_x area. c) Micrograph of the formation of the membrane on the electrode. d) Thickness of the membrane is visible.

6.1.3. CHARACTERIZATION

Since it was difficult to compare the ion-selective membrane formation visually by SEM, EDX (introduced in Chapter 3) was employed to understand the element distribution on the electrodes (Fig. 6.7). The analysis and the SEM image revealed the functionalized surface to be inhomogeneous. The left side of the sensing area (Spot 1 in Fig. 6.7) resembled the pristine Ti electrode. On the right side of the sensing area (Spot 2 in Fig. 6.7), membrane formation was more apparent. However, EDX analysis gave a similar result for both sides. Spot 1 showed higher Ti concentration. Since the selective membrane layer was thin (estimated as less than $1\mu m$, when Fig. 6.6 d is inspected), the electron beam reached the Ti substrate (underneath the selective membrane). Since both spot 1 and spot 2 gave the same composition, we concluded that Spot 1 also had a functionalized surface but with thinner membrane.

MEASUREMENTS WITH KCL

To test the sensors, 2 mM, 10 mM, and 20 mM KCl solutions were introduced at the sensing area between DI water cleaning steps. This range was chosen due to its clinical rel-

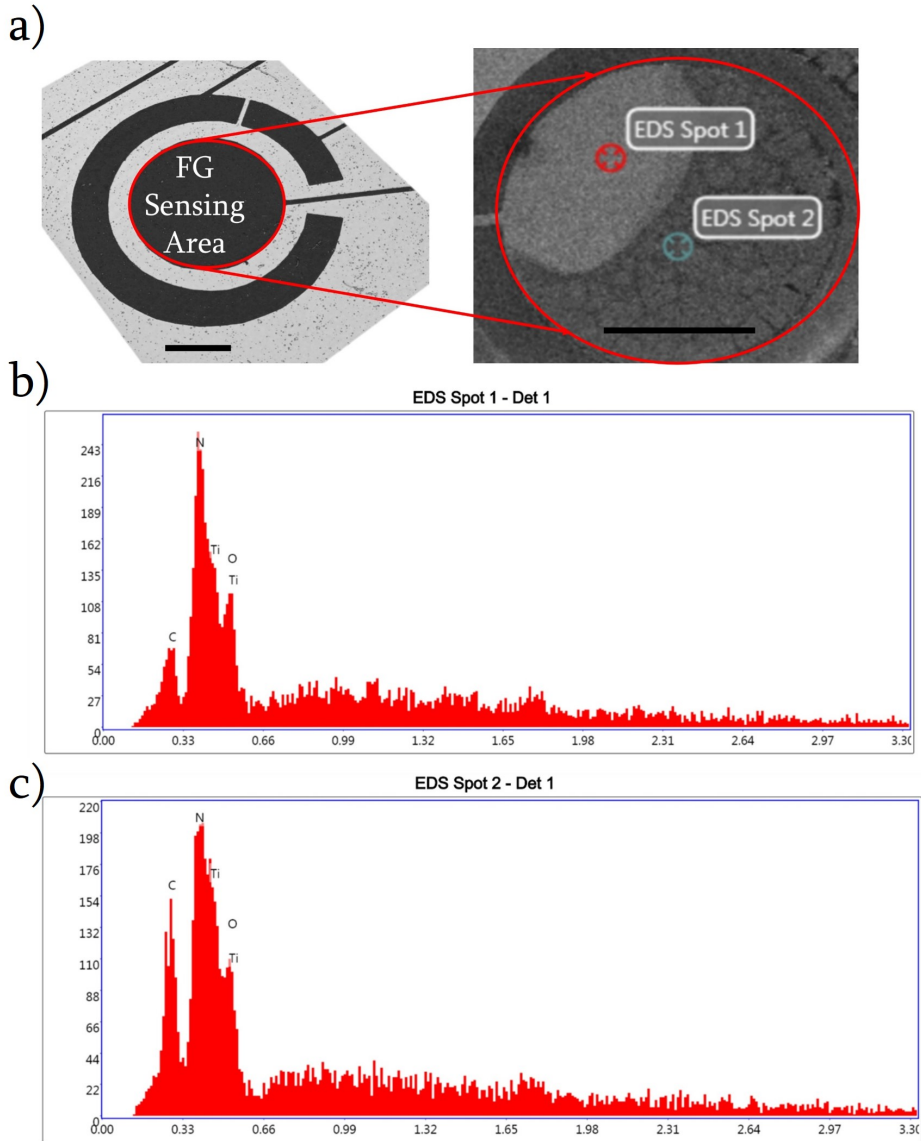


Figure 6.7: EDX analysis of the sensor area after selective membrane coating. a) The sensing area is shown with a confocal microscopy image without functionalization (left) and with functionalization (right). Both scale bars are $200\mu\text{m}$. b-c) EDX analysis of Spot 1 2. Although the functionalization was not homogeneous in the sensing area, the elemental composition of both sides was similar. However, at Spot 1, the count of Ti was higher than Spot2, meaning that Spot 2 had a thicker functionalized membrane surface.

evance [16, 12]. The chip used for testing was left in the KCl solution before testing for conditioning and later flushed with DI water (same protocol from Chapter 5 was em-

ployed, Fig. 5.15).

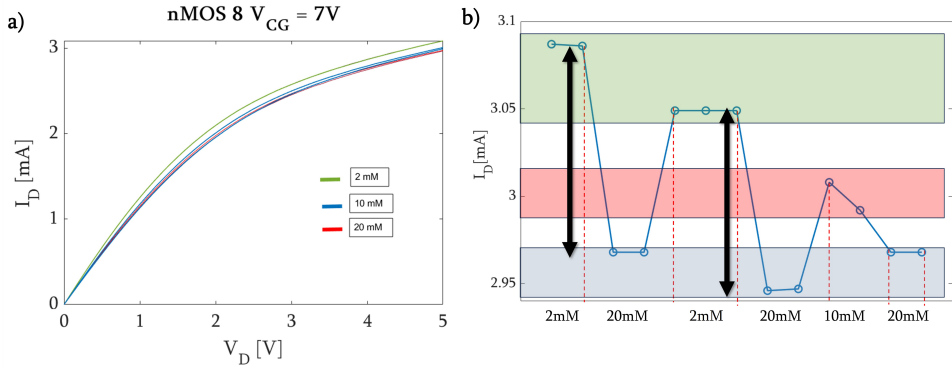


Figure 6.8: Measurements with a chip with K^+ -functionalized sensing area. KCl concentrations of 2 mM, 10 mM, and 20 mM were used. a) I_D decreases with increasing concentration of KCl, a phenomenon we also observed with higher pH solutions in previous chapters. Hence, the measurements gave the same kind of response. b) Introducing different concentrations with random order with steps of DI cleaning in between. Black arrows show the change in I_D with a 2mM concentration of KCl. Even though the initial I_D was different, the shift was equal with the same concentration. Green shows 2 mM, the red area shows 10 mM, and the blue area shows 20 mM of KCl.

Fig. 6.8 a shows measurements with a semiconductor parameter analyzer and the change in I_D , with respect to different molarity of KCl solutions. We observed a decrease in I_D with increasing concentration of KCl, a phenomenon we observed with higher pH solutions in previous chapters. In Fig. 6.8 b, we wanted to show the effect of the disordered introduction of different molarity solutions. We introduced the solutions of 2mM - 20mM - 2mM - 10mM and 20mM to observe the response of the chip and its reversibility. The measurements revealed a similar trend for similar concentrations.

To show the effect of the functionalized membrane towards K^+ selectivity, a chip without the functionalized layer was tested with 2mM and 20mM KCl solutions. The I_D shifts were not distinguishable. Fig. 6.9 shows the difference between two chips: 1) without functionalization and 2) with functionalization.

These preliminary experiments indicate the sensitivity and potential selectivity to K^+ by means of the ionophore cocktail and the versatility of the FG-FET electrodes. In the future, a chemically-durable photoresist should be used for patterning. For example, polyimide or SU-8 can function as an insulating layer and also as a hard mask for the functionalization of the sensing surface. Additionally, different solutions should be introduced to the sensing area to evaluate the selectivity coefficients of the sensor.

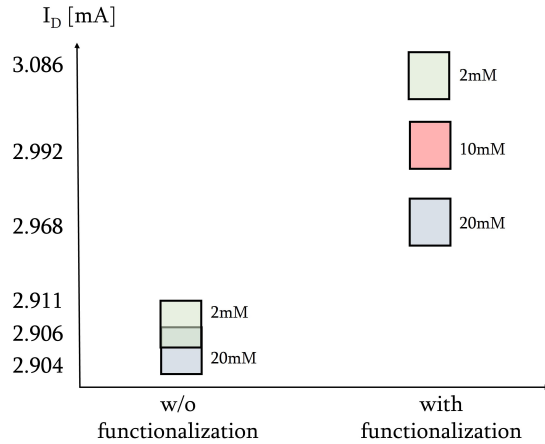


Figure 6.9: 5 consecutive measurements of chips without K^+ -selective membrane and with functionalized membrane. 2mM and 20mM KCl solutions were non-distinguishable with the FET without functionalization, whereas clear I_D shifts were observed with the functional membrane.

6.2. SENSING SURFACE ALTERATION VIA GOLD NANOFILMS

Sensing surface alterations are important when the surface chemistry dominates the properties of the materials. One such field is electrochemistry, where surface mechanical properties such as roughness and chemical properties such as the number of binding sites in electrode-electrolyte interactions become important. For instance, the roughness of the electrode surface will increase the surface area in direct contact with the solution-under-test, thus increasing the sensitivity and decreasing the impedance.

In order to investigate the surface decoration of an FG electrode suspended on a PDMS membrane, we implemented gold nanoparticle (AuNPs) films. Biosensors commonly use gold layers due to their biocompatibility and inertness [17, 18, 19]. One interesting aspect of gold nanoparticles is that they have a direct electron-transfer capability without mediators [20]. Increasing the surface area between the electrode and the solution-under-test by means of the AuNP film was expected to increase the EDL area and, therefore, the sensitivity.

Another possibility with rough gold electrodes is to minimize the impedance at the electrode/electrolyte interface [21]. The next section describes the fabrication and characterization steps.

6.2.1. POST-PROCESSING FOR ELECTRODE SURFACE STRUCTURING

Even though Au is beneficial for biosensing applications, its non-compatibility with CMOS process makes it difficult to combine with active devices. However, it can be integrated into the sensing area as a post-processing step. After completing the cleanroom processing and dicing the wafers, we used a spark ablation device (VSParticles) to locally deposit Au nanofilms on the sensing area. The deposition works with the inertial impaction of pure Au nanoparticle (NP) aerosol generated by spark ablation. It is a maskless process,

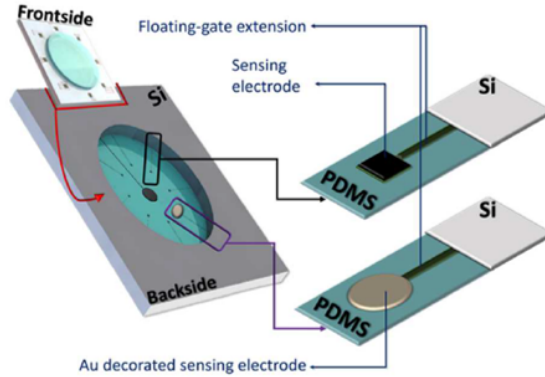


Figure 6.10: Schematic of the chip from frontside and backside with suspended FG electrodes on PDMS membrane with and without Au film decoration.

meaning that no further lithography step is needed on a topographically-challenging surface, conducted at room temperature and relatively fast compared to lithography. Most importantly, we could observe that it does not harm the flexible and suspended polymeric membranes with extended electrodes. Moreover, no additional processing is needed as in the case of other methods, such as e-beam evaporation, sputtering, and atomic layer deposition (Fig. 6.10).

More specifically, the Au NP aerosols were generated by a spark discharge generator (VSP G1) and deposited utilizing a nanoporous material printer (NMP) prototype developed by VSParticle B.V. The NMP operates at <1 mbar pressure to create an ultrasonic gas jet, which by its inertia sends the nanoparticles to the substrate [22] (Fig. 6.11 a). The deposition process used 99.999% Au electrodes and N_2 as the carrier gas, producing pure and clean NP film surfaces. A 5 s deposition resulted in $< 500\mu\text{m}$ spot size (Fig. 6.11 b). The deposition did not damage the PDMS membrane (Fig. 6.11 c, Fig. 6.12).

6.2.2. CHARACTERIZATION OF AU NP FILM DECORATED FG ELECTRODES

Due to the higher surface-to-volume ratio compared to bulk Au, AuNPs have higher surface energies, which can translate to affinity towards more interactions with the ions in the solutions [23]. For this set of experiments, we measured different analytes, such as KCl solution and poly-d-lysine, with a semiconductor parameter analyzer.

Poly-d-lysine, a polypeptide widely used in cell culturing [24] and stem cell research [25], was introduced to the Au-decorated sensing area. The measurements were conducted before and after the evaporation of the solution ($10\mu\text{L}$ poly-d-lysine ($\frac{0.1\text{mg}}{\text{mL}}$)). Fig. 6.13 a shows a decrease in I_D from the measurements in the air to the measurements when there is a poly-d-lysine layer at the sensing surface. One possible reason for the decrease in I_D is the applied voltages. We applied $V_{CG1} = 0\text{V}$ and $V_{CG2} = 2\text{V}$, suggesting that the potential of the bulk solution was higher than the potential at the FG. This suggests the initial impact due to solution introduction to the sensing area did not create additional mechanical stress on the membrane, and ΔI_D was primarily due to the charges bound

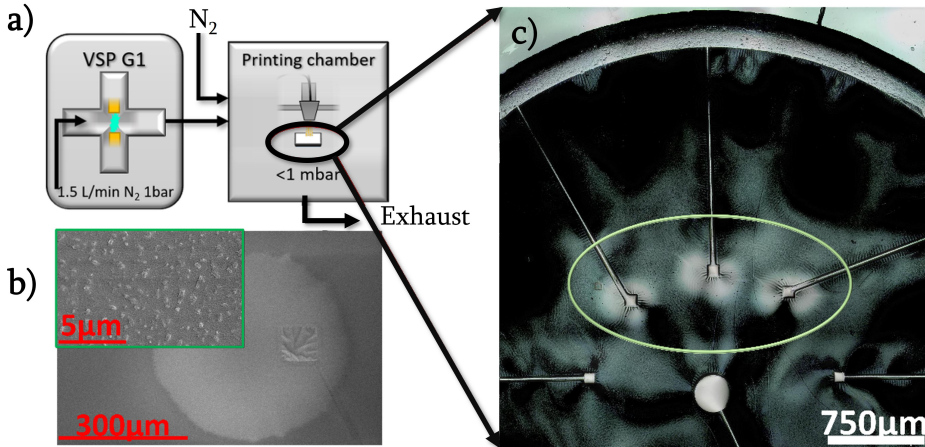


Figure 6.11: a) Schematic view of the nanomaterial printer setup. b) SEM image of the sensing area after formation of Au nanolayer with film morphology in the inset. c) Confocal microscopy image from the backside of the chip showing local decoration on 3 FG extensions on PDMS membrane.

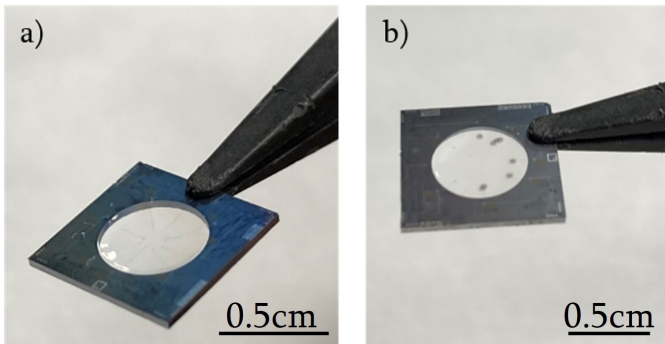


Figure 6.12: Optical images of the OoC device a) before and b) after Au thin film formation on the PDMS membrane.

on the sensing electrode. When a positive V_{CG1} was applied and $V_{CG1} > V_{CG2}$, the initial I_D increased since V_{FG} also increased, and overall ΔI_D became positive. This is also consistent with the findings of Chapter 5: when CG_2 had positive or negative potential, the response towards pH solution was dependent on V_{CG2} . We also experienced a greater shift in I_D when the electrode was coated with AuNP, compared to the non-coated electrode (Fig. 6.13 b), supporting the increase in sensitivity.

Next, on another chip from the same wafer, 2.5 mM and 1.25 mM KCl solutions and poly-d-lysine with the same concentration as prior were introduced to the sensing area with AuNP-decorated electrode. V_{CG1} was 5 V, and V_{CG2} was swept from -2 V to 2 V. Different solutions showed different I_D shifts (Fig. 6.14). First, 2.5 mM KCl solution was introduced to the sensing area, measured and the sensing area was cleaned by DI water.

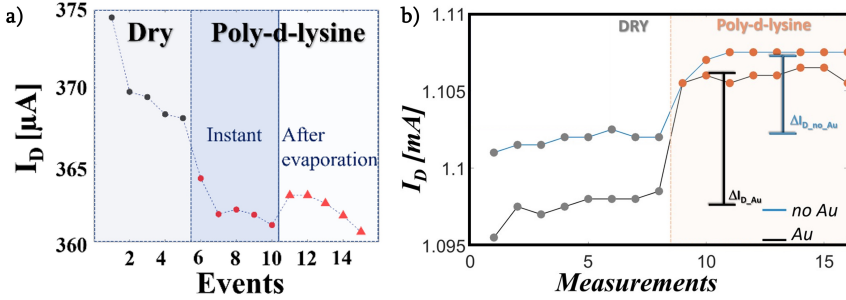


Figure 6.13: Consecutive measurements with Poly-d-lysine. a) Au decorated sensor in air (dry) and with poly-d-lysine, when $V_{CG1} = 0V$ and $V_{CG2} = 2V$. The evaporation time was over an hour. Before and after evaporation values of I_D suggested a uniform layer binding and stability, even after a short period. b) I_D response with poly-d-lysine introduction when $V_{CG1} = 5V$ and $V_{CG2} = 0V$. The Au-coated electrode showed a greater I_D shift. Increase in I_D with poly-d-lysine addition is related to the potential difference between V_{CG1} and V_{CG2} .

Then, 1.25 mM KCl solution was introduced, and measurements were collected. Lastly, poly-d-lysine was introduced in the sensing area. Shifts in I_D were attributed to different charge concentrations in each solution.

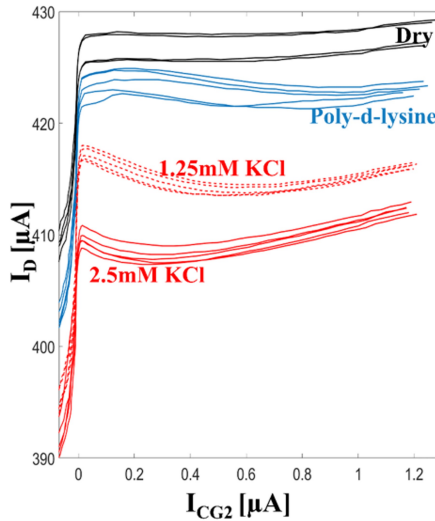


Figure 6.14: I_D shifts due to different liquids on Au-decorated electrode. $V_{CG2} = -2V$ to $2V$ and $V_{CG1} = 5V$. Black = measurements in air, blue = poly-d-lysine, red = KCl with different molarities. The low current from CG_2 (I_{CG2}) might be due to the breakthrough of the native TiO_x layer on the CG_2 electrode.

6.3. DISCUSSION & CONCLUSION

We showed two approaches to functionalize the sensing area for silicon FG-FET and silicon-polymer FG-FET sensors. The first approach used an ionophore cocktail-based membrane to enhance selectivity towards K^+ ions. The second approach altered the surface composition and roughness of the electrodes with gold nanoparticles. Though not shown, both approaches are useable for both kinds of devices, and could also be combined.

Our preliminary results suggested a higher sensitivity to K^+ when there was K^+ ionophore decoration on the sensing electrode. With the AuNPs, due to the surface area increase, we accumulated more charge and enhanced sensitivity.

Both approaches allow CMOS-compatible device fabrication, since the sensing surface functionalization was integrated as a post-processing step.

To evaluate more in depth the influence of the different metal layers such as Au or Ti at an atomic level, it is necessary to analyze the difference between the atomic density of the elements over the same structure (for example, face-centered cubic (FCC)) concerning the interatomic spacing. The adsorption of the analyte can be compared accordingly.

With both sensors, K^+ concentrations were evaluated. As mentioned in this chapter, K^+ are crucial indicators for the well-being of mammalian physiology. For instance, K^+ levels should be 150 mM intracellular and 5 mM extracellular [26]. Therefore, both approaches should be feasible for further studies with neuronal activities. However, biocompatibility tests should be performed prior to cell culture analysis, and parallel to these studies, the action potential of the neurons should be recorded.

In the next chapter, the first steps towards biological application of the to silicon-polymer devices will be introduced.

BIBLIOGRAPHY

- [1] Jinbo Hu, Andreas Stein, and Philippe Bühlmann. “Rational design of all-solid-state ion-selective electrodes and reference electrodes”. In: *TrAC Trends in Analytical Chemistry* 76 (2016), pp. 102–114.
- [2] Samuel O Thier. “Potassium physiology”. In: *The American journal of medicine* 80.4 (1986), pp. 3–7.
- [3] *Hypokalemia*. <https://www.ncbi.nlm.nih.gov/books/NBK482465/>. Accessed: 2023-10-02.
- [4] Quentin R Smith and Stanley I Rapoport. “Cerebrovascular permeability coefficients to sodium, potassium, and chloride”. In: *Journal of neurochemistry* 46.6 (1986), pp. 1732–1742.
- [5] Yujie T Tang et al. “Minimum conditions for the induction of cortical spreading depression in brain slices”. In: *Journal of neurophysiology* 112.10 (2014), pp. 2572–2579.
- [6] Blaine R Roberts et al. “Rubidium and potassium levels are altered in Alzheimer’s disease brain and blood but not in cerebrospinal fluid”. In: *Acta neuropathologica communications* 4.1 (2016), pp. 1–8.
- [7] Michiel LAJ Wieërs et al. “Potassium and the kidney: a reciprocal relationship with clinical relevance”. In: *Pediatric Nephrology* 37.10 (2022), pp. 2245–2254.
- [8] *action potential*. <https://www.moleculardevices.com/applications/patch-clamp-electrophysiology/what-action-potential>. Accessed: 2023-10-02.
- [9] Sanjiv Sharma et al. “An integrated silicon sensor with microfluidic chip for monitoring potassium and pH”. In: *Microfluidics and nanofluidics* 10 (2011), pp. 1119–1125.
- [10] *ionophore*. <https://agscientific.com/blog/ionophores-carriers-and-channels.html>. Accessed: 2023-10-05.
- [11] *valinomyacin*. https://saylordotorg.github.io/text_general-chemistry-principles-patterns-and-applications-v1.0/s25-05-the-s-block-elements-in-biolog.html. Accessed: 2023-10-05.
- [12] Mathieu Odijk et al. “Microfabricated solid-state ion-selective electrode probe for measuring potassium in the living rodent brain: Compatibility with DC-EEG recordings to study spreading depression”. In: *Sensors and Actuators B: Chemical* 207 (2015), pp. 945–953.
- [13] Christian F Chamberlayne and Richard N Zare. “What role does the electric double layer play in redox reactions at planar electrostatically charged insulating surfaces?” In: *Topics in Catalysis* 65.1-4 (2022), pp. 228–233.

- [14] Philippe Bühlmann and Li D Chen. “Ion-selective electrodes with ionophore-doped sensing membranes”. In: *Supramolecular Chemistry: From Molecules to Nanomaterials* 5 (2012), p. 2539.
- [15] S Nakamoto et al. “A lift-off method for patterning enzyme-immobilized membranes in multi-biosensors”. In: *Sensors and Actuators* 13.2 (1988), pp. 165–172.
- [16] C Day et al. “Impedance-based sensor for potassium ions”. In: *Analytica Chimica Acta* 1034 (2018), pp. 39–45.
- [17] Sergio Martinoia et al. “Development of ISFET array-based microsystems for bioelectrochemical measurements of cell populations”. In: *Biosensors and Bioelectronics* 16.9-12 (2001), pp. 1043–1050.
- [18] Peng Lin et al. “The application of organic electrochemical transistors in cell-based biosensors”. In: *Advanced Materials* 22.33 (2010), pp. 3655–3660.
- [19] Min-Ho Park et al. “Mechanism of label-free DNA detection using the floating electrode on pentacene thin film transistor”. In: *The Journal of Physical Chemistry C* 120.9 (2016), pp. 4854–4859.
- [20] Kalyan Kumar Mistry et al. “A review on amperometric-type immunosensors based on screen-printed electrodes”. In: *Analyst* 139.10 (2014), pp. 2289–2311.
- [21] Anil Koklu, Ahmet C Sabuncu, and Ali Beskok. “Rough gold electrodes for decreasing impedance at the electrolyte/electrode interface”. In: *Electrochimica acta* 205 (2016), pp. 215–225.
- [22] Andreas Schmidt-Ott. *Spark Ablation: Building Blocks for Nanotechnology*. CRC Press, 2019.
- [23] Hendrik Heinz et al. “Polarization at metal–biomolecular interfaces in solution”. In: *Journal of the Royal Society Interface* 8.55 (2011), pp. 220–232.
- [24] Baozhen Chen, Archana Parashar, and Santosh Pandey. “Folded floating-gate CMOS biosensor for the detection of charged biochemical molecules”. In: *IEEE Sensors Journal* 11.11 (2011), pp. 2906–2910.
- [25] Pierre Rocheteau et al. “Sepsis induces long-term metabolic and mitochondrial muscle stem cell dysfunction amenable by mesenchymal stem cell therapy”. In: *Nature communications* 6.1 (2015), p. 10145.
- [26] Gerson Florence, Tiago Pereira, and Jürgen Kurths. “Extracellular potassium dynamics in the hyperexcitable state of the neuronal ictal activity”. In: *Communications in Nonlinear Science and Numerical Simulation* 17.12 (2012), pp. 4700–4706.

7

MICROELECTRODES FOR MONITORING ELECTRICALLY-ACTIVE CELLS

7.1. HIPSC-DERIVED CORTICAL NEURONS IN SILICON-POLYMER FG-FET DEVICE

In this chapter, we show how to configure our silicon-polymer hybrid FG-FETs to house Human-Induced Pluripotent Stem Cells (hiPSC)-derived cortical neuron culture to monitor the electrogenic activity. We implemented two methods: 1) Use of FG-FET extensions as passive microelectrodes to use our chip as an MEA device, in addition to the already described charge sensing, in combination with a commercially-available MEA read-out setup. 2) Configure of FG-FETs as active sensors with mobile measurement setup to monitor the changes in I_D in real-time.

7.1.1. INTRODUCTION TO HIPSCS

Human-induced pluripotent Stem Cells (hiPSCs) are crucial for the development of personalized medicine and for the OoC field. hiPSCs are usually generated from somatic cells obtained from a patient and, using gene transfer [1], reprogrammed and can be differentiated to generate most cell lineages, including neural, muscle, blood, and bone, to name a few examples (Fig. 7.1). Therefore, in theory, cells extracted from patients can be used to study patient-specific mutations in relation to diseases and hold promise for the successful development of personalized medicine treatments, thereby including OoCs. To cite examples from the literature, Magdy et al. showed that hiPSC-derived cardiomyocytes can retain patient-specific genetic make up and are therefore relevant for patient-specific cardiotoxicity screenings [2]. Similarly, Pal et al. investigated how hiPSC-derived bone marrow can be used for the treatment of leukemia [3]. Palasantzas et al. described how intestinal hiPSCs-derived organoids and OoC models could be used to recreate patient-specific microbiomes [4]. For the brain, hiPSCs derived from patients have been successfully cultured and differentiated into various neuronal cultures exhibiting diseased phenotypes that can be used to model certain neurological disorders [5]. These brain-like models will be addressed and further discussed in the next section.

7.1.2. UTILIZATION OF SILICON-POLYMER FG-FETs AS RECORDING ELECTRODES

The chips that were used as MEA can be seen in Fig. 5.12. The custom-designed PCBs, which were also introduced in Fig. 5.12, were compatible with commercially-available MEA read-out systems. In other words, the packaging made the chips compliant with existing laboratory infrastructure and directly usable for action-potential recordings of electrically-active cells without requiring additional technical knowledge background by the end-user. Including an opening at the center of the PCB allows end-users to have optical access to the cell culture on the transparent PDMS membrane. In addition, as explained in Chapter 5, a custom-made, compact, and mobile electronic readout analyzer was developed to enhance the portability of the OoC device, to be able to use FG-FET sensors and also the MEAs continuously in relevant environments, e.g., incubators at 37°C and 5% CO_2 .

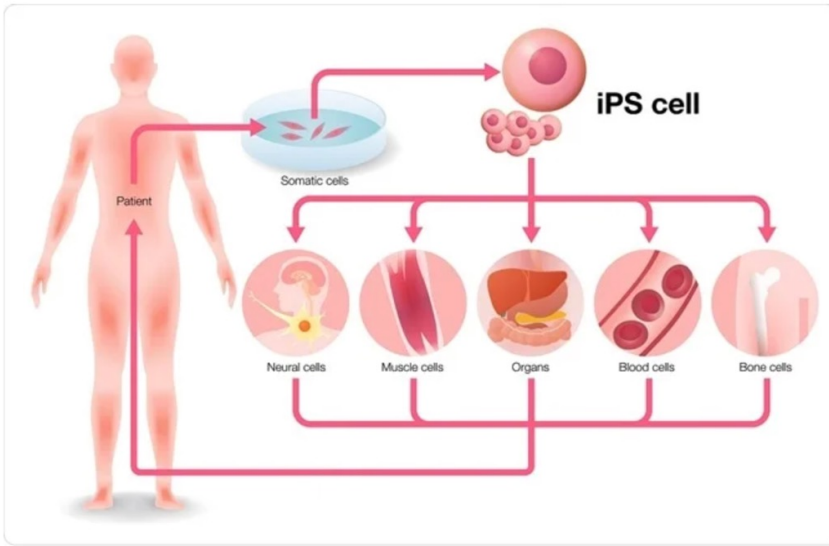


Figure 7.1: Generation of hiPSC cell lines. Somatic cells are taken from a patient, reprogrammed into inducible pluripotent stem cells (iPSC) and differentiated into different cell lineages, paving the way for personalized medicine treatments. Adapted from [6].

7.2. BIOCOMPATIBILITY TESTS WITH SILICON-POLYMER FG-FETS

Before electrophysiological recording of action potentials by the MEA, the biocompatibility of the chip was tested by Dr. J.P. Frimat and Michel Hu, in the Department of Human Genetics, Leids Universitair Medisch Centrum (LUMC). Progenitor cells (NPCs) were differentiated for seven days and matured for two weeks on the chip before the cells were fixed and stained for neuronal markers.

Staining showed mature neuron marker (*/33 tubulin/* green) and the production of synaptic vesicles (synaptophysin in red). The successful maturation of the hiPSC-derived cortical neurons demonstrated the biocompatibility of the chips for live measurements (Fig. 7.2). The cell culturing protocol and the immunohistochemistry protocols are described in more detail in Appendix F [7].

7.3. MULTI-ELECTRODE ARRAY-COMPATIBLE RECORDINGS

The MEA2100 system (Fig. 7.3, Multi Channel Systems, Reutlingen, Germany) was used to record the electrophysiological activity of the on-chip neurons with the heating stage set at 37°C.

We recorded electrophysiological signals of hiPSC-derived cortical neurons (Fig. 7.4 a). This system is commercially available and commonly used for electrophysiology measurements in laboratories. Several recordings of 1 min duration at 10 kHz sampling rate were taken at 21 days *in vitro* (DIV) (i.e., after 7 days of differentiation and 14 days of

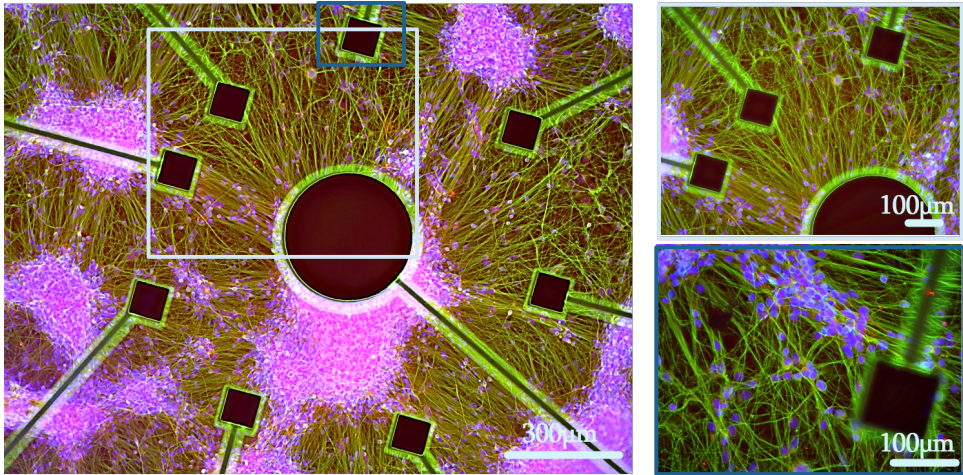


Figure 7.2: Biocompatibility tests on-chip after differentiation and maturation of the hiPSC-derived neurons. Staining of the cell culture showed mature neuronal markers (Beta 3 tubulin-positive: green), synaptic vesicles (red), and cell nucleus (blue), and that the chip was biocompatible with neuronal cultures for at least 3 weeks.



Figure 7.3: Commercially available MultiChannel Systems MEA recording setup. [8].

maturation). The data was collected with a Butterworth High-Pass filter with a cutoff frequency of 200 Hz.

Raw recording files (.msrd) were obtained from the MEA2100 system and were converted into HDF5 files using MCS software. We used MEA-ToolBox [9] to analyze the MEA data in MATLAB 2018b (Mathworks, Massachusetts, USA). MEA-ToolBox was set at a threshold of 5· RMS (root mean square) of the baseline noise for spike detection. From the post-processing of the recorded signal, the average firing rate was 0.97 Hz. To test the response of the FG, which was employed as a passive recording electrode, Picrotoxin was added to the cell culture to induce an epileptic-like condition in the cell culture and to determine whether the chip could measure changes in the electrophysiological signal of the neurons. We introduced the Picrotoxin ($50\mu M$) 20 seconds after the recordings were started, as shown in Fig. 7.4 b (blue line). The fire rate increased on average ($N = 3$) from 0.31 ± 0.1 Hz to 1.38 ± 0.25 Hz after Picrotoxin was added (Fig. 7.4 c).

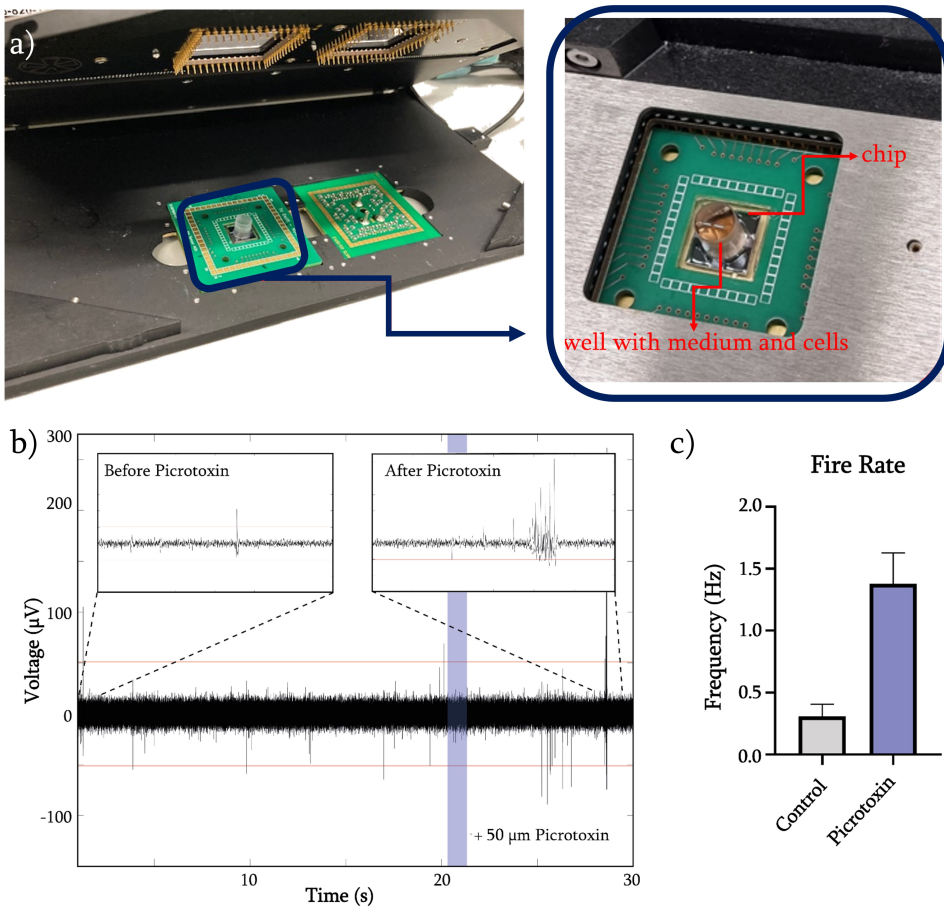


Figure 7.4: a) Compatibility with MultiChannel Systems MEA recording setup of the packaging of the chip. The inset shows the chip and the well with medium and cells. b) Single-electrode trace signal from the MEA recordings. c) The addition of Picrotoxin ($50\mu M$) caused an increase in firing rate which was detected by the OoC device.

7.3.1. TOWARDS MEASUREMENTS WITH MOBILE MEASUREMENT DEVICE

As explained in Chapter 5, a mobile measurement setup was designed and employed to bias and read-out from the electrical devices in order to facilitate continuous measurements when the OoC is inside the incubator or placed under an optical microscope. We measured the sensor inside the incubator (Fig. 7.5) as a proof of concept to test how the sensor behaved in a $37^{\circ}C$ incubator environment, supplied with 5% CO_2 and 95% humidity.

From Fig. 7.6 a, we observed the I_D values when cells were cultured and matured on the sensing area. I_D is correlated to the charges at the sensing area. Changes in I_D can be due to the ions present in the solutions and cell medium, changes in CO_2 in the environment, humidity, and the segregated ions from the cells. As we saw from the tests

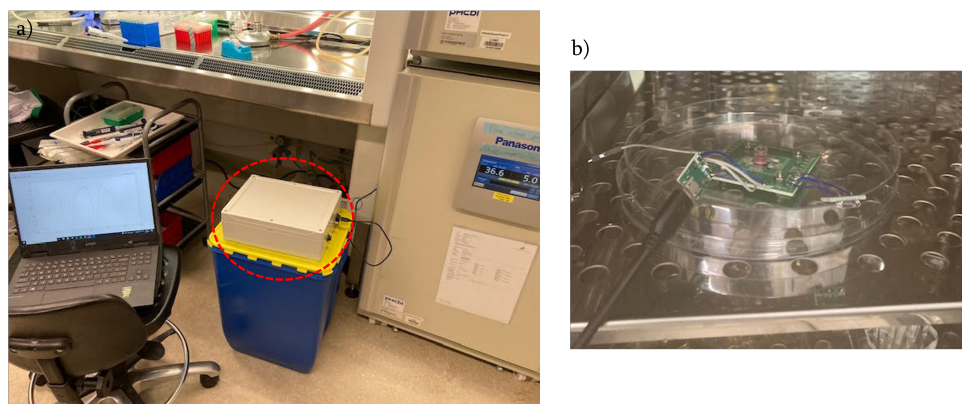


Figure 7.5: Measurement setup: a) The mobile measurement system was connected to the computer via Bluetooth for real-time I_D measurements, b) The chip on PCB and electrical connections inside the incubator. The culture well on the chip can be seen in the center.

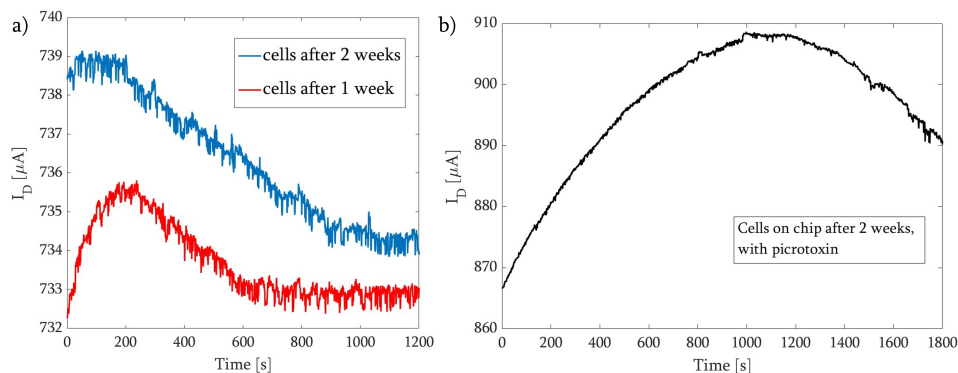


Figure 7.6: a) I_D response of the chip after the cells were cultured at the sensing area after one week (red line) and two weeks (blue line). Measurements were conducted while the chip was inside the incubator. The I_D values show a slight change (approximately $2\mu\text{A}$) after the signals reached the steady-state (After 900 s), supporting the consistency of the measurements via the measurement setup and the sensor. b) Introduction of Picrotoxin to two-week-old cells.

with pH buffer liquid measurements (Section 5.10), with this chip surface and the applied CG_2 voltage, I_D tends to decrease with higher pH. Measurements after one week and two weeks showed only a slight change in the output current, showing consistency in the measurements. We also observed fluctuations such as peaks that resembled action potential events that are usually reported with voltage potential values. However, the sampling time of the mobile measurement setup was 1 s. Hence, the action potential events could not be captured fully.

After the long measurement periods, cells were still viable, and Fig. 7.6 b shows an increase of I_D when Picrotoxin was introduced to this 2-week-old cell culture.

We also observed a change in the amplitude of the peaks of the signal after introducing

Picrotoxin (the figure can be seen in the Appendix F.1). However, as a preliminary study, it was difficult to extract relevant information and directly correlate the change in the amplitude of the peaks to ionic fluctuation from the cells.

On another chip and another FG-FET (nMOS 5), cells were cultured and measured with the mobile measurement setup also after two weeks. The I_D was monitored in real-time, and Picrotoxin was introduced at the cell culturing area while the measurements were ongoing. We observed that Picrotoxin increased the overall I_D , but also caused more fluctuations in the signal (Fig. 7.7). The overall increase in I_D was also observed with the previous measurement with nMOS 7 (Fig. 7.6).

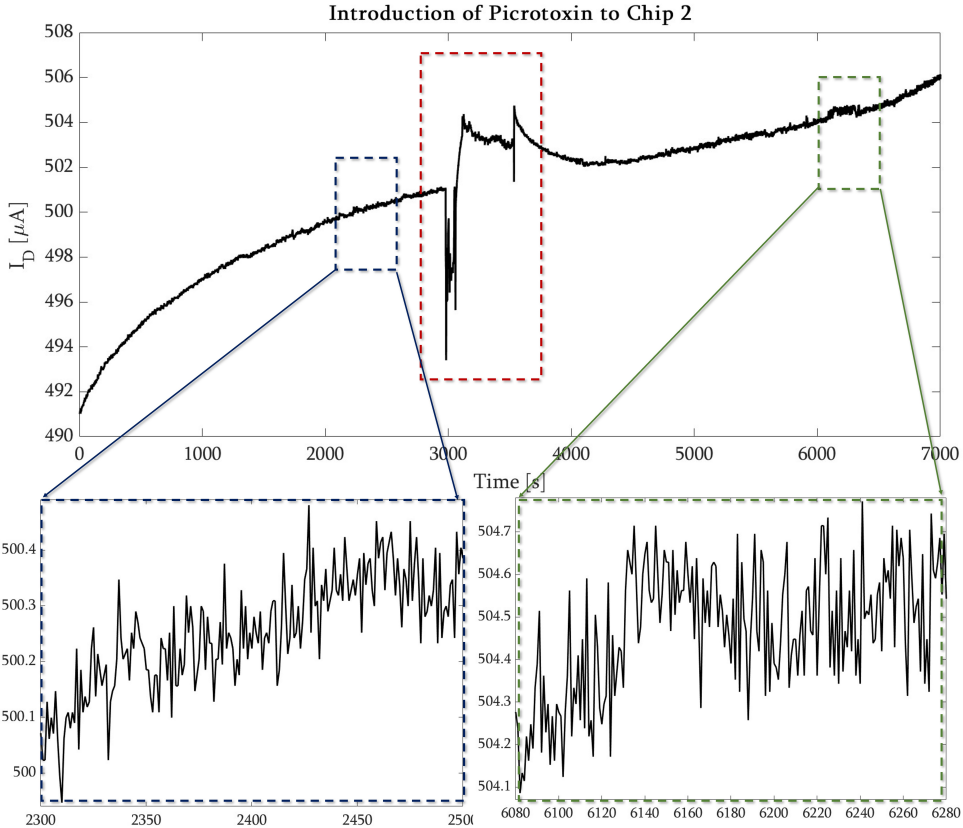


Figure 7.7: Real-time I_D measurement of FG-FET by mobile measurement device with 2-week matured neuronal cell culture at the sensing area. The addition of Picrotoxin is visible (red square) on the electrical measurement. Insets show the change in fluctuations before and after the Picrotoxin addition.

As a third test, we again showed the change in I_D values with another sensor (nMOS 8). Again, Picrotoxin increased the I_D on 2-week matured neuronal cell culture (Fig. 7.8).

The behaviour of the cells monitored with the mobile measurement setup showed a consistent increase of I_D with the addition of Picrotoxin to the sensing area over a 2-week

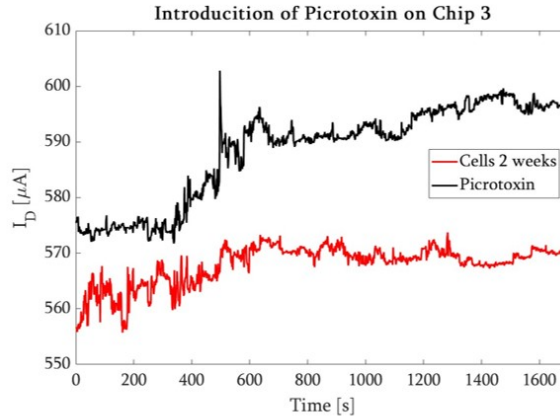


Figure 7.8: Change in I_D values before and after introduction of Picrotoxin with another device (nMOS 8). The mobile measurement setup was used to record I_D in real-time while the device was placed in the incubator.

matured neuronal cell cultures on 3 different sensors. This behaviour might be due to the depolarization of cells associated with local field potential since the downward shift of the potential signal in 1-second periods, rather than the millisecond range, was reported before [10]. Here, our recordings tracked the I_D of the sensor, which alters with charges in close proximity to the sensing area. A flow of ions traversing through the cell membrane creates transmembrane ion currents. Transmembrane currents are the sum of all the currents which determine the membrane potential [11]. Hence changes in I_D should correlate with changes in local field potential.

7.4. DISCUSSION

The activity of neuronal networks can be recorded at different frequencies, depending on the information to be examined. For the pH sensor, a sampling rate of 1 Hz was chosen. Although action potential events usually occur at higher frequencies, as shown above, the same setup without modifications can also be used for electrophysiology, e.g., for analyzing local field potentials.

Depending on the frequency range of the recording, the noise due to the electrode-analyte interface arises, and it is related to the electrode impedance. At low frequencies (< 300 Hz) and for local field potentials, an electrode's larger size is desired to record as many neurons as possible. Additionally, the noise is directly related to the frequency of the recording (1/f noise), and larger electrodes are more favorable to decrease it [12]. Since the electrodes employed for this study are relatively large compared to typical cell size (up to $100\mu m$), they might be good candidates for local-field-potential recordings. The thermal noise, another important noise source for neuronal recordings that can be coupled to the extracellular action potential recordings, is observed more at higher frequencies (300 Hz - 30000 Hz) [12].

Additionally, the potential differences on CG_2 and FG terminals can enhance the local

electric field and could be used to examine directional neurite growth [13] and perhaps even determine the direction in which axons will grow. Galvanotropism studies have shown that it is possible to guide the growth of axons depending on the field gradient. This could be a more natural approach than using mechanical constraints on brain-on-chip models such as grooves to direct axons to mimic, for example, the spatial organization as seen in the brain cortex [14, 15, 16].

To enhance the measurements, the sampling rate can be increased to have direct correlation between the MEA recordings and I_D values. The I_D values represent how the ionic gradient from the cell membrane is changing. Since the cell membrane can be modeled as a capacitor, the correlation of the ΔI_D and the change in potential due to firing can be determined by Ohm's law.

We used a low number of recording electrodes as proof of concept. However, by virtue of cleanroom processing capabilities, the number of microelectrodes can be increased without compromising the small area of the chip (1 cm^2).

7.5. CONCLUSION

In this chapter, we showed how to use the FG-FET as a passive recording device in a commercially available MEA setup. After biocompatibility tests, we showed a recording of the activity of cortical neurons with the addition of a drug, Picrotoxin. The FG-FET electrode was able to record the difference in the neurons when the drug was introduced. Additionally, we demonstrated preliminary recordings with the FG-FET devices and I_D monitoring with the mobile measurement setup in real-time. We showed that the mobile measurement setup is a good candidate for cell culturing measurements when the culture is inside the incubator, only the sampling rate should be adjusted for direct relation to potential recordings from firing of the neurons. We also recorded the change in I_D when Picrotoxin was introduced, on 3 different devices by employing the mobile measurement setup and FG-FETs, showing the repeatability of different devices.

We showed these preliminary results with cortical neurons. In the future, pH sensing can be combined with the electrical activity recordings within the same multi-modal OoC sensing device, leading the way for understanding various disease mechanisms, as described in Chapters 1 and 2.

BIBLIOGRAPHY

- [1] Eun-Ah Chang et al. “Human induced pluripotent stem cells: Clinical significance and applications in neurologic diseases”. In: *Journal of Korean Neurosurgical Society* 62.5 (2019), pp. 493–501.
- [2] Tarek Magdy et al. “Human induced pluripotent stem cell (hiPSC)-derived cells to assess drug cardiotoxicity: opportunities and problems”. In: *Annual review of pharmacology and toxicology* 58 (2018), pp. 83–103.
- [3] Deepali Pal et al. “hiPSC-derived bone marrow milieu identifies a clinically actionable driver of niche-mediated treatment resistance in leukemia”. In: *Cell Reports Medicine* 3.8 (2022).
- [4] Victoria EJM Palasantzas et al. “iPSC-derived organ-on-a-chip models for personalized human genetics and pharmacogenomics studies”. In: *Trends in Genetics* 39.4 (2023), pp. 268–284.
- [5] Kaveena Autar et al. “A functional hiPSC-cortical neuron differentiation and maturation model and its application to neurological disorders”. In: *Stem Cell Reports* 17.1 (2022), pp. 96–109.
- [6] News Medical Life Sciences. *Induced Pluripotent Stem (iPS) Cells in Medicine and Research*. <https://www.news-medical.net/life-sciences/Induced-Pluripotent-Stem-Cells-in-Medicine-and-Research.aspx> [Accessed: 26/10/23]. 2023.
- [7] Ronald AM Buijsen et al. “Generation of 3 spinocerebellar ataxia type 1 (SCA1) patient-derived induced pluripotent stem cell lines LUMCi002-A, B, and C and 2 unaffected sibling control induced pluripotent stem cell lines LUMCi003-A and B”. In: *Stem Cell Research* 29 (2018), pp. 125–128.
- [8] Multichannel Systems. *MEA2100*. <https://www.multichannelsystems.com/products/mea2100-systems> [Accessed: 26/3/24]. 2024.
- [9] Michel Hu et al. “MEA-ToolBox: an Open Source Toolbox for Standardized Analysis of Multi-Electrode Array Data”. In: *Neuroinformatics* (2022), pp. 1–16.
- [10] Bjørg Elisabeth Kilavik et al. “Evoked potentials in motor cortical local field potentials reflect task timing and behavioral performance”. In: *Journal of neurophysiology* 104.5 (2010), pp. 2338–2351.
- [11] David A McCormick. “Membrane potential and action potential”. In: *From molecules to networks*. Elsevier, 2014, pp. 351–376.
- [12] Marie Engelene J Obien et al. “Revealing neuronal function through microelectrode array recordings”. In: *Frontiers in neuroscience* 8 (2015), p. 423.

- [13] Ronald Deumens et al. "Alignment of glial cells stimulates directional neurite growth of CNS neurons in vitro". In: *Neuroscience* 125.3 (2004), pp. 591–604.
- [14] Kimberly K Gokoffski et al. "Physiologic electrical fields direct retinal ganglion cell axon growth in vitro". In: *Investigative ophthalmology & visual science* 60.10 (2019), pp. 3659–3668.
- [15] Masayuki Yamashita. "Weak electric fields serve as guidance cues that direct retinal ganglion cell axons in vitro". In: *Biochemistry and biophysics reports* 4 (2015), pp. 83–88.
- [16] Colin D McCaig et al. "Controlling cell behavior electrically: current views and future potential". In: *Physiological reviews* 85 (2005), pp. 943–978.

8

CONCLUSION & PERSPECTIVES

8.1. CONCLUSIONS

In this thesis, the integration into OoC devices of electrochemical real-time sensing based on the working principles of the field-effect transistor was shown. The integrated sensors are based on an FG-FET-based active component and are sensitive to local electric charge. The active device provides inherent amplification, which translates to higher sensitivity and resolution for smaller changes in segregated analytes. The contributions of the thesis are summarized below.

CONTRIBUTION 1: SILICON-BASED ELECTROCHEMICAL pH SENSOR FOR OoCs

We integrated an electrochemical charge sensor into a compact OoC device. The sensor was based on an FG-FET that was capacitively coupled to two control-gates to determine the working point of the transistor. The sensing area (FG extension) was separated from the active FET area. The use of a silicon-based active sensor as part of an OoC device eliminated the need for a bulky external reference electrode and 3-electrode measurement setups. We demonstrated the device can sense the pH of different liquids.

To understand the working mechanism of the sensor, we developed a numerical model that included the description of FG-FETs with two CGs. We investigated how the dimensions of the FET, sensing area, and the material at the sensing area can alter the sensitivity.

CONTRIBUTION 2: INVESTIGATION OF ALTERNATIVE MO_x SENSING LAYERS

We designed and fabricated silicon-based FG-FETs with TiO_x , HfO_x , and AlO_x as pH-sensitive layers over the sensing electrodes. We explored and electrically characterized the layers with pH4, pH7, and pH9 solutions. The comparison revealed that HfO_x enables greater sensitivity around pH7, and AlO_x around pH4. TiO_x showed rather uniform sensitivity for the whole pH range tested (pH 4 to 9).

In addition, devices functionalized with a thin layer (21 nm) of HfO_x were more sensitive to pH4-pH9 than with a thick layer (120 nm); and thin HfO_x -functionalized devices resulted in higher sensitivity than those with AlO_x of the same thickness.

CONTRIBUTION 3: SILICON-POLYMER FG-FET CHARGE SENSOR FOR OoCs

We showed the integration of transparent polymer membranes embedded with FG-FET extension electrodes in the sensing area of the OoC devices. By implementing the silicon-polymer hybrid OoC devices, we combined the superior electrical characteristics of a conventional semiconductor (silicon) compared to transparent organic counterparts and the transparency and biocompatibility of polymers (PDMS) into a single OoC device. This combination is especially crucial to visually inspect the well-being of the cell cultures.

To enable the portability of OoC-based sensing without the need for bulky and expensive laboratory equipment, we developed a mobile measurement setup with a wireless connection to continuously track the changes in transistor characteristics in real-time in environments such as incubators in cell biology laboratories.

CONTRIBUTION 4: POST-PROCESS FUNCTIONALIZATION OF FG-FET SENSING ELECTRODES

In addition to metal oxide functionalization, we investigated the functionalization of the sensing surface for both the silicon- and silicon-polymer-based devices using post-processing techniques. We investigated K^+ selectivity for the silicon-based device by introducing a K^+ -selective polymer membrane at the sensing area. We compared the results recorded with and without the functional surface with the same concentration of KCl solutions, and showed the higher sensitivity introduced by the membrane. For the silicon-polymer device, we introduced films of Au nanoparticles as a post-processing step to increase the surface area of the sensing electrode. We showed that the polymer membrane survives the impact of Au nanofilm formation. We introduced poly-d-lysine and KCl to the sensing area and monitored the changes in I_D , thereby evidencing higher sensitivity with Au-decorated electrodes.

CONTRIBUTION 5: FG-FET EXTENSIONS AS RECORDING ELECTRODES FOR CORTICAL NEURONS

FG-FET extensions were used as passive microelectrode array electrodes to record electrical activity of hiPSC-derived cortical neurons. We designed a PCB to package the chip and to be compatible with commercially-available and frequently-used MEA setups in cell biology laboratories. The recordings showed the effect of the introduction of Picrotoxin, an epilepsy-inducing drug. We also demonstrated preliminary experiments with FG-FETs and the mobile measurement setup when the cells were cultured in the OoC device under incubator conditions. The introduction of Picrotoxin increased the overall I_D values, as well as the fluctuations of the I_D signal.

8.2. RECOMMENDATIONS AND FUTURE WORK

8.2.1. MULTIMODAL SENSING

As a preliminary result, we showed the charge sensing working principle of our devices with different pH liquids, in addition to preliminary action-potential recordings of neurons with MEA setup.

However, as it was stated in Chapter 2 of this thesis, monitoring the change in pH while tracking the firing events from electrically-active cells can be beneficial to discover new disease mechanisms. Multimodal sensing can correlate more than one parameter (for example, a decrease in pH and firing rates), and could be achieved by the further development of the recording devices developed in this thesis. A differential measurement strategy can be beneficial. For instance, a device can be used to sense liquids with different pH values, and this set of values can be used as the calibration data set. Further, the device can be used with cell culture, and the shifts in I_D can be correlated to the pH of the medium. These tests can be performed with the mobile measurement setup and, on the same chip, one electrode can be used at the same time with MEA recording setup to record the electrical activity from the electrically-active cells.

8.2.2. INTEGRATION OF FG-FET CHIPS IN THE TOP

As introduced in Chapter 1, OoC platforms are convenient ways of connecting several relevant sensors and tissue chips in a convenient structure. In this way, it is possible to examine organ-organ relations, and in the future, to host a complete multi-organ-on-chip system which can better mimic human physiology.

In addition, even though the OoC field is rapidly evolving, it is difficult to standardize the chips to make them useful for more than one laboratory or test. It is convenient to have a microfluidic board with standard size for sensor or culture modules, that can house several components together. Additionally, batch production of the chips can be beneficial for having a standard and improve reliability and reproducibility.

Fluidic circuit boards (FCBs) with ISO-standardized interface can connect different chips into a platform [1, 2]. This approach is pursued by the TOP (Translation OoC Platform) from the University of Twente.

To confirm the feasibility of the approach embodied in the TOP, we wanted to integrate our FG-FET pH sensor to the TOP, where a blood-vessel-on-chip module was also present [3]. The benefit of such a platform is that it can house several chips and cultures from different research groups. The open-platform structure allows researchers to plug their chips into a single microfluidic board, without the hassle of a closed read-out equipment, as in the case of several commercially-available OoC read-out setups.

In order to place our silicon-polymer hybrid chip into the TOP, a PDMS slab with a 1 mm inlet and outlet openings was glued onto the backside of the sensor, after the sensor was already placed onto a PCB and wirebonded (Fig. 8.1). The fluidic circuit board had less than 1 mm diameter fluidic connections for the chip to be placed. Hence, the chip was packaged and integrated to the system as a module. The hydraulic resistance of the microfluidic channel was changing due to the addition on the sensing area volume to the microfluidic circuit.

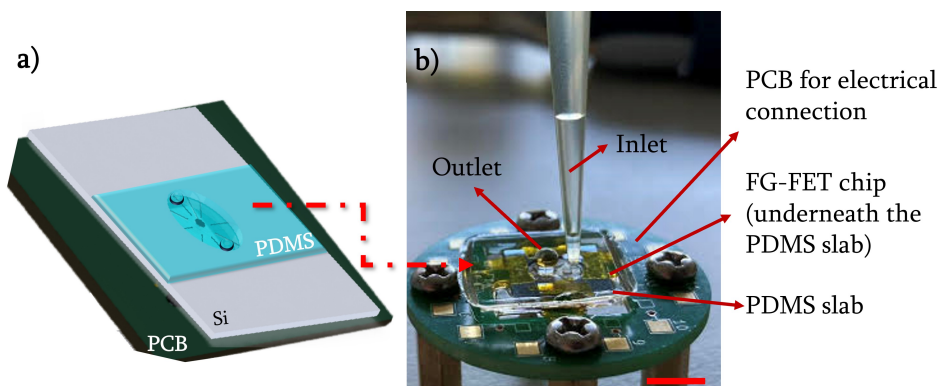


Figure 8.1: Microfluidic packaging of the chip with PDMS slab. a) Schematic of the chip with PCB and PDMS slab. b) The PDMS slab was placed on the backside of the chip where the sensing area was open, with inlet and outlet openings. The system was tested with a micropipette and DI water, and the outlet of the PDMS slab was observed for liquid flow. To prevent damage to the wirebonds, which were on the frontside, four screws were placed onto the PCB to serve as spacers.

The aim was to monitor real-time pH changes in the cell metabolism. Fig. 8.2a shows

the schematic of the open platform with pH sensor and a blood-vessel chip. There are also spaces for other modules on the fluidic board. Fig. 8.2b shows the connection of microfluidics with silicon-PDMS device, and leak-free flow, demonstrating the successful connection of the FG-FET sensor to TOP. Fig. 8.2c shows initial measurements with a silicon-PDMS device and how the output current increased with the cell medium in real-time. The I_D values were $250\mu A$ when there was the DI water at the sensing area. When the medium was introduced, we observed a downward spike at 600 s since there was an air bubble in the microchannel when the DI water holder was replaced with the medium from the inlet. When the medium arrived at the sensing area, I_D increased. Open platforms are crucial for standardization and repeatability. They unite chips and

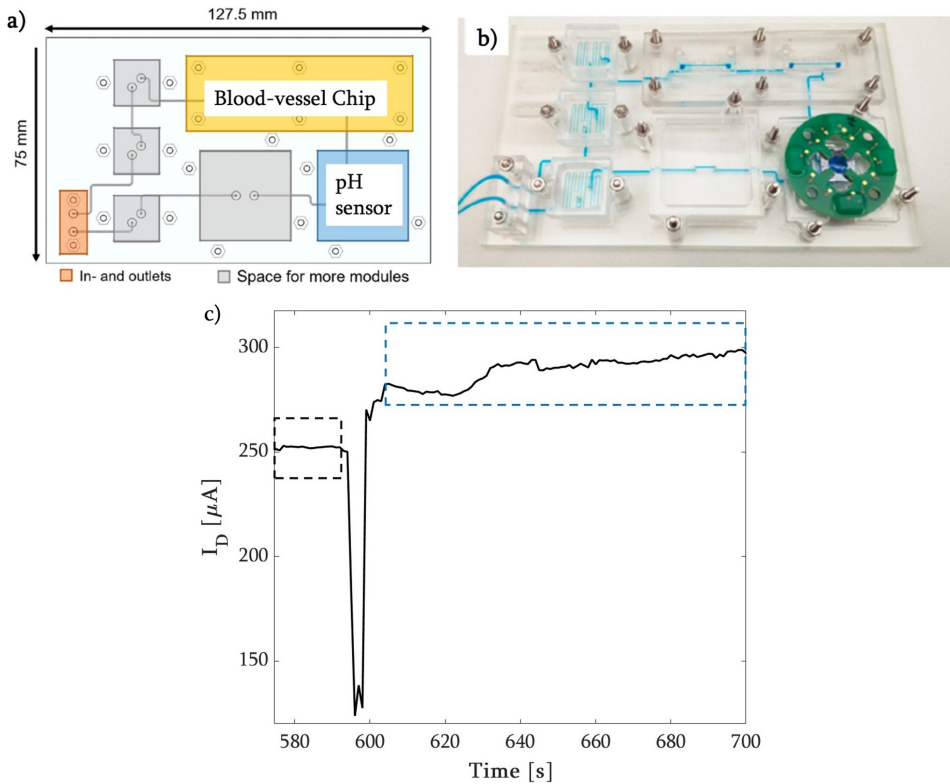


Figure 8.2: Integration of the FG-FET device to TOP. a) The schematic of the platform. b) The flow was shown with blue-dyed DI water when the silicon-PDMS device (Chapter 4) was integrated. c) Functionality of the FG-FET-based module integrated into the TOP. I_D measurement shows the effect of the introduction of the medium by means of the microfluidics.

organ modules at a higher level, including organ-to-organ signaling and different sensors. However, with the PDMS-silicon FG-FETs, the connections were not robust enough for the platform to be tested and measured at the same time. More robust connection approaches must be pursued before integrating additional modules and performing more measurements. Silicon-based FG-FET chips can be a better option to avoid the delicate

PDMS membranes. Wirebonds also create a secondary problem. The bonds should be covered with a material such as parylene to eliminate breakage, and novel packaging methods should be investigated.

8.2.3. GOING TO HIGH FREQUENCIES: USING MICROWAVE RESONATORS FOR MONITORING THE CELL WELLBEING

Until this point, we showed how electrochemical sensors can be beneficial for tracking the condition of the cell cultures. For future studies, we also propose to implement another sensing mechanism based on microwave resonators in OoCs. We acknowledge that integration of ion sensing elements to BBB can be helpful to further investigate disease mechanisms [4]. The monitoring of the formation of the barriers such as BBBs usually depends on TEER, a measurement protocol explained in Chapter 1. Since commercially-available TEER measurement setups such as voltohmmeters implement two electrodes, the electrical field between the electrodes is sometimes not uniform. Even if it is assumed to obtain information about the barrier throughout the microfluidic channel where the cells are cultured, only spatial information can be extracted. The spatial information might lack the characteristics of the whole channel area. Additionally, electrodes need to be placed relatively close to the cell culture to extract impedance information.

PATCH SENSOR

Some microwave sensors employ broadband frequency range. There are complex permittivity sensors with microwave patch electrodes which can extract layer-by-layer information about stacked materials. The systems employ a single-ended patch as the near-field sensing element [5]. Operation up to a few GHz will provide field penetration advantages in order to more accurately extract material characteristics [6, 7]. This is the main reason for using frequencies in the microwave regime. The reason to choose a patch rather than two-terminal capacitors is that the latter confine their electric field to the surface of the material under test. Therefore, they have limited detection depth, which is related to the permittivity characteristics of the material-under-test [5].

The working principle is as follows: When there is a lossy material in contact with the excited patch, the electric field lines that are flowing from the excited patch to the ground plane will be distorted (Fig. 8.3). This distortion depends on the complex permittivity of the material. In principle, the real and imaginary part of permittivity affect the capacitance and conductance, respectively, although a cross-correlation can still exist, depending on the geometry and the element's self-conductance and capacitance [6]. Hence, the lossy capacitance can be modeled with admittance $Y = G + j\omega C$, which is in direct relation to the complex permittivity of the material.

As a preliminary trial, we wanted to test a patch electrode with off-the-shelf components and a PDMS slab and monitor how the PDMS slab changes the signal output parameters of the patch electrode in a broadband frequency measurement. Fig. 8.4a shows the front and back sides of the patch electrode PCB, which was obtained from Dr. Marco Spirito's group (ELCA, TU Delft). Fig. 8.4b shows the measurement setup with a vector network analyzer (VNA). VNAs were used to extract S-parameters, a way to monitor the characteristics of microwave and high-frequency sensors, and extract information such

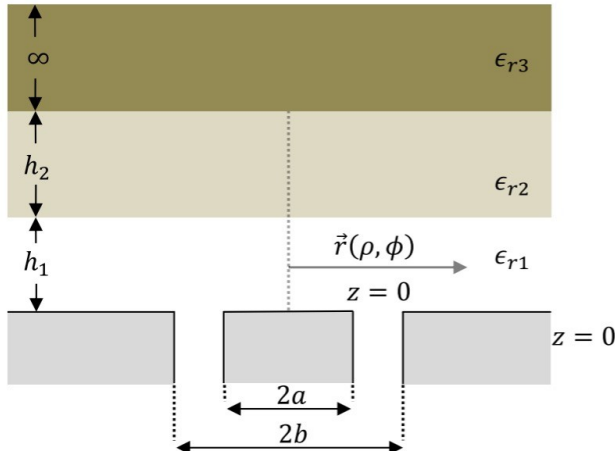


Figure 8.3: Schematic of a coaxial probe as complex permittivity sensor. The probe can be employed to extract the permittivity of layered materials. Adapted from [8].

as impedance and permittivity. Fig. 8.4c shows preliminary measurements in DI water with a patch electrode and $64\mu\text{m}$ -thick film of PDMS cured on top of it, compared to patch electrode only. We recorded a shift in the S11 parameter when there was the PDMS layer on top of the sensor. This is due to different electrical properties (such as the permittivity) of the PDMS layer compared to DI water. This shift shows the sensitivity of the sensor and is promising for future measurements, for instance, with cell layers.

Additionally, a matrix of sensors might be used to obtain local information. For instance, if there is a deformation on the tight junctions of a blood-brain-barrier, we can extract the admittance information of the local change due to the deformation and track it in a more confined manner.

MICROWAVE RESONATOR

Microwave resonators (or sensors) that work at microwave frequencies are excellent candidates for non-intrusive measurement of impedance information of cell layers. They do not require bio-functionalization while maintaining the cell viability and sensitivity of the sensor. Additionally, they do not require close contact with the cell culture, compared to TEER measurement setups.

In general, when there is a change in the permittivity of the media under test, the resonance frequency of the device will also change. This alteration can be tracked by the scattering (S)-parameters of the microwave device. These parameters form the relation between the incident, reflected, and transmitted waves (Fig. 8.5 a). The characteristics of the frequency will alter depending on the permittivity of the media. Research for microwave sensors in biology has been ongoing for the last 2 decades [9, 10, 11, 12, 13] (Fig. 8.5 b).

We mentioned patch electrodes with static cell culturing. Another approach can be implemented to integrate microfluidics and microwave resonant sensors. The main work-

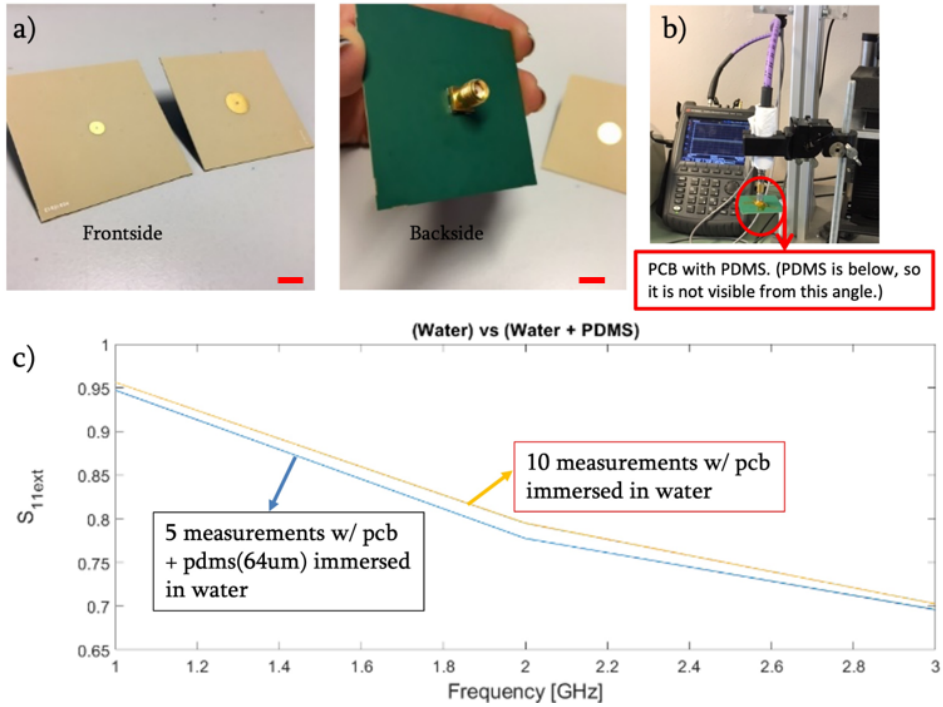


Figure 8.4: Prototype of patch electrode-based microwave sensor. a) Image of patch electrode with PCB from the frontside and backside (Scale bars = 1cm). b) Measurement setup. The PDMS layer is on the backside and it is not visible from this angle. c) Measurements with and without PDMS slab, immersed in DI water, with identical patch electrodes.

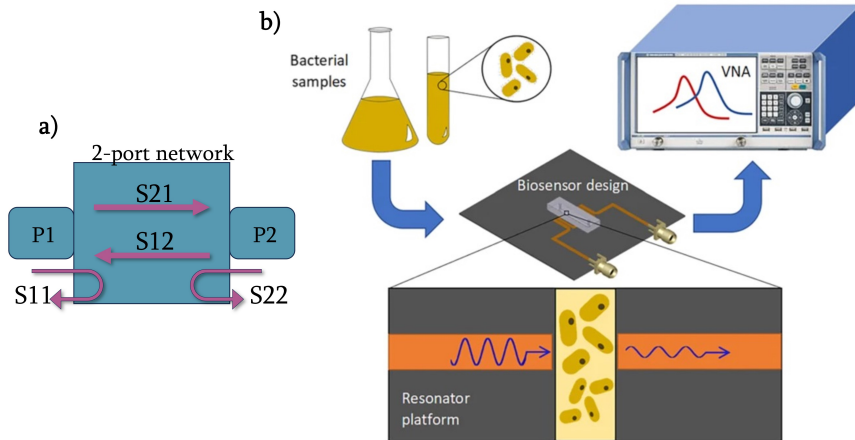


Figure 8.5: a) Schematic of S-parameters in a 2-port network. b) Example of a microwave biosensor. The growth of bacteria samples was analyzed by tracking the change in microwave resonance. Adapted from [14].

ing principle is based on how the change in the electrical permittivity of media (for example, forming of BBB so replacing the medium with cell layer) affects the change in the resonance frequency of the microwave sensor. If we implement this sensing principle to focus only on the resonance frequency, high sensitivity can be achieved due to the peak amplitude value at resonance. Hence, forming the cell layer can be monitored non-intrusively and with high accuracy. However, if researchers are interested in understanding how the frequency response and not only a single resonance changes with the cell layer formation, resonant sensors cannot be implemented.

The sensing principle of microwave resonator-based biosensors can be summarized as follows: First, the resonant frequency can be calculated from the material properties (for instance, before introducing an analyte or cells). Then, when the material changes at the sensing area, it will induce a shift in resonance frequency (as in the case of Fig. 8.5). By monitoring the shift in the resonance frequency, we can observe the change in permittivity and electrical volume of the analytes, which can be a good indicator for cell layer formation. To form the sensing area, we envisioned a chip with two transmission lines coupled with a gap at the center, which will be mentioned as a slit from now on. By encapsulating the sensing area with a PDMS microchannel, we can form a microfluidic device integrated with the microwave resonator (Fig. 8.6).

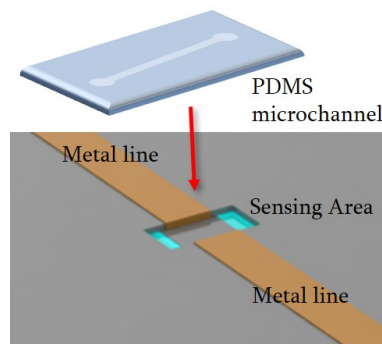


Figure 8.6: Schematic of a split-resonator. Two metal lines (signal lines) have a gap (slit) in between, which can serve as the cell culturing area. Two transparent areas (shown as blue) were left to serve as the visual inspection areas. A PDMS microchannel will be bonded to the top of the microwave sensor, to introduce cells or analytes to the sensing area.

In order to evaluate this approach, we developed a COMSOL model to find eigenfrequencies in electromagnetic domain. We created a microstripline resonator with a slit in the middle to house the cell culture (Fig. 8.7 a). The dimensions of the center sensing area were $300\mu\text{m} \times 300\mu\text{m}$, and the resonator chip had dimensions of $10\text{ mm} \times 5\text{ mm} \times 0.5\text{ mm}$ to keep the volume of cells as low as possible, and when fabricated, obtain more than 50 chips from a 4-inch wafer. In the COMSOL model, we used perfect electric conductor for the metal lines and lumped ports for the input and output of the signal. In order to increase the sensitivity at the sensing area, we included the side walls of the sensing area to the metal lines (Fig. 8.7 b, shown in green). We changed the permittivity of the material at the sensing area ($\Delta\epsilon = 1$) in order to evaluate the change in the resonance frequency, with and without the inclusion of the side walls to the signal lines (Fig.

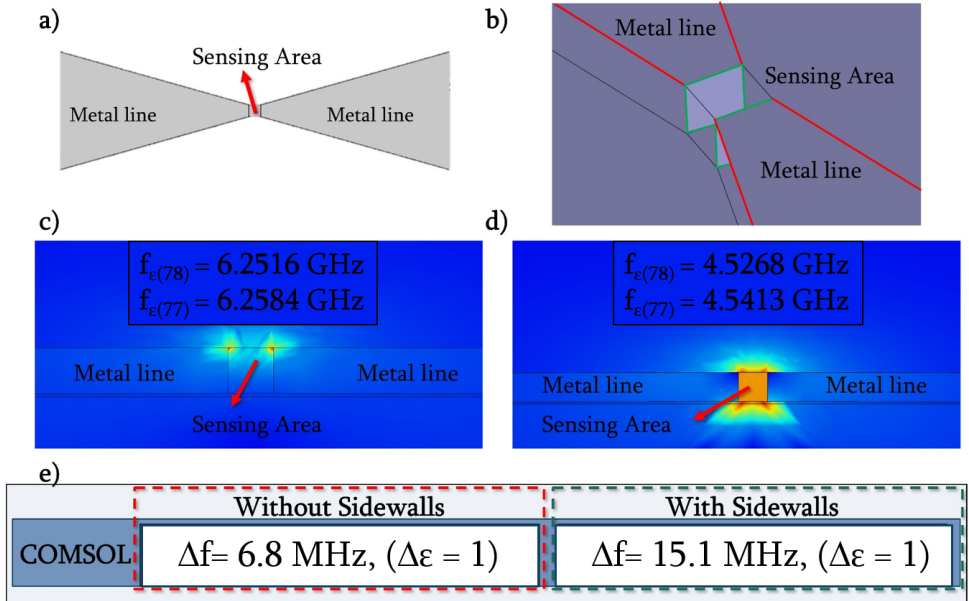


Figure 8.7: Schematic of the top view of the signal lines and the sensing area (the gap between two microstrip lines), used for the COMSOL model. b) The inclusion of side walls as signal lines in the Comsol model, shown in green. c,d) Side view of the solution from the COMSOL model when c) the metal line did not go through the side walls and d) the metal line includes the side walls. The change in resonance frequency for the first case was 6.8 MHz, and for the second case was 15.1 MHz, when the sensing area material was changed ($\Delta\epsilon = 1$).

8.7 c, d). When the side walls were included in the analysis, we observed an increase in the frequency shift (hence the sensitivity).

This model can be considered as a strip-line resonator with the gap in between as a series capacitor. The perturbation method shows how the change in dielectric permittivity changes the resonant frequency [15].

For fabricating the chips, the gap should be etched with DRIE and metallization should be performed by sputtering. To perform lithography and form side wall metallization, spray coating can be used for patterning due to the high aspect ratio of the device.

Here, we wanted to implement the gap coupling to the microstrip line resonator to form a sensing area for cell culturing or analyte sensing. By creating the slit coupling, we envisioned an easier fabrication method rather than having a sensing area in between two metal lines (as in the case of general microstrip lines). When a microstripline is employed, the material-under-test should be in between two conductive plates, therefore a bonding methodology should be investigated. With a slit-coupled device, only etching and metallization steps are needed. To increase the sensitivity, we proposed to include the metallization on the side walls of the sensing area.

BIBLIOGRAPHY

- [1] Stefan Dekker et al. “From chip-in-a-lab to lab-on-a-chip: A portable Coulter counter using a modular platform”. In: *Microsystems & nanoengineering* 4.1 (2018), p. 34.
- [2] Anke R Vollertsen et al. “Facilitating implementation of organs-on-chips by open platform technology”. In: *Biomicrofluidics* 15.5 (2021), p. 051301.
- [3] Anke Ricarda Vollertsen et al. “Connecting labs for higher level organ-on-chip systems: integration of a pH sensor and a blood vessel-on-chip on a standardized platform”. In: *EUROoCS Annual Meeting 2022*. 2022.
- [4] Monica Mir et al. “Biosensors integration in blood–brain barrier-on-a-chip: Emerging platform for monitoring neurodegenerative diseases”. In: *ACS sensors* 7.5 (2022), pp. 1237–1247.
- [5] Gerasimos Vlachogiannakis et al. “A 40-nm CMOS permittivity sensor for chemical/biological material characterization at RF/microwave frequencies”. In: *2016 IEEE MTT-S International Microwave Symposium (IMS)*. IEEE. 2016, pp. 1–4.
- [6] G Vlachogiannakis et al. “A compact energy efficient CMOS permittivity sensor based on multiharmonic downconversion and tunable impedance bridge”. In: *2018 IEEE International Microwave Biomedical Conference (IMBioC)*. IEEE. 2018, pp. 1–3.
- [7] Gerasimos Vlachogiannakis et al. “A 40-nm CMOS complex permittivity sensing pixel for material characterization at microwave frequencies”. In: *IEEE Transactions on Microwave Theory and Techniques* 66.3 (2017), pp. 1619–1634.
- [8] Harshitha Thippur Shivamurthy et al. “Complex permittivity extraction of layered biological samples”. In: *2018 IEEE/MTT-S International Microwave Symposium-IMS*. IEEE. 2018, pp. 1573–1576.
- [9] T Chen et al. “Microwave biosensor dedicated to the dielectric spectroscopy of a single alive biological cell in its culture medium”. In: *2013 IEEE MTT-S International Microwave Symposium Digest (MTT)*. IEEE. 2013, pp. 1–4.
- [10] Hee-Jo Lee and Jong-Gwan Yook. “Biosensing using split-ring resonators at microwave regime”. In: *Applied Physics Letters* 92.25 (2008), p. 254103.
- [11] Mohammad Hossein Zarifi et al. “Noncontact and nonintrusive microwave-microfluidic flow sensor for energy and biomedical engineering”. In: *Scientific reports* 8.1 (2018), pp. 1–10.
- [12] Jonathan Leroy et al. “Microfluidic biosensors for microwave dielectric spectroscopy”. In: *Sensors and Actuators A: Physical* 229 (2015), pp. 172–181.
- [13] Claire Dalmay et al. “Ultra sensitive biosensor based on impedance spectroscopy at microwave frequencies for cell scale analysis”. In: *Sensors and Actuators A: Physical* 162.2 (2010), pp. 189–197.

-
- [14] Rakesh Narang et al. "Sensitive, real-time and non-intrusive detection of concentration and growth of pathogenic bacteria using microfluidic-microwave ring resonator biosensor". In: *Scientific reports* 8.1 (2018), p. 15807.
 - [15] David M Pozar. *Microwave engineering*. John wiley & sons, 2011.

APPENDIX

A

CIRCUIT ANALYSIS OF THE DEVICE

Falstad, open circuit modeling software was used to model the FET device at the circuit level. Fig. A.1a shows the building blocks of the circuit, the change in I_D due to charges at the sensing area, modeled as changing the capacitor value. When the capacitor at the sensing area increased, I_D decreased, matching with the results from the previous sections.

Fig. A.1b shows real-time I_D response. When V_{CG2} was smaller than V_{CG1} , the I_D showed the characteristics of a charging current (as mentioned in Section 5.10).

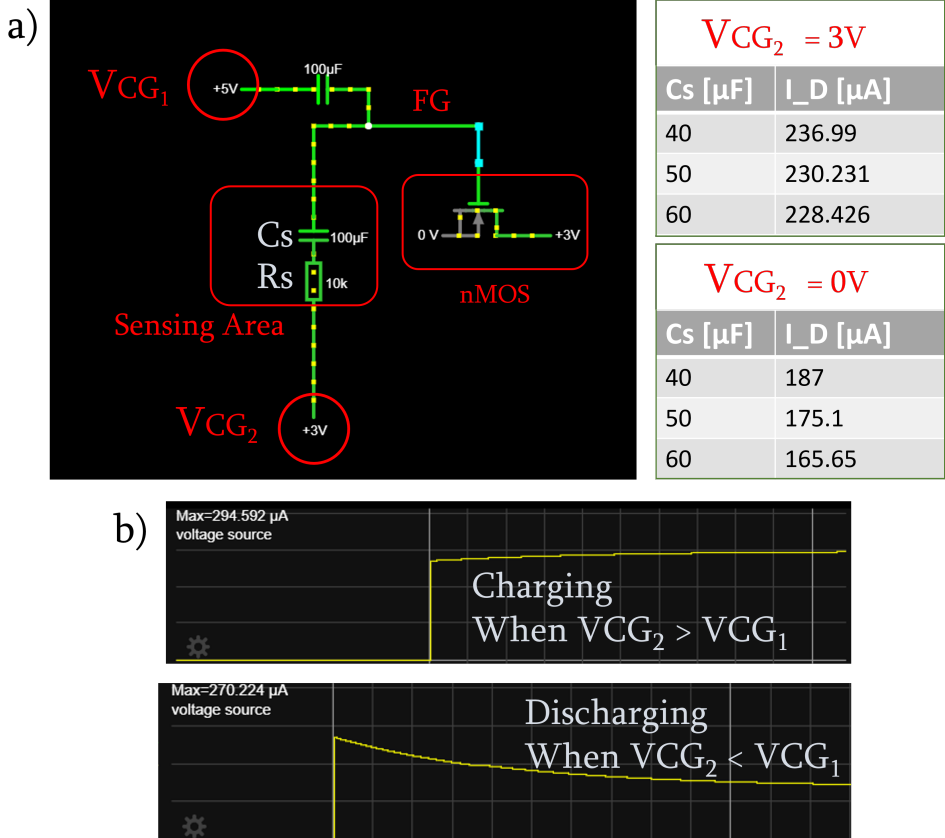


Figure A.1: Analysis of the FET circuit. a) Schematic of the circuit. V_{CG_1} and V_{CG_2} , sensing area and the FET are shown. The MOSFET is capacitively coupled to CG_1 and the sensing area. The sensing area is shown with a resistor and capacitor components in series. When the charge increases at the sensing area, C_S increases and I_D decreases since the coupling of the sensing area and V_{CG_1} modulates the V_{FG} . b) When $V_{CG_2} > V_{CG_1}$, the behavior of the I_D in time resembles charging and discharging for the opposite convention.

B

MATLAB MODEL OF THE FET DEVICE

```
%Sensor dimensions:
t_CF = 53E-9; %Control gate capacitor dielectric
    thickness
t_metal = 600E-9; %Floating gate Al thickness
t_ox_undoped = 105E-9; %Oxide thickness over undoped
    areas
t_ox_doped = 210E-9; %Oxide thickness over NW, SN and SP
    doped areas

eps_0 = 8.85418782E-12; %Vacuum permittivity
eps_ox = 3.8*eps_0; %Oxide permittivity
eps_tio = 21*eps_0; %tio2 permittivity, cited from an
    article
eps_CF = 5*eps_0; %Control gate capacitor dielectric
    permittivity
eps_w = 78*eps_0;

A_CF = (490E-6)^2; %Control gate capacitor mutual area
P_CF = 4*sqrt(A_CF); %Control gate capacitor perimeter

%Capacitances:
C_CF = A_CF*eps_CF/t_CF + pi*eps_CF/log(t_CF/t_metal);
%+ eps_CF*pi/log(2)
```

```

%+ pi*eps_CF/log(t_CF/t_metal);
C_FB = A_CF*eps_ox/t_ox_undoped;

%MOSFET parameters
L_m = 2E-6; %Channel length
W_m = 10E-6; %Channel width

x_d = 1E-6;
lambda = x_d/L_m; %Channel length modulation
mu_n = 0.1350; %Carrier mobility
theta = 0.1529; %Mobility attenuation
c_i = eps_ox/t_ox_doped; %Oxide capacitance per unit
    area
C_ox = c_i*W_m*L_m; %Mosfet oxide capacitance

V_t0 =0.5; %Initial Threshold voltage, seen from CG

%Sensing Area: parameters
A_s = (50*(10^-6))^2; %Sensing pad surface area
t_ox_SG = 0.1*20E-9; %Sensing pad oxide thickness
t_ox_SG_tio = 21E-9;
t_ox_SG_sio = 5E-9;
C_SG = A_s*eps_ox/t_ox_SG_tio; %Sensing pad oxide
    capacitance
C_Stern = A_s*10*eps_0*0.01/(5E-10); %Stern capacitance
%C	CG2 = ((150*10^-6)*(300*10^-9)*eps_w)/(150*10^-6); %
    CG2 electrode sides
%parallel with pdms:
%C	CG2 = (((150*10^-6)*(300*10^-9)*eps_w)/(150*10^-6))
    +(((150*10^-6)*(300*10^-9)*2.69*eps_0)/(150*10^-6));
%C	CG2 = (eps_w/pi)*log(1+2*((150*10^-6)/(1000*10^-6))) +
    ((150*10^-6)*(300*10^-9)*eps_w)/(1000*10^-6);

%C_tot = C_CF+C_FB+C_SG;

C_PDMS = eps_0*(2.38)*(20*10^-6)*(100*10^-6)/(500*10^-6);

%assuming oxide layer on top of circular is also 2*C_SG
C	CG2 = C_Stern + ((eps_0*eps_ox)*((pi*(150*10^-6)^2)/(
    t_ox_SG_sio)))

C_tot = C_CF+C_FB+C_SG+C	CG2;

Ns =8E18; %Total fixed number of binding sites per unit
    area.96 PAPERINDA DA BOYLE.

```

```
k = 1.3806E-23; %Boltzmann constant
T = 293; %Temperature

z = 1; %Ion charge number
eps_w = 78; %Relative permittivity of water
q = 1.602E-19; %Elementary charge

%Sensing Area: Solution parameters
N_a = 6.02E23*9E-5; %Ion concentration
debye = sqrt(eps_w*eps_0*k*T/(2*N_a*(z^2)*(q^2))); %Debye
    length
B = 2*eps_w*eps_0*k*T/(q*debye);

%Bias point
V_DS = 3; %Drain-source voltage
%Q_0 = 10^-15; %Floating gate trapped charge
Q_0 = 10^-12;

steps = 5;
pHsteps = 21;
V_CG = 5;

V_CG2 = 0;

V_ref = 0;

%initialize solution matrices
val_E_ox = zeros(steps, pHsteps);

val_V_t1 = zeros(steps, pHsteps);

val_V_FG = zeros(steps, pHsteps);
val_Psi_0 = zeros(steps, pHsteps);
val_Psi_DL = zeros(steps, pHsteps);
val_sigm_0 = zeros(steps, pHsteps);
val_sigm_DL = zeros(steps, pHsteps);

I_D0 = zeros(steps, pHsteps);

V_DSsat = zeros(steps, pHsteps);
alpha = zeros(steps, pHsteps);

pH = zeros(0, pHsteps);

%Double layer model definition
```

```

syms V_FG Psi_0 Psi_DL sigm_0 sigm_DL

for pHstep = 1:21
pH(pHstep) = 0.5 + 0.5*pHstep;
H_plus = 10^(-pH(pHstep)) %H-plus bulk concentration

for i = 1:steps

pK_A = 8;
pK_B = 4.5;
K_A = 10^(-pK_A); %Dissociation constant A
K_B = 10^(-pK_B); %Dissociation constant B

%%%%%%%%%%%%%% System of equations

eqn1 = V_FG == C_CF*V_CG/C_tot + (Q_0)/C_tot - C_SG*Psi_0
      /C_tot + C_CG2*V_CG2/C_tot;

eqn2 = Psi_0 == (V_FG - A_s*(sigm_0 - sigm_DL)/C_SG);

eqn3 = Psi_DL == (Psi_0 - A_s*sigm_DL/C_Stern);

%% first terms are from the circular gate side
eqn4 = sigm_0 == +(-q*Ns/(1+(H_plus/K_A)*exp(-q*(Psi_0-
      V_ref)/(k*T)))) ...
+ q*Ns/(1+(K_B/H_plus)*exp(q*(+Psi_0-V_ref)/(k*T))));

eqn5 = sigm_DL == (B*sinh(q*(Psi_DL-V_CG2)/(2*k*T)));

eqns = [eqn1, eqn2, eqn3, eqn4, eqn5];

%Equation solver
S = vpasolve(eqns, [V_FG, Psi_0, Psi_DL, sigm_0, sigm_DL
  ]);

%fill in solver value
val_V_FG(i, pHstep) = double(S.V_FG);

val_Psi_0(i, pHstep) = double(S.Psi_0);

val_Psi_DL(i, pHstep) = double(S.Psi_DL);

val_sigm_0(i, pHstep) = double(S.sigm_0);

```

```

val_sigm_DL(i, pHstep) = double(S.sigm_DL);

%electric field in the oxide
val_E_ox(i, pHstep) = (val_V_FG(i, pHstep)-val_Psi_0(i,
    pHstep))/(t_ox_SG_tio);
%val_E_ox(i, pHstep) = (val_V_FG(i)-val_Psi_0(i))/(
    t_ox_SG_tio);
val_V_t1(i, pHstep) = -V_CG*(C_CF/C_tot) + (C_SG/C_tot)*
    val_Psi_0(i, pHstep)+ val_V_FG(i,pHstep) - (C_CF/C_tot
    )*V_t0;
%%%%%% according to Barbaro 2006
%val_V_t1(i, pHstep) = V_CG - val_V_FG(i,pHstep)+V_t0;

%Effective carrier mobility
mu_eff = mu_n/(1+theta*(val_V_FG(i, pHstep) -val_V_t1(i,
    pHstep)));

%Saturation drain-source voltage
V_DSsat(i, pHstep) = + V_DS - val_V_t1(i,pHstep);

alpha(i,pHstep) = mu_eff*c_i*W_m/(2*L_m)*(1+lambda*(V_DS-
    V_DSsat(i,pHstep)));

%Saturation region drain current
I_D0(i, pHstep) = ((alpha(i,pHstep)*(val_V_FG(i,pHstep) -
    val_V_t1(i,pHstep))^2));

end
end

hold on;

plot(pH, I_D0)
xlabel('pH');
ylabel('Drain Current')

```


C

SURFACE ANALYSIS OF MO_x LAYERS WITH EDX

Fig. C.1 shows a rich oxygen ratio towards Al atoms (324:72). When the thickness of HfO_x increased, Hf dominates the stoichiometry (Fig. C.2).

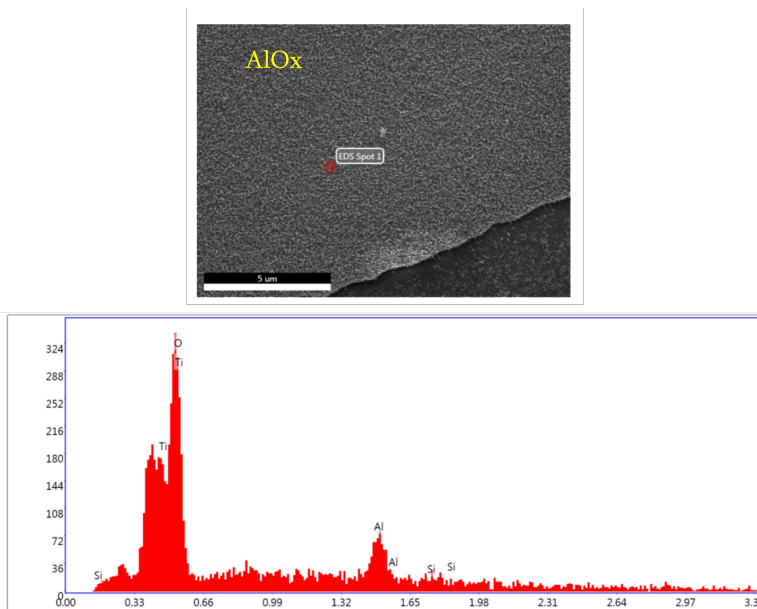


Figure C.1: EDX analysis of AlO_x , showing the elemental composition. The analysis showed rich oxygen concentration, compared to Al.

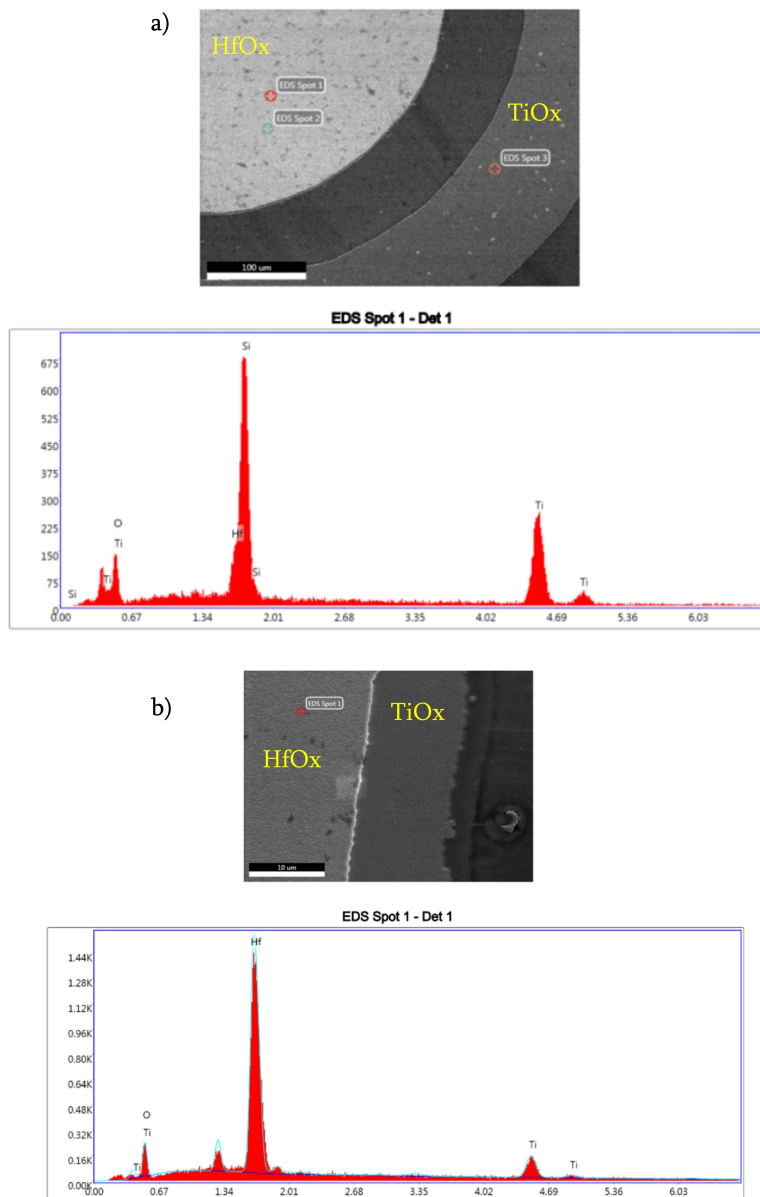


Figure C.2: EDX analysis of a) 20nm and b) 120nm HfO_x layers. When the thickness of HfO_x increased, the ratio between Hf and O atoms also changed. Thicker HfO_x layer showed an increase in Hf concentration.

D

FLOWCHART OF THE SILICON-POLYMER FG-FET DEVICE

- Coating HMDS (hexamethyldisilazane) vapor, with nitrogen as a carrier gas, spin coating of Shipley SPR3012 positive resist, dispensed by a pump, a soft bake at 95C for 90 seconds Always check the relative humidity (48 ± 2 %) in the room before coating, and follow the instructions for this equipment. Use program "Co - 3012 – 1.4um-no EBR".
- Exposure Processing will be performed on the ASML PAS5500/80 automatic wafer stepper. Expose masks COMURK, with job "ZEFWAM" and the correct exposure energy 150mJ. This results in alignment markers for the stepper and contact aligner.
- Develop Post-exposure bake at 115C for 90 seconds, developing with Shipley MF322 with a single puddle process, a hard bake at 100C for 90 seconds. Use program "Dev - SP".
- Inspection Visually inspect the wafers through a microscope, and check the line width and overlay. No resist residues are allowed.
- Plasma Etching Alignment markers (URK's) in Silicon Use Rapier
- Layer Stripping: Photoresist Strip resist Use the Tepla Plasma 300 system to remove the photoresist in an oxygen plasma. Follow the instructions specified for the Tepla stripper, and use the quartz carrier. Use program 1: 1000 watts power and automatic endpoint detection + 2 min. overetching.
- Cleaning: HNO₃ 99% and 69.5%
Clean: 10 minutes in fuming nitric acid at ambient temperature. This will dissolve

organic materials. Use wet bench "HNO₃ 99% (Si)" and the carrier with the red dot. Rinse in the Quick Dump Rinser with the standard program until the resistivity is 5 Mohm. Clean: 10 minutes in concentrated nitric acid at 110 °C. This will dissolve metal particles. Use wet bench "HNO₃ 69,5%110C (Si)" and the carrier with the red dot. Rinse in the Quick Dump Rinser with the standard program until the resistivity is 5 Mohm. Dry: Use the Semitool "rinser/dryer" with the standard program, and the white carrier with a red dot.

- Dip Etch to remove native oxide
0.55% HF solution, 4 minutes
- Dry Oxidation: Dirt Barrier
Furnace no: A1 Program name: DIBARVAR Total time: 1 hr 50 min Program no: N13, 950C, 35 minutes
- Measurement: Oxide Thickness
Use Woolam ellipsometer. Oxide thickness: 20-22 nm
- Coating & Baking
Use the coater station of the EVG120 system to coat the wafers with photoresist. The process consists of: a treatment with HMDS (hexamethyldisilazane) vapor, with nitrogen as a carrier gas spin coating of Shipley SPR3012 positive resist, dispensed by a pump a soft bake at 95C for 90 seconds Always check the relative humidity (48 ± 2%) in the room before coating, and follow the instructions for this equipment. Use program "Co - 3012 – 2.1µm-no EBR".
- Exposure – NW definition Alignment and exposure will be done with the ASML PAS5500/80 automatic wafer stepper.
Use the mask "EC2204V1NWSNSPCO" in box 486, jobname "Diesize 10mm DIE 10 x 10 4IMG", layer "IMAGE 03", with an energy of 320 mJ cm⁻² . MASK ID: 2X2
- Develop
Use the developer station of the EVG120 system to develop the wafers. The process consists of: a post-exposure bake at 115C for 90 seconds developing with Shipley MF322 with a single puddle process a hard bake at 100C for 90 seconds Use program "Dev - SP"
- Inspection: Linewidth and overlay
Visually inspect the wafers through a microscope, and check the line width and overlay. No resist residues are allowed.
- Implantation
P⁺, 150keV, 6E12
- Layer Stripping: Photoresist
Strip resist Use the Tepla Plasma 300 system to remove the photoresist in an oxygen plasma. Follow the instructions specified for the Tepla stripper, and use the quartz carrier. Use program 1: 1000 watts power and automatic endpoint detection + 2 min. overetching.

- **Cleaning: HNO₃ 99% and 69.5%**
Clean: 10 minutes in fuming nitric acid at ambient temperature. This will dissolve organic materials. Use wet bench "HNO₃ 99% (Si)" and the carrier with the red dot. Rinse in the Quick Dump Rinser with the standard program until the resistivity is 5 Mohm. Clean: 10 minutes in concentrated nitric acid at 110 °C. This will dissolve metal particles. Use wet bench "HNO₃ 69,5%110C (Si)" and the carrier with the red dot. Rinse in the Quick Dump Rinser with the standard program until the resistivity is 5 Mohm. Dry: Use the Semitool "rinser/dryer" with the standard program, and the white carrier with a red dot.
- **Annealing Program 5, 240 minutes, 1150C**
- **Measurement: Oxide Thickness**
Use Woolam ellipsometer. Oxide thickness: 20-22 nm
- **Oxide stripping**
Etchant: Use wetbench "BHF (1:7)"; use the carrier with the blue dot Etch time: Depends on the oxide thickness and composition. Etch until the whole wafer is hydrophobic. The etch rate of thermally grown oxide is 1.3 ± 0.2 nm/s at 20 °C. (approx. 3 min) QDR: Rinse in the Quick Dump Rinser with the standard program until the resistivity is 5 Mohm. Dry: Use the μ Process Avenger with the standard program, and the white carrier with a red dot.
- **Cleaning: HNO₃ 99% and 69.5%**
Clean: 10 minutes in fuming nitric acid at ambient temperature. This will dissolve organic materials. Use wet bench "HNO₃ 99% (Si)" and the carrier with the red dot. Rinse in the Quick Dump Rinser with the standard program until the resistivity is 5 Mohm. Clean: 10 minutes in concentrated nitric acid at 110 °C. This will dissolve metal particles. Use wet bench "HNO₃ 69,5%110C (Si)" and the carrier with the red dot. Rinse in the Quick Dump Rinser with the standard program until the resistivity is 5 Mohm. Dry: Use the Semitool "rinser/dryer" with the standard program, and the white carrier with a red dot.
- **Dip Etch to remove native oxide**
0.55% HF solution, 4 minutes
- **Dry Oxidation: Dirt Barrier**
Furnace no: A1 Program name: DIBARVAR Total time: 1 hr 50 min Program no: N13, 950C, 35 minutes
- **Measurement: Oxide Thickness**
Use Woolam ellipsometer. Oxide thickness: 20-22 nm
- **Coating & Baking**
Use the coater station of the EVG120 system to coat the wafers with photoresist. The process consists of: a treatment with HMDS (hexamethyldisilazane) vapor,

with nitrogen as a carrier gas spin coating of Shipley SPR3012 positive resist, dispensed by a pump a soft bake at 95C for 90 seconds Always check the relative humidity ($48 \pm 2\%$) in the room before coating, and follow the instructions for this equipment. Use program "Co - 3012 – 1.4 μ m-no EBR".

- Exposure – SN definition
Alignment and exposure will be done with the ASML PAS5500/80 automatic wafer stepper. Use the mask "EC2204-V1 NW-SN-SP-CO" in box 486, jobname "Diesize 10mm/DIE10x10 4IMG", layer "IMAGE 04", with an energy of 150 mJ cm⁻² . MASK ID: 2X2
- Develop
Use the developer station of the EVG120 system to develop the wafers. The process consists of: a post-exposure bake at 115C for 90 seconds developing with Shipley MF322 with a single puddle process a hard bake at 100C for 90 seconds
- Inspection: Linewidth and overlay
Visually inspect the wafers through a microscope, and check the line width and overlay. No resist residues are allowed.
- Implantation As^+ , 40keV, $5E15$ ions/cm²
- Layer Stripping: Photoresist Strip resist Use the Tepla Plasma 300 system to remove the photoresist in an oxygen plasma. Follow the instructions specified for the Tepla stripper, and use the quartz carrier. Use program 1: 1000 watts power and automatic endpoint detection + 2 min. overetching.
- Cleaning: HNO3 99% and 69.5%
Clean: 10 minutes in fuming nitric acid at ambient temperature. This will dissolve organic materials. Use wet bench "HNO3 99% (Si)" and the carrier with the red dot. Rinse in the Quick Dump Rinser with the standard program until the resistivity is 5 Mohm. Clean: 10 minutes in concentrated nitric acid at 110 °C. This will dissolve metal particles. Use wet bench "HNO3 69,5%110C (Si)" and the carrier with the red dot. Rinse in the Quick Dump Rinser with the standard program until the resistivity is 5 Mohm. Dry: Use the Semitool "rinser/dryer" with the standard program, and the white carrier with a red dot.
- Coating & Baking
Use the coater station of the EVG120 system to coat the wafers with photoresist. The process consists of: a treatment with HMDS (hexamethyldisilazane) vapor, with nitrogen as a carrier gas spin coating of Shipley SPR3012 positive resist, dispensed by a pump a soft bake at 95C for 90 seconds Always check the relative humidity ($48 \pm 2\%$) in the room before coating, and follow the instructions for this equipment. Use program "Co - 3012 – 1.4 μ m-no EBR".
- Exposure – SP definition
Alignment and exposure will be done with the ASML PAS5500/80 automatic wafer stepper. Use the mask "EC2204-V1 NW-SN-SP-CO" in box 486, jobname "Diesize

10mm/DIE10x10 4IMG”, layer “IMAGE 01”, with an energy of 150 mJ cm⁻² . MASK ID: 2X2

- **Develop**
Use the developer station of the EVG120 system to develop the wafers. The process consists of: a post-exposure bake at 115C for 90 seconds developing with Shipley MF322 with a single puddle process a hard bake at 100C for 90 seconds Use program "Dev - SP"
- **Inspection: Linewidth and overlay**
Visually inspect the wafers through a microscope, and check the line width and overlay. No resist residues are allowed.
- **Implantation: SP Definition B⁺, 20keV, 4E14 ions/cm²**
- **Cleaning: HNO3 99% and 69.5%**
Clean: 10 minutes in fuming nitric acid at ambient temperature. This will dissolve organic materials. Use wet bench "HNO3 99% (Si)" and the carrier with the red dot. Rinse in the Quick Dump Rinser with the standard program until the resistivity is 5 Mohm. Clean: 10 minutes in concentrated nitric acid at 110 °C. This will dissolve metal particles. Use wet bench "HNO3 69,5%110C (Si)" and the carrier with the red dot. Rinse in the Quick Dump Rinser with the standard program until the resistivity is 5 Mohm. Dry: Use the Semitool "rinser/dryer" with the standard program, and the white carrier with a red dot.
- **Annealing and Oxidation Program 6, 2 hours and 25 minutes, 1000C**
- **Measurement: Oxide Thickness**
Use Woolam ellipsometer. Oxide thickness: 100 nm
- **Coating & Baking**
Use the coater station of the EVG120 system to coat the wafers with photoresist. The process consists of: a treatment with HMDS (hexamethyldisilazane) vapor, with nitrogen as a carrier gas spin coating of Shipley SPR3012 positive resist, dispensed by a pump a soft bake at 95C for 90 seconds Always check the relative humidity (48 ± 2%) in the room before coating, and follow the instructions for this equipment. Use program "Co - 3012 – 1.4µm-no EBR".
- **Exposure**
Use the mask “EC2204-V1 NW-SN-SP-CO” in box 486, jobname “Diesize 10mm/DIE10x10 4IMG”, layer “IMAGE 02”, with an energy of 150 mJ cm⁻²
- **Develop**
Post-exposure bake at 115C for 90 seconds, developing with Shipley MF322 with a single puddle process, a hard bake at 100C for 90 seconds. Use program "Dev - SP".
- **Inspection**
Visually inspect the wafers through a microscope, and check the line width and overlay. No resist residues are allowed.

- **Window Etching**
 Rinse: Use wetbench "H₂O/TRITON X-100" and the special carrier with the blue dot; added to the tank: 1 ml Triton X-100 per 5000 ml demi water. Rinse for 1 minute. Etchant: Use wetbench "SiO₂-ets (1:7)"; use the carrier with the blue dot. Buffered HF solution (Merck LSI selectipur, SiO₂ 1:7). Etch time: The oxide in the SN regions is about 200 nm thick, the oxide thickness outside the SN regions and on the backside of the wafer is about 100 nm thick. Therefore, the required etch-time for the CO-SN combinations is about twice the time to obtain a hydrophobic back side of the wafer. Etch till the CO-windows in the SN areas are open. QDR Rinse: in the Quick Dump Rinser with the standard program until the resistivity is 5 Mohms. Drying: Use the single wafer dryer.
- **Inspection**
 Visually inspect the wafers through a microscope, and check the line width and overlay. No resist residues are allowed.
- **Cleaning: HNO₃ 99% and 69.5%**
 Clean: 10 minutes in fuming nitric acid at ambient temperature. This will dissolve organic materials. Use wet bench "HNO₃ 99% (Si)" and the carrier with the red dot. Rinse in the Quick Dump Rinser with the standard program until the resistivity is 5 Mohm. Clean: 10 minutes in concentrated nitric acid at 110 °C. This will dissolve metal particles. Use wet bench "HNO₃ 69,5%110C (Si)" and the carrier with the red dot. Rinse in the Quick Dump Rinser with the standard program until the resistivity is 5 Mohm. Dry: Use the Semitool "rinser/dryer" with the standard program, and the white carrier with a red dot.
- **Marangoni**
 Marangoni drying is a passivation, which helps the wafer to be without oxide layer.
- **AlSi Sputtering: First metallization**
 Use the TRIKON SIGMA. The target must exist of 99%Al and 1%Si.
 Use recipe "AlSi 675nm 350" to sputter a 600 nm thick layer. Note: Check the wafers after aluminum deposition. Metal residuals should be not present on the edge neither on the frontside nor the backside of the wafer.
- **Coating & Baking**
 Use the coater station of the EVG120 system to coat the wafers with photoresist. The process consists of: a treatment with HMDS (hexamethyldisilazane) vapor, with nitrogen as a carrier gas spin coating of Shipley SPR3012 positive resist, dispensed by a pump a soft bake at 95C for 90 seconds Always check the relative humidity (48 ± 2%) in the room before coating, and follow the instructions for this equipment. Use program "Co - 3012 – 1.4µm-no EBR".
- **Exposure**
 Alignment and exposure will be done with the ASML PAS5500/80 automatic wafer stepper. Use the mask "EC2204-V1 M1-VIA-M2-CO3" in box 486, jobname "Die-size 10mm/DIE10x10 4IMG", layer "IMAGE 03", with an energy of 150 mJ cm⁻². MASK ID: 2X2

- **Develop**
Post-exposure bake at 115C for 90 seconds, developing with Shipley MF322 with a single puddle process, a hard bake at 100C for 90 seconds. Use program "Dev - SP".
- **Inspection**
Visually inspect the wafers through a microscope, and check the line width and overlay. No resist residues are allowed.
- **Plasma Etching of AlSi**
For aluminum etching use the Trikon mega 210 plasma etcher. Use program "AlSi06 350" and set the platen temperature to 25 °C in order to etch the aluminum layer. Total etch time must be 2 mins 30 secs to etch the aluminium completely and land on oxide layer underneath. (There is endpoint detection here)
- **Inspection**
Visually inspect the wafers through a microscope, and check the line width and overlay. No resist residues are allowed.
- **Layer Strip: Photoresist**
Strip resist: Use the Tepla Plasma 300 system to remove the photoresist in an oxygen plasma. Follow the instructions specified for the Tepla stripper, and use the quartz carrier. Use program 1: 1000 watts power and automatic endpoint detection + 2 min. overetching.
- **Cleaning: HNO3 99% (metals)** Clean 10 minutes in fuming nitric acid at ambient temperature. This will dissolve organic materials. Use wet bench "HNO3 99% (Si)" and the carrier with the red dot. Rinse in the Quick Dump Rinser with the standard program until the resistivity is 5 Mohm. Dry: Use the Semitool "rinser/dryer" with the standard program, and the white carrier with a red dot.
- **Alloying**
50 minutes, C 4, 400C
- **Electrical characterization**
- **Cleaning: HNO3 99% (metals)** Clean 10 minutes in fuming nitric acid at ambient temperature. This will dissolve organic materials. Use wet bench "HNO3 99% (Si)" and the carrier with the red dot. Rinse in the Quick Dump Rinser with the standard program until the resistivity is 5 Mohm. Dry: Use the Semitool "rinser/dryer" with the standard program, and the white carrier with a red dot.
- **PECVD Deposition (backside), 6000nm**
Use the Novellus Concept One PECVD reactor. Use group: undoped oxides (recipe xxxsiostd) to deposit a 6000 nm thick SiO2 layer. Change time to get the right thickness.
- **Measurement: Oxide Thickness**
Use Woolam ellipsometer. Oxide thickness: 6000nm

- Coating (Backside)
Use the coater station of the EVG120 system to coat the wafers with photoresist. The process consists of:
Use negative photoresist for 3.1 μm , no EBR
- Exposure
Use contact aligner, hard contact, (soft is also fine). Approx. 40sec. Use alignment markers on the frontside.
- Develop
Use the developer station of the EVG120 system to develop the wafers. Use developing procedure for negative photoresist: 1) Baking for cross-linking, 2) lift-off
- Inspection Visually inspect the wafers via microscope
- Plasma Etching
Use the Drytek Triode 384T plasma etcher. It is not allowed to change the process conditions from the etch recipe, except for the etch times! Use recipe STDOXIDE to etch the oxide layer with a soft landing on the layer underneath.
- Inspection
Visual Inspection. Also use profilometer.
- Layer Stripping: Photoresist
Strip resist Use the Tepla Plasma 300 system to remove the photoresist in an oxygen plasma. Follow the instructions specified for the Tepla stripper, and use the quartz carrier. Use program 1: 1000 watts power and automatic endpoint detection + 2 min. overetching.
- Cleaning: HNO₃ 99% (metals)
Clean 10 minutes in fuming nitric acid at ambient temperature. This will dissolve organic materials. Use wet bench "HNO₃ 99% (Si)" and the carrier with the red dot. Rinse in the Quick Dump Rinser with the standard program until the resistivity is 5 Mohm. Dry: Use the Semitool "rinser/dryer" with the standard program, and the white carrier with a red dot.
- PECVD Deposition, 100nm, dielectric definition
Use the Novellus Concept One PECVD reactor. Use group: undoped oxides (recipe xxxsiostd) to deposit a 6000 nm thick SiO₂ layer. Change time to get the right thickness.
- Measurement: Oxide Thickness
Use Woolam ellipsometer.
- Coating & Baking
Use the coater station of the EVG120 system to coat the wafers with photoresist. The process consists of: a treatment with HMDS (hexamethyldisilazane) vapor,

with nitrogen as a carrier gas spin coating of Shipley SPR3012 positive resist, dispensed by a pump a soft bake at 95C for 90 seconds Always check the relative humidity ($48 \pm 2\%$) in the room before coating, and follow the instructions for this equipment. Use program "Co - 3012 – 1.4 μ m-no EBR".

- **Exposure**
Alignment and exposure will be done with the ASML PAS5500/80 automatic wafer stepper. Use the mask "EC2204-V1 M1-VIA-M2-CO3" in box 486, jobname "Die-size 10mm/DIE10x10 4IMG", layer "IMAGE 04", with an energy of 150 mJ cm⁻² . MASK ID: 2X2
- **Develop**
Post-exposure bake at 115C for 90 seconds, developing with Shipley MF322 with a single puddle process, a hard bake at 100C for 90 seconds. Use program "Dev - SP".
- **Inspection**
Visually inspect the wafers through a microscope, and check the line width and overlay. No resist residues are allowed.
- **Plasma etching of VIAs**
Use recipe (OXSFTLND) to etch the oxide layer with a soft landing on the layer underneath.
- **Inspection**
Visual Inspection. Also use profilometer.
- **Layer Stripping: Photoresist**
Strip resist Use the Tepla Plasma 300 system to remove the photoresist in an oxygen plasma. Follow the instructions specified for the Tepla stripper, and use the quartz carrier. Use program 1: 1000 watts power and automatic endpoint detection + 2 min. overetching.
- **Cleaning: HNO3 99% (metals)**
Clean 10 minutes in fuming nitric acid at ambient temperature. This will dissolve organic materials. Use wet bench "HNO3 99% (Si)" and the carrier with the red dot. Rinse in the Quick Dump Rinser with the standard program until the resistivity is 5 Mohm. Dry: Use the Semitool "rinser/dryer" with the standard program, and the white carrier with a red dot.
- **Manual coating Polyimide**
Use the Brewer Science manual coater system to coat the wafers with Polyimide LTC 9305. The process consists of:
Use the membrane chuck for non-contaminated wafers
spin coating of Fujifilm LTC9305 negative polyimide, dispensed by a manual syringe Use program "test hande". (600rpm 10 seconds + 6000rpm 75sec)
- **Baking**
Use the hotplate of manual coater system to soft bake the wafers with Polyimide LTC 9305. The process consists of: Bake 120 s @ 100C

- **Inspection and clean**
Visually inspect the back side of the wafers and clean with acetone. Also clean the edge of the wafer with a Q-tip with HTRD2 developer. No polyimide residues are allowed.
- **Alignment and exposure**
Processing will be performed on the contact aligner. Follow the operating instructions from the manual when using this machine. Expose mask Polyimide 1. Calculate the exposure time from the manual.
- **Post exposure bake**
PEB: 60s @ 50C ('x handepb', 90sec 90C)
- **Developing manual**
Developing with HTRD2, time 90seconds + 90 sec of RER A hard bake at 100 C for 90 seconds
- **Final Cure Koyo**
In vacuum and under low N2 flow. Use dedicated Al carrier plate for clean wafers under the process wafer. Standard Cure 4 hours @ 350 °C (Program 6)
- **Inspection**
Measure the polyimide layers. Visually inspect under microscope.
- **LUR test**
Substrate needs to be input inside the deposition chamber under vacuum while continuously monitoring the pressure of the chamber for 10 minutes. The initial and the final pressure of the chamber is recorded and the leak-up rate calculated based on these values and the volume of the chamber.
- **Ti Sputtering**
Use recipe "Ti 200nm 1kW 25C" to sputter a 200 nm thick layer. Check other recipe, low T and low Power is better. NOTE: Use a test wafer.
- **Coating & Baking**
Use the coater station of the EVG120 system to coat the wafers with photoresist. The process consists of: a treatment with HMDS (hexamethyldisilazane) vapor, with nitrogen as a carrier gas spin coating of Shipley SPR3012 positive resist, dispensed by a pump a soft bake at 95C for 90 seconds Always check the relative humidity ($48 \pm 2\%$) in the room before coating, and follow the instructions for this equipment. Use program "Co - 3012 - 1.4 μ m-no EBR".
- **Exposure**
Alignment and exposure will be done with SUS mask aligner. Use the correct dose and Ti mask.
- **Develop**
Post-exposure bake at 115C for 90 seconds, developing with Shipley MF322 with a single puddle process, a hard bake at 100C for 90 seconds. Use program "Dev - SP".

- **Inspection**
Visually inspect the wafers through a microscope, and check the line width and overlay. No resist residues are allowed.
- **Plasma Etching of Ti/TiN**
For titanium etching use the Trikon Omega 210 plasma etcher. Use program “tin-tisvo” and set the platen temperature to 25 °C in order to etch the titanium layer. Adjust total time according to layer thickness. Check the etch time with the test wafer first, then inspect. The total etch time should be 60 seconds + 60 seconds to etch 200 nm of Ti.
- **Layer strip Photoresist**
Strip resist: Use the Tepla Plasma 300 system to remove the photoresist in an oxygen plasma. Follow the instructions specified for the Tepla stripper, and use the quartz carrier. Use program 2 flash. Note: If there are residues, use 1 min of acetone after flash.
- **Inspection**
- **Manual coating Polyimide**
Use the Brewer Science manual coater system to coat the wafers with Polyimide LTC 9305. The process consists of:
Use the membrane chuck for non-contaminated wafers
spin coating of Fujifilm LTC9305 negative polyimide, dispensed by a manual syringe Use program "test hande". (600rpm 10 seconds + 6000rpm 75sec)
- **Baking**
Use the hotplate of manual coater system to soft bake the wafers with Polyimide LTC 9305. The process consists of: Bake 120 s @ 100C
- **Inspection and clean**
Visually inspect the back side of the wafers and clean with acetone. Also clean the edge of the wafer with a Q-tip with HTRD2 developer. No polyimide residues are allowed.
- **Alignment and exposure**
Processing will be performed on the contact aligner. Follow the operating instructions from the manual when using this machine. Expose mask Polyimide 2. Calculate the exposure time from the manual.
- **Post exposure bake**
PEB: 60s @ 50C ('x handepeb', 90sec 90C)
- **Developing manual**
Developing with HTRD2, time 90seconds + 90 sec of RER A hard bake at 100 C for 90 seconds
- **Final Cure Koyo**
In vacuum and under low N2 flow. Use dedicated Al carrier plate for clean wafers under the process wafer. Standard Cure 4 hours @ 350 °C (Program 6)

- **Inspection**
Measure the polyimide layers. Visually inspect under microscope.
- **Coating & Baking**
Use the coater station of the EVG120 system to coat the wafers with photoresist. The process consists of: a treatment with HMDS (hexamethyldisilazane) vapor, with nitrogen as a carrier gas spin coating of Shipley SPR3012 positive resist, dispensed by a pump a soft bake at 95C for 90 seconds Always check the relative humidity ($48 \pm 2\%$) in the room before coating, and follow the instructions for this equipment. Use program "Co - 3012 - 2.1 μ m-no EBR".
- **Exposure**
Alignment and exposure will be done with the ASML PAS5500/80 automatic wafer stepper. Use the mask "EC2204-V1 M1-VIA-M2-CO3" in box 486, jobname "Die-size 10mm/DIE10x10 4IMG", layer "IMAGE 02", with an energy of 320 mJ cm⁻². MASK ID: 2X2
- **Develop**
Post-exposure bake at 115C for 90 seconds, developing with Shipley MF322 with a single puddle process, a hard bake at 100C for 90 seconds. Use program "Dev - SP".
- **Dry etching of contact openings**
Use recipe OXSFTLND to etch the oxide layer with a soft landing on Al
- **Inspection**
- **Layer Stripping: Photoresist**
Strip resist Use the Tepla Plasma 300 system to remove the photoresist in an oxygen plasma. Follow the instructions specified for the Tepla stripper, and use the quartz carrier. Use program 2
- **Low power plasma before PDMS 100W, 1min, O2, venting time: 1min. Program 5.**
- **Manual Photoresist coating, backside**
Use manual coater system to coat the wafers with photoresist. The process consists of: Spin coat the Shipley SPR3027 positive resist by dispensing it with manual syringe Use the Non-vacuum edge-chuck
- **PDMS preparation**
In this step the preparation of the PDMS will be done using the elastomer PDMS Sylgard 184 and its curing agent. Use the ratio of 10:1 for PDMS elastomer and the curing agent.
- **PDMS Mixing and Degassing**
For mixing the PDMS elastomer and curing agent use the Thinky Speedmixer. Make sure that the cup holder is properly located in the machine. Determine the total weight of the cup and the holder and adjust the machine according to this value. Follow the instructions established for this machine.

Select program 01, check the parameters for each step if necessary and then start the process.

- **PDMS Layer Deposition**
For the deposition of the $20\mu\text{m}$ PDMS layer use the Polos Manual Spinner 1 C1100. Cover both the bottom and the ring of the spinner with aluminum foil to avoid residues of the polymer on the machine. Pour the PDMS elastomer and curing agent mixture to cover about 2/3 parts of the wafer. Select the right recipe 20 PDMS.
- **PDMS Curing**
For baking of the PDMS layer use the Memmert Oven with the dedicated carrier (PDMS). Set the temperature level to $90\text{ }^{\circ}\text{C}$. Bake the PDMS layer for 60 min or leave the PDMS for curing overnight at room temperature. **DON'T FORGET TO STRIP THE RESIST FROM THE BACKSIDE.**
- **Backside photoresist removal with Acetone**
Use the membrane chuck for non-contaminated wafers Use program: acetone cleaning
- **Inspection**
Visually inspect the wafers through a microscope, and check the line width and overlay. No resist residues are allowed.
- **LUR test**
- **Al sputtering frontside**
Use Trikon Sigma with Al target to sputter Al hard mask at room temperature.
- **Inspection**
Plasma Etching Silicon Backside Use the Rapier Omega i2L DRIE etcher. Use sequence Waferlayer (with a platen temperature of 20°C) to etch the Si layer and stop on SiO_2 . First etch 50 cycles and calculate the etch rate. Check cycles. Landing on SiO_2 .
- **Wet Etching in SAL**
Prepare your own BHF bath. Time: 30min approx. Inspect every few minutes.
- **Wet Etching of AlSi (SAL)** Use PES to remove AlSi hardmask on PDMS
NOTE: If the etching is not uniform with rapier, etch until few dies are open, dice the wafer, then continue etching with a carrier wafer. You need to remove the Al mask for this otherwise you cannot see where to dice.

E

ELECTRICAL CHARACTERIZATION

MEASUREMENT ERROR WITH pH SOLUTION

For one set of measurements, we observed non-standard behavior with the chip. When examined optically, the interconnects and the SiO_2 area in between had a chemical reaction from the pH solution. This is due to the leakage of the solution from the sensing area and the PDMS slab, and bad adhesion between PDMS and the chip. (Fig.E.1).

EFFECT OF LIGHT

Silicon is very sensitive to light. If not isolated properly, all the pn-junctions we use in our devices can also work as photodiodes. Therefore, measurements with changing light conditions have to be avoided. In our case, the wafers with high resistivity can work as isolation regions (Fig.E.2).

Fig.E.2 shows little difference when the light was present while measuring. This test is crucial for FET devices, which can work with different light conditions. For example, when a biologist wants to take our chip from the incubator (which is a dark environment) to investigate the cells under the microscope while continuing the measurement of the pH with a mobile measurement setup (See Chapter 7), the change of the environmental factors should affect the working point of the FET minimally.

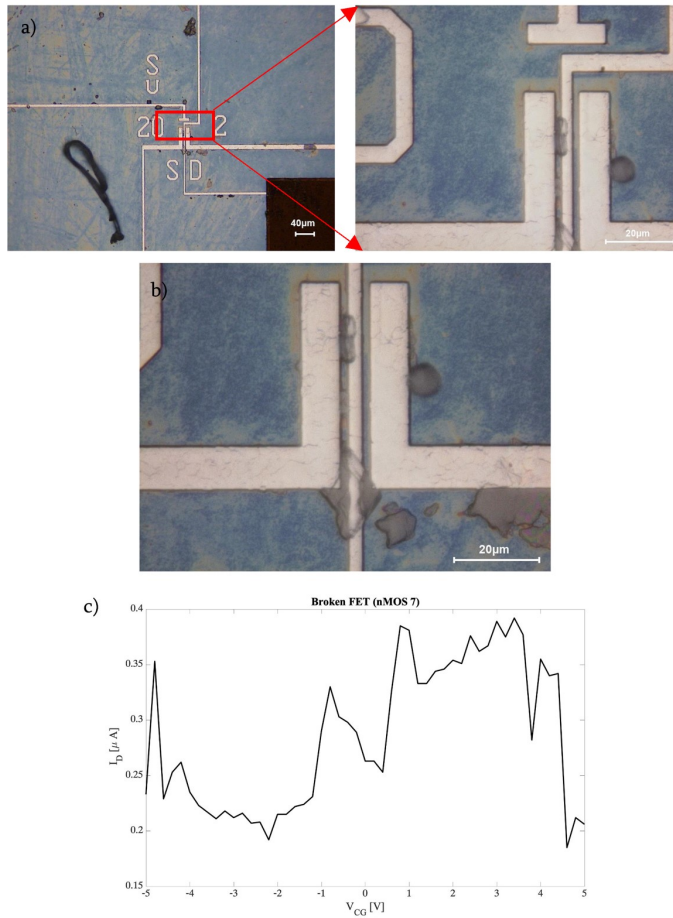


Figure E.1: Error in the measurement. a) Defect on the chip. b) Micrograph of the S-D terminals and the CG. Particle covering all the terminals and chemical reactions are visible. c) Measurement of I_D vs. V_{CG} with defective chip.

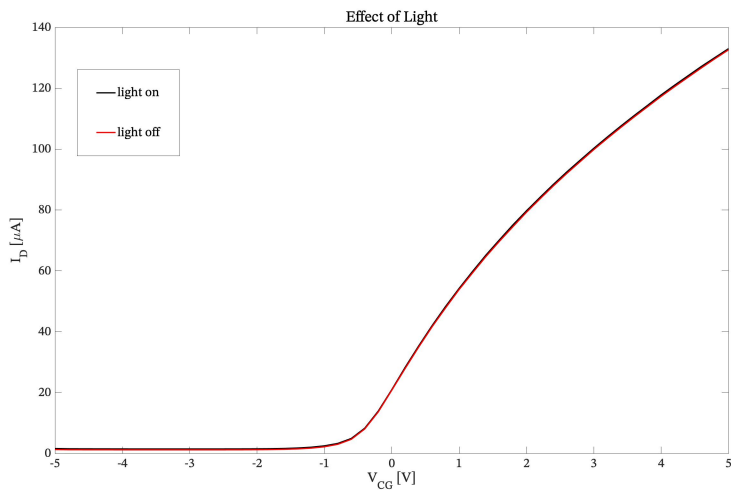


Figure E.2: Effect of light on the transistor (nMOS 6). $V_D = 0.1\text{V}$. The difference in I_D is $6\mu\text{A}$ at $V_{CG} = 5\text{V}$.

F

BIOLOGICAL PROTOCOL

MEASUREMENTS WITH MOBILE MEASUREMENT SETUP WITH TWO-WEEKS OLD CELLS

As explained in Section 7.4.1, we also observed a change in the amplitude of the peaks before and after introducing PicROTOXIN to the 2-week matured cells (Fig. E1). In order to remove the drift from the signals and compare them, the data was processed by fitting a 6-order polynomial to the raw data, and subtracting it from the raw data. In this way, the peaks were normalized at 0, and it was possible to observe the change in the amplitude of the peaks.

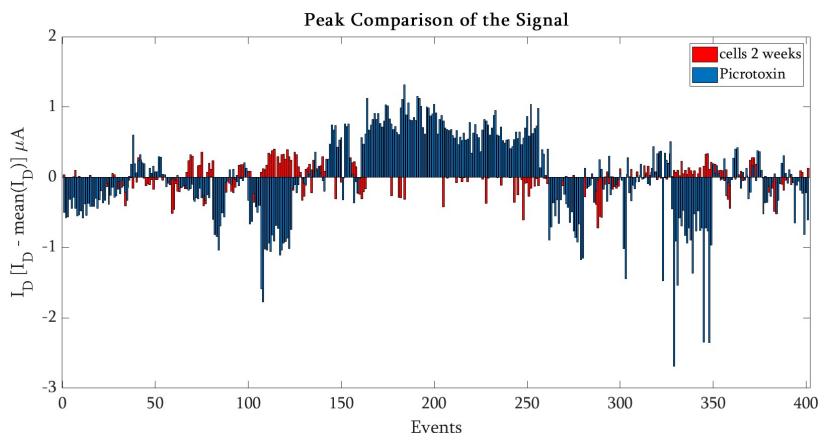


Figure E1: 2-weeks old cells (red) vs. after the introduction of PicROTOXIN (blue). When the peaks of the I_D were detrended towards 0, the difference was more apparent.

hiPSC- DERIVED CORTICAL NEURONAL CULTURES

The hiPSC line LUMC0114iCTRL01 (hPSCreg number LUMCi003-A) was used to derive neural progenitor cells (NPCs) using the STEMdiff SMADi Neural Induction kit (05835, StemCell Technologies). The chip was plasma treated (50 W, 50 KHz, 45 seconds with CUTE Plasma System from Femto Science, Selangor, Malaysia) prior to coating with Poly-L-Ornithine (P3655, Sigma Aldrich) with a concentration of 100 $\mu\text{g}/\text{mL}$ and incubated at room temperature (RT) overnight. The next day the chip was incubated at 4°C for 30 minutes before a laminin coating (200 $\frac{\mu\text{g}}{\text{mL}}$) was applied. After which the chip was incubated at 37°C for 2 hours. NPCs were seeded at a concentration of 100.000 cells $\cdot \text{cm}^{-2}$ on the chip and were subsequently differentiated into cortical neurons for 7 days using the STEMdiff Midbrain Neuron Differentiation Kit (100-0038, StemCell Technologies). Lastly, the hiPSC-derived cortical neurons were matured and maintained in BrainPhys hiPSC Neuron kit media (05795, StemCell Technologies) for the remainder of the experiment. All media were supplemented with 1% penicillin/streptavidin. For the drug experiments, to block inhibition, picrotoxin (P1675-1G, Sigma Aldrich) was prepared at a concentration of 50 μM in BrainPhys medium and was added 20 seconds after which the recordings were started.

IMMUNOHISTOCHEMISTRY

The hiPSC-derived cortical neurons were fixed at DIV 21 in 4% paraformaldehyde for 20 min at room temperature (RT) and permeabilized with 1% Triton X-100 (Sigma-Aldrich, St. Louis, MI, USA) in phosphate-buffered saline (PBS, Sigma-Aldrich) for 20 min. After the permeabilization step, the cells were washed three times in PBS for 5 min each at RT. Cells were then incubated with 1% bovine serum albumin (BSA; no 9048468, SigmaAldrich) for 30 min to block non-specific binding and again washed in PBS three times for 5 min each at RT. The primary antibodies used were β 3 tubulin (rabbit polyclonal PA5-86069, ThermoFisher, Waltham, MA, USA), synaptophysin (mouse monoclonal ab8049, Abcam, Cambridge, UK). These primary antibodies were diluted 1:200 in 1% BSA in dPBS (does not contain magnesium and calcium) and incubated for 1 h at RT. The secondary antibodies were Texas red (Goat anti-mouse, ab7066, Abcam) and Alexa Fluor® 488 nm (Goat anti-rabbit, ab150077, Abcam) which were diluted 1 : 500 in 1% BSA in dPBS. These secondary antibodies were incubated for 1 h at RT in dark before washed with PBS three times for 5 min each. Cell nuclei were stained using NucBlue (Life Technologies, Carlsbad, CA, USA) for 20 min. Fluorescent images were taken using a Keyence BZ-810 microscope system (Osaka, Japan).

ACKNOWLEDGEMENTS

It was truly a unique experience to be a part of such an interdisciplinary project. First of all, I would like to thank my promotors, Prof. Sarro and Dr. Mastrangeli, for all the support, advices, and guidance over the past years. So many hours have been spent on ideas and discussions. I truly appreciate all the contributions. Thank you.

I would like to thank all my committee members: Prof. Dekker, Prof. Hanay, Prof. Barillaro, Dr. Frimat, Dr. Zevenbergen, and Prof. van Driel for accepting to be part of the promotion committee and for taking the time to read my thesis and give me very valuable feedback.

For me, the journey of interdisciplinary work in biosensing and biomechanics started during my MSc studies at Bilkent University. I am (and always will be) truly grateful for all the experience I gained during these years. I would like to thank Prof. Hanay for everything he taught me, including how to connect different research fields and all the scientific support. I cannot skip my gratitude to my fellow lab members: Berk, Tufan, Mohammed, Levent, Selcuk, Ezgi, Mert, Arda, Atakan, Cagatay, Utku and Kelleci. Kelleci, you will always be like a brother to me and a true collaborator. It was truly an honor to work on such a big project and have a great article out of it with Hanay Lab. I wish great success for all of you brilliant people.

Since my MSc studies, cleanroom was always a safe space and an amazing field to explore more every day. Of course, as great as it is, frustration comes hand in hand. Cleanroom work needs all the support and I was lucky enough to be part of (also during my work life) a great team. First of all, I would like to thank Else Kooi Laboratory for providing me with the tools for my unbelievably long flowchart and fabricating active devices during my PhD studies. Paolo, my boss, thank you for teaching me more about processing and active devices and, in general, for all the support you provided during my PhD studies and work years. Bruno and Pieter, my other bosses, thank you for trusting me in my work and the friendly and good working environment you created. My dear colleagues, Vincent, Bianca, Daniel, Mario, Johannes, Tom, Tristan, Engin, Samantha, Jasper, Niels, Sara, Juan, Silvana, Koos, Joost, Robert, Anastasiia, Mike, Dennis, Dylan, Nerea and Maria, thank you for all the support; technical or non-technical. Francesco, it was great to work with you on all of the projects and ease so many days with so many jokes and memories. Also, thank you to my ECTM colleagues, Henk, Marian, Nikki, Filip, Roberto, Alireza, Elena, Feyza, Sten, Clementine, Brahim, Jiarui, Nele, Marta, Yaren, Javad, Nikolas, Cinzia, William, Bjorn, Yaqian, Shin, Jian, Romina, Xinrui, Joost and Joost, Leandro, Elida, Zhen, Dong, Suzanne, Violeta, Debarun and Pratik, and many more new members. Pratik, thank you for being more than a collaborator and a true friend. Aleksandar, thank you for being the big brother figure for all these years, inside and outside the cleanroom. My dear master students, Lovro and Danai, thank you for your hard work and dedication.

Thank you to the lovely group of Bioelectronics people: Gandhiii, Andra, Ronaldo, Nasim,

Tawab, Cesc, Raphael, and Konstantina, and thank you for adopting us during BIOEL. This interdisciplinary work was only possible due to the Netherlands Organ on Chip Initiative and the brilliant people with whom I had the chance to work and collaborate (and party). First, my deepest gratitude goes to LUMC, JP, and Michel for their extensive support in making my chips 'organ-on-chips.' All my NOCI people, thank you for all the discussions, dances, presentations, lab activities, conversations. I am lucky to be a part of such a unique group.

My little Turkish community in NL, I do not know what I would do without you, especially during Covid times. Alev, my ex-neighbor, Ozgun, my vegiterenians, thank you for all our beautiful memories, barbeques, and parties together. Levent, Eda, Dilan, Evren, and Ata, you made my time here more enjoyable; thank you. Another group of NL friends; a special thanks goes to the Brutal Assault group, for all the fun times at festivals together.

My dear Bilkent Mechanical Engineering family, more than decade-long friendships, thank you all. Thank you to Eren, Irmak, Irem, Kelleci, and Selcuk (again), and everyone who was at least once in Sakal with us or had sleepless nights while studying in a mechanical lab. Thank you, Ozan Umit Kardas, for your years-long support.

My paranymphs...Where to start? Milica and Paul, I think it would not be superficial to say you made this possible. Two of the three musketeers, thank you for all of these years. I will always cherish the strong bond we have. We have such a good balance of talking about life crises, research, injustices, world problems, partying (Nijmegen, rolling down the grass hill?), binging TV shows, walking after work for hours, and traveling. Milika, my fellow country-woman. It is wild to find your best friend in your late twenties in a foreign country, in a stressful environment. You are so strong and resilient, and I feel very lucky that we can understand each other so well. Paul, my ex-neighbor, I always admired how determined you are, especially for your research. It was always so nice to walk and talk home after work, and I just want to write here night bus after Den Haag to give you a small smile when you read this from 20 years on. Thank you both once again, and as Dr. Dostanic said once: 'House of Delft!'

My dear family, here in the Netherlands, in Turkey, and in the USA, thank you for everything. Hylke, Tessie, Martijn, and Marieke, thank you for creating such a loving and peaceful environment, it truly felt like home. Sytse, who would have thought? I am very lucky to have you as my life partner, the sweetest and kindest man; thank you for supporting me through my (illogical) thoughts and tough times and having all the best times. I am looking forward to each of our days together. My biggest thanks to my core family: Mom, Dad, Zeynep, Rahim, and Mia. Mom and dad, you are the best parents and inspiration to me. Zeynep, clearly you are the best sister in the world. Thank you all for showing me unconditional support for all of my life and for your love.

LIST OF PUBLICATIONS

JOURNAL PAPERS

- H. Aydogmus, M. Hu, L. Ivancevic, J.P. Frimat, A.M.J.M. van den Maagdenberg, P.M. Sarro, M. Mastrangeli. (2023). "An organ-on-chip device with integrated charge sensors and recording microelectrodes". In: *Scientific Reports, Volume 13, Issue 8062, 2023*.
- D. Nahon, R. Moerkens, H. Aydogmus, B. Lendemeijer, A. Martinez-Silgado, J.M. Stein, M. Dostanic, J.P. Frimat, C. Gontan, M. de Graaf, M. Hu, D. Kasi, L.S. Koch, K. Le, S. Lim, H. Middelkamp, J. Mooiweer, P. Motreuil-Ragot, E. Niggel, C. Pleguezuelos, J. Puschhof, N. Revyn, J.M. Rivera-Arbelaez, J. Slager, L.M. Windt, M. Zakharova, B.J. van Meer, V. Orlova, F. de Vrij, S. Withoff, M. Mastrangeli, A.D. van der Meer, C.L. Mummery. (2022). Taking microphysiological systems to the next level: Why quantification of physiological features is essential, Accepted to *Nature Biomedical Engineering*.
- M. Kelleci, H. Aydogmus, L. Aslanbas, S.O. Erbil, M.S. Hanay. (2018). "Towards microwave imaging of cells". *Lab on a Chip*, 18(3), 463-472.

CONFERENCE PAPERS

- A. Lodewijk, D. Boesten, U. Wyder, J. Bernards, P. Sberna, F. Stallone, H. Aydogmus, R. Nieuwland, M. Hoek, H.W. Zeijl, G. Liere, J. Bolte. (2023). "MRI-Compatible Cascaded Blood Pressure Microsensor." in: *Proceedings of the 8th International Conference on Advances in Sensors, Actuators, Metering and Sensing*.
- H. Aydogmus, M. Hu, J.P. Frimat, A.M.J.M. van den Maagdenberg, G. Zhang, M. Mastrangeli, P.M. Sarro. (2021). "Dual-gate FET-based charge sensor enhanced by in situ electrode decoration in a MEMS organs-on-chip platform." In: *Proceedings of the 21st Int. Conf. on Solid-State Sensors, Actuators and Microsystems (TRANSDUCERS 2021)*.
- M. Mastrangeli, H. Aydogmus, M. Dostanic, P. Motreuil-Ragot, N. Revyn, B. de Wagenaar, R. Dekker; P.M. Sarro, Microelectronmechanical organs-on-chip, In 21st Int. Conf. on Solid-State Sensors, Actuators and Microsystems (TRANSDUCERS 2021)
- H. Aydogmus, M. Dostanic, M. Jahangiri, R. Sinha, W.F. Quiros Solano, M. Mastrangeli, P.M. Sarro. (2020). "FET-based integrated charge sensor for organ-on-chip applications". In: *IEEE Sensors 2020*.

CONFERENCE PRESENTATIONS AND POSTERS

- H. Aydogmus; M. Hu; J.-P. Frimat; A. M. J. M. van den Maagdenberg; P. M. Sarro; M. Mastrangeli; (2022). "Hybrid Silicon-Polymer Multi-Modal Sensing Device for Organ-on-Chip". In: *EUROoCS Conference 2022, 4-5 July 2022*.

- A. R. Vollertsen, H. Aydogmus, A. Pollet, B. van Meer, A. van den Berg, M. Mastrangeli, J. Den Toonder, M. Odijk, A. van der Meer (2022). "Connecting labs for higher level organ-on-chip systems: integration of a pH sensor and a blood vessel-on-chip on a standardized platform." In: *EUROoCS Conference 2022, 4-5 July 2022*.
- H. Aydogmus, M. Hu, L. Ivancevic, J.P. Frimat, A.M.J.M. van den Maagdenberg, P.M. Sarro, M. Mastrangeli. (2022). "Modular FET-Based Sensor for Organ-on-Chip Platforms". In: *BIOEL, International Winterschool on Bioelectronics, Kirchberg in Tirol, Austria, 12-19 March, 2022*.
- H. Aydogmus; H. J. van Ginkel; A.-D. Galiti; M. H. Y. Hu; J.-P. Frimat; A. M. J. M. van den Maagdenberg; G.Q. Zhang; M. Mastrangeli; P. M. Sarro. (2021). "FET-based integrated charge sensing in a MEM organ-on-chip platform". In: *EUROoCS Conference 2021, online, 1-2 July, 2021*.
- H. Aydogmus; H. J. van Ginkel; M. Mastrangeli; GuoQi Zhang; P.M. Sarro. (2020). "FET-based charge sensor for organs-on-chip with in-situ electrode decoration." In: *International MicroNano Conference, December 2020*.
- H. Aydogmus, M. Dostanic; M. Jahangiri; R. Sinha; W. F. Quiros-Solano; M. Mastrangeli; P. M. Sarro. (2019). "Sensor applications for organ-on-chip platforms." In: *International MicroNanoConference, Utrecht (NL), December 10-11, 2019*.
- H. Aydogmus; M. Dostanic; P. Motreuil-Ragot; M. Mastrangeli; P. M. Sarro. (2019). "Micro-engineered organs-on-chip". In: *Poster, presented at QBio Symposium, Utrecht (NL), October 29, 2019*.
- H. Aydogmus, L. Aslanbas, E. Orhan, M.S. Hanay. (2016). "Fabrication Of Silicon Nitride Membranes For Inertial Imaging in 2D." In: *13th International Workshop on Nanomechanical Sensing, Delft, The Netherlands, 22-24 June 2016*.